

ADAPTATIONS OF URANIUM HYDROMETALLURGY:
CASE STUDIES IN COPPER IN SITU LEACHING AND SUPERCRITICAL
EXTRACTION OF RARE EARTH ELEMENTS

A Dissertation

Presented to the Faculty of the Graduate School
of Cornell University

In Partial Fulfillment of the Requirements for the Degree of
Doctor of Philosophy

by

Laura Katherine Sinclair
May 2018

© 2018 Laura Katherine Sinclair

ADAPTATIONS OF URANIUM HYDROMETALLURGY:
CASE STUDIES IN COPPER IN SITU LEACHING AND SUPERCRITICAL
EXTRACTION OF RARE EARTH ELEMENTS

Laura Katherine Sinclair, Ph. D.
Cornell University 2018

ABSTRACT

In this work, two uranium hydrometallurgical processes were adapted for other metals: in situ leaching was adapted to copper and supercritical extraction was adapted to rare earth elements.

In situ leaching offers a way to extract copper from the subsurface without costly fragmentation. Applicability of in situ leaching is limited to deposits where sufficient permeability and leachable copper mineralogy exists. A computational copper in situ leaching model was developed to forecast recovered solution composition. This requires incorporating chemical reaction kinetics, mass transfer, and hydrology. These phenomena act over a range of length scales from centimeters up to hundreds of meters. Laboratory-scale leaching of ore provided data which was used to develop a list of geochemical reactions and associated rate laws. The risk of short-circuiting was treated probabilistically through geostatistical analysis of hydrophysical flow profiles, fracture spacing from Florence Copper's drill core database, and pumping tests. The geochemical reaction set and the geostatistical characteristics of hydraulic conductivity were brought together in a MATLAB model with a plugin to link to Geochemist's Workbench for

computing chemical reaction pathways. Results highlighted the importance of large-scale flow patterns in copper recovery.

The second part of this work pertains to rare earth element separation with supercritical carbon dioxide. Rare earth nitrates can be complexed with tributyl phosphate, thus forming a metal-ligand complex which is soluble in supercritical CO₂. Rare earth elements were recovered from roasted and sodium hydroxide digested bastnäsite concentrate using supercritical carbon dioxide extraction with nitric acid/tributyl phosphate adducts. A range of tributyl phosphate/nitric acid adduct compositions were tested. A drop in recovery at higher acidities may indicate condensation of aqueous droplets which create an equilibrium limitation. To investigate the role of water, neodymium and holmium nitrate were extracted into supercritical CO₂ with varying amounts of tributyl phosphate and water. Absorption spectroscopy was used to measure supercritical metal and water concentrations. It was found that holmium is preferentially extracted over neodymium. The results indicated that supercritical CO₂ can be used to extract and separate rare earth elements from primary materials.

BIOGRAPHICAL SKETCH

Laura Sinclair was born in Toronto, Canada. She showed an early interest in both science and art, but ultimately chose to pursue an engineering career. After obtaining her bachelor's degree in Chemical Engineering from the University of Toronto, she worked as a process engineer primarily focused on precious metal and copper hydrometallurgy. After taking a year off for a tri-continental bicycle trip, she began her graduate work at Cornell University.

ACKNOWLEDGEMENTS

I would like to thank Jeff, for always asking questions that pushed me to learn, John for providing an invaluable perspective, Larry for his direction and focus, and Don for his mathematical insight. A special thanks to Bob and his colleagues for teaching me so many cool new skills and introducing me to the beautiful state of Idaho. Polly and Bailey, thank you for everything you do for our group. I would like to thank Lou Derry and his whole group for letting me use his lab and all the loaned equipment and software. Thank you to Jared for all his help with statistics. To all the amazing students that I've met at Cornell (especially Arna), this experience would not have been the same without you! Lastly, to my family and Joey, for always believing in me and encouraging me to pursue my passions.

TABLE OF CONTENTS

Part I – In Situ Leaching of Copper	1
CHAPTER 1	2
1.1 In Situ Leaching	2
1.1.1 Background.....	2
1.1.2 Recovery Challenges	4
1.1.3 Containment.....	5
1.1.4 Restoration.....	5
1.2 The Florence Deposit	6
1.2.1 Geology	7
1.2.2 Hydrology.....	8
1.2.3 History	9
1.3 Goal and Scope.....	9
CHAPTER 2	12
2.1 Ground Ore Leach Tests	12
2.1.1 Samples.....	12
2.1.2 Procedure	12
2.1.3 Results	14

2.2	Box Leaching Tests	14
2.2.1	Samples.....	14
2.2.2	Procedure	14
2.2.3	Results	16
2.3	Geochemical Interpretation	16
2.3.1	Reaction Set.....	16
2.3.2	Acid Consumption.....	20
2.3.3	Kinetics.....	20
CHAPTER 3	25
3.1	Goal and Scope.....	25
3.2	Series Leach Test	25
3.2.1	Samples.....	25
3.2.2	Procedure	25
3.2.3	Results	27
3.3	Comparison with Geochemical Model.....	28
3.4	Petrographic Examination of Tails.....	30
CHAPTER 4	34
4.1	Goal and Scope.....	34
4.2	Available Data.....	36
4.2.1	Flow Profiles.....	36
4.2.2	Fracture Intensity	37
4.2.3	Pumping Tests	39
4.2.3.1	Single Well Pumping Tests.....	39
4.2.3.2	Multi-Well Pumping Tests	40
4.3	Hydraulic Conductivity from FEC Flow Profiles and Single Well Pumping Tests.....	41
4.3.1	Statistical Distribution of Values.....	42
4.3.2	Autocorrelation.....	43
4.3.2.1	Theory	43
4.3.2.2	Results	44
4.4	Test #1: Fracture Intensity Data	45
4.4.1	Approach	45
4.4.2	Distribution of Values	46
4.4.3	Subtraction of Global Trend.....	46
4.4.4	Correlogram.....	47

4.5	Test #2: Multi-Well Pumping Tests	48
4.5.1	Approach	48
4.5.2	Map Generation	49
4.5.3	Effective Conductivity.....	51
4.5.4	Pressure Field Computation.....	52
4.5.5	Results	53
CHAPTER 5	56
5.1	Model Structure.....	56
5.2	Model Results.....	60
5.2.1	Cases.....	60
5.2.2	Residence Time Distribution for Cases 1-6.....	61
5.2.3	Leachate Composition for Cases 1-6.....	63
5.2.4	Streamline Composition Maps	63
5.3	Discussion	67
CHAPTER 6	71
	Part II – Supercritical Extraction of Rare Earth Elements	75
CHAPTER 7	76
7.1	Rare Earth Elements.....	76
7.2	Conventional Processing.....	79
7.2.1	Concentration and Upstream Processing.....	79
7.2.2	Solvent Extraction	79
7.2.3	Extractants	81
7.2.3.1	Cationic Exchangers.....	81
7.2.3.2	Anionic Exchangers	82
7.2.3.3	Solvating Extractants.....	82
7.3	Supercritical Fluid Extraction	84
7.3.1	Background.....	84
7.3.2	Metal Complex Solubility Behavior.....	84
7.3.2.1	Models.....	84
7.3.2.2	Effect of Metal Properties	86
7.3.2.3	Effect of Temperature and Pressure	86
7.4	Supercritical Actinide and Lanthanide Extraction	87
7.4.1	Previous Work	87
7.4.2	Extraction Mechanism.....	89

7.4.3	Potential Application	91
7.5	Goal and Scope.....	93
7.5.1	Supercritical Extraction from Rare Earth Element Ores/Concentrates	93
7.5.2	The Role of Water in Extraction and Separation.....	94
7.5.3	Feasibility of Metal Separation with Pressure Reduction	94
CHAPTER 8	95
8.1	Goal and Scope.....	95
8.2	Materials.....	95
8.2.1	Reagents.....	95
8.2.2	Bastnäsite Concentrate	96
8.3	Pretreatment Methods	97
8.3.1	Roasting.....	97
8.3.1.1	Chemistry	97
8.3.1.2	Procedure.....	98
8.3.1.3	Characterization	98
8.3.2	Sodium Hydroxide Digestion	100
8.3.2.1	Chemistry	100
8.3.2.2	Procedure.....	100
8.3.2.3	Characterization	101
8.4	Atmospheric Leaching	102
8.5	Adduct Preparation.....	102
8.6	Supercritical Extraction.....	104
8.7	Results	109
8.7.1	Effect of Adduct Composition.....	109
8.7.2	Effect of Adduct Concentration in CO ₂	109
8.7.3	Selectivity	110
8.8	Discussion	113
8.8.1	Kinetics.....	113
CHAPTER 9	117
9.1	Goal and Scope.....	117
9.2	Materials.....	117
9.3	Procedure.....	118
9.4	Calibration.....	121
9.4.1	Neodymium	121

9.4.2	Holmium.....	122
9.4.3	Water	122
9.5	Results	124
9.5.1	TBP/H ₂ O/Supercritical CO ₂ System: Water Saturation	124
9.5.2	TBP/H ₂ O/REE nitrate/Supercritical CO ₂ System: Effect of Water Concentration ..	125
9.5.3	TBP/H ₂ O/REE nitrate/Supercritical CO ₂ System: Effect of TBP Concentration	126
9.5.4	Effect of Pressure.....	127
9.6	Equilibrium Model	128
9.6.1	Supercritical Phase Activities	128
9.6.2	Aqueous Phase Activities	129
9.6.3	Equilibrium Reactions	130
9.6.4	Fitting.....	135
CHAPTER 10	138
10.1	Goal and Scope.....	138
10.2	Materials and Procedure.....	138
10.3	Results	138
CHAPTER 11	140
11.1	Summary	140
11.2	Implications	142
11.3	Recommendations	143
	APPENDIX A – DATA FROM PREVIOUS COPPER IN SITU LEACHING PROJECTS.....	145
	APPENDIX B – GROUND ORE LEACHING TEST RESULTS	148
	APPENDIX C – BOX LEACHING TEST RESULTS.....	150
References	158

LIST OF FIGURES

Figure 1: Idealized diagram of an in situ leaching system for intact material	2
Figure 2: Some illustrations of past ISL projects. Left: the Mineral Park test site (Arizona, USA), in which wells were drilled into a hill adjacent to an open pit. Right: the Casa Grande well field (Arizona, USA), in which wells were drilled from an underground drift underneath a block caved leaching area. Drawings adapted from (Schmidt & Earley, 1997) and (M J Friedel, 1993).	3
Figure 3 - Aerial picture of the Florence Copper property (left) and pilot leaching wells at Florence (right). Photos courtesy of Florence Copper(Zimmerman et al., 2013).....	7
Figure 4 - Cross section of Florence Deposit. Adapted from(Zimmerman et al., 2013)	8
Figure 5 - Illustration of various length scales involved for in situ leaching	10
Figure 6 - Photographs of the drill core sections used to prepare the four ground ore leaching samples.....	13
Figure 7 - Cores in boxes being sealed with wax (left) and boxes being leached (right). Photo: SGS Metcon	15
Figure 8 - Modeled versus measured acid consumption.....	20
Figure 9 - Rate constant regressions from ground ore leach tests	23
Figure 10 - Core in shrink wrap before heating (left) and the seven vessels (right, courtesy of SGS)	26
Figure 11 – Elemental profiles from series leach test.....	27
Figure 12 - Measured and modeled concentrations of major ions in series leach test.....	29
Figure 13 – Iron oxide grain from PRT29 (left) and PRT33 (right).....	30
Figure 14 – Photomicrographs from core PRT35 from the series leach tests. The left-hand images are transmitted light, and the right-hand images are reflected light. The circular shapes are resin	

bubbles formed during the thin section impregnation process. Note the rimming of the iron oxides in the right-hand images..... 31

Figure 15 – X Ray Fluorescence scans of leached sample from PRT35. The x and y axes are in millimeters. 32

Figure 16 – Map view of the Florence resource showing locations where the three data types were sourced. The names of wells with flow profiles are shown. The coordinate system is Arizona Central State Plane Coordinates (NAD27 in feet) 36

Figure 17 – Flow rate profiles. Dashed lines indicate the screened interval. 38

Figure 18 - Statistical distribution of $\log_{10} K_{\text{profile}}$, fitted using maximum likelihood estimation. Points are plotted in increments of 0.5. Conductivities below $10^{-6.5}$ m/s are not graphed because this is where censorship begins..... 43

Figure 19 – Correlogram of the $\log_{10} K_{\text{profile}}$ dataset..... 45

Figure 20 – Fracture intensity data fit to a normal distribution. $\mu = 46.6$ (46.3, 47.0) fractures per meter and a $\sigma = 26.5$ (26.3, 26.8)..... 46

Figure 21 - Fracture intensity trend with depth. Binned averages are shown for comparison. Note that the parabolic function was fit to the raw (un-binned) data. 47

Figure 22 – Vertical and horizontal correlograms for fracture intensity, plotted with correlogram for $\log_{10} K_{\text{profile}}$ 48

Figure 23 – Example of one hydraulic conductivity map (left) and illustration of simulated pumping test (right). Note the cone of depression representing the pressure drop around the pumping well. 51

Figure 24 - Distribution of $\log_{10} K_{\text{pump, multi}}$ from the multi-well pumping tests, $\log_{10} K_{\text{simulation}}$ from simulations with correlated maps, and $\log_{10} K_{\text{simulation}}$ from simulations with uncorrelated maps 54

Figure 26 – Left: sample set of flow paths in map view for the heterogeneous cases (1-4). Note that the paths will be different for each of the 100 maps. Right: flow paths from homogenous cases (5 and 6)	62
Figure 27 - Residence time distributions of heterogeneous cases (100 maps) and homogenous case (1 map)	63
Figure 28 – Pregnant leach solution composition for Cases 1-6. Translucent areas represent 95% prediction intervals.....	64
Figure 29 - Maps of percent copper in ore along each streamline at the end of 4-year leaching period. Note that for Cases 1-4, only one of the 100 maps is shown.....	65
Figure 30 - Maps of pH along each streamline at the end of the 4-year leaching period. Note that for Cases 1-4, only one of the 100 maps is shown.....	66
Figure 31 – World mine production of rare earth oxides by country(United States Geological Survey, 2017).....	78
Figure 32 - Lighter (left) and heavier (right) rare earth oxide prices(United States Geological Survey, 2017).....	78
Figure 33 - Structure of REEs in concentrated nitrate solution, and coordinated with 1-4 TBP molecules	92
Figure 34 - XRD patterns of bastnäsite (CeCO ₃ F: PDF#00-011-0340. NdCO ₃ (OH): PDF#00-038-0400. BaSO ₄ : PDF#00-005-0448(The International Centre for Diffraction Data, 2013).....	96
Figure 35 - XRD pattern for roasted bastnäsite concentrate ((La,Ce)O ₂ F: PDF#00-057-0608. (Ce _{0.56} La _{0.44})O _{1.78} : PDF#01-071-6545)(The International Centre for Diffraction Data, 2013)....	99
Figure 36 - Measured particle size distribution of roasted and NaOH digested bastnäsite	99
Figure 37 - Setup for NaOH digestion.....	101

Figure 38 - XRD pattern of NaOH digested bastnäsite concentrate ($\text{Ba}_4\text{La}_2\text{O}_7$: PDF# 00-052-1324. $\text{Ce}(\text{OH})_3$: PDF#00-055-0556. $\text{Nd}(\text{OH})_3$: PDF#00-006-0601(The International Centre for Diffraction Data, 2013).....	102
Figure 39 - Process flow diagram of supercritical extraction setup.....	105
Figure 40 - Photograph of extraction system.....	106
Figure 41 - Equilibrium reactor and paced column. The column was later shortened and submerged in a constant temperature bath.	106
Figure 42 - Drawing of packed column	107
Figure 43 – Cerium recovery curves with various adduct compositions for roasted bastnäsite (left) and NaOH digested bastnäsite (right). Conditions: 34 MPa, 65°C, 5.2 +/-0.8 mol% adduct in CO_2	109
Figure 44 – Cerium recovery curves for various adduct concentrations for roasted bastnäsite (left) and NaOH digested bastnäsite (right). Conditions: 34 MPa, 65°C, 4 mol/L H^+ adduct composition	110
Figure 45 – Lanthanum reaction rate constant versus TBP concentration in CO_2 phase (left) and cerium reaction constant rate constant versus HNO_3 concentration in CO_2 phase (right).....	115
Figure 46 – Schematic of supercritical extraction system	118
Figure 47 - Photograph of extraction system.....	119
Figure 48 - Cell with Nd and Ho nitrate salts	119
Figure 49 - Diagram of spectroscopy cell (courtesy of Thar Technologies Inc.).....	120
Figure 50 - Spectra for Nd and Ho calibration. 17 MPa, 60°C.....	122
Figure 51 - Calibration curves for neodymium and holmium. 17 MPa, 60°C.....	122

Figure 52 - Spectra from water calibration showing two example TBP concentrations. 24 MPa, 60°C	123
Figure 53 - Calibration parity plot for water and TBP from water calibration. 24 MPa, 60°C. “Sc” abbreviation indicates supercritical phase.	124
Figure 54 - Equilibrium concentration of water in supercritical CO ₂ as a function of TBP concentration. “Sc” abbreviation indicates supercritical phase.	125
Figure 55 – Extraction of Nd, Ho, and H ₂ O as a function of water added	125
Figure 56 - Percent extraction of Nd, Ho, and H ₂ O at varying TBP concentrations with and without water added	126
Figure 57 - Fit supercritical Nd and Ho concentrations from equilibrium model. “Sc” abbreviation indicates supercritical phase.	137
Figure 58 – Experimentally determined pressure versus extraction curves for Nd and Ho nitrate salts extracted with varying amounts of TBP	139

LIST OF TABLES

Table 1 - Samples for ground ore leach tests	13
Table 2 - Mineralogy of adjacent head samples (by MLA) and leach test residues (by QEMSCAN)	15
Table 3 - Summary of conditions and results for box leach tests	16
Table 4 - Set of leaching and alteration reactions for geochemical model	18
Table 5 – Input values for Equations 1 and 2	21
Table 6 - Assumed rate controlling mechanism for each geochemical reaction	24
.Table 7 - Samples used in series leach test	25
Table 8 - Fracture intensity ratings used in drill core database	39
Table 9 – Data from single well pumping tests	39
Table 10 – Data from multi-well pumping tests	40
Table 11 – Fit parameters of the form $R=a*\exp(-Distance/d)$ for fracture intensity and $\log_{10} K_{profile}$ correlograms	48
Table 12 - Results from simulated pumping tests.....	54
Table 13 – Model inputs	58
Table 14 - Model scenarios.....	61
Table 15 - Applications of rare earth elements(Charalampides, Vatalis, Apostoplos, & Ploutarch- Nikolas, 2015).....	76
Table 16: Most commonly used REE extractants.....	83
Table 17: Elemental Composition of Raw and Pretreated Bastnäs site Samples.....	99
Table 18 - Nitric acid leaching recoveries of REEs in raw and pretreated bastnäs site concentrate samples.....	102

Table 19 - Stoichiometries in the form of $\text{TBP}(\text{HNO}_3)_x(\text{H}_2\text{O})_y$ for different adduct compositions	103
Table 20 - Supercritical extraction results. All runs were performed at 65°C and 34 MPa.....	111
Table 21 – Experimental Nd, Ho, and water extraction results	127
Table 22 – Adjustable fit parameters for the extended Pitzer equations based on literature(He et al., 2011; Z.-C. Wang et al., 2006)	132
Table 23 - Fit affinity constants for water extraction with TBP at 60°C	135
Table 24 – Fit affinity constants for 21 MPa, 60°C data	136

LIST OF ABBREVIATIONS

Abbreviation	Meaning
ICP OES	Inductively Coupled Plasma Atomic Emission Spectroscopy
ISL	In Situ Leaching
MLA	Mineral Liberation Analysis
QEMSCAN	Quantitative Evaluation of Minerals by Scanning Electron Microscopy
REE	Rare Earth Element
RTD	Residence Time Distribution
TBP	Tributyl Phosphate
XRD	X Ray Diffraction

LIST OF SYMBOLS

Symbol	Meaning	Unit
a	y intercept (nugget) for exponential correlogram	Unitless
A	Empirical constant in Chrastil model	Kelvin
$A_0 \dots A_7$	Linear interpolation coefficients	Unitless
a_s	Activity of species s	Unitless
A_ϕ	Parameter in extended Pitzer model as defined elsewhere (He, Dong, & Li, 2011; Pitzer, Wang, Rard, & Clegg, 1999; Z.-C. Wang, He, Wang, & Li, 2006)	$\text{kg}^{1/2}/\text{mol}^{1/2}$
b	Parameter in extended Pitzer model as defined elsewhere (He et al., 2011; Pitzer et al., 1999; Z.-C. Wang et al., 2006)	$\text{kg}^{1/2}/\text{mol}^{1/2}$
B	empirical constant in Chrastil model	Unitless
b_{screen}	Screened interval of well	m
b_{AB}	Stoichiometric ratio of mineral B to acid	mol/mol
C	Covariance matrix	Unitless
$C^{(0)}_{Nd(NO_3)_3}$	Parameter in extended Pitzer model as defined elsewhere (He et al., 2011; Pitzer et al., 1999; Z.-C. Wang et al., 2006)	kg^2/mol^2
$C^{(1)}_{Nd(NO_3)_3}$	Parameter in extended Pitzer model as defined elsewhere (He et al., 2011; Pitzer et al., 1999; Z.-C. Wang et al., 2006)	kg^2/mol^2
$C^{(2)}_{Nd(NO_3)_3}$	Parameter in extended Pitzer model as defined elsewhere (He et al., 2011; Pitzer et al., 1999; Z.-C. Wang et al., 2006)	kg^2/mol^2
$C^{(3)}_{Nd(NO_3)_3}$	Parameter in extended Pitzer model as defined elsewhere (He et al., 2011; Pitzer et al., 1999; Z.-C. Wang et al., 2006)	kg^2/mol^2
$C^{(0)}_{Ho(NO_3)_3}$	Parameter in extended Pitzer model as defined elsewhere (He et al., 2011; Pitzer et al., 1999; Z.-C. Wang et al., 2006)	kg^2/mol^2
$C^{(1)}_{Ho(NO_3)_3}$	Parameter in extended Pitzer model as defined elsewhere (He et al., 2011; Pitzer et al., 1999; Z.-C. Wang et al., 2006)	kg^2/mol^2
$C^{(2)}_{Ho(NO_3)_3}$	Parameter in extended Pitzer model as defined elsewhere (He et al., 2011; Pitzer et al., 1999; Z.-C. Wang et al., 2006)	kg^2/mol^2
$C^{(3)}_{Ho(NO_3)_3}$	Parameter in extended Pitzer model as defined elsewhere (He et al., 2011; Pitzer et al., 1999; Z.-C. Wang et al., 2006)	kg^2/mol^2
C_A	Concentration of acid	mol/m^3
d	Correlation length scale (range) for exponential correlogram	m
D_e	Effective diffusivity	m^2/s
D_{M1}	Distribution ratio of metal M_1	Unitless
I	Ionic strength	mol/kg
i, j, k	Indices for x, y, and z-dimension	Unitless
k	Surface reaction rate constant	m/s
k_{Chrastil}	Association number from Chrastil model	Unitless
k'	Simplified reaction rate constant (equivalent to $\frac{k b_{AB} M_B C_A (1 - \frac{Q}{K_{sp}})}{\rho_B r_g}$)	s^{-1}
k_{Chrastil}	Number of CO_2 molecules associated with a dissolved complex (parameter in Chrastil model)	Unitless
K	Hydraulic conductivity (general)	m/s
K_{profile}	Hydraulic conductivity estimated from flow profiles	m/s
$K_{\text{pump, single}}$	Hydraulic conductivity estimated from single-well pumping tests in field	m/s
$K_{\text{pump, multi}}$	Hydraulic conductivity estimated from multi-well pumping tests in field	m/s
$K_{\text{simulation}}$	Hydraulic conductivity estimated from simulated pumping tests	m/s
K_{sp}	Solubility product	Variable Units
M_B	Molar mass of mineral B	kg/mol
$m_C/m_X/m_i$	Molar concentration of cation C/ anion X/ ion i/salt CX/total salts	mol/kg
m_{CX}/m_T	Mass of species s in system	kg

M_w	Molecular weight of water	kg/mol
N_s	Moles of species s in system	moles
N_x, N_y, N_z	Number of grid points in x, y, and z directions	Unitless
p	Pressure	m (of water)
p_{in}	Pressure (inner solution)	m
p_{reg}	Pressure (regular term from interpolation of finite difference grid)	m
p_{well}	Pressure in well	m
$q(z)$	Flowrate per meter of screen out of well as a function of depth (z)	m ² /s
Q	Activity product	Variable units
Q_{well}	Total flowrate from well	m ³ /s
R	Autocorrelation function	Unitless
r	Distance between pumping and observation well	m
r_c	Radius of shrinking mineralized core	m
r_f	Radius of ore fragment	m
r_g	Radius of individual mineral grain	m
R_B	Reaction rate of mineral B per kg of ore	mol/s kg
R_{well}	Radius of well	m
S	Solubility of solute	kg/m ³
S_B	Surface area of mineral B per kg of ore	m ² /kg
t	Time	s
T	Temperature	Kelvin
V	Volume of system	L
x, y, z	Coordinates in 3-dimensional space	m
X_B	Fraction of mineral B reacted	Unitless
x_{well}, y_{well}	Coordinates of well	m
$x_{well\ interp}$	Distance between well coordinate and the adjacent x, y grid point	m
$y_{well\ interp}$		
y	Vector of values satisfying covariance relationship	Unitless
y_s	Mole fraction of species s in supercritical phase	Unitless
$y_{\Sigma C}$	Total mole fraction of cation C in supercritical phase (all species)	Unitless
$z_C/z_X/z_i$	Charge of cation C/ anion X/ ion i	Unitless
α	Proportionality constant between q(z) and K _{profile}	m ⁻¹
α_{B1}	Parameter in extended Pitzer model as defined elsewhere (He et al., 2011; Pitzer et al., 1999; Z.-C. Wang et al., 2006)	kg ^{1/2} /mol ^{1/2}
α_{B2}	Parameter in extended Pitzer model as defined elsewhere (He et al., 2011; Pitzer et al., 1999; Z.-C. Wang et al., 2006)	kg ^{1/2} /mol ^{1/2}
α_{C1}	Parameter in extended Pitzer model as defined elsewhere (He et al., 2011; Pitzer et al., 1999; Z.-C. Wang et al., 2006)	kg/mol
α_{C2}	Parameter in extended Pitzer model as defined elsewhere (He et al., 2011; Pitzer et al., 1999; Z.-C. Wang et al., 2006)	kg/mol
α_{C3}	Parameter in extended Pitzer model as defined elsewhere (He et al., 2011; Pitzer et al., 1999; Z.-C. Wang et al., 2006)	kg/mol
$\beta^{(0)}_{Nd(NO3)3}$	Parameter in extended Pitzer model as defined elsewhere (He et al., 2011; Pitzer et al., 1999; Z.-C. Wang et al., 2006)	kg/mol
$\beta^{(1)}_{Nd(NO3)3}$	Parameter in extended Pitzer model as defined elsewhere (He et al., 2011; Pitzer et al., 1999; Z.-C. Wang et al., 2006)	kg/mol
$\beta^{(2)}_{Nd(NO3)3}$	Parameter in extended Pitzer model as defined elsewhere (He et al., 2011; Pitzer et al., 1999; Z.-C. Wang et al., 2006)	kg/mol
$\beta^{(0)}_{Ho(NO3)3}$	Parameter in extended Pitzer model as defined elsewhere (He et al., 2011; Pitzer et al., 1999; Z.-C. Wang et al., 2006)	kg/mol
$\beta^{(1)}_{Ho(NO3)3}$	Parameter in extended Pitzer model as defined elsewhere (He et al., 2011; Pitzer et al., 1999; Z.-C. Wang et al., 2006)	kg/mol
$\beta^{(2)}_{Ho(NO3)3}$	Parameter in extended Pitzer model as defined elsewhere (He et al., 2011; Pitzer et al., 1999; Z.-C. Wang et al., 2006)	kg/mol
$\beta_{M1/M2}$	Separation factor between metals M ₁ and M ₂	Unitless

γ_{\pm}	Mean ionic activity coefficient as defined elsewhere (He et al., 2011; Pitzer et al., 1999; Z.-C. Wang et al., 2006)	Unitless
$\Delta x, \Delta y, \Delta z$	Grid spacing in x, y, and z directions	m
ε	Porosity	Unitless
θ_{NaEr}	Parameter in extended Pitzer model as defined elsewhere (He et al., 2011; Pitzer et al., 1999; Z.-C. Wang et al., 2006)	kg/mol
μ_1, μ_2	Local mean at points 1 and 2	Variable Units
μ_{global}	Mean of entire dataset	Variable Units
$\hat{\mu}_1, \hat{\mu}_2$	Sample estimator of local mean at points 1 and 2	Variable Units
$\hat{\mu}_{global}$	Sample estimator of mean of entire dataset	Variable Units
τ	Tortuosity	Unitless
$\nu_C/\nu_X/\nu_i/\nu_{CX}$	Stoichiometric coefficient of cation C/ anion X/ ion i/salt CX as defined elsewhere (He et al., 2011; Pitzer et al., 1999; Z.-C. Wang et al., 2006). Additional subscript "s" denotes species s.	Unitless
ρ	Density (general)	kg/m ³
ρ_f	Density of ore fragment	kg/m ³
ρ_B	Density of mineral B	kg/m ³
σ_1, σ_2	Local standard deviation at points 1 and 2	Variable Units
σ_{global}	Standard deviation of entire dataset	Variable Units
$\hat{\sigma}_1, \hat{\sigma}_2$	Sample estimator of local standard deviation at points 1 and 2	Variable Units
$\hat{\sigma}_{global}$	Sample estimator of standard deviation of entire dataset	Variable Units
$\psi_{NaErNO3}$	Parameter in extended Pitzer model as defined elsewhere (He et al., 2011; Pitzer et al., 1999; Z.-C. Wang et al., 2006)	kg ² /mol ²

PREFACE

Developing novel metallurgical extraction processes can be challenging. Ores can contain complex mineral mixtures which may require a series of physical and chemical mechanisms to separate. Furthermore, a novel process may not be transferrable between different deposits because of differences in mineralogy, economics, or other factors. The cyclical nature of metal markets presents an additional challenge to planning and executing long-term research goals.

Uranium is unique among metals. The high cost of radioactive waste disposal creates a strong incentive to minimize waste generation at every stage of the life cycle. This constraint has required hydrometallurgists to develop novel and unique waste-minimizing technologies. This includes uranium in situ leaching, which circumvents the need for waste rock and tailings. This also includes supercritical extraction for fission product separation, which eliminates the contaminated organic waste issues associated with solvent extraction.

While these technologies were initially only applicable for uranium, these processes may find applications for other metals as technical and economic circumstances change. For example, declining copper ore grades and increasing strip ratios may now present opportunities for copper in situ leaching. The challenges in separating rare earth elements may require advanced supercritical separation processes that were previously only applicable to uranium. Because of its unique constraints, uranium may therefore serve as a stepping stone to bring forward new hydrometallurgical processes which may become applicable to other metals.

Part I – In Situ Leaching of Copper

CHAPTER 1

INTRODUCTION

1.1 *In Situ Leaching*

1.1.1 Background

In situ leaching (ISL) is the circulation of a fluid through an ore deposit to dissolve a target metal or mineral, with subsequent return of the liquor to the surface for processing. Lixiviant is often applied to formations using a system of injection and recovery wells (Ahlness & Pojar, 1983) (see Figure 1). ISL has been commercially applied to a range of commodities, most notably in the extraction of uranium from roll front sandstone deposits. Both sulfuric acid and carbonate-based lixivants are used for uranium ISL, typically resulting in mineralization recoveries ranging from 70% to 90% for acid and 60% to 70% for carbonate (Taylor, Farrington, Woods, Ring, & Molloy, 2004). ISL has also been used for the recovery of evaporites such as soda ash, potash, and salt (Bartlett, 1998). In situ leaching has been applied for supplemental recovery of copper from established open pit and underground mines, but no commercial greenfield copper ISL projects have been constructed to date (Ahlness & Pojar, 1983). Past copper ISL projects were summarized in a recent review paper (L.K. Sinclair, 2015).

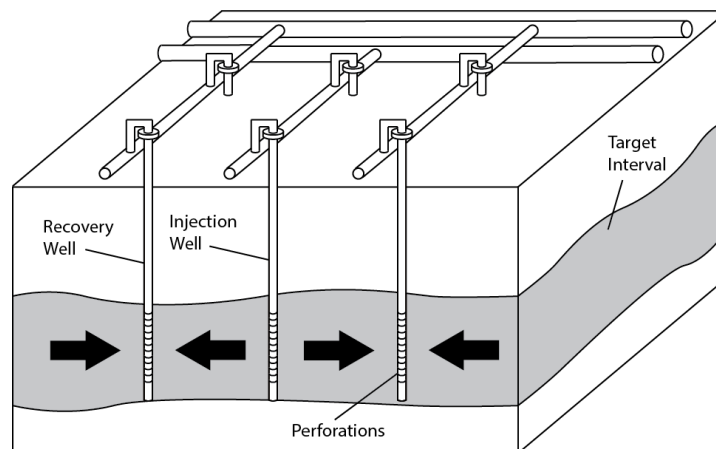


Figure 1: Idealized diagram of an in situ leaching system for intact material

Significant past projects include three detailed field tests by the Bureau of Mines: Santa Cruz, Casa Grande, and Mineral Park (see Figure 2). Projects undertaken by industry include Kimbley, Nacimiento, San Manuel, Florence (1997 pilot leach test), Mina Sur, and Safford. Of these, only San Manuel developed a commercial scale ISL system, which involved injection of lixiviant from the benches of an open pit. Available data from past projects are listed in Appendix A.

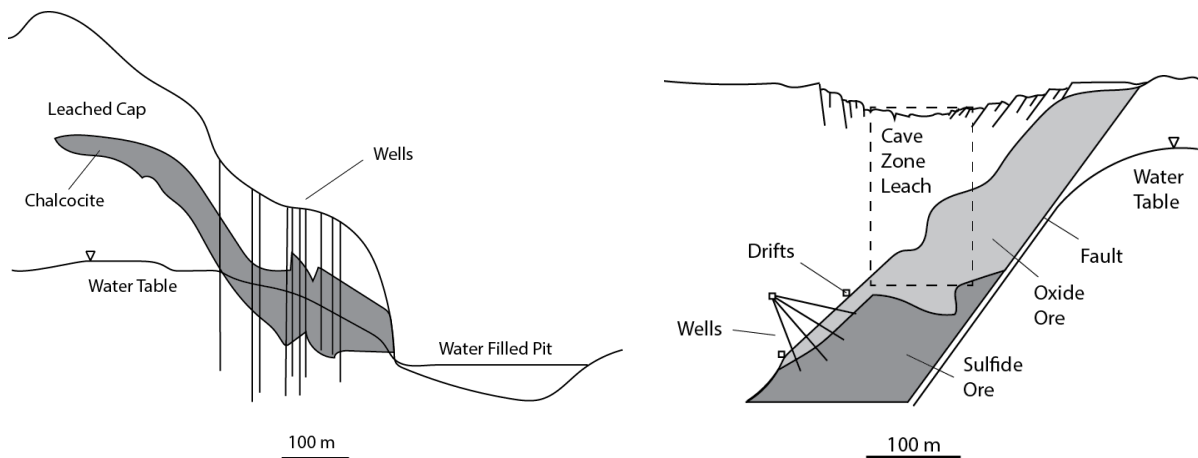


Figure 2: Some illustrations of past ISL projects. Left: the Mineral Park test site (Arizona, USA), in which wells were drilled into a hill adjacent to an open pit. Right: the Casa Grande well field (Arizona, USA), in which wells were drilled from an underground drift underneath a block caved leaching area. Drawings adapted from (Schmidt & Earley, 1997) and (M J Friedel, 1993).

Copper ISL has the potential to address many of the cost and environmental challenges resulting from declining ore grades and increased stripping ratios. Average U.S. copper ore grades, for example, have dropped from 3.5% in 1900 to less than 0.7% today (Classen et al., 2007). Low grades result in greater excavation, haulage, and comminution costs, and also pose environmental challenges including greater volumes of waste rock and tailings (J. Liu & Brady, 1998; Norgate, Jahanshahi, & Rankin, 2007; United States Congress Office of Technology Assessment, 1988). ISL is therefore well suited to low grade deposits because stripping, mining, hauling, and comminution are circumvented. It is potentially applicable to low grade deposits at a range of scales which would be uneconomical with conventional open pit or underground methods, or at

existing mines for extraction of copper ore below the cutoff grade (Hiskey, 1994; Rawlings & Johnson, 2006, pp. 58–59; United States Bureau of Mines, 1989). Major environmental benefits of ISL relative to conventional mining could include reduced energy consumption, near-elimination of waste rock and tailings, reduced land disturbance, reduced dust and noise, and potentially lower water consumption (Committee on Technologies for the Mining Industry, Committee on Earth Resources, & National Research Council, 2002; Hiskey, 1994; O’Gorman, Michaelis, & Olson, 2004; United States Bureau of Mines, 1989).

1.1.2 Recovery Challenges

The major economic challenge of ISL is limited exposure of copper minerals to the leach solution in complex subsurface flow paths (United States Bureau of Mines, 1989). Fractured systems have high permeability in areas of high fracture density or wide fracture aperture, which causes the leach solution to channel along these preferential pathways (Ramey & Beane, 1995). For example, flow profiles in boreholes found significant non-uniformity in flow rate along the screened interval at Safford, Santa Cruz, San Manuel, Mineral Park, and Florence (BHP Copper Growth and Technology Group, 1997a; L.M. Cathles et al., 1978; Nelson, 1991; Schmidt & Earley, 1997; Weber, Barter, & Kreis, 2000; Williamson, 1998). At Casa Grande, post-leach drill cores revealed that most fractures had seen no contact with leach solution (Schmidt, Earley, & Friedel, 1994), and post-leach drill cores at Safford revealed major channeling issues (L.M. Cathles et al., 1978). Largely as a result of this channeling behavior, copper ISL operations have reported estimated recoveries in the range of 20%-70% (Bernal & Venero, 1985; Lewis, Chase, & Bhappu, 1976; Niemuth, 1994; O’Gorman et al., 2004), whereas conventional heap leaching generally results in 65%-90% recovery (S. Young, 1999).

Evidence from several projects seems to suggest flow channeling increases as leaching progresses, just as flow channeling increases over time in conventional heap leaching (Bartlett, 1998; Catanach, 1976). For example, comparison of pre-leaching and post-leaching bromide tracer tests at Santa Cruz showed enhanced connectivity of primary flow paths (Weber et al., 2000). At Casa Grande, an analysis of well pressure and flow rate data over a two year leaching period showed that the statistical distribution of hydraulic conductivity became bimodal as leaching progressed (Schmidt et al., 1994).

1.1.3 Containment

One of the greatest environmental challenges for ISL is the containment of the leaching fluids in the target ore zone to prevent contamination of groundwater outside of the leached area (Bhappu, 1985; United States Bureau of Mines, 1989). The design of the pumping system for containment can draw upon existing groundwater remediation technology. Containment of leach solutions below the water table generally requires maintaining constant inward flow of groundwater by applying a production pumping rate that exceeds the injection rate and either discharging or evaporating the excess water (Huss, Welhener, Driehick, Roman, & Lenton, 2014; Kreis, 1994; Zimmerman et al., 2013). Net inward groundwater flow was used at Santa Cruz (Kreis, 1994) and the 1997 Florence pilot (Zimmerman et al., 2013). Unsaturated formations represent an additional challenge for solution containment due to the downward gravity-driven movement of leach solutions. For example, the pilot leaching project at San Manuel saw 13.5% of injected solutions lost during well-to-well leaching above the water table (Beane & Ramey, 1995).

1.1.4 Restoration

Post-leach restoration draws upon existing environmental groundwater remediation technologies, including water treatment technology, hydrologic geochemical modeling, and well

configurations. Past experience in uranium ISL illustrates the range of options available for aquifer restoration. In general, most uranium ISL operators begin by withdrawing water from the wellfield to stimulate inward flow within the formation. This water may be sent to the plant to recover additional uranium with the raffinate directed to water treatment, disposal wells, or evaporation ponds. At later stages, water is continuously pumped from the field to a water treatment plant (typically reverse osmosis) and recirculated to the formation. Reducing agents such as hydrogen sulfide or reducing bacteria may be added to the formation to decrease the solubility of contaminants such as uranium and heavy metals (J. Davis & Curtis, 2007; Taylor et al., 2004). Formation rinsing can be complicated by a range of geochemical interactions which can result in mobilization or sequestration of ions. This can include the re-dissolution of gypsum precipitates formed during the leaching phase (Earley & Johnson, 2012; G M Mudd, 2001) and the release of ions adsorbed onto clays (J. Davis & Curtis, 2007).

Many previous copper and uranium ISL operations did not attempt any groundwater restoration, in some cases resulting in aquifer contamination that required major cleanup operations. Examples include the Nacimiento copper ISL operation in New Mexico (Coward, Rudy, & Milne, 2004), and the Soviet-era Königstein uranium ISL operation in East Germany (Lottermoser, 2003, p. 207; Gavin M. Mudd, 2001).

1.2 The Florence Deposit

The Florence Copper resource in central Arizona consists of copper oxide mineralization hosted by quartz monzonite and granodiorite porphyry intrusions (see Figure 3). The reserve is 313 million metric tonnes with an average copper grade of 0.358% Cu. Copper is primarily hosted in chrysocolla, copper-bearing clays, and copper-bearing iron oxides. The most common fracture coatings are iron oxides (45%) bare fractures (25%), clays (24%), gypsum and/or calcite (4%), and

chrysocolla (2%). Fracturing is very dense, with fractures spaces just a few inches apart on average (J. R. Davis, 1997; Johnson, 2017; Zimmerman et al., 2013).



Figure 3 - Aerial picture of the Florence Copper property (left) and pilot leaching wells at Florence (right). Photos courtesy of Florence Copper (Zimmerman et al., 2013)

1.2.1 Geology

The basement rock consists of Pinal Schist, formed 1.7 billion years ago. The Schist was then intruded by quartz monzonite and Precambrian diabase dikes, ranging from centimeters to meters in thickness. The monzonite was also cut by several Laramide intrusions which consisted primarily of granodiorite porphyry about 62 million years ago, resulting in fracturing and alteration by hydrothermal fluids (J. R. Davis, 1997; Zimmerman et al., 2013).

Faulting and uplift then resulted in oxidation and further fracturing. From 36 to 17 million years ago, several sedimentary units were deposited, including weathered bedrock, breccias, and gravels. Later faulting uplifted the Florence deposit as a horst block, and it was exposed to weathering. Coarse conglomerate from the surrounding mountains then filled the basin and buried the deposit, followed by several layers of sand, silt, gravel, mud, and clay (Zimmerman et al., 2013).

Today, the several layers of clay and conglomerate overlies a highly fractured copper oxide zone, which itself overlies a copper sulfide zone (see Figure 4). The transition from oxide to sulfide is sharp with very little secondary enrichment present. Structural features include a series of

northwest trending faults zones formed after mineralization. This includes the Party Line fault and the Sidewinder fault. These faults are associated with the presence of sheared breccia material, measuring up to 15 m in thickness (BHP Copper Growth and Technology Group, 1997b).

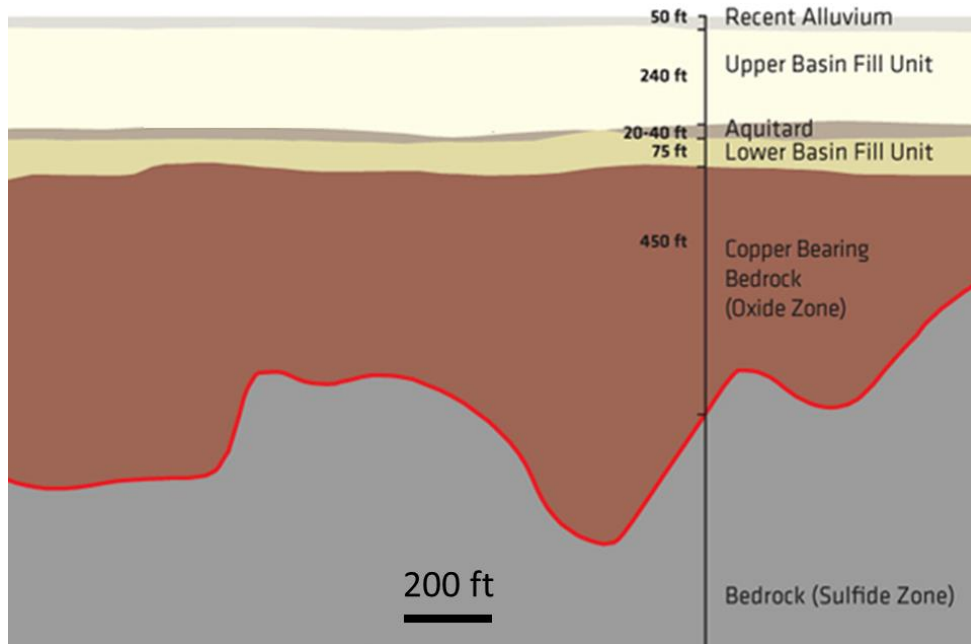


Figure 4 - Cross section of Florence Deposit. Adapted from (Zimmerman et al., 2013)

1.2.2 Hydrology

The depth to the water table ranges from approximately 30 to 70 m. Two aquifers are present in the Florence region, separated by a low-permeability clay layer approximately 120 m below ground surface. As discussed in later sections, hydraulic conductivity within the targeted oxide zone ranges from approximately 10^{-8} to 10^{-4} m/s. Hydraulic conductivity is approximately 2 orders of magnitude lower in the sulfide unit. Hydraulic conductivity in the low-permeability clay layer is approximately 10^{-10} m/s. The background gradient is minimal: the regional groundwater flow is to the north-north west at a rate of approximately 55 m per year. The water levels tend to rise in the winter and fall in the summer, but have remained relatively stable since the early 1980s (BHP Copper Growth and Technology Group, 1997a; Zimmerman et al., 2013).

1.2.3 History

The Florence property has passed between many different owners over the last 40 years, including Conoco, Magma, and BHP Copper. The property has been evaluated for in situ leaching several times. Most significantly, BHP Copper conducted a 100-day pilot in situ leaching test at Florence using four injection wells and nine recovery wells in 1997. The BHP pilot also included tracer testing before and after leaching. Florence Copper Inc. (now a subsidiary of Taseko Mines Ltd.) purchased the property from BHP Copper in 2000.

The copper oxide zone at Florence will be developed using ISL technology for copper recovery. Florence is an ideal target for in situ leaching due to the very dense fracturing, high permeability, and soluble copper mineralization (J. R. Davis, 1997; Zimmerman et al., 2013). Copper recovery will involve direct injection of 10 g/L aqueous sulfuric acid and recovery of copper-laden solution using an array of injection and recovery wells. Resource blocks will be developed sequentially from east to west across the deposit, with injection and recovery wells arranged in a five-spot pattern with 15 m spacing. Copper will be recovered from the pregnant leach solution with solvent extraction and electrowinning, and the raffinate will then be reconstituted with acid and recirculated to the deposit. Maintaining a constant inward flow of groundwater will confine the lixiviant to the target formation. After four years of leaching, each resource block will undergo a two-year rinse cycle to restore groundwater quality.

1.3 Goal and Scope

The goal of this study is to model in situ leaching of the Florence resource to forecast key metrics such as copper recovery and acid consumption. This requires incorporating chemical reaction kinetics, mass transfer, and hydrology. These phenomena act over a range of length scales from centimeters up to hundreds of meters (see Figure 5).

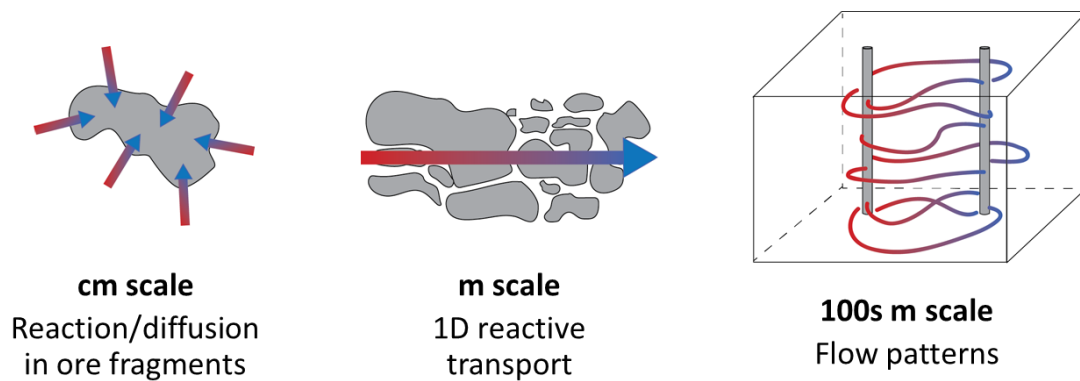


Figure 5 - Illustration of various length scales involved for in situ leaching

At the centimeter level, acid interacts with mineral grains in a set of leaching, alteration, and precipitation reactions. If the mineral grains lie on fracture surfaces, they will react directly with leach solution. If the mineral grains lie within the rock fragments, reaction rates will be limited by the rate of diffusion through micropores. Modeling in situ leaching therefore requires understanding which geochemical reactions take place, and forecasting reaction rates based on principles of kinetics and/or diffusion mass transfer. As discussed in the following sections, key data for centimeter-level phenomena comes from two sets of experiments: bottle roll tests performed at Cornell on samples of ground ore, and a set of 16 leaching experiments performed on whole core sections by a contractor.

At the meter level, solution chemistry evolves as the fluid moves from injection to recovery well. Acid concentration is highest near the injection well and depletes as the fluid moves downstream and acid is consumed. Various ions accumulate, including copper, aluminum, magnesium, potassium, iron, and calcium. This can lead to precipitation reactions as the fluid moves away from the injection point. Understanding these long-range reactive transport phenomena can be important for forecasting copper recovery. Key data for meter-scale phenomena come from a contractor's leaching tests on seven cores connected in series.

Finally, at the scale of tens to hundreds of meters, spatial patterns of hydraulic conductivity influence the degree of short-circuiting between wells. This has important implications for metal recovery during in situ leaching. Because the Florence system will involve over two thousand wells, and because hydrology data is not available from every well spot, the risk of short-circuiting is treated probabilistically. Key data for this exercise comes from hydrophysical flow profiles gathered in 1996 by the consultant Colog Inc., fracture spacing data from Florence Copper's drill core database, and pumping tests conducted by Magma Copper Company and Brown and Caldwell in the years 1994-1995.

As discussed in the following sections, the leaching system was investigated at each of these length scales using a range of data types. The results were brought together into a computational model of the Florence system. The model is capable of outputting probabilistic distribution curves of the recovered solution composition.

CHAPTER 2

CENTIMETER SCALE – GROUND ORE AND BOX LEACHING TESTS

2.1 *Ground Ore Leach Tests*

2.1.1 Samples

The first stage in understanding the Florence system was to identify the key geochemical reactions when the Florence ore is contacted with sulfuric acid, and to measure the reaction kinetics at the mineral grain level (in the absence of diffusion limitations). Three drill cores from the Florence deposit were sent to Cornell University, where four samples were selected to cover a range of rock types. Each sample was ground to -10 mesh (1.68 mm) in a mechanical grinder. Particle size distributions were measured by dry sieving. Elemental compositions were measured by hydrofluoric and nitric acid digestion followed by Inductively Coupled Plasma Optical Emission Spectrometry (ICP OES). The drill holes, depths, descriptions, elemental composition, and particle size distributions are summarized in Table 1 and photographs of the ore samples (before grinding) are shown in Figure 6. It should be noted that Si assays could not be obtained due to evaporation of SiF_6 during hydrofluoric acid digestion.

2.1.2 Procedure

In each test, 100 g of ore was combined with 300 mL of dilute sulfuric acid solution. Acid concentrations ranged from 2 to 16 g/L to observe leaching behavior over a range of pH values. Each slurry was leached for 72 hours in a rotating polypropylene bottle. 5 mL samples were taken at 1, 2, 4, 8, 24, 48, and 72 hours. These samples were centrifuged, and the aqueous phase was submitted for ICP OES to determine elemental concentrations. At each sample point, the leach solution was titrated for free acid and more acid was added if needed to maintain a constant pH.

At the end of the run, the tails were filtered, washed, and dried. The elemental composition of the tails was measured by hydrofluoric acid and nitric acid digestion followed by ICP OES.



Figure 6 - Photographs of the drill core sections used to prepare the four ground ore leaching samples

Table 1 - Samples for ground ore leach tests

Sample		1	2	3	4
Drill Hole Code		CMP 11-06	CMP 11-06	CMP 11-06	CMP 11-01
Depth (m)		237	234	183	189
Description		Broken rock fragments in fine grained matrix. Probably fault breccia.	Soft, moderately fractured rock. Chrysocolla visible on fractures.	Highly fractured, red colored rock.	Very white rock. Lots of chrysocolla.
Elemental composition (wt%)	Al	6.23	5.84	7.02	6.12
	Ca	0.54	0.79	0.69	0.33
	Cu	0.46	0.42	0.41	0.84
	Fe	1.63	1.66	1.47	0.67
	K	4.36	4.38	4.86	4.79
	Mg	0.21	0.23	0.38	0.39
	Na	1.37	1.72	1.79	0.97
Particle size distribution by weight (μm)	-1680 +500	60%	53%	63%	68%
	-500 +354	10%	9%	9%	7%
	-354 +177	7%	11%	12%	12%
	-177 +88	10%	8%	7%	10%
	-88 +53	6%	6%	3%	3%
	-53	8%	13%	7%	0%

2.1.3 Results

Elemental concentrations are shown in Appendix B. Mass balances for major elements were satisfactory, generally within 5%.

2.2 *Box Leaching Tests*

2.2.1 Samples

The purpose of the box leaching tests were to observe the reaction rates in intact drill core for a variety of acid concentrations. Cores from six drill holes were submitted to SGS Metcon in Tucson, Arizona for acid leach testing. Chemical and mineralogical compositions of the cores prior to leaching could not be measured directly. Therefore, core sections adjacent to the leached intervals were used for characterization, since they were the closest available proxies. These adjacent head samples were crushed to 100% passing 10 mesh (1.68 mm) and underwent mineralogy and particle size distribution evaluation using Mineral Liberation Analysis (MLA). This is a mineral identification system which uses Scanning Electron Microscopy and Energy Dispersive X Ray Spectroscopy.

2.2.2 Procedure

Sixteen 71 x 41 x 11 cm Plexiglass boxes were constructed, and each box was loaded with four sections from the same drill core (see Figure 7). Paraffin wax was used to coat the bottom and top of the box and to seal the ends of the core to prevent solution channeling along the sides. The spaces between the drill core sections were filled with acid-washed silica sand. Sulfuric acid at 5, 10, or 20 g/L was fed to the boxes at 5 liters per day, with flow directed perpendicular to the long axes of the drill cores. Leaching periods ranged from 134 to 228 days. The outlet solution was collected daily for copper and iron assaying as well as free acid titration. Each week, the cumulative daily outlet solutions were assayed for a suite of elements using ICP OES. If the copper

tenor exceeded 1.8 g/L Cu, the solution underwent solvent extraction to remove the copper and was then recirculated to the feed tank. If the copper tenor was below 1.8 g/L, the solution was recirculated without solvent extraction. Acid was added to the feed tank to maintain the desired inlet acidity. The goal was to simulate commercial operation, in which pregnant solution undergoes solvent extraction and acidification before recirculation to the injection wells.

After leaching, each box was rinsed with site water for periods ranging from 8 to 78 days. The leach residues were then dried, weighed, crushed, and submitted for QEMSCAN (a method similar to MLA – see Table 2). Copper and iron assays were also performed on the residues.



Figure 7 - Cores in boxes being sealed with wax (left) and boxes being leached (right). Photo: SGS Metcon

Table 2 - Mineralogy of adjacent head samples (by MLA) and leach test residues (by QEMSCAN)

Mineral	Formula	Head (vol%)	Residue (vol%)
Quartz	SiO ₂	17-42%	25-42%
K-feldspar/ K Al Silicate	KAlSi ₃ O ₈ / KAlSiO ₄	40-53%	31-59%*
Plagioclase	(Na,Ca)(Al,Si) ₄ O ₈	3-23%	
Albite	NaAlSi ₃ O ₈	0.03-4%	
Calcite	CaCO ₃	0-3%	0-0.8%
Gypsum	CaSO ₄ ·2H ₂ O	0-0.01%	0-1%**
Iron Oxides	FeO(OH) / Fe ₂ O ₃	1-4%	0.4-2%***
Biotite	K(Mg,Fe) ₃ (AlSi ₃ O ₁₀)(OH) ₂	1-4%	0.9-4%****
Chlorite	(Mg ₃ ,Fe ₂)Al(AlSi ₃)O ₁₀ (OH) ₈	0.3-2%	
Muscovite/Kaolinite	KAl ₂ (AlSi ₃ O ₁₀)(OH) ₂ / Al ₂ Si ₂ O ₅ (OH) ₄	0.02-1%	4-22%

*Sum of all feldspars

**Sum of gypsum, alunite, and jarosite

***Sum of iron and manganese oxides

****Sum of all biotites and chlorites

2.2.3 Results

Conditions for the box leach tests are shown in Table 3 and aqueous assays are shown in Appendix C. Many of the leach tests showed an initial high rate of copper leaching followed by an abrupt shift to slower recovery. Copper grade of the original drill cores was calculated by mass balance, based on the aqueous assays and the measured copper content the solid leach residue. The same method was used to calculate original iron grades. Acid consumption was calculated based on daily titrations of the feed and discharge solutions.

Table 3 - Summary of conditions and results for box leach tests

Box leach test #	Feed acid concentration (g/L)	Calculated copper grade (wt%)	Calculated iron grade (wt%)	Days leached	Average fracture spacing (cm)	Copper recovery (wt%)*	Acid consumption (kg acid/kg Cu)*
1	5	0.46	1.82	152	1.4	34.6	7.2
2	10	1.00	1.96	152	3.1	81.6	6.4
3	10	0.58	1.30	152	1.9	71.8	11.1
4	20	0.49	0.69	152	2.0	26.5	82.0
5	5	1.22	1.55	152	3.5	32.4	4.4
6	10	0.32	1.70	152	2.7	62.2	24.3
7	10	0.52	1.67	154	3.1	50.6	21.1
8	20	0.74	0.78	154	1.0	68.5	15.9
9	5	0.77	2.38	186	1.0	42.7	8.0
10	10	0.55	1.38	134	1.8	53.9	13.0
11	10	0.87	1.69	186	1.9	64.5	11.3
12	20	0.48	0.65	176	2.4	39.6	24.5
13	5	0.33	1.27	176	1.3	30.6	13.6
14	10	0.47	1.21	134	2.9	38.8	10.5
15	10	0.38	1.75	228	2.0	65.0	13.3
16	20	0.28	1.65	227	1.3	62.7	33.6

*Both copper recovery and acid consumption apply to the leaching period only (the rinsing period is not included)

2.3 Geochemical Interpretation

2.3.1 Reaction Set

The first step in the geochemical interpretation was to identify the set of leaching, alteration, and precipitation reactions taking place during the ground ore leach tests and the box leach tests. The geochemical software package Geochemist's Workbench was used. Geochemist's Workbench

has an extensive database of minerals, with their associated properties and solubility products. The B-dot method is used to calculate activity coefficients. This is a modified version of Debye-Hückel, which is considered acceptable for dilute solutions (<1 M) (Bethke, 1996).

The feed sample mineralogy, solid/liquid ratio, and acid concentration was inputted into Geochemist's Workbench. Both the ground ore leach tests and box leach tests were modeled as mixed systems with a constant pH to reflect the periodic acid addition. Using a trial and error approach, a set of reactions was identified which showed reasonable agreement with the following constraints:

- Aqueous ion concentrations in ground ore and box leaching tests
- Measured acid consumption in ground ore and box leaching tests
- Mineralogical examination of head and tail samples (available for box leach tests only)
- Previous metallurgical and petrographic studies of the Florence resource
- Previous studies of similar fluid-rock interactions

The list of reactions is shown in Table 4. Further details on the geochemical interpretation work is outlined in two recent conference presentations (L.K. Sinclair, 2015; Laura K. Sinclair, 2016).

Table 4 - Set of leaching and alteration reactions for geochemical model

Name	Reaction	Evidence
Anorthite Leaching	$\text{CaAl}_2\text{Si}_2\text{O}_8(\text{s}) + 8\text{H}^+(\text{aq}) \rightarrow \text{Ca}^{2+}(\text{aq}) + 2\text{Al}^{3+}(\text{aq}) + 2\text{SiO}_2(\text{aq}) + 4\text{H}_2\text{O}(\text{aq})$	<ul style="list-style-type: none"> Anorthite was the only mineral that could explain the increase in aqueous aluminum concentrations. Potassium feldspar and sodium plagioclase (albite) likely did not undergo significant leaching, given the minimal increase in potassium and sodium concentrations. This is supported by previous studies which have shown that anorthite leaches much more quickly than potassium feldspar or albite under acidic conditions (Brantley, Kubicki, & White, 2008). Calcium concentrations reached gypsum saturation in all the ground ore and box leach tests, even those with no calcite present. This supports the assertion that calcium is released by anorthite.
Anorthite Alteration	$\text{CaAl}_2\text{Si}_2\text{O}_8(\text{s}) + 2\text{H}^+(\text{aq}) + \text{H}_2\text{O}(\text{aq}) \rightarrow \text{Al}_2\text{Si}_2\text{O}_5(\text{OH})_4(\text{s}) + \text{Ca}^{2+}(\text{aq})$	<ul style="list-style-type: none"> A significant increase in the volume of muscovite/kaolinite clays was observed in the mineralogy analysis of the box tests (see Table 2). Alteration of feldspars to kaolinite is a well-known geochemical phenomenon during supergene alteration of porphyry deposits (Hackman, 1982). Because alteration to kaolinite is more favorable under high pH conditions, it is postulated that the alteration occurred at the beginning of the box tests.
Calcite Leaching	$\text{CaCO}_3(\text{s}) + \text{H}^+(\text{aq}) \rightarrow \text{Ca}^{2+}(\text{aq}) + \text{HCO}_3^-(\text{aq})$	<ul style="list-style-type: none"> Calcite reacted completely in most of the box tests (test # 4 was an exception, with 0.8% calcite in the residue). This is consistent with the high reaction rate of calcite observed in previous studies (Brantley et al., 2008; Murphy, Oelkers, & Lichtner, 1989).
Goethite Leaching	$\text{FeO}(\text{OH})_{(\text{s})} + 3\text{H}^+(\text{aq}) \rightarrow \text{Fe}^{3+}(\text{aq}) + 2\text{H}_2\text{O}(\text{aq})$	<ul style="list-style-type: none"> MLA suggest that a mixture of iron oxides constitute approximately half of the iron content of the ore. Goethite was used to model this iron oxide mixture because it was identified on fracture surfaces by Davis (J. R. Davis, 1997) and previously used in geochemical modeling of the Florence system by Brewer (Brewer, 1998) and Earley (Earley & Johnson, 2012). However, it is recognized that in reality the Florence ore contains a range of iron oxides including goethite, jarosite, hematite, etc. (J. R. Davis, 1997).

Name	Reaction	Evidence
Montmorillonite Alteration	$\text{Ca}_{0.11}\text{K}_{0.11}\text{Mg}_{0.33}\text{Al}_{1.67}\text{Si}_4\text{O}_{10}(\text{OH})_{2(s)} + 0.99\text{H}^+_{(aq)} \rightarrow 0.11\text{Ca}^{2+}_{(aq)} + 0.11\text{K}^+_{(aq)} + 0.33\text{Mg}^{2+}_{(aq)} + 0.66\text{SiO}_{2(aq)} + 0.66\text{H}_2\text{O}_{(aq)} + 0.835\text{Al}_2\text{Si}_4\text{O}_{10}(\text{OH})_{2(s)}$	<ul style="list-style-type: none"> • MLA studies of the box leach test ore indicated significant montmorillonite clay. Previous fracture coating studies have indicated significant clay content in the Florence resource, with montmorillonite as the most common clay type (J. R. Davis, 1997). • Previous cation exchange capacity experiments on fracture scrapings from Florence found that calcium and lesser magnesium were the dominant cations released by ion exchange. Other test work confirmed the release of calcium, and also minor magnesium, sodium, and potassium from clays (BHP Copper Growth and Technology Group, 1997a). • Previous Electron Dispersive X Ray Spectroscopy measurements indicated that clay samples contained approximately 1% Mg and 1.5% Ca (Brewer, 1998).
Chrysocolla Leaching	$\text{CuSiO}_3 \cdot 2\text{H}_2\text{O}_{(s)} + 2\text{H}^+_{(aq)} \rightarrow \text{Cu}^{2+}_{(aq)} + \text{SiO}_{2(aq)} + 3\text{H}_2\text{O}_{(aq)}$	<ul style="list-style-type: none"> • Chrysocolla is the dominant copper mineral in the Florence resource, and is the most easily leached (J. R. Davis, 1997). Although leachable copper likely consists of a mixture of several minerals, chrysocolla was used as a proxy for this mixture.
Gypsum Precipitation	$\text{Ca}^{2+}_{(aq)} + \text{SO}_4^{2-}_{(aq)} + 2\text{H}_2\text{O}_{(aq)} \rightarrow \text{CaSO}_4 \cdot 2\text{H}_2\text{O}_{(s)}$	<ul style="list-style-type: none"> • Final solutions in the ground ore leach tests and box leach tests were saturated with gypsum • Gypsum was present in the box leach residues
Antlerite Precipitation and Re-Dissolution	$3\text{Cu}^{2+}_{(aq)} + 4\text{H}_2\text{O}_{(aq)} + \text{SO}_4^{2-}_{(aq)} \rightarrow \text{Cu}_3(\text{SO}_4)(\text{OH})_{4(s)} + 4\text{H}^+_{(aq)}$	<ul style="list-style-type: none"> • Modeling indicated that the solution will become saturated with antlerite as it moves away from the injection point, at a pH of approximately 4.5.
Diaspore Precipitation and Re-Dissolution	$\text{Al}^{3+}_{(aq)} + 2\text{H}_2\text{O}_{(aq)} \rightarrow \text{AlOOH}_{(s)} + 3\text{H}^+_{(aq)}$	<ul style="list-style-type: none"> • Modeling indicated that the solution may become saturated with diaspore as it moves away from the injection point, depending on the aluminum concentration. • Aluminum precipitation was observed in the BHP pilot leaching test in 1997. This was attributed to precipitation of aluminum hydroxides.

2.3.2 Acid Consumption

The model of each metallurgical test resulted in reasonable agreement with the measured acid consumption (see Figure 8). This provides a useful test of the geochemical model. On average, the model slightly underestimates acid consumption, possibly because of constraints imposed by Geochemist's Workbench. For example, montmorillonite clays in the Geochemist's Workbench database contained little calcium, but more calcium-rich clays in the geochemical model would have resulted in a higher modeled acid consumption.

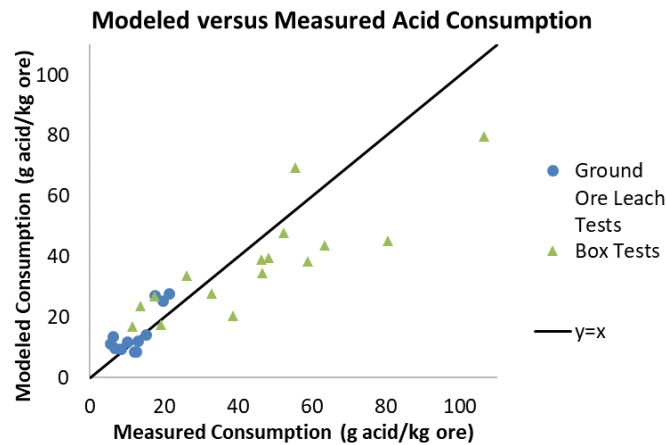


Figure 8 - Modeled versus measured acid consumption

2.3.3 Kinetics

After the set of reactions had been identified, the next step was to establish a rate law for each reaction. Two models were used: reaction limited and diffusion limited.

If mineral grains are present on fracture surfaces where they can easily contact solution, the reaction rate is expected to be reaction limited. The kinetic rate law is given in Equation 1 (see Nomenclature for definitions of symbols) (Smith, 1970). Note that the activity product Q quantifies the degree of saturation of the mineral, therefore implying that the mineral will stop leaching when saturation is reached, and will precipitate if oversaturated.

$$R_B = kC_A S_B (1 - X_B)^2 \left(1 - \frac{Q}{K_{sp}}\right) \quad \text{Eq 1}$$

Where R_B is the rate of reaction for mineral B, k is a rate constant, C_A is the acid concentration, S_B is the surface area per kilogram, X_B is the reaction extent, Q is the activity product, and K_{sp} is the solubility product (see Definitions of Symbols). If grains of a mineral are distributed within the rock fragment, the reaction rate will be limited by the rate of acid diffusion through the micropore network. (It was found that the Thiele modulus (Smith, 1970) is approximately 10, which implies diffusion-limited reactions for matrix minerals.) This results in a reaction rate given below (Smith, 1970):

$$R_B = \frac{3D_e C_A}{\rho_f r_f^3 \left(\frac{1}{r_c} - \frac{1}{r_f}\right)} \left(1 - \frac{Q}{K_{sp}}\right) \quad \text{where } D_e \equiv \frac{D_A \varepsilon}{\tau} \quad \text{Eq 2}$$

Where D_A is the molecular diffusivity of acid, ε is the fragment porosity, τ is the tortuosity, ρ_f is the fragment density, r_f is the fragment radius, and r_c is the radius of the unreacted core (additional variables defined under Equation 1). Variables from Equations 1 and 2 were estimated as follows:

Table 5 – Input values for Equations 1 and 2

Variable	Value	Source
r_f	0.017 m	(J. R. Davis, 1997)
ρ_f	2403 kg/m ³	(Dixon, 2011)
ε	1%	Assumption
τ	2	(Bartlett, 1973)
D_A	2 x 10 ⁻⁹ m ² /s	(Leaist, 1984)
S_B	100 m ² /kg	(Raghavan & Fuerstenau, 1977)

To estimate the reaction rate constant " k ", the aqueous elemental concentrations from the ground ore leach tests were fitted to a simple shrinking core model (this is an re-arranged version of Equation 1) (Smith, 1970).

$$1 - (1 - X_B)^{\frac{1}{3}} = \frac{kb_{AB}M_B C_A (1 - \frac{Q}{K_{sp}})}{\rho_B r_g} t \quad \text{Eq 3}$$

Where b_{AB} is the stoichiometric ratio between acid and mineral B, M_B is the atomic mass of mineral B, r_g is the radius of a mineral grain, and t is time (remaining variables defined below Equations 1 and 2). This equation relies on the assumption that each mineral grain is fully liberated.

The regressions are shown in Figure 9. The fit k values are shown on the charts. Each reaction underwent an initial rapid transient phase for the first 1-2 hours. This is a common phenomenon in leaching – reaction rates are high at short time scales due to fines, roughness on the particle surface, and non-stoichiometric mineral dissolution (Brantley et al., 2008). Allowing for a y intercept effectively removes the initial transient phase from the regression. Sample 4 had a very different anorthite transient phase from the other three samples, but the slope was the same. This is potentially due to fast aluminum leaching from chrysocolla at short time scales followed by slower aluminum leaching from anorthite at longer time scales.

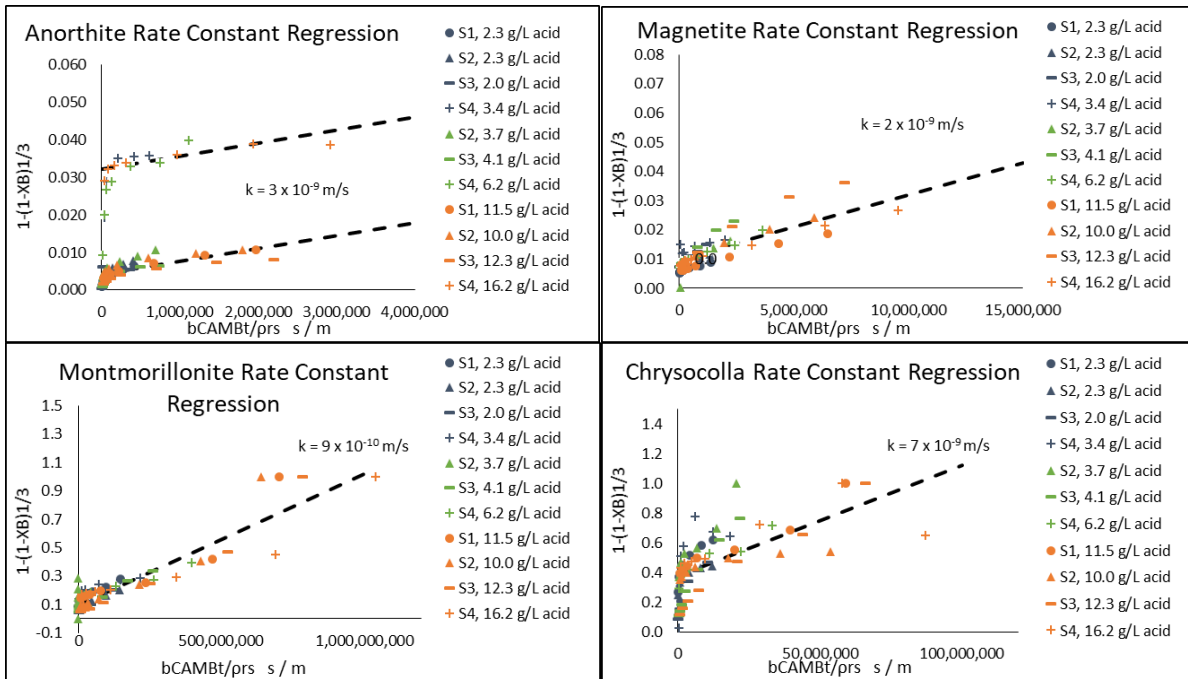


Figure 9 - Rate constant regressions from ground ore leach tests

For each reaction, several pieces of evidence were used to determine the rate-limiting mechanism (diffusion or reaction control). Types of evidence included:

- Comparing elemental concentration profiles in the ground ore and box leaching tests
- Previous petrographic and geochemical studies of the Florence ore
- Knowledge of the geologic mechanism by which each mineral formed

The assumed rate controlling mechanism for each reaction is listed in Table 6, along with justifying evidence.

Table 6 - Assumed rate controlling mechanism for each geochemical reaction

Reaction	Assumed Rate Law	Evidence
Anorthite Leaching	Diffusion controlled	Anorthite is a rock-forming mineral, and is therefore present in the bulk rock matrix
Anorthite Alteration	Diffusion controlled	It was found in the box tests that approximately half of the anorthite leached, whereas the remaining half was altered to kaolinite. Therefore, the anorthite leaching and alteration rates were assumed to be equal.
Calcite Leaching	Reaction controlled	Although the rate constant for calcite leaching could not be calculated from the ground ore leach tests due to complications from gypsum saturation, it is well known that calcite reacts very quickly (Murphy et al., 1989).
Goethite Leaching	Reaction controlled	Significant iron oxides are present on fracture surfaces (J. R. Davis, 1997).
Montmorillonite Alteration	Diffusion controlled	The box leaching tests showed a much slower rate of magnesium leaching than the ground ore leach tests. This was surprising as previous petrographic examination has shown significant montmorillonite presence on fracture surfaces (BHP Copper Growth and Technology Group, 1997a; J. R. Davis, 1997). It is possible that fractures containing clays are not easily accessed by acid due to low permeability, and therefore acid can only access the clay in these fractures by diffusion.
Chrysocolla Leaching	Half diffusion controlled and half reaction controlled	Petrographic examination of the Florence ore has revealed that chrysocolla is approximately equally distributed between the matrix and fracture surfaces (Ramey & Beane, 1995). Most of the box leaching tests showed an initial high rate of copper dissolution followed by a period of slower copper dissolution (see Appendix C).
Gypsum Precipitation	Reaction controlled	Precipitation is generally very fast
Antlerite Precipitation and Re-Dissolution	Reaction controlled	Precipitation is generally very fast Precipitates form on fracture surfaces, and therefore face no diffusion limitations during re-dissolution
Diaspore Precipitation and Re-Dissolution	Reaction controlled	Precipitation is generally very fast Precipitates form on fracture surfaces, and therefore face no diffusion limitations during re-dissolution

CHAPTER 3

METER SCALE – SERIES LEACHING TEST

3.1 *Goal and Scope*

Once the geochemical model (reaction set and associated rate laws) had been established, the next step was to validate the model using larger-scale test work. This also allows for observing the effect of evolving solution composition as the fluid moves through the subsurface, including important low-acidity phenomena such as precipitation.

3.2 *Series Leach Test*

3.2.1 Samples

Seven sections of drill core, each sixty centimeters in length, were delivered to SGS in Tucson. All samples were of the Precambrian Quartz Monzonite rock type. These were named PRT 29 through PRT 35. Characteristics of these drill core sections are shown in Table 7. Based on mass balance calculations performed at the end of testing, the calculated copper grade of the seven cores as a whole was 0.64%.

Table 7 - Samples used in series leach test

Sample Name	Drill Hole Number	Depth Interval ft	Fractures per ft	Dry Weight kg
PRT29	CMP11-05	645-647	>15	7.54
PRT30	CMP11-05	648-650	>15	7.21
PRT31	CMP11-06	595-597	11-15	7.47
PRT32	CMP11-06	598-600	11-15	6.72
PRT33	CMP11-06	758-760	>15	7.57
PRT34	CMP11-02	651.5-653.5	Breccia	7.32
PRT35	CMP11-02	662-664	Breccia	7.72
Total				51.6

3.2.2 Procedure

The drill core sections were sealed inside individual cylindrical vessels using a combination of wax and shrink wrap (see Figure 10). The cores were connected end to end in series, thus forming 4.2 m of total core length. Water was fed at 0.8 L/day to fill the pores; this took 12 days.

The total effective pore volume, based on the water required to saturate the cores, was 10.3 L. Days 13 and 14 were used for pressurization to the formation pressure of approximately 830 kPa.

On day 15, leaching began using a mature raffinate solution from previous experiments, acidified to 10 g/L. Recycled raffinate was used because it more accurately reflects the re-acidified solvent extraction raffinate which will be used for leaching in the field. The elevated gangue ion concentrations in the recycled raffinate were expected to have important effects on the solution chemistry, particularly on precipitation behavior.

On day 35, when copper was first detected at the series outlet, the outlet solution underwent solvent extraction and the raffinate was returned to the feed. Recirculation continued for the remainder of the test. The outlet solution from PRT 31 and 35 was collected daily, and the outlet solution from the remaining five vessels was sampled weekly on a rotating basis. These samples were analyzed for copper, iron, ORP, pH, and free acid. It should be noted that although the nominal flow rate was 800 mL/day, the samples taken totaled 50 mL/day. Each week, the cumulative daily outlet solutions were combined and assayed for a suite of elements using ICP OES. The leaching period lasted for 211 days in total, with 171.3 L (16.6 equivalent pore volumes) pumped though including both open cycle and locked cycle phases.



Figure 10 - Core in shrink wrap before heating (left) and the seven vessels (right, courtesy of SGS)

After the copper concentration in the outlet fell below 0.5 g/L, the leaching period was terminated and the rinsing period began. Rinsing included several stages, including rinsing with site water, and site water with sodium bicarbonate, ferric iron, and chloride. Rinsing lasted 342 days in total. This analysis focuses on the leaching period – an analysis of the rinsing behavior is not included. At the end of rinsing, the residue was dried, weighed, and crushed. Samples were assayed for total copper, sequential copper, and iron analyses.

3.2.3 Results

Overall copper recovery during the leach period was 68.1%. The total acid consumption during the leaching phase was 1151 g (5.12 kg of acid/kg of copper). It should be noted that additional acid consumption and copper recovery also occurred during the subsequent rinsing phase. The profiles of all major elements are shown in Figure 11. Note that the copper concentration increases and then decreases again due to the solvent extraction of copper from the weekly leach solutions.

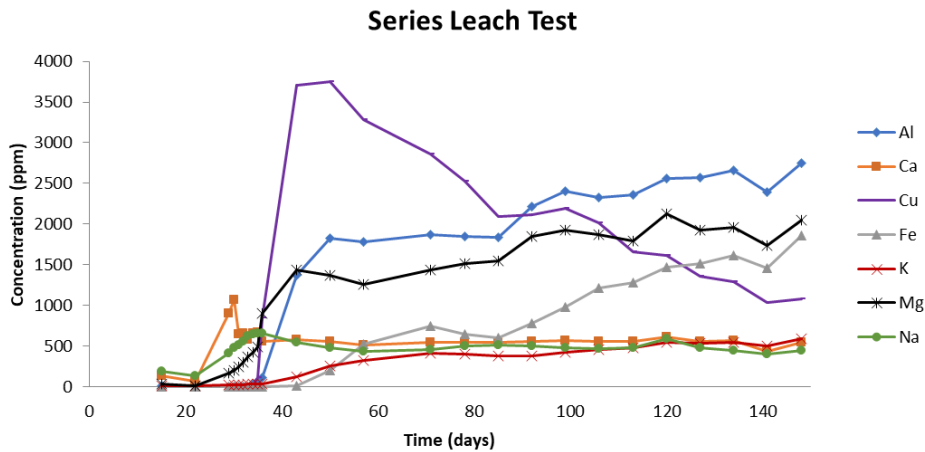


Figure 11 – Elemental profiles from series leach test

3.3 *Comparison with Geochemical Model*

To validate the geochemical model derived in section 2.3, the series leach test was modeled using a one-dimensional reactive transport model in Geochemist's Workbench, and the model output was compared to the experimental results. The solution from the series leach test had a maximum ionic strength of approximately 0.5 mol/L, within the acceptable range for the B-dot activity coefficient method.

First, the properties of the ore were inputted into Geochemist's Workbench. Mineralogical information on the samples was not available, so the mineral composition of the cores was assumed to be the average composition from the box tests. The only exception to this was chrysocolla and goethite: because copper and iron assays for the series leach tests were available, the assumed chrysocolla and goethite content were adjusted to reflect this. The feed solution was initialized to reflect the measured composition of mature raffinate.

Second, the reaction list with their associated rate laws was inputted into the model. Recall that each reaction was assigned either a surface-limited rate law (see Equation 1), or a diffusion-limited rate law (see Equation 2).

Finally, flow through the ore was simulated. Time steps were automatically selected by the software as required. Solvent extraction, reacidification, and recirculation of the weekly leachate solutions was incorporated into the model using a MATLAB plug-in feature.

The elemental composition of the outlet solution is compared with the measurements in Figure 12. The model shows reasonable agreement with the measurements. It was decided that further adjustment of the geochemical model was not necessary. The model also showed good agreement with the outlet pH and ORP throughout the leaching period. As an additional check, the acid

consumption predicted by the model was approximately 70% of the measured acid consumption. This was considered satisfactory agreement.

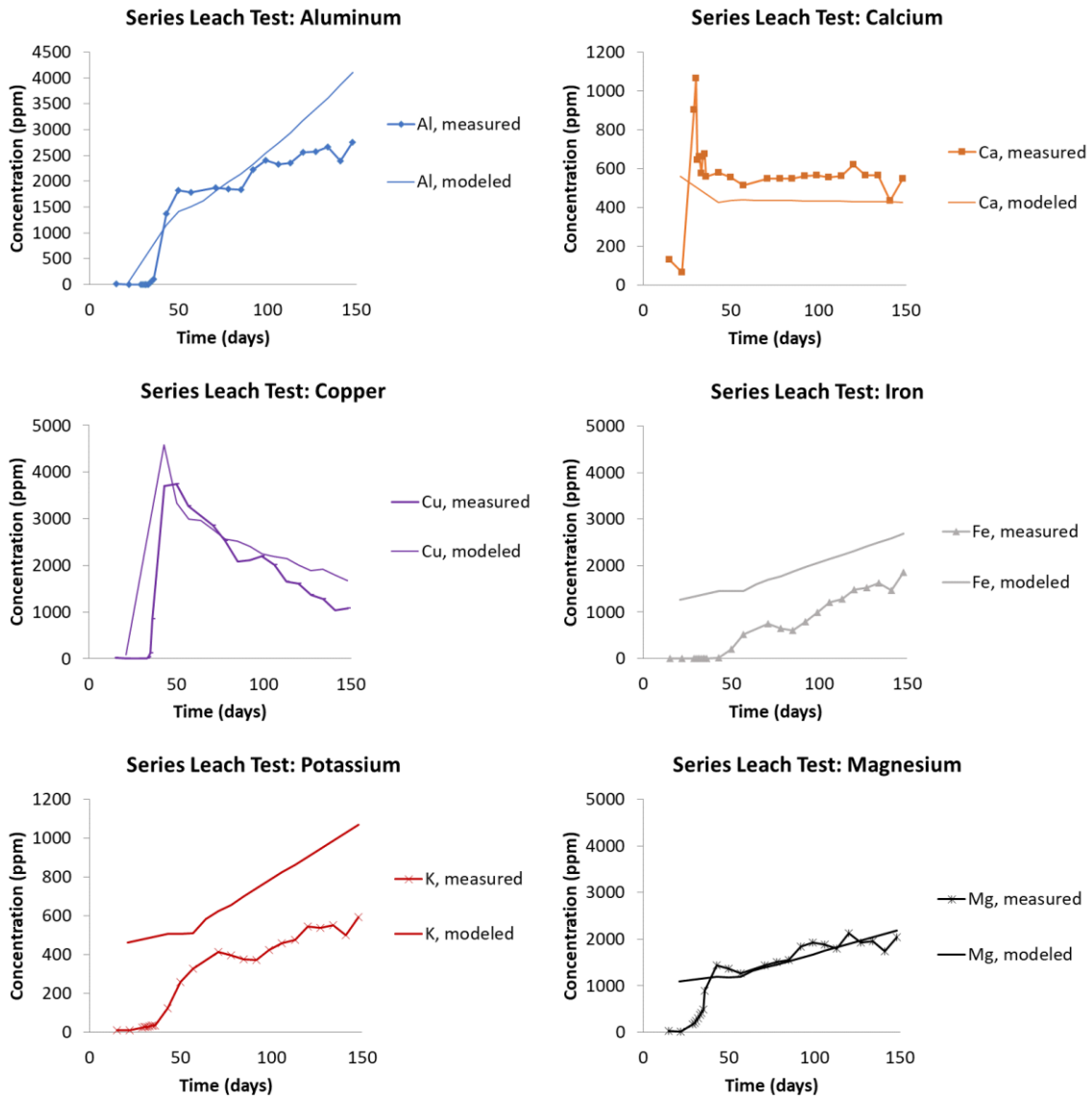


Figure 12 - Measured and modeled concentrations of major ions in series leach test

The model shows that a high-acid zone develops near the inlet, which slowly migrates downstream as the acid-consuming minerals are depleted. Surface-controlled leaching of fracture coated chrysocolla results in a copper front which slowly moves through the ore. The copper front is abated by the precipitation of antlerite at first, but the antlerite re-dissolves as the acid front

advances. An aluminum front follows behind (abated by diaspore precipitation), and a small iron front which roughly coincides with the high-acid zone. These precipitation reactions buffer the outlet pH at approximately 4 at first, and then the pH decreases gradually with the depletion of acid-consuming minerals.

3.4 Petrographic Examination of Tails

At the end of the rinsing phase, small pieces of the leached cores were sent to Cornell for examination. One piece was recovered from PRT29 (first core in series), one from PRT33 (fifth core in series), and one from PRT35 (last core in series). Thin sections were made from these ore pieces to observe mineral grains at the micron scale. Microscopy of these thin sections focused on iron oxide grains adjacent to fractures because they are easy to identify and because they are expected dissolution and precipitation points. Some examples of these iron oxide grains are shown in Figure 13.

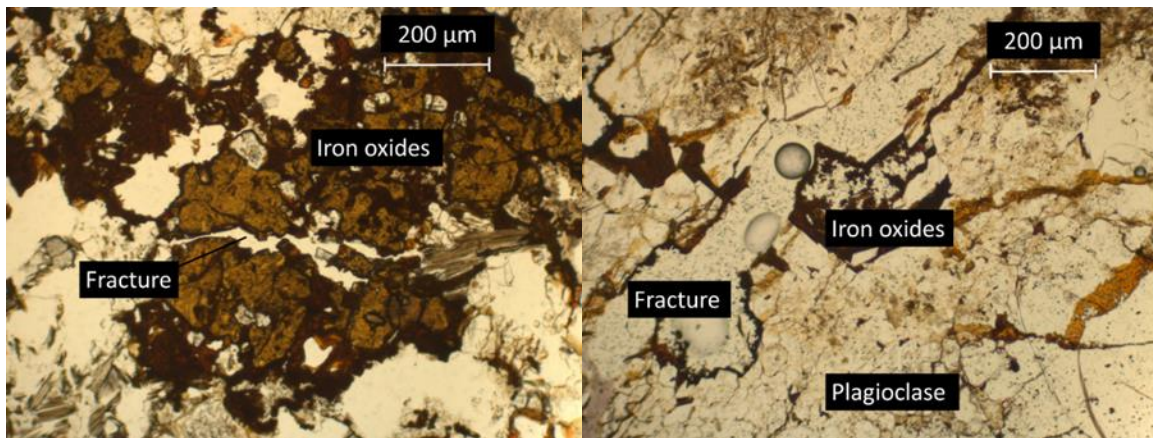


Figure 13 – Iron oxide grain from PRT29 (left) and PRT33 (right)

Two iron oxide grains observed in PRT35 were particularly interesting as they showed rimming of the iron oxide grains when observed with reflected light (see Figure 14). This can be indicative of leaching and/or re-precipitation of iron oxide minerals. Though such alteration may

have taken place during the weathering process, the delicate texture of this iron rimming is more likely to be the result of the leaching process rather than weathering over thousands of years.

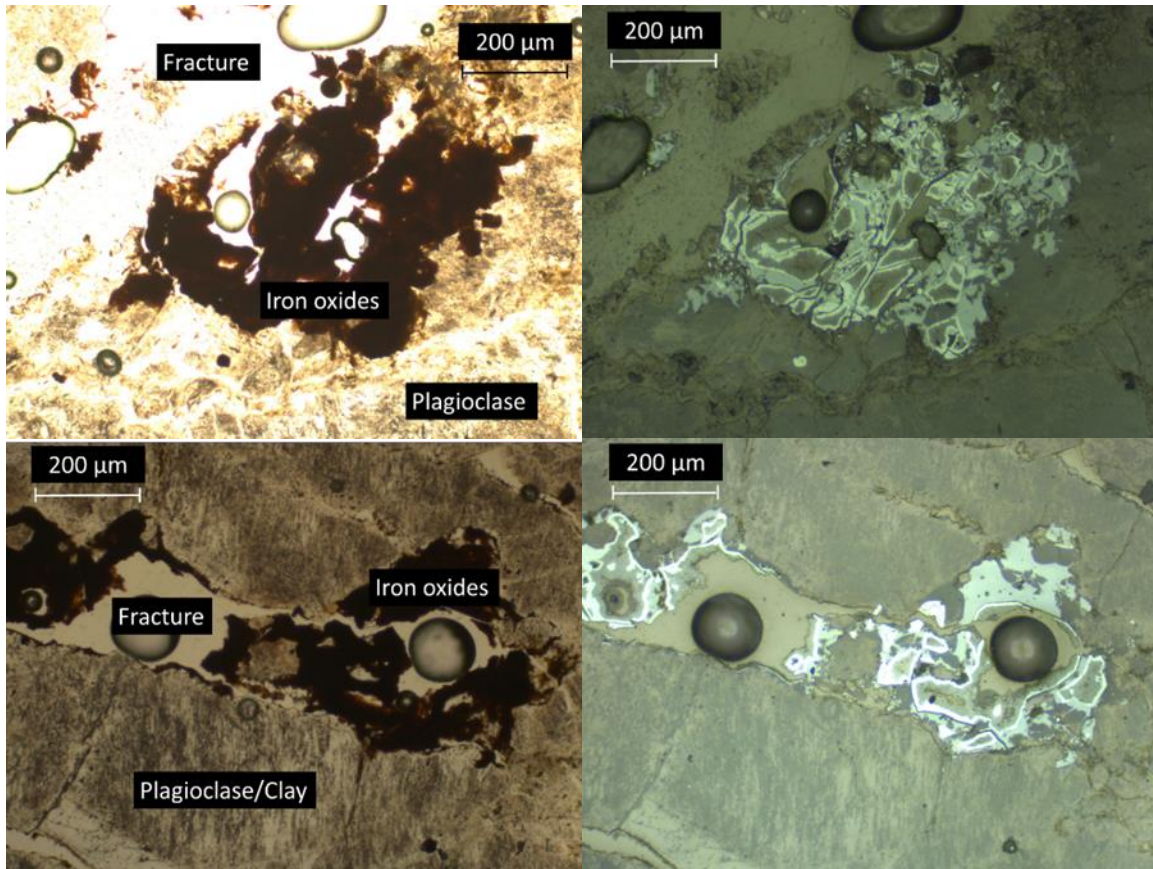


Figure 14 – Photomicrographs from core PRT35 from the series leach tests. The left-hand images are transmitted light, and the right-hand images are reflected light. The circular shapes are resin bubbles formed during the thin section impregnation process. Note the rimming of the iron oxides in the right-hand images.

X Ray Fluorescence at the Cornell University CHESS synchrotron facility was also used to create elemental maps of the leached sample from PRT35. The scan was taken with 50 μm step size and 0.02 second exposure time. The Vortex detector was set to a 90° angle to the X Ray beam path, and the sample surface was 45° to both incident X Rays and the detector. The ore was taped on 4 sides therefore the shadow of tape can be identified on some of the element maps. It should be noted that absolute concentrations can be difficult to measure with this method, and therefore

the color bar is included without units. These color maps are useful for qualitative comparison – for example, for seeing whether a particular element is present primarily on the fragment surface, in microfractures, or in the rock matrix.

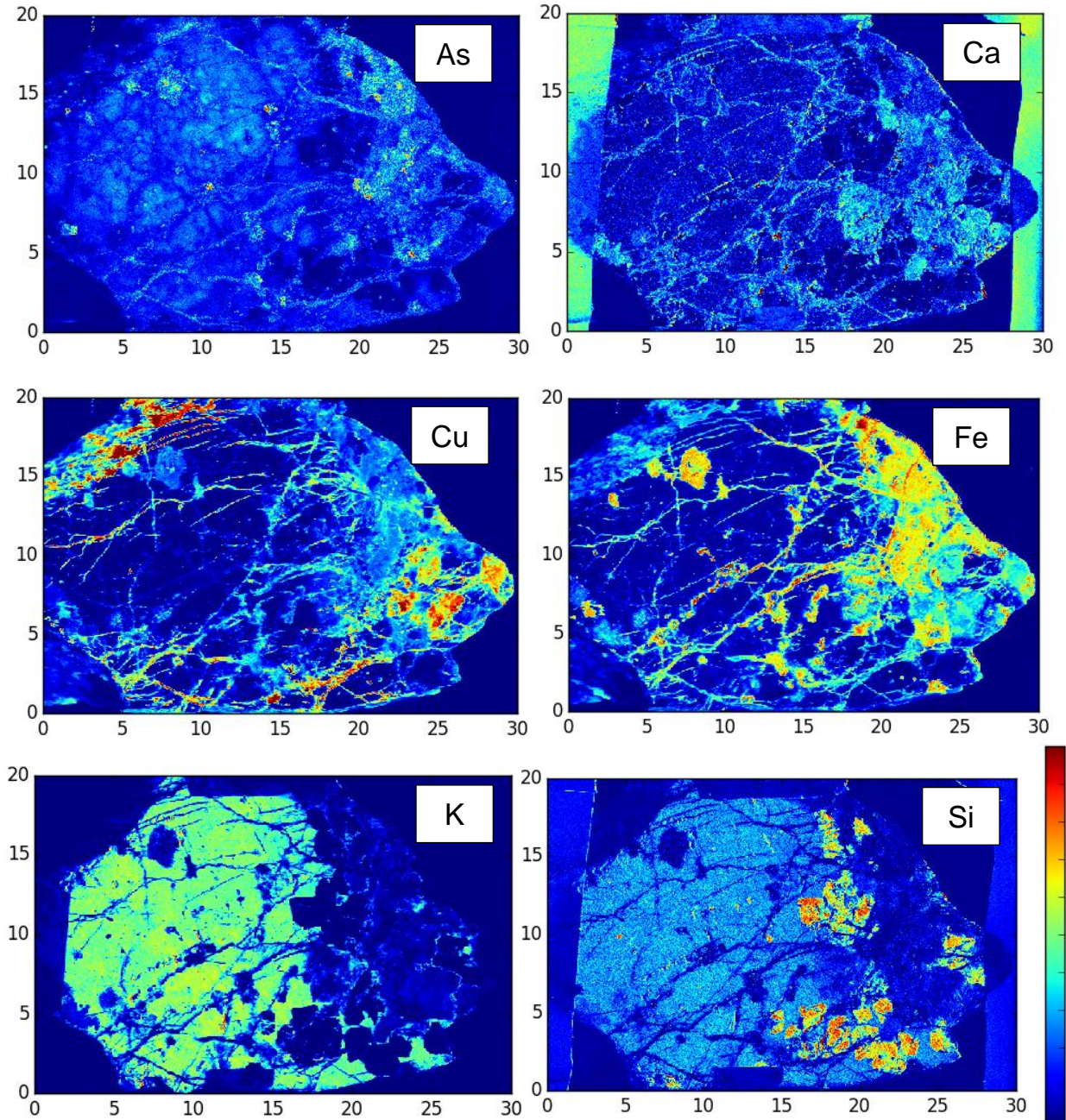


Figure 15 – X Ray Fluorescence scans of leached sample from PRT35. The x and y axes are in millimeters.

These scans show qualitative agreement with several assumptions which relate to the geochemical model:

- The copper is present both in microfractures and near the surface of the fragment. This agrees with the use of both diffusion-limited and reaction-limited reaction models for copper minerals.
- Calcium is present primarily in the matrix, which agrees with the use of a diffusion-limited model for anorthite leaching
- The presence of iron primarily on the right side of the fragment surface agrees with the use of a reaction-limited model for goethite leaching. It should be noted that some of the non-fracture iron shown on the elemental map may coincide with biotite grains.

CHAPTER 4

HUNDREDS OF METERS SCALE – HYDRAULIC CONDUCTIVITY

4.1 Goal and Scope

At the largest length scale, copper recovery via in situ leaching is affected by large-scale flow patterns through the fractured rock. While fracturing in the Florence deposit is very dense, with fractures spaced just a few centimeters apart on average (J. R. Davis, 1997; Zimmerman et al., 2013), the uneven distribution of fractures and hydraulic conductivity throughout a well spot can lead to channeling. The channeling of fluids through high-conductivity zones can limit contact with less conductive zones and affect recovery (L.K. Sinclair & Thompson, 2015). Several previous in situ leaching projects in fractured reservoirs have been hindered by channeling through preferential pathways; examples include the Casa Grande project and the Safford project (L.M. Cathles et al., 1978; Schmidt et al., 1994). It is therefore vital to understand the geostatistical characteristics of hydraulic conductivity.

The Florence deposit is modeled as a continuum with spatially varying hydraulic conductivity. Because of the large number of wells which will eventually be used for leaching (2218), and because hydrologic data is not available at every well spot location, this study aims to characterize the hydraulic conductivity on a geostatistical basis across the wellfield as a whole, rather than at any particular location. In this way, the risk of channeling can be evaluated in a probabilistic fashion. This probabilistic approach to flow modeling builds upon previous stochastic in situ leaching models at Casa Grande (M J Friedel, 1993) and Mineral Park (Yegulalp & Kim, 1996).

To this end, several different datasets from the Florence deposit were analyzed. This data includes eight Fluid Electrical Conductivity (FEC) flow profiles gathered in 1996 by the consultant Colog Inc., approximately 22,000 fracture spacing measurements from Florence Copper's drill

core database, and 36 pumping tests conducted by Magma Copper Company and Brown and Caldwell in the years 1994-1995. As discussed further below, each dataset gives a statistical distribution of measured properties (fracture intensity, hydraulic conductivity, etc.) collected at several locations spread across the deposit. Each dataset was assumed to be statistically representative of the site as a whole.

The approach is outlined as follows:

1. Using an assumption of radial flow, the FEC flow profiles and single well pumping tests were combined to estimate hydraulic conductivity ($K_{profile}$) at one-meter intervals along the screened interval of eight wells.
2. A geostatistical model of hydraulic conductivity was constructed using this $K_{profile}$ dataset. This included the statistical distribution of hydraulic conductivities as well as its vertical autocorrelation.
3. Two tests were performed to confirm compatibility between the geostatistical model and the other datasets:
 - a. Fracture intensity data was used for the first test. Because fractures are the main driver of hydraulic conductivity, $K_{profile}$ and fracture intensity are expected to have approximately the same spatial autocorrelation. A correlogram was constructed using the fracture intensity data and compared to the $K_{profile}$ correlogram.
 - b. Multi-well pumping tests were used for the second test. Whereas the flow profile data provides hydraulic conductivity estimates on the scale of 1 meter, the multi-well pumping tests measure hydrologic behavior at the scale of tens to hundreds of meters. To simulate these larger-scale flow patterns, a set of Monte Carlo pumping test simulations were conducted using 3-dimensional unconditional hydraulic

conductivity maps. The results were compared with the multi-well pumping test results to evaluate agreement.

4.2 Available Data

4.2.1 Flow Profiles

The first dataset consists of flow profiles measured using FEC logs. Eight flow profiles were measured in 1996 by the consultant Colog Inc. See Figure 16 for the locations of these wells. The purpose of the flow profile tests was to characterize hydraulic heterogeneities as a function of depth along each well's screened interval.

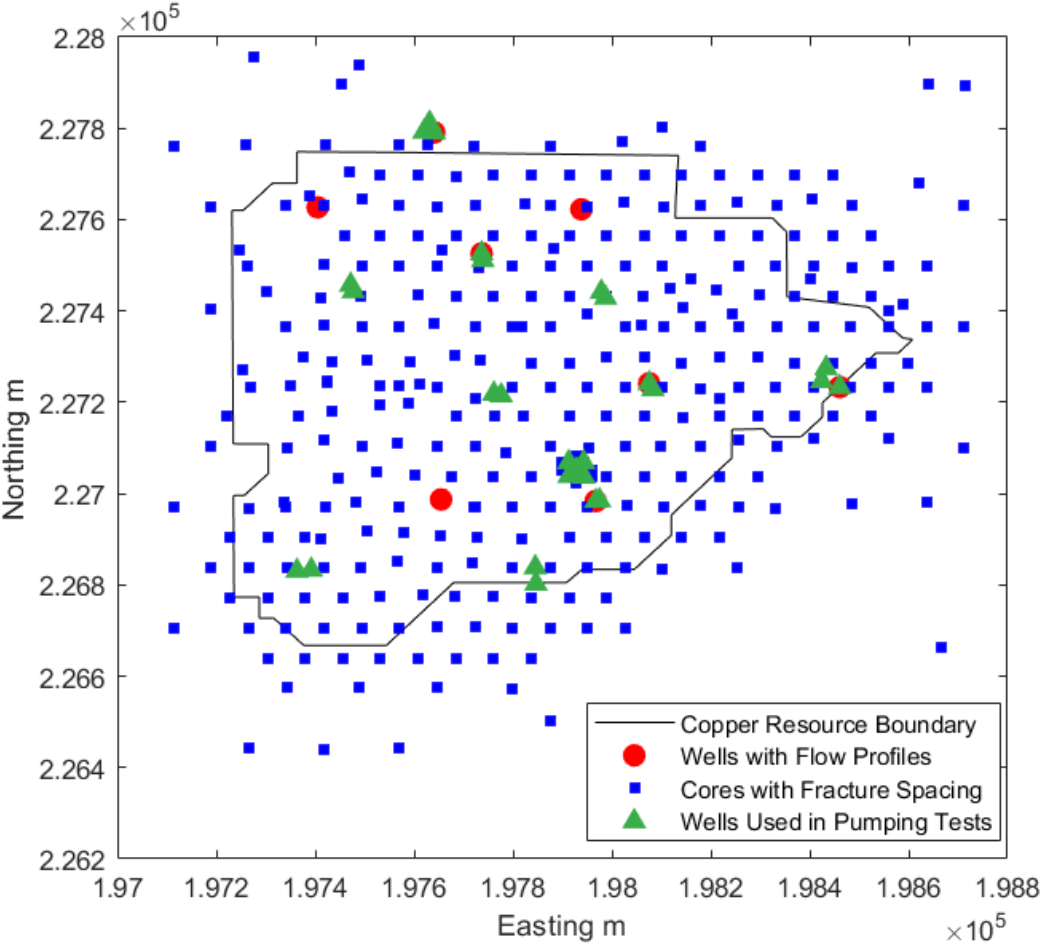


Figure 16 – Map view of the Florence resource showing locations where the three data types were sourced. The names of wells with flow profiles are shown. The coordinate system is Arizona Central State Plane Coordinates (NAD27 in feet)

FEC logging has been described in literature (Doughty & Tsang, 2005). During these tests at Florence, groundwater was first pumped from a well at a constant rate. Then deionized water was pumped into the bottom of the well using an injection riser at approximately $\frac{1}{4}$ of the withdrawal rate until the head and flow rates reached a reasonably constant value. The well therefore contained a column of water with a high electrical resistivity. A probe was then used to measure the electrical resistivity profile as a function of depth along the screened interval. The inflow of high ionic strength ground water at a certain point along the screen will result in a step change in electrical resistivity at that point – therefore, the electrical resistivity profile can be translated into a flow rate profile using software packages such as BORE (BHP Copper Growth and Technology Group, 1997a). The flow profiles as calculated by Colog Inc. are shown in Figure 17.

4.2.2 Fracture Intensity

The second dataset is fracture intensity (fractures per meter) as logged in the Florence drill core database. See Figure 16 for the locations of these cores. During logging, fracture intensity was recorded every 5 feet, using a 1 to 5 scale (see Table 8). Note that the scale was based on imperial units and needed to be converted to metric units for this study. The database contains 21,958 data points within the oxide zone. These points are spread across 325 core holes (Figure 16). While ratings 1-3 correspond to definite ranges in fracture spacing, the definitions of ratings 4 and 5 were more qualitative and needed to be translated into quantitative ranges based on a Master's thesis which contained detailed fracture spacing information (J. R. Davis, 1997).

Though this five-point scale does not capture key parameters such as aperture, tortuosity, and connectivity, it is expected that highly fractured rock will correlate with high hydraulic conductivity. The dataset has the benefit of being logged at close intervals in both vertical and horizontal directions, allowing for a 3-dimensional understanding of short-range variability.

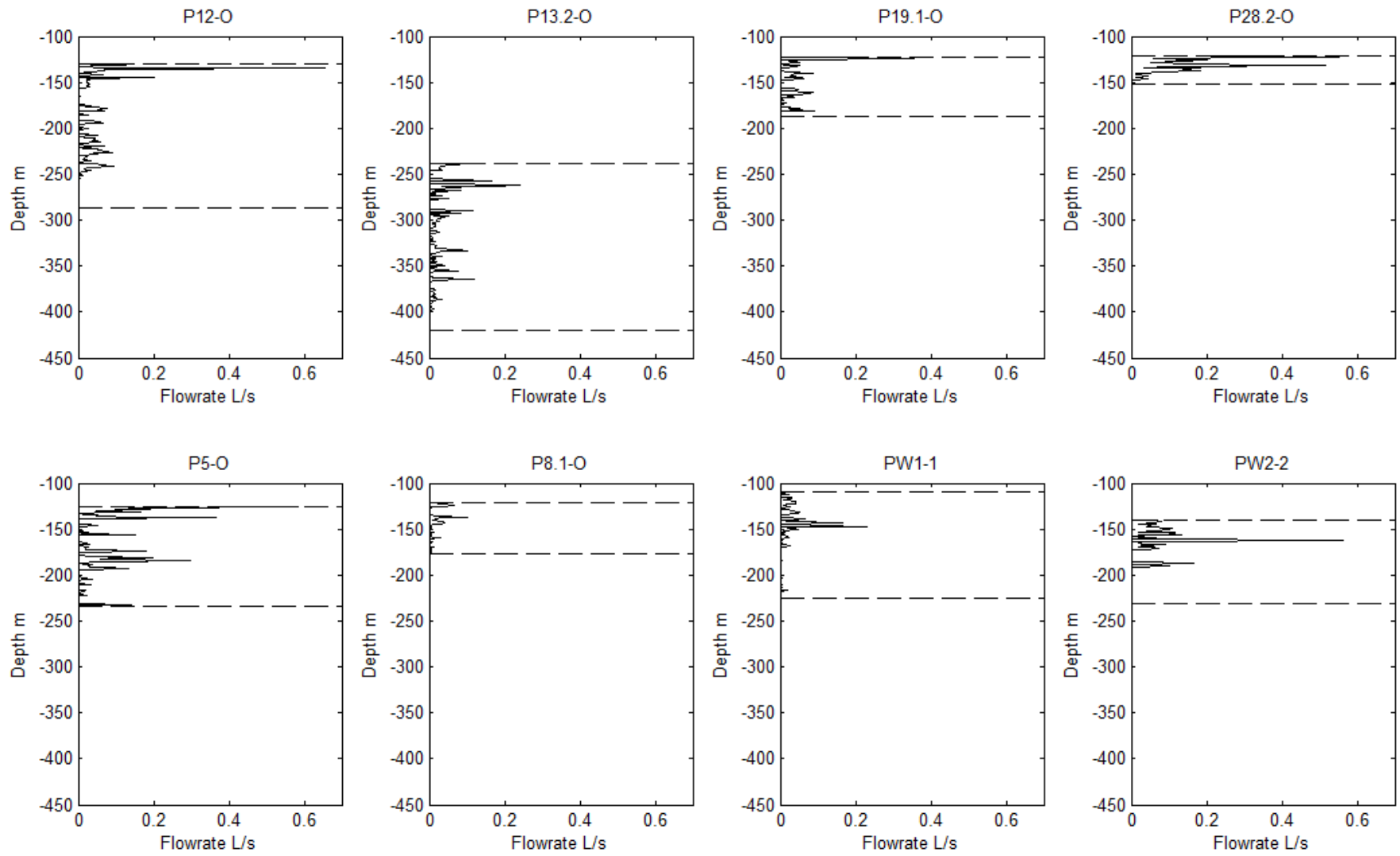


Figure 17 – Flow rate profiles. Dashed lines indicate the screened interval.

Table 8 - Fracture intensity ratings used in drill core database

Rating	Definition	Number of Points
1	0-5 fractures/ft	2930
2	6-10 fractures/ft	3874
3	11-15 fractures/ft	4647
4	>15 fractures/ft (estimated as 15-20 fractures/ft) (J. R. Davis, 1997)	5368
5	Fault or fault breccia (estimated as 20-30 fractures/ft) (J. R. Davis, 1997)	5139

4.2.3 Pumping Tests

4.2.3.1 *Single Well Pumping Tests*

Single well pumping tests were performed on the same eight wells which underwent FEC flow profile testing. These tests were performed by Magma Copper Company and the consulting firm Brown and Caldwell in the years 1994-1995. The single well pumping tests involved withdrawing water at a constant rate and measuring the change in pressure in the well over time. Golder Associates used the data to estimate hydraulic conductivity ($K_{pump, single}$) using the computer programs FLOWDIM and AQTESOLV, which fits time series pressure data using standard hydrologic models. Depending on the situation, Golder used either two-dimensional confined flow (fitting hydraulic conductivity and storativity), three-dimensional confined flow (fitting hydraulic conductivity and storativity), or two-dimensional flow in a leaky aquifer (fitting transmissivity, storativity, wellbore storage, skin factor, and two leakage parameters). The hydraulic conductivities calculated from these single well pumping tests are shown in Table 9.

Table 9 – Data from single well pumping tests

Pumping well	\log_{10} hydraulic conductivity (m/s)	Duration of test (days)	Pump well screened interval (m)	Pumping rate (L/s)
P12-O	-5.9	7	156.6	4.1
P13.2-O*	-6.2	8	182.3	2.9
P19.1-O	-6.2	4	64.5	1.5
P28.2-O	-5.0	4	30.2	4.8
P5-O	-5.3	6	114.0	4.2
P8.1-O	-5.7	4	54.9	0.8

Pumping well	log ₁₀ hydraulic conductivity (m/s)	Duration of test (days)	Pump well screened interval (m)	Pumping rate (L/s)
PW1-1	-6.5	8	116.2	2.1
PW2-2	-6.0	13	91.4	2.8

*This pumping test was performed at a well approximately 2.5 m away from well P13.2-O.

4.2.3.2 Multi-Well Pumping Tests

A series of multi-well pumping tests was also conducted across the Florence deposit. These tests were performed by Magma Copper Company, Brown and Caldwell, and BHP Copper during the years of 1994-1997. See Figure 16 for the locations of the wells. In each pumping test, water was withdrawn from the pumping well at a constant rate. The pumping well was then shut in while groundwater inflow caused the pressure to recover. The change in head was measured in a series of nearby observation wells during both the pumping and shut in phases. Pumping well screened intervals were at least 30 m and the distance from pumping to observation well was at least 7 m (BHP Copper Growth and Technology Group, 1997a).

Table 10 – Data from multi-well pumping tests

Pumping well	Observation well	log ₁₀ hydraulic conductivity (m/s)	Duration of test (days)	Distance between wells (m)	Pump well screened interval (m)	Observation well screened interval (m)	Pumping rate (L/s)
P28.1-O	O28.1-O	-5.1	4	29.9	30.5	30.5	5.4
P28.1-O	P28.2-O	-5.0	4	38.8	30.5	30.2	5.4
P49-O	O49-O	-6.5	6	28.9	126.2	126.5	2.6
PW2-1	OB2-1	-5.7	14	15.2	67.1	67.1	3.2
P19.1-O	O19-O	-6.2	4	20.9	64.5	60.4	1.5
P19.1-O	P19.2-O	-6.5	4	22.7	64.5	60.4	1.5
P39-O	O39-O	-6.0	2	36.0	108.2	126.8	3.5
P5-O	O5.2-O	-5.1	6	7.9	114.0	18.0	4.2
PW1-1	OB1-1	-6.0	8	14.9	116.2	115.8	2.1
PW2-2	OB2-2	-5.4	13	15.0	91.4	91.4	2.8
PW3-1	OB3-1	-5.8	9	15.1	85.3	85.3	3.7
PW7-1	OB7-1	-6.5	6	15.3	103.6	103.6	2.4
BHP1	BHP2	-5.7	1 to 3	22.1	109.7	146.3	Unknown
BHP1	BHP3	-5.7	1 to 3	21.7	109.7	158.2	Unknown
BHP1	BHP4	-5.9	1 to 3	22.5	109.7	122.2	Unknown

Pumping well	Observation well	\log_{10} hydraulic conductivity (m/s)	Duration of test (days)	Distance between wells (m)	Pump well screened interval (m)	Observation well screened interval (m)	Pumping rate (L/s)
BHP1	BHP5	-5.5	1 to 3	20.6	109.7	122.2	Unknown
BHP2	BHP1	-5.7	1 to 3	22.1	146.3	109.7	Unknown
BHP2	BHP3	-5.6	1 to 3	32.0	146.3	158.2	Unknown
BHP2	BHP4	-5.8	1 to 3	44.6	146.3	122.2	Unknown
BHP2	BHP5	-5.6	1 to 3	30.6	146.3	122.2	Unknown
BHP4	BHP1	-6.0	1 to 3	22.5	122.2	109.7	Unknown
BHP4	BHP2	-5.8	1 to 3	44.6	122.2	146.3	Unknown
BHP4	BHP3	-5.8	1 to 3	30.2	122.2	158.2	Unknown
BHP4	BHP5	-5.75	1 to 3	30.1	122.2	122.2	Unknown
BHP5	BHP1	-5.5	1 to 3	20.6	122.2	109.7	Unknown
BHP5	BHP2	-5.6	1 to 3	30.6	122.2	146.3	Unknown
BHP5	BHP3	-5.5	1 to 3	42.3	122.2	158.2	Unknown
BHP5	BHP4	-5.8	1 to 3	30.1	122.2	122.2	Unknown

Golder Associates and BHP Copper used the time series pressure data to calculate an effective hydraulic conductivity ($K_{pump, multi}$) using AQTESOLV, using the same procedure described above. The calculated hydraulic conductivity values and other test parameters are shown in Table 10.

4.3 Hydraulic Conductivity from FEC Flow Profiles and Single Well Pumping Tests

The flow profiles and single-well pumping tests were combined to estimate hydraulic conductivity profiles along each of the eight wells. This was done by assuming that the flow out of the well is purely radial. This implies that the flow rate at each point along the screened interval is proportional to the hydraulic conductivity at that point:

$$K_{profile} = \alpha q(z) \quad \text{Eq 4}$$

Where $K_{profile}$ is the hydraulic conductivity as calculated from the flow profiles, $q(z)$ is the flowrate as a function of depth, and α is a constant (see Definitions of Symbols). The radial flow

assumption also implies that the measured conductivity from single-well pumping tests (as listed in Table 9) represents the mean conductivity along the screen:

$$\frac{1}{b_{screen}} \int_{z=0}^{z=b} K_{profile} dz = K_{pump, single} \quad \text{Eq 5}$$

Where b is the screened interval, z is depth, and $K_{pump, single}$ is the hydraulic conductivity as calculated using the single well pumping tests. Using Equations 4 and 5, $K_{profile}$ was calculated along each of the screened intervals at a 1 m spatial resolution. It should be noted that approximately half of the total well screen length had flowrates below the FEC detection limit; this is a common challenge in measuring flow rate profiles (Wen, 1994). Depending on the well, the FEC detection limit varied between $K=10^{-6.5}$ m/s and $K=10^{-8}$ m/s. These low-flow or no-flow zones were therefore assumed to have a hydraulic conductivity of 10^{-8} m/s.

4.3.1 Statistical Distribution of Values

The distribution of $\log_{10} K_{profile}$ is shown in Figure 18. Maximum likelihood estimation of parameters is an accepted method for fitting statistical distributions when a significant fraction of the data is censored, or below detection limits (Kroll & Stedinger, 1996). This method is able to account for different detection limits, as was the case with this dataset (Bantis, 2012). The maximum likelihood estimates of the mean and standard deviation were -6.8 (-6.93 -6.73) and 1.2 (1.13 1.30) respectively. The values in the brackets denote the 95% confidence limits.

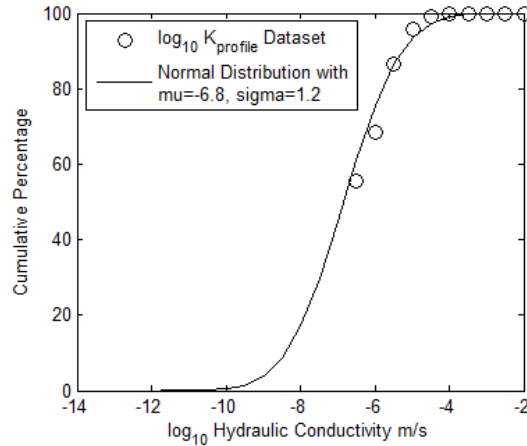


Figure 18 - Statistical distribution of $\log_{10} K_{profile}$, fitted using maximum likelihood estimation. Points are plotted in increments of 0.5. Conductivities below $10^{-6.5}$ m/s are not graphed because this is where censorship begins.

4.3.2 Autocorrelation

4.3.2.1 *Theory*

The autocorrelation function was used to quantify the spatial variations in $\log_{10} K_{profile}$. This is a standard approach in studying spatial relationships of variables in geostatistics (Hohn, 1999). The autocorrelation (R) between two $\log_{10} K_{profile}$ values, measured at locations 1 and 2, is defined as:

$$R = \frac{\langle (\log_{10}[K_{profile,1}] - \mu_1)(\log_{10}[K_{profile,2}] - \mu_2) \rangle}{\sigma_1 \sigma_2} \quad \text{Eq 6}$$

Where μ_1 and μ_2 are the means at locations 1 and 2, and σ_1 and σ_2 are the standard deviations at locations 1 and 2, and the angled brackets represent the average over the dataset (see Definitions of Symbols). If μ shows a global trend throughout the domain, a fit function can be used to estimate local averages μ_1 and μ_2 . If there are no global trends in the spatial domain of the data, the two means can be considered equal to the global mean ($\mu_1 = \mu_2 = \mu_{global}$). A similar logic can be applied to σ .

Constructing a correlogram involves calculating the sample estimates of the autocorrelation, R , for each pair of points in a dataset. Then these point pairs are binned depending on the vector linking points 1 and 2 (if R shows a dependence only on separation distance and not vector direction, then the autocorrelation is isotropic). The binned averages of R are then fit with a curve known as the correlogram. The curve may intersect the y axis below 1, indicating short-range spatial variations and/or measurement error (Hohn, 1999, p. 30). The length scale over which the correlogram decays to zero indicates the length scale of autocorrelation.

4.3.2.2 Results

The $\log_{10} K_{profile}$ dataset was inspected for any global trends in the sample estimates of μ and σ in all three dimensions. No consistent global trends were found. Therefore, the global sample mean and sample standard deviations were used: $\hat{\mu}_1 = \hat{\mu}_2 = \hat{\mu}_{global} = -6.8$ and $\hat{\sigma}_1 = \hat{\sigma}_2 = \hat{\sigma}_{global} = 1.2$.

Points below FEC detection limits were assigned values of $K=10^{-8}$ m/s, because this corresponded to the minimum measurable hydraulic conductivity. It is recognized that the assumption of constant K in zones below the detection limit will impact the calculated autocorrelation structure. While some more sophisticated methods exist for estimating autocorrelation structure (including Indicator Kriging (Goovaerts, 2009), Stochastic Approximate Expectation Maximization (Barbosa, 2016), and Simulated Annealing (Sedda, Atkinson, Barca, & Passarella, 2012)), these methods were not considered applicable in this case because they are more suited to conditional simulation.

A correlogram of $\log_{10} K_{profile}$ was constructed by calculating the sample estimates of R for all point pairs along each well, and then the data were binned according to separation distance. The plot is shown in Figure 19. An exponential function of the form $R=a*\exp(-Distance/d)$, where a and d are constants, was fit to the data with a simple numerical least squares minimization

(exponentially correlated log conductivity has also been used in several previous studies (Beaudoin & De Dreuzy, 2013; Bohling et al., 2012; Englert, Vanderborght, & Vereecken, 2006; Gelhar & Axness, 1983)). The fit parameters were $a = 0.47$ and $d = 8.1$ m. The fact that the y intercept was significantly below 1 reflects the highly erratic nature of the flow profiles. It should be noted that for each point pair, both points were selected from the same well. This is because the wells were too far apart to evaluate R for cross-hole point pairs. Note that this implies the vector between each point pair is vertical.

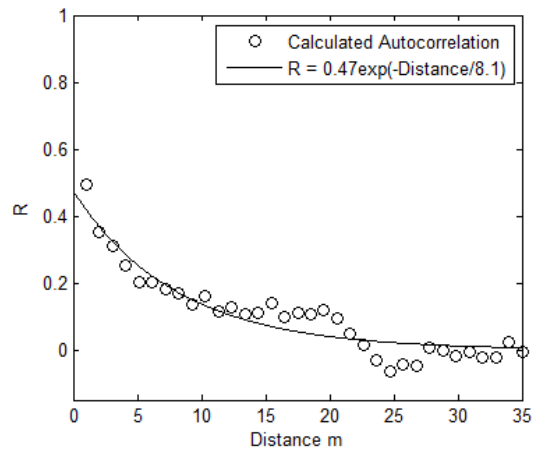


Figure 19 – Correlogram of the $\log_{10} K_{profile}$ dataset

Figure 18 (statistical distribution) and Figure 19 (autocorrelation) together constitute a geostatistical model of hydraulic conductivity, based on the $K_{profile}$ dataset. This geostatistical model is tested using other data types in the following sections.

4.4 Test #1: Fracture Intensity Data

4.4.1 Approach

To test the $K_{profile}$ geostatistical model, a geostatistical analysis was performed on the fracture intensity data. Although the link between fracture intensity and hydraulic conductivity can be tenuous and depends on many unmeasured variables, fractures are the main driver for hydraulic conductivity in hard rock, and is therefore expected to have a similar autocorrelation length scale.

4.4.2 Distribution of Values

The fracture intensity data tabulated in Table 8 was fit with a normal distribution. Recall that the logging system was based on a five-point scale, meaning that only five data points could be used for this curve fit. The data is in good agreement with a normal distribution with an average of $\mu = 46.6$ (46.3, 47.0) fractures per meter and a standard deviation of $\sigma = 26.5$ (26.3, 26.8) fractures per meter (see Figure 20).

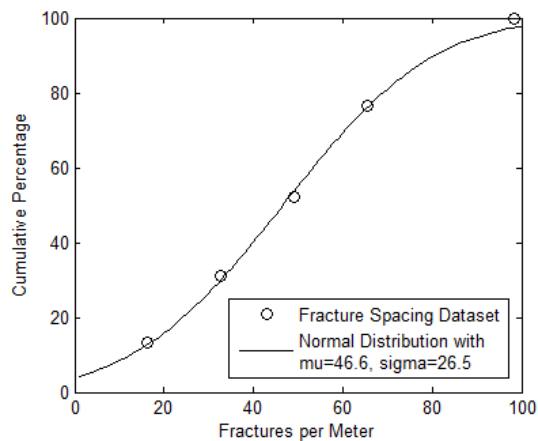


Figure 20 – Fracture intensity data fit to a normal distribution. $\mu = 46.6$ (46.3, 47.0) fractures per meter and a $\sigma = 26.5$ (26.3, 26.8)

4.4.3 Subtraction of Global Trend

The dataset was inspected for evidence of any global trends in the sample average ($\hat{\mu}$) or sample standard deviation ($\hat{\sigma}$). It was found that fractures become more widely spaced with depth. The trend with depth is shown in Figure 21. A parabolic function of the form $y=p_1*z^2+p_2*z+p_3$ was fit to the dataset using a simple numerical least squares minimization. The fit coefficients were $p_1 = -0.00024$ (-0.00028, -0.00021), $p_2 = 0.10$ (0.077, 0.12), and $p_3 = 39$ (36, 41). This function was used to calculate the vertically varying averages μ_1 and μ_2 , as shown in Equation 6. No global trends in $\hat{\sigma}$ were found.

It is interesting to note that the $K_{profile}$ dataset had no trend with depth, whereas the fracture spacing decreased with depth. This may be illustrative of trends in unmeasured fracture characteristics such as aperture or connectivity.

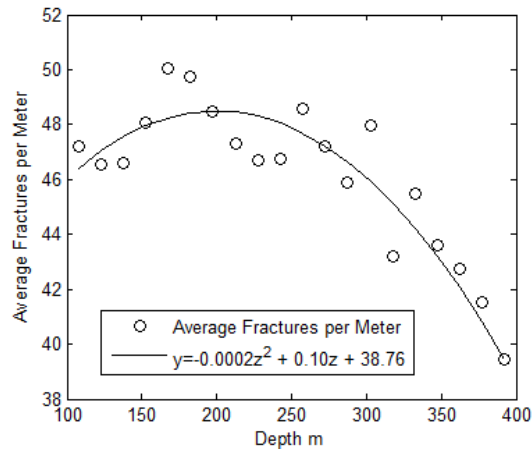


Figure 21 - Fracture intensity trend with depth. Binned averages are shown for comparison. Note that the parabolic function was fit to the raw (un-binned) data.

4.4.4 Correlogram

To investigate whether the fracture intensity was isotropically autocorrelated, horizontal and vertical directional correlograms were constructed and compared. First, a vertical correlogram was constructed by calculating the sample estimate of R for all point pairs within each of the 325 cores. This data was then binned. Next, a horizontal correlogram was constructed by dividing the dataset into 8 depth intervals of 30 m thickness each. Within each depth interval, the sample estimate of R was calculated for all cross-well point pairs. The data were then binned and checked for any anisotropy in the cardinal directions; no consistent directionality was found for the horizontal autocorrelation.

The resulting vertical and horizontal correlograms were compared to the $\log_{10} K_{profile}$ correlogram (see plots in Figure 22 and fit parameters in Table 11). The vertical fracture correlogram and $\log_{10} K_{profile}$ correlogram share similar y intercepts and correlation length scales.

This supports the assertion that fractures are the main driver of hydraulic conductivity. It was found that the horizontal fracture correlogram shows evidence of a much longer correlation length scale; the best fit was 32 m. It was therefore assumed that the correlation length scale for hydraulic conductivity is 8.1 m in the vertical direction, and 32 m in the horizontal directions.

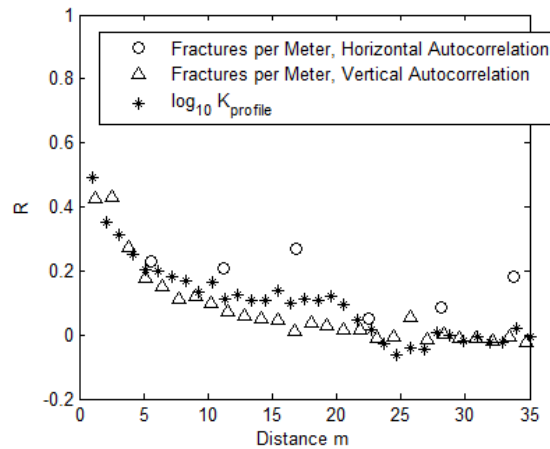


Figure 22 – Vertical and horizontal correlograms for fracture intensity, plotted with correlogram for $\log_{10} K_{profile}$

Table 11 – Fit parameters of the form $R=a*\exp(-Distance/d)$ for fracture intensity and $\log_{10} K_{profile}$ correlograms

Parameter	Fractures per meter, horizontal	Fractures per meter, vertical	$\log_{10} K_{profile}$
Nugget: a	0.26	0.55	0.47
Range: d (m)	32	4.9	8.1

4.5 Test #2: Multi-Well Pumping Tests

4.5.1 Approach

A second test of the $K_{profile}$ geostatistical analysis was performed using the multi-well pumping test data. Whereas $K_{profile}$ provides hydraulic conductivity estimates on the scale of 1 meter, the pumping tests measure hydrologic behavior at the scale of tens or hundreds of meters. Therefore, this test requires simulating larger-scale flow patterns to confirm that the flow behavior reproduces the multi-well pumping test results.

As discussed in detail below, a set of 3-dimensional maps was generated, conforming to the statistical distribution and spatial autocorrelation of $K_{profile}$. Unconditional simulation was used,

meaning that the maps were not constrained by any measured K values. This set of unconstrained maps is meant to be representative of the range of expected hydrologic behavior across the deposit. Each map was then subjected to a simulated pumping test. This involved simulating a pumping well in the center of each map, solving for the pressure field, and then calculating the overall effective conductivity of the well's zone of influence. This set of effective conductivities ($K_{simulation}$) was then compared with the set of 28 measured conductivities from the multi-well pumping tests ($K_{pump, multi}$) to confirm that the simulated maps effectively capture the observed range of large-scale hydrologic behavior.

4.5.2 Map Generation

The first step in this exercise was to generate a set of maps using MATLAB. Each map consisted of a 3-dimensional grid with a hydraulic conductivity value assigned to each point. The maps were 90 m x 90 m wide and 30 to 146 m deep. The grid resolution was 1.5 m because it was large enough to permit timely computation, but still small relative to the map size. It was assumed that the target formation was of constant thickness, confined by impermeable layers above and below, and that the screened interval intersected the formation completely.

As shown in Table 10, each pumping test had its own screened interval (ranging from 30 to 146 m) and its own separation distance between pumping and observation well (ranging from 8 to 45 m). Therefore for every pumping test, ten maps were generated with that test's screened interval and well distance. This resulted in 280 maps which reflected the range of parameters used in the pumping tests.

Hydraulic conductivity values were assigned to each grid point. If C is the covariance matrix between grid points, a suitable set of hydraulic conductivity values y will, in expectation, satisfy the covariance relationship given by:

$$\langle (\mathbf{y} - \boldsymbol{\mu})(\mathbf{y} - \boldsymbol{\mu})' \rangle = \mathbf{C} \quad \text{Eq 7}$$

Several algorithms can be used to generate these randomized maps. Some examples include Cholesky decomposition, the turning band method, and simulated annealing (Hohn, 1999). In this study, a Cholesky decomposition algorithm was used because of its speed. Further details on this method can be found elsewhere (Constantine & Wang, 2012; M. W. Davis, 1987).

The set of maps was designed to reflect the statistical distribution and spatial autocorrelation of the $\log_{10} K_{profile}$ dataset. As discussed in section 4.3.1, the maps require a normal $\log_{10} K$ distribution, with a mean of -6.8 and a standard deviation of 1.2, with the distribution truncated at $\log_{10} K = -8$. The maps also require an autocorrelation relationship with a y intercept of 0.47, a vertical correlation length scale of 8.1 m, and a horizontal correlation length scale of 32 m. An iterative approach was used to satisfy these requirements. Normally distributed maps with a mean of -6.8, a standard deviation of 1.2, and various autocorrelation parameters were generated using Cholesky decomposition. The $\log_{10} K$ values were truncated at -8, and the sample estimates of R were calculated for 5000 point pairs within the map. This was repeated until a good fit was achieved with the target autocorrelation structure.

An example of one 3-dimensional map is shown in Figure 23. Notice that the maps are spatially correlated, with high-conductivity and low-conductivity zones on the scale of approximately 8 meters in the vertical direction and 32 m in the horizontal directions. A set of "uncorrelated" maps was also generated for comparison. These had the same statistical distribution of K values, but no spatial autocorrelation.

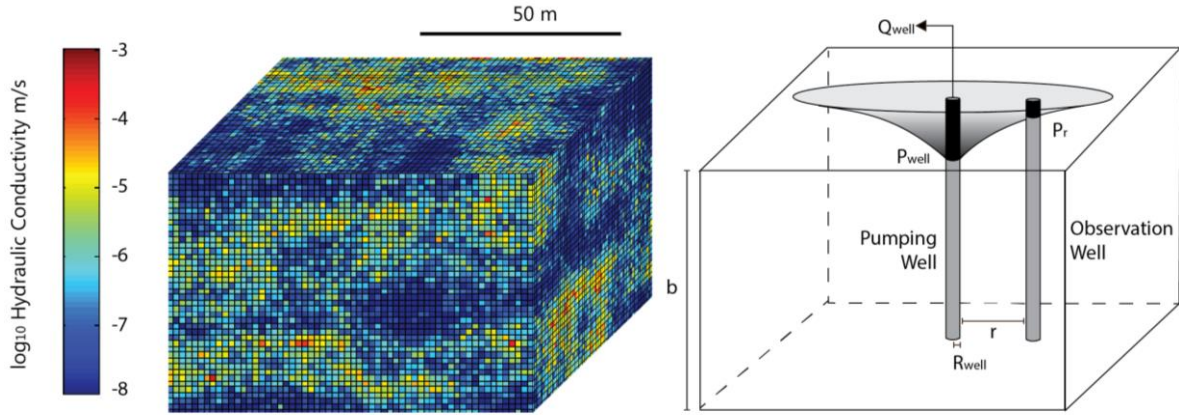


Figure 23 – Example of one hydraulic conductivity map (left) and illustration of simulated pumping test (right). Note the cone of depression representing the pressure drop around the pumping well.

4.5.3 Effective Conductivity

Once the maps had been generated, the next step was to perform a simulated pumping test with each map. The simulated pumping tests involved placing a pumping well in the center of the map, and simulating a constant water withdrawal rate (Q_{well}). The withdrawal rate was set as 3.2 L/s, which is the average flow rate from the multi-well pumping tests. As noted above, the observation distance (r) ranged from 8 to 45 m to reflect the range of well separation distances used in the multi-well pumping tests. The effective large-scale conductivity of each generated map ($K_{simulation}$) can be calculated based on the pressure field (where R_{well} is the radius of the well, b_{screen} is the length of the screened interval, p_{well} is the pressure in the well, and p_r is the pressure at distance r):

$$K_{simulation} = \frac{Q_{well} \ln\left(\frac{r}{R_{well}}\right)}{2\pi b_{screen} (p_{well} - p_r)} \quad \text{Eq 8}$$

4.5.4 Pressure Field Computation

The final step is to compute the pressure field. To derive the governing equations, we begin with the combined Darcy Flow and conservation equation:

$$\nabla \cdot (K\nabla p) = \frac{q(z)}{dx dy} \delta(x - x_{well}) \delta(y - y_{well}) \quad \text{Eq 9}$$

Where K is hydraulic conductivity, p is pressure, $q(z)$ is flowrate as a function of depth, dx and dy are the grid spacing in x and y directions, and $\delta(x-x_{well})\delta(y-y_{well})$ is a line source at the well location. Conventional finite difference was used. Zero flux boundary conditions were used at the top and bottom of the domain, and constant pressure boundary conditions were used at the North/South/East/West edges of the domain. Equation 9, along with the boundary conditions, corresponds to $(N_x-2)(N_y-2)N_z$ equations.

Next, the total flowrate out of the pumping well is constrained using Equation 10:

$$\int_0^{b_{screen}} q(z) dz = Q_{well} \quad \text{Eq 10}$$

Finally, because the grid size (1.5 m) is much greater than the well radius (6.3 cm), it is necessary to derive a subgrid approximation for the pressure close to the well. The subgrid solution (p_m) is the linear superposition of two components: an analytically derived logarithmic term corresponding to the radial flow out of the well, and a regular trilinear function (p_{reg}) with eight coefficients $A_0 \dots A_7$:

$$p_{in} = -\frac{q(z)}{2\pi K} \ln\left(\frac{r}{R_{well}}\right) + p_{reg}(x, y, z) \quad \text{Eq 11}$$

$$p_{reg}(x, y, z) \equiv A_0 + A_1x + A_2y + A_3z + A_4xy + A_5xz + A_6yz + A_7xyz$$

The eight coefficients in the p_{reg} term can be obtained by requiring the subgrid solution to equal the outer solution obtained from the finite difference computation at the eight pressure nodes surrounding each element along the well. This provides $8(N_z-1)$ equations. In the limit as r approaches 0 (x approaches $x_{well\ interp}$, y approaches $y_{well\ interp}$, and $z=\Delta z/2$), the inner pressure approaches the well pressure (p_{well}):

$$\lim_{r \rightarrow 0}(p_{in}) = p_{well} = p_{reg}(x_{well\ interp}, y_{well\ interp}, \frac{\Delta z}{2}) \quad \text{Eq 12}$$

4.5.5 Results

Figure 24 illustrates the distribution of measured conductivities from the multi-well pumping tests, the distribution of simulation results using correlated maps, and the distribution of simulation results using uncorrelated maps (recall that the uncorrelated maps had the same statistical distribution of hydraulic conductivity as the correlated maps, but had no spatial autocorrelation). All three were approximately normally distributed with the parameters given in Table 12. The simulations with correlated maps showed reasonable agreement with the distribution of pumping test results.

An F test failed to reject the null hypothesis that the variances were equal (p value of 0.674). Because the distribution of $K_{pump, multi}$ deviated slightly from a normal distribution, the nonparametric Ansari-Bradley test was also applied; this also failed to reject the null hypothesis

that the variances were equal (p value of 0.879). This shows that the simulations with correlated maps showed satisfactory agreement with the distribution of measurements made in the field.

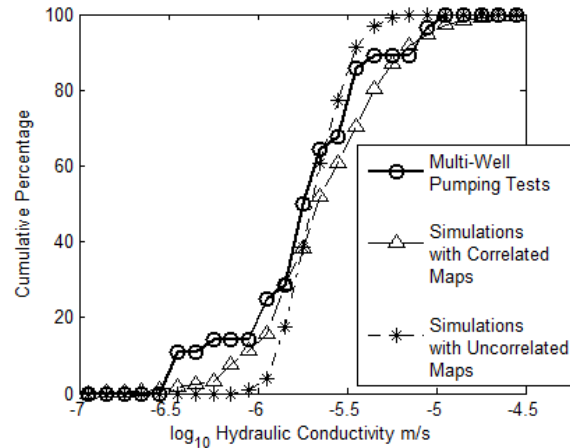


Figure 24 - Distribution of $\log_{10} K_{pump, multi}$ from the multi-well pumping tests, $\log_{10} K_{simulation}$ from simulations with correlated maps, and $\log_{10} K_{simulation}$ from simulations with uncorrelated maps

Table 12 - Results from simulated pumping tests

	Multi-well pumping tests ($\log_{10} K_{pump, multi}$)	Simulations with correlated maps ($\log_{10} K_{simulation}$)	Simulations with uncorrelated maps ($\log_{10} K_{simulation}$)
Number of values	28	280	280
Mean	-5.7	-5.6	-5.6
Standard deviation	0.4	0.4	0.2

The uncorrelated maps showed a narrower distribution of $K_{simulation}$ values. The F and Ansari-Bradley tests were also applied to the uncorrelated maps. Both tests rejected the null hypothesis of equal variance (p values of 1.956×10^{-12} for the F test and 9.267×10^{-4} for the Ansari-Bradley test). This indicates that the uncorrelated maps failed to replicate the distribution of measurements made in the field, and illustrates the importance of simulating using geostatistical correlations.

These results are consistent with a fundamental characteristic of heterogeneous materials: measured properties depend on the scale over which the measurement is made. Every heterogeneous material has a characteristic length scale of its heterogeneous features (or a range of length scales). In the case of the Florence deposit, the characteristic length scale of heterogeneity is the autocorrelation length scale (8 m to 32 m). The correlated maps reflect this. In the

uncorrelated maps, the characteristic length scale is simply the grid spacing (1.5 m). The greater the scale of measurement relative to the characteristic length scale of heterogeneity, the more the material will behave homogeneously due to the "averaging out" of its properties. This explains why $\log_{10} K_{simulation}$ was more widely distributed with the correlated maps than the uncorrelated (standard deviation of 0.4 versus 0.2). This also explains why the small-scale measurements $\log_{10} K_{profile}$ were more widely distributed than the large-scale measurements $\log_{10} K_{pump, multi}$ (standard deviation of 1.2 versus 0.4).

CHAPTER 5

MODEL OF IN SITU LEACHING SYSTEM

5.1 Model Structure

A model of the in situ leaching system was constructed which brings together the geochemical model as outlined in section 2.3 and the geostatistical characteristics of hydraulic conductivity as outlined in section 4. The model was constructed in MATLAB, with a plugin used to link to Geochemist's Workbench for computing chemical reaction pathways. The model user specifies a set of well locations, pumping rates, mineralogy of the ore block, screened interval, and an injected fluid composition. The algorithm is outlined as follows:

1. The model uses Cholesky decomposition to generate a 3-dimensional map of hydraulic conductivity. As discussed in section 4, the hydraulic conductivity maps follow a truncated lognormal distribution, with a log-space mean of $10^{-6.8}$ m/s, a log-space standard deviation of $10^{-1.2}$ m/s, a lower cutoff of 10^{-8} m/s, and an autocorrelation length scale of 8 m in the vertical direction and 32 m in the horizontal directions. The geostatistical characteristics of hydraulic conductivity are outlined in section 4.3.1 and 4.3.2, and the map generation process is outlined in section 4.5.2. As discussed in the following sections, the model can also be run with a homogenous map for comparison. A homogenous map would have the same geochemistry with the same reaction and diffusion rates, but hydraulic conductivity would be constant across the map. As discussed in the following sections, comparing the simulation results to a homogenous case allows for the effect of flow channeling to be quantified.

2. Based on the given well locations and flow rates, MATLAB computes a pressure field based on the procedure outlined in section 4.5.4. A velocity field is then computed using the Darcy equation:

$$(V_x, V_y, V_z) = \frac{-K\nabla p}{\varepsilon} \quad \text{Eq 13}$$

Where V_x , V_y , and V_z are the velocity in x , y , and z directions, K is hydraulic conductivity, p is pressure, and ε is porosity. Porosity was assumed constant at 6% (Zimmerman et al., 2013). Several previous studies have also assumed a constant porosity given its secondary importance relative to conductivity for calculating the velocity field (Beaudoin & De Dreuzy, 2013; Dogan et al., 2014; Fiori, Dagan, Jankovic, & Zarlenga, 2013; Gelhar & Axness, 1983; Phanikumar, Hyndman, Zhao, & Dybas, 2005).

3. The streamline method (Becker & Shapiro, 2003; Ginn, 2001; Kang et al., 2015) is used to generate a residence time distribution for each map. In this method, the injected fluid is discretized into a set of independent pathways, and the trajectory of each path is tracked using the velocity field until termination at a recovery well. Dispersion within each streamline is neglected, as large-scale dispersion is predominantly caused by the differing velocities among streamlines (Kang et al., 2015). As with previous studies, mixing between streamlines is neglected (Becker & Shapiro, 2003; Ginn, 2001; Kang et al., 2015). Two hundred streamlines are initialized at each injection well. The streamline initiation points are positioned along the screened interval in proportion to the flow rate. The velocity field was used to trace the trajectory of each streamline using Runge Kutta integration and a variable integration step size.

4. Each streamline is effectively treated as a one-dimensional reactive transport system. MATLAB sends Geochemist's Workbench the injected fluid composition, the composition of the subsurface fluid, and the composition of the ore. Geochemist's Workbench computes the reaction pathway for each streamline based on the geochemical model as outlined in section 2.3, and returns the solution and ore composition after a time interval.
5. MATLAB uses the Geochemist's Workbench output to calculate the fluid composition recovered from each recovery and perimeter well.
6. Steps 4-5 are repeated for 4 years of simulated leaching time.
7. Steps 1-5 are repeated for 100 randomly generated maps. Note that each map is not meant to represent a particular location, but rather the set of maps is meant to be representative of the deposit as a whole. The 100 resulting copper recovery curves are used to generate a prediction interval on the recovered solution composition. If a homogenous map is used for the model, only one iteration is necessary.

Key inputs for the model along with sources are listed in Table 13.

Table 13 – Model inputs

Input	Value	Source
Well configuration	Five spot well patterns with 50 foot spacing	(Zimmerman et al., 2013), section 16.1.3.3
Average thickness of oxide zone to be leached	400 feet minus 40-foot exclusion zone	Deposit average. (Zimmerman et al., 2013), section 7.5.1
Background groundwater flow	0.0015 m/day to the northwest	(Brewer, 1998), section 2.3.
Flow rates in injection and recovery wells	0.1 gpm/linear foot	(Zimmerman et al., 2013), section 16.2
Total copper grade	0.358%	Deposit average. (Zimmerman et al., 2013), section 1.1
Fraction of copper that is leachable	68%	Deposit average. (Zimmerman et al., 2013), section 14.4
Fracture spacing	3.3 cm	Average from (J. R. Davis, 1997) page 31
Fracture porosity	6%	Based on bromide tracer tests. BHP field test report, page 29.

Input	Value	Source
Bulk density	12.5 ft ³ /ton	(Zimmerman et al., 2013), section 13.3
Initial groundwater composition	Acid: 0 ppm Al: 2 ppm Ca: 61 ppm Cu: <1 ppm Cl: 160 ppm Fe: <1 ppm HCO ₃ : 160 ppm K: 6 ppm Mg: 14 ppm Na: 120 ppm P: <1 ppm Si: 50 ppm ORP: 150 mV	Florence Copper UIC Permit Application Attachment H Table 3.1 makeup water column. ORP from PRT29-35 outlet at start of leaching period, as reported in M794-01 Florence Copper Interim Report Rev3 Oct 25 2016. Silicon from BHP Field Tests data.
Injected fluid composition (fresh acid)	Acid: 10 000 ppm Al: 2 ppm Ca: 61 ppm Cu: <1 ppm Cl: 159 ppm Fe: <1 ppm HCO ₃ : 159 ppm K: 6 ppm Mg: 14 ppm Na: 119 ppm P: <1 ppm Si: 50 ppm ORP: 296 mV	Equilibrium concentration after acidifying groundwater to 10 g/L H ₂ SO ₄
Injected fluid composition (mature raffinate)	Acid: 10 000 ppm Al: 1161 ppm Ca: 480 ppm Cu: 352 ppm Cl: 160 ppm Fe: 1209 ppm HCO ₃ : 160 ppm K: 386 ppm Mg: 972 ppm Na: 391 ppm P: 169 ppm Si: 50 ppm ORP: 600 mV	PRT29-35 leach study feed. Cl, Si, and HCO ₃ were assumed to be equal to the groundwater composition. ORP from PRT29-35 outlet composition at end of leaching period, as reported in M794-01 Florence Copper Interim Report Rev3 Oct 25 2016
Mineralogical composition by weight	Anorthite: 5.2% Goethite: 0.44% Kaolinite: 0.4% Montmorillonite: 7.2% Chrysocolla: 0.68%	Average from box tests. Chrysocolla based on 0.358% copper, 68% leachable, assuming all leachable copper is chrysocolla.

5.2 *Model Results*

5.2.1 Cases

Several model cases were run to provide a best estimate of the leaching results at Florence (Case 1), and to illustrate the model's sensitivity to high-uncertainty parameters (Cases 2-6). The injected solution composition, percent of copper minerals on fracture surfaces, and the extent of flow channeling were varied among the model cases as outlined in Table 14.

The injected solution composition was considered a parameter with high uncertainty, since it will change over time as gangue ions accumulate in the recirculating solution. To demonstrate the sensitivity to this parameter, cases with both acidified groundwater and mature raffinate were run as outlined in Table 14. Note that the assumed mature raffinate composition was based on the feed to the series leach test.

The percent of copper on fracture surfaces is also considered a parameter of high uncertainty. The box tests were estimated to have an average of 10% copper on fracture surfaces. The series leach test showed a very rapid rate of copper leaching and was estimated to have 80% of copper on fracture surfaces. A previous petrographic study noted that chrysocolla at Florence was approximately evenly distributed between fractures and permeations in feldspars (Beane & Ramey, 1995). As a middle ground, the percent of copper on fracture surfaces was estimated at 50%; this was used for Case 1. To test the sensitivity to this parameter, cases were also run with 10% and 90% of copper on fracture surfaces as outlined in Table 14.

Finally, the degree of heterogeneity in flow was a variable of high uncertainty. To demonstrate sensitivity to flow channeling, cases were run with both homogeneous and heterogeneous maps. For Case 1 and the other heterogeneous cases, 100 of the maps described in section 4.5.2 were used because these reflected the geostatistical characteristics of hydraulic conductivity at Florence.

For the homogeneous cases, the hydraulic conductivity was assumed to be uniform throughout the deposit. It should be noted that while the homogenous cases have no large-scale variations in hydraulic conductivity, reaction rates are still modeled based on acid diffusion into discrete ore fragments. In effect, it is assumed that the ore is still fractured, without large-scale variations in hydraulic properties.

For all cases, a single five-spot well pattern was simulated, with four injection wells and a central recovery well. The injected solution composition was held constant to simplify comparisons among cases.

Table 14 - Model scenarios

	Case 1	Case 2	Case 3	Case 4	Case 5	Case 6
Injected fluid composition*	Fresh acid	Mature raffinate	Fresh acid	Fresh acid	Fresh acid	Fresh acid
Hydraulic conductivity	100 heterogeneous maps	100 heterogeneous maps	100 heterogeneous maps	100 heterogeneous maps	1 homogenous map	1 homogenous map
Percent of copper on fracture surfaces	50%	50%	90%	10%	50%	90%

*See Table 13 for assumed elemental composition of fresh acid and mature raffinate

5.2.2 Residence Time Distribution for Cases 1-6

The model begins by calculating a set of three-dimensional streamlines from the injection to recovery well. A sample set of flow paths is shown in Figure 25. Note that the flow paths will be different for each of the 100 maps, ranging from relatively even flow to highly channeled behavior. The flow paths from the homogenous case are shown for comparison.

In both the heterogeneous and homogenous cases, the flow paths represent a discretization of the advancing fluid front. The time required for each streamline to terminate at the central recovery well was used to generate a cumulative residence time distribution (RTD). For the heterogeneous

cases, 100 RTDs were generated from 100 different maps to capture the distribution of channeling behavior that can be expected throughout the deposit (see Figure 26). The RTD for a homogenous medium is shown for comparison.

Most of the heterogeneous RTDs show faster initial breakthrough relative to the homogenous case due to high-conductivity channels which connect the injection wells to the central recovery well. The RTDs all show much longer tails relative to the homogenous case because of low-conductivity zones which result in a combination of low flow velocities and circuitous flow paths. Both of these observations are in agreement with previous studies of flow patterns in heterogeneous rock (Becker & Shapiro, 2003; Berkowitz, Cortis, Dentz, & Scher, 2006; Ginn, 2001; Le Borgne & Gouze, 2008).

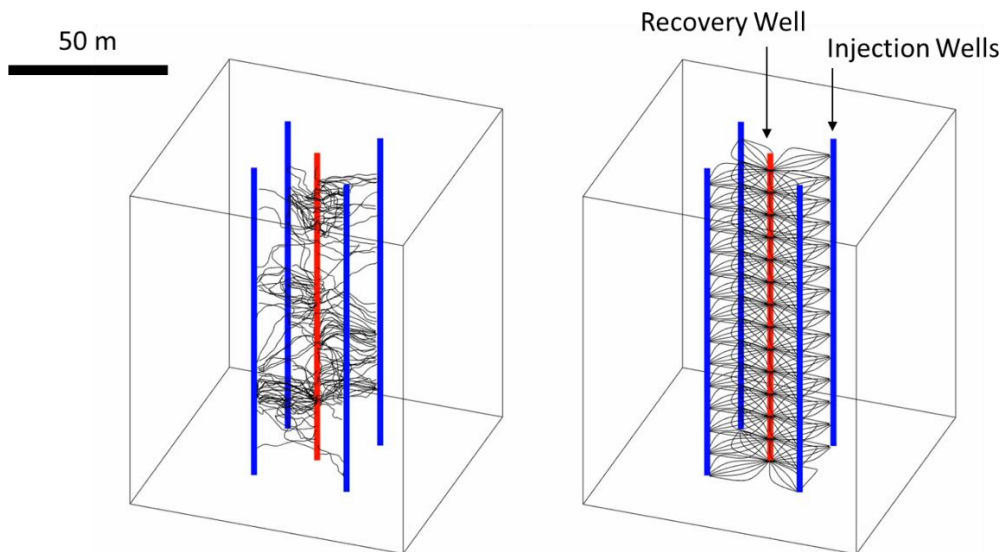


Figure 25 – Left: sample set of flow paths in map view for the heterogeneous cases (1-4). Note that the paths will be different for each of the 100 maps. Right: flow paths from homogenous cases (5 and 6)

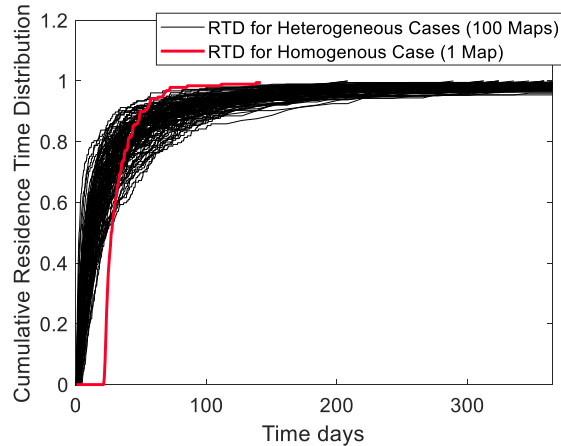


Figure 26 - Residence time distributions of heterogeneous cases (100 maps) and homogenous case (1 map)

5.2.3 Leachate Composition for Cases 1-6

The recovered solution compositions for Cases 1-6 are shown in Figure 27. Note that for Cases 1-4, 100 iterations of the model (100 maps) resulted in 100 compositions. Because Cases 5 and 6 only involved one homogenous map, only one composition is outputted.

It should be noted that the elevated concentrations in Case 2 are largely due to the injected fluid composition. For example, the injected solution for Case 2 contains 352 ppm Cu, which accounts for the increased copper concentration relative to Case 1.

5.2.4 Streamline Composition Maps

The model can also generate compositional information along each streamline as a function of time. For example, Figure 28 shows the percent copper along each streamline and Figure 29 shows the pH along each streamline at the end of the four-year leaching period.

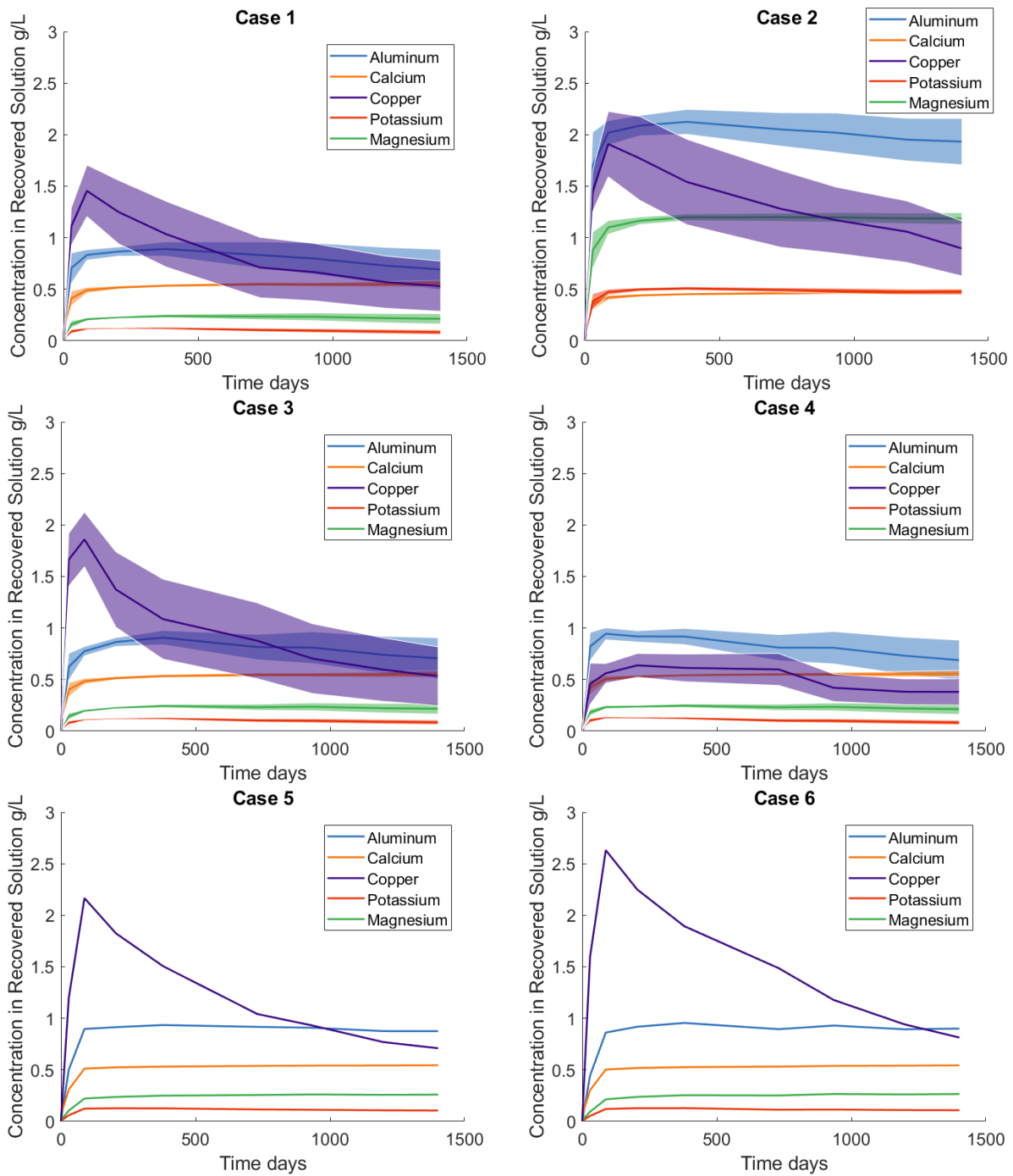


Figure 27 – Pregnant leach solution composition for Cases 1-6. Translucent areas represent 95% prediction intervals

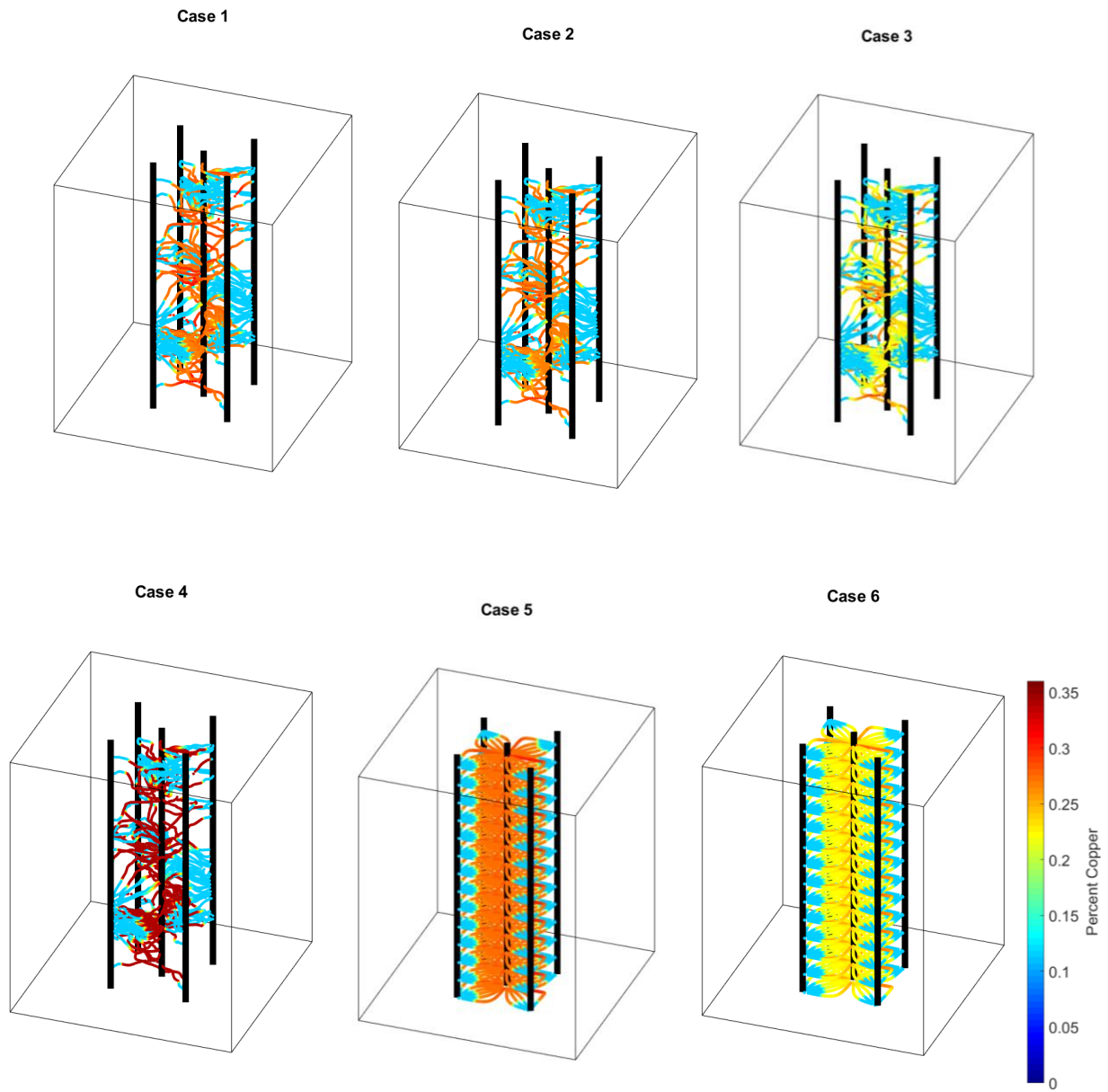


Figure 28 - Maps of percent copper in ore along each streamline at the end of 4-year leaching period. Note that for Cases 1-4, only one of the 100 maps is shown.

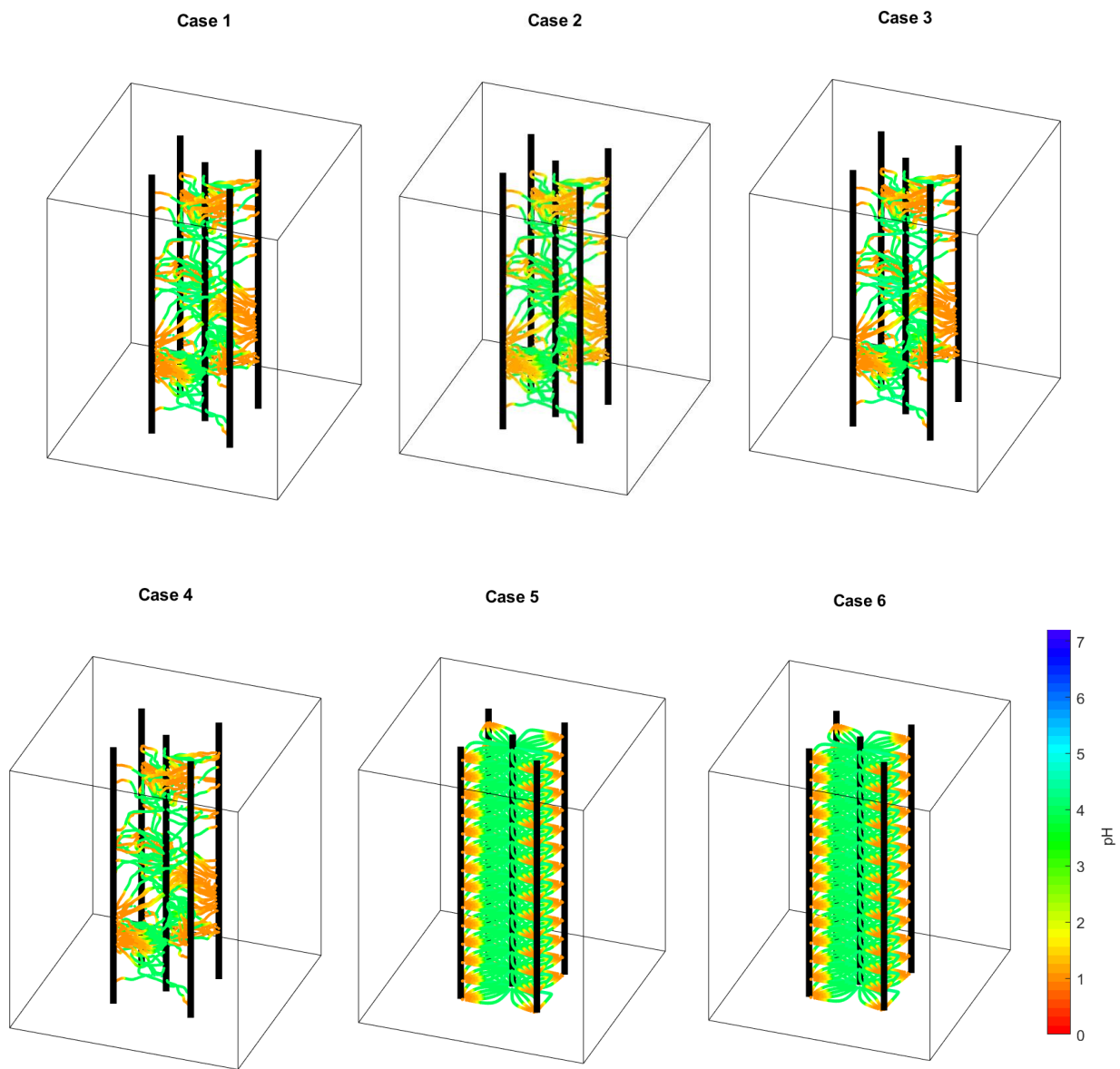


Figure 29 - Maps of pH along each streamline at the end of the 4-year leaching period. Note that for Cases 1-4, only one of the 100 maps is shown.

5.3 *Discussion*

All six cases share some common characteristics. At the beginning of the leaching period, as the solution flushes its first pore volumes out of the formation, the pH is lowered throughout the well spot to an intermediate value (approximately 4-5), which corresponds to near-complete consumption of the injected acid by various acid-consuming minerals. At this point reaction rates throughout the entire well spot proceed at a slow rate which corresponds to the mild acidic conditions.

Simultaneously, a high-acid zone with a pH between 1 and 2 forms around the injection well (see Figure 29). Within the high-acid zone, reactions are significantly accelerated. The high-acid zone slowly advances away from the injection well throughout the four-year leaching period. In the heterogeneous cases, this zone penetrates from injection to recovery well in an uneven fashion, depending on the velocity of the individual streamline. As shown in Figure 29, the zone has broken through to the recovery well after four years for some streamlines but not for others. In the homogeneous cases, the high-acid zone advanced from the injection well in a much more even way, and does not break through to the recovery well within the first four years.

Within the high-acid zone, copper is rapidly leached, first from fracture surfaces and then from the matrix. As the copper-containing solution moves downstream and leaves the high-acid zone, some copper is precipitated as antlerite. In cases with more copper on fracture surfaces, more antlerite precipitates. The antlerite gradually re-dissolves as the high-acid zone advances. In all cases, little antlerite remains at the end of the 4-year leaching period. Gangue reactions including anorthite leaching, anorthite alteration, goethite leaching, and montmorillonite alteration result in modest Al, Ca, Fe, K, and Mg concentrations in the recovered solution. Ca is abated by gypsum precipitation. No diasporite precipitates in any of the four cases.

At the end of the leaching period, ore within the high-acid zone has been almost completely depleted of leachable copper, leaving only unleachable copper behind. This is clear when comparing Figure 28 and Figure 29. Outside of the high-acid zone, the slow reaction rates (corresponding to the mildly acidic conditions) result in only partial depletion of copper.

By contrasting Cases 1-6, several general observations can be made regarding the impact of high-uncertainty parameters on recovery:

Case 1 (fresh acid injected) and Case 2 (mature raffinate injected) had a similar copper recovery, as illustrated in Figure 28. In general, the elevated concentrations of gangue ions in Case 2 did not have a significant effect on leaching of gangue minerals. In particular, anorthite remained well under saturation, and this is the primary acid-consuming mineral in the geochemical model. Further study could focus on whether further gangue ion accumulation would influence copper recovery.

Cases 1, 3, and 4 (50%, 90%, and 10% of copper on fracture surfaces) showed large differences in leachate composition. Figure 28 illustrates the key mechanism behind this difference. In all cases, the high-acid zone penetrates the same extent away from the injection wells, and leachable copper was completely depleted within the high-acid zone. However, outside of the high-acid zone, where copper leaching proceeded slowly at pH 4-5, the extent of copper dissolution is strongly influenced by the percent of copper on fractures surfaces.

Homogeneous cases (Cases 5 and 6) showed higher copper concentration in the recovered solution than the heterogeneous cases. Figure 29 illustrates the reason for this difference. In the heterogeneous cases, the high-acid zone spreads unevenly throughout away from the injection wells. Some low-conductivity pathways are not effectively acidified. The fluid instead channels through high-conductivity pathways, even after their copper minerals have already been depleted.

In the homogeneous cases, the copper depletion front advanced from the injection well in a much more even way.

Case 1 (expected case) shows a lower leachate copper concentration than the laboratory series leach test. There are several reasons for this difference:

- In the series leach test, the copper grade (0.64%) was higher than the deposit average copper grade (0.358%)
- In the series leach test, almost all of the copper appeared to be acid soluble. For the deposit as a whole, the copper is expected to be 68% soluble
- The series leach test had an estimated 80% of copper minerals on fracture surfaces. Case 1 has 50% copper on fracture surfaces.
- In the series leach tests, all flow was directed axially through the core, thus minimizing any flow channeling effects. In the field, significant flow channeling is expected because of heterogeneous hydraulic conductivity.
- In the series leach tests, the distance from injection to recovery point was 4.2 m, so the acid zone has sufficient time to migrate all the way to the outlet. Therefore all of the ore in the series leach test was eventually exposed to high-acid conditions. The flow paths are significantly longer in the field, and for most of the streamlines the high-acid zone does not have time to reach the recovery well (see Figure 29). This highlights the importance of the copper recovery delay associated with downstream migration of the high-acid zone. This is an important consideration when scaling results up from the laboratory to the well spot scale.

It is important to note that each of the parameters in the model can be updated and changed as new information becomes available. For example, the model may be used moving forward to

interpret the results of the upcoming pilot leach test. This will involve leaching of a set of test wells to demonstrate copper recovery. The wells will be rinsed after leaching to demonstrate the feasibility of groundwater restoration. During this pilot test, parameters such as reaction rates, percent copper on fracture surfaces, or flow heterogeneity may be changed as new evidence comes to light.

CHAPTER 6

CONCLUSION

In this study, a computational model was built to represent the in situ leaching system at Florence. Leaching test work was performed on ground ore and intact drill core sections. The results were used to generate a set of geochemical reactions which agreed with the chemical, mineralogical, and acid consumption data. Important reactions included leaching and alteration of anorthite, leaching of iron oxides, leaching of calcite, alteration of clays, leaching of copper minerals, and precipitation of antlerite and diaspore. A rate law was assigned to each reaction based on either a surface-controlled mechanism for fracture coating minerals, or a diffusion-limited mechanism for mineral grains in the rock matrix. The geochemical model showed general agreement with experimental leaching of seven drill cores in series. Petrographic examination of tails from the series leach test were in general agreement with the proposed rate mechanisms for each mineral.

To model the flow paths throughout the leached well spots, several datasets pertaining to hydraulic conductivity were analyzed. These included eight flow profiles measured via electrical conductivity logs, approximately 22,000 fracture density measurements logged from drill cores, 8 single-well pumping tests, and 28 multi-well pumping tests. It was determined that hydraulic conductivity follows a truncated lognormal distribution, with a log space mean of $10^{-6.8}$ m/s, a lower cutoff of 10^{-8} m/s, and a log space standard deviation of $10^{-1.2}$ m/s. The autocorrelation length scale was found to be approximately 8 m in the vertical direction and 32 m in the horizontal directions. Monte Carlo simulations of multi-well pumping tests were used to test this geostatistical model and showed reasonable agreement with the measured data.

The geochemical model and the analysis of hydraulic conductivity were then brought together into a computational model of in situ leaching at Florence. The model user specifies a set of well locations, pumping rates, ore mineralogy, screened interval, and an injected fluid composition. The user can also specify whether the block should be treated as heterogeneous (using hydraulic conductivity maps which conform to the geostatistical characteristics at Florence) or homogeneous (constant hydraulic conductivity throughout). The model begins by computing a set of flow paths from the injection to the recovery well, each of which is treated as a one-dimensional reactive transport system. MATLAB connects to Geochemist's Workbench to apply a set of geochemical reactions along each flow pathway. If running in heterogeneous mode, the model will compute 100 iterations to observe the range of results; if running in homogeneous mode, only one iteration is necessary.

The model was used to run six case studies to observe the effect of high-uncertainty parameters. These include injected fluid composition, the percent of copper on fracture surfaces, and the extent of channeling through the well spot. All cases showed that the entire well spot is first rendered mildly acidic (pH 4-5) during the first few pore volumes. A high-acid zone then develops around the injection wells and migrates slowly downstream throughout the leaching period. Copper is rapidly depleted from this high-acid zone, but is leached very slowly elsewhere in the well spot. By contrasting these six cases, several general conclusions can be drawn:

- The model is not very sensitive to whether fresh acid or mature raffinate composition is used. If other raffinate compositions are of interest, these can be modeled to observe the effect on copper recovery.
- Copper recovery is moderately sensitive to the percent of copper on fracture surfaces, as copper is leached more quickly from surface-coated copper.

- Copper recovery is highly sensitive to flow heterogeneity. Recovery is higher when a homogenous map is assumed, as the high-acid zone penetrates more evenly away from the recovery wells.

The computational model provides valuable insight on the chemical and physical mechanisms behind in situ leaching at Florence. For example, this study has highlighted the critical importance of percent copper on fracture surfaces and flow heterogeneity. This model also points to the importance of flow path length when translating laboratory-scale test work to the field scale. Because copper recovery is largely driven by downstream migration of the high-acid zone, longer path lengths delay copper recovery.

Further work is required to establish the economic viability of in situ leaching at Florence. An upcoming pilot leach test will demonstrate leaching behavior on the well spot scale. Data from this pilot test may be incorporated into the model as it becomes available. Interpreting the field test results will present some challenges. For example, the geostatistical analysis of hydraulic conductivity illustrated that channeling behavior is highly variable across the deposit. The extent of channeling observed in the pilot test may therefore not be representative of flow behavior across the deposit. Tracer or flow profile tests in the pilot leach area may help establish flow and channeling behavior within the pilot area and aid in interpreting recovery behavior.

The computational framework established in this study, particularly the Monte Carlo approach to flow in heterogeneous systems, could be useful for advancing in situ leach modeling in fractured rock. For example, previous in situ leaching field tests have attempted to use borehole flowmeters (BHP Copper Growth and Technology Group, 1997a; L.M. Cathles et al., 1978; Nelson, 1991; Schmidt & Earley, 1997; Weber et al., 2000; Williamson, 1998) pumping tests (BHP Copper Growth and Technology Group, 1997a; L.M. Cathles et al., 1978; Schmidt & Earley, 1997; Weber

et al., 2000; Williamson, 1998), fracture spacing measurements (L.M. Cathles et al., 1978; Dahl, 1989, 1994; J. R. Davis, 1997; Nelson, 1991; Schmidt & Earley, 1997; Williamson, 1998; Yegulalp & Kim, 1996), and/or tracer tests (Huff, Axen, & Baughman, 1988; Pallauta, 1985; Schmidt & Earley, 1997; Weber et al., 2000; Zimmerman et al., 2013) to characterize hydrologic parameters within the target formation. This study illustrates a stochastic approach to translate these various types of hydrologic data into a prediction interval for residence time distribution which can be used for probabilistic forecasting of metal recovery. Such an approach could also be applied to environmental groundwater modeling, fossil fuels, and geothermal energy.

Part II – Supercritical Extraction of Rare Earth Elements

CHAPTER 7

IINTRODUCTION

7.1 *Rare Earth Elements*

Rare earth elements (REEs) consist of the 15 lanthanides (atomic numbers 57 to 71). Scandium and yttrium are sometimes included in REEs because of their similar electronic structure and geologic occurrence. Major applications in the United States include catalysts (55%), metallurgical applications and alloys (15%), ceramics and glass (10%), and polishing (10%) (United States Geological Survey, 2017). Applications for each metal are listed in Table 15.

Table 15 - Applications of rare earth elements (Charalampides, Vatalis, Apostoplos, & Ploutarch-Nikolas, 2015)

Element	N	Application
Scandium	21	High-strength Al-Sc alloys, electron beam tubes
Yttrium	39	Capacitors, phosphors, microwave filters, glasses, oxygen sensors, radars, lasers, superconductors
Lanthanum	57	Glasses, ceramics, car catalysts, phosphors, pigments, accumulators
Cerium	58	Polishing powders, ceramics, phosphors, glasses, catalysts, pigments, mischmetal, UV filters
Praseodymium	59	Ceramics, glasses, pigments
Neodymium	60	Permanent magnets, catalysts, IR filters, pigments for glass, lasers
Promethium	61	Sources for measuring devices, miniature nuclear batteries, phosphors
Samarium	62	Permanent magnets, microwave filters, nuclear industry
Europium	63	Phosphors
Gadolinium	64	Visualization of images in medicine, optical and magnetic detection, ceramics, glasses, crystal scintillators
Terbium	65	Phosphors
Dysprosium	66	Phosphors, ceramics, nuclear industry
Holmium	67	Ceramics, lasers, nuclear industry
Erbium	68	Ceramics, dyes for glass, optical fibers, lasers, nuclear industry
Thulium	69	Electron beam tubes, visualization of images in medicine
Ytterbium	70	Metallurgy, chemical industry
Lutetium	71	Single crystal scintillators

REEs are often categorized into light and heavy rare earths. The light REEs have lower atomic numbers (lanthanum to gadolinium) and heavy REEs have higher atomic numbers (terbium to lutetium). In general, the lighter REEs are more abundant in the earth's crust. Rare earth ores of

primary importance are bastnäsite (La, Ce)FCO₃ and monazite (Ce, La, Y, Th)PO₄; these ores are rich in the lighter REEs such as cerium and lanthanum. Typical ore grades are 5-10% rare earth oxides (Haque, Hughes, Lim, & Vernon, 2014). Xenotime is a minor resource which tends to be richer in heavy REEs and yttrium. Other minor resources include apatite, brannerite, euxenite, gadolinite, loparite, uraninite, and ion-adsorbed rare earth deposits in clays (Krishnamurthy & Gupta, 2004).

Global 2016 rare earth oxide consumption was 126,000 metric tonnes (United States Geological Survey, 2017). Historical mine production of rare earth oxides by country is shown in Figure 30. The United States was once the major global producer of REEs, via the Mountain Pass bastnäsite mine in California. As China developed its rare earth resources, Mountain Pass curtailed and eventually suspended operation amid a series of economic and environmental issues. By the mid-2000s, United States had become over 95% dependent on Chinese REE imports (United States Geological Survey, 2017).

A 2010 dispute between China and Japan resulted in restricted REE exports and a drastic increase in prices, which highlighted the world's dependence on China for its REE supplies (United States Department of Energy, 2011; United States Geological Survey, 2017). This prompted the United States Department of Energy to examine the United States' dependence on imported REEs. Many applications of REEs are critical for strategic technologies in clean energy and defense, and therefore dependence on Chinese exports was seen as a strategic vulnerability (Xie, Zhang, Dreisinger, & Doyle, 2014). The Critical Materials Institute was launched in 2011 to reduce the United States' dependence on imports of several REEs (United States Department of Energy, 2011). Part of this strategy was to reopen Mountain Pass and pursue new domestic production via mining and/or recycling. Mountain Pass briefly resumed production in 2012, but

was put on care and maintenance status in 2015. Australian REE production began at the Mount Weld mine in 2011, which somewhat alleviated China's dominance. As of 2016, REE prices have largely returned to pre-2010 levels (see Figure 31) (United States Geological Survey, 2017).

Part of the Department of Energy's strategy is the development of improved methods for the recovery of individual REEs from ores and recycled streams with reduced costs and environmental impact. Conventional extraction and separation of REEs from ores is outlined below.

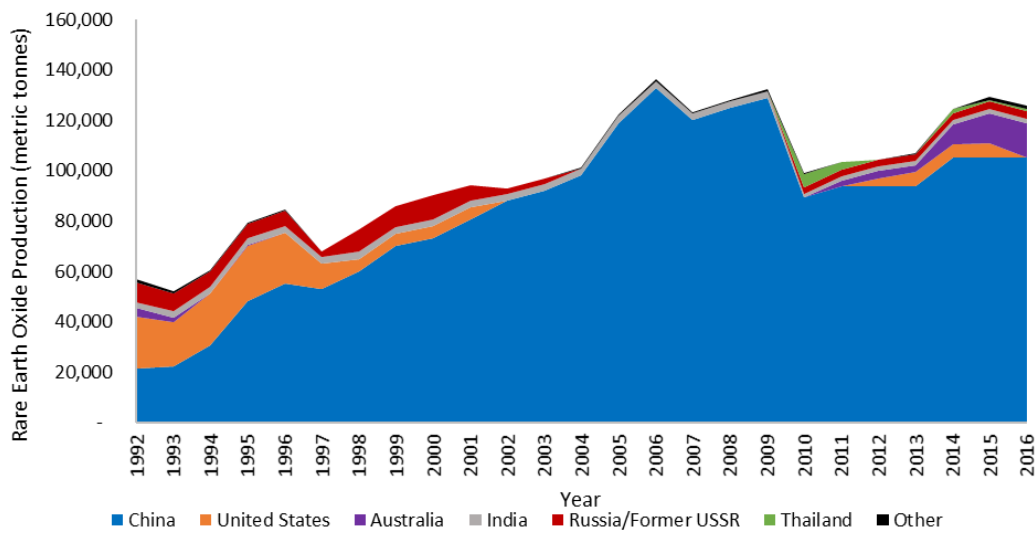


Figure 30 – World mine production of rare earth oxides by country (United States Geological Survey, 2017)

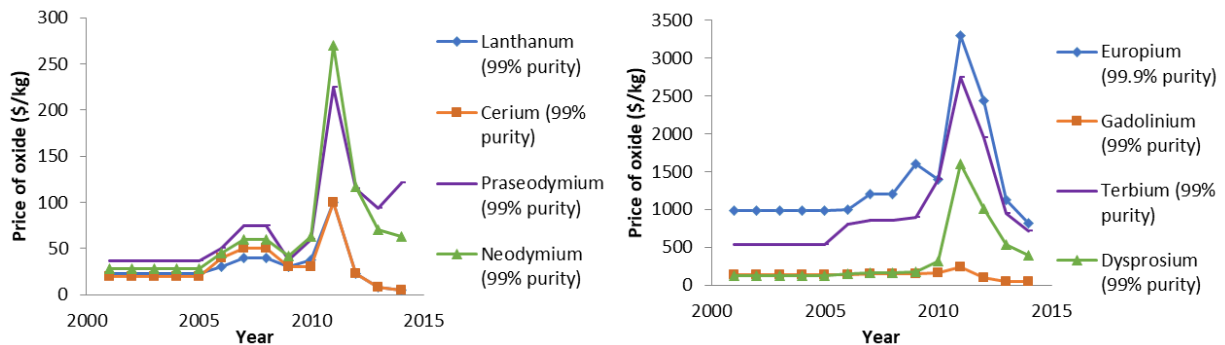


Figure 31 - Lighter (left) and heavier (right) rare earth oxide prices (United States Geological Survey, 2017)

7.2 *Conventional Processing*

7.2.1 Concentration and Upstream Processing

Rare earth ores usually require concentration prior to chemical treatment. The purpose of the concentration step is to reject grains of gangue minerals in order to produce a higher-grade intermediate product known as a concentrate (Krishnamurthy & Gupta, 2004). Bastnäs site ore is usually concentrated by froth flotation to separate the bastnäs site minerals from gangue minerals such as calcite, barite, and strontianite. Monazite placers generally require gravity separation, followed by magnetic and electrostatic separation and/or froth flotation to separate out other heavy minerals such as ilmenite, garnet, and rutile (Krishnamurthy & Gupta, 2004).

Ore concentration is usually followed by chemical and/or thermal digestion to break apart the rare earth matrix, generating an acidic solution containing REEs as well as gangue elements. Some examples include roasting with concentrated sulfuric acid followed by dissolution in water, digestion with NaOH followed by dissolution in acid, and baking followed by dissolution in acid. The digestion step may also involve initial separation of thorium and/or cerium by making use of the +4 oxidation state. More detailed descriptions of the various digestion processes can be found elsewhere (Krishnamurthy & Gupta, 2004; J. Zhang & Zhao, 2016). Some impurities such as iron may be removed with selective precipitation, and the solution then goes on to solvent extraction (Krishnamurthy & Gupta, 2004).

7.2.2 Solvent Extraction

Solvent extraction is a liquid/liquid extraction process in which organic extractant molecules in a nonpolar solvent preferentially bind to REEs, thus pulling them into the organic phase. Solvent extraction is generally done in a series of mixer-settlers, which consist of a mixing compartment feeding into a long settling chamber. In the mixing tank, the organic and aqueous phases are

brought into intimate contact, resulting in an equilibrium distribution of metals between the two phases. The residence time of the mixing stage is generally a few seconds to a few minutes. In the settling compartment, the two phases coalesce and separate. The residence time of the settling stage is generally 2.5 times longer than the mixing stage. Multiple mixer-settlers are used in series to effectively separate REEs. A scrubbing stream often introduced midway through mixer/settler bank to scrub contaminants from the loaded organic. The organic phase then goes on to stripping, in which an aqueous solution strips the metals back out of the organic phase in a series of mixer-settlers (Krishnamurthy & Gupta, 2004; Xie et al., 2014; J. Zhang & Zhao, 2016).

Solvent extraction may be used as a bulk purification process to produce a mixed rare earth material, which can be further treated with processes such as ion exchange used to produce high purity (up to 99.99999%) rare earth products (Krishnamurthy & Gupta, 2004; J. Zhang & Zhao, 2016). Alternatively, solvent extraction can be used to generate relatively pure (up to 99.999%) individual rare earths by exploiting the slightly different binding affinity of each REE due to the decreasing ionic radius across the lanthanide series (Krishnamurthy & Gupta, 2004; Xie et al., 2014; J. Zhang & Zhao, 2016). Because these binding affinity differences are so minor, only slight separation can be achieved in each stage, necessitating tens to hundreds of stages to effectively separate adjacent REEs (Xie et al., 2014). For example, Rhône-Poulenc was capable of producing all REEs at 99.999% purity almost entirely by solvent extraction, but required at least 50 mixer-settler stages per metal (Krishnamurthy & Gupta, 2004; Xie et al., 2014).

To quantify the separation performance of a solvent extraction system, the distribution ratio (D_{M1}) and separation factor ($\beta_{M1/M2}$) are defined as follows:

$$D_{M1} = \frac{[M_1]_o}{[M_1]_{aq}} \qquad \beta_{M1/M2} = \frac{D_{M1}}{D_{M2}} \qquad \text{Eq 14}$$

The higher the separation factor between adjacent lanthanides, the more effective the separation. There are many types of REE extractants as discussed below.

7.2.3 Extractants

7.2.3.1 *Cationic Exchangers*

Cationic exchanging extractants exchange a proton for an REE cation:



The subscript ‘o’ denotes the organic phase. Commercial cationic exchangers include organophosphorus acids and carboxylic acids (see Table 16 for a summary of the most common commercialized extractants). Extraction increases with atomic number, due to increased electrostatic attraction as atomic radius decreases (Krishnamurthy & Gupta, 2004).

Because protons are released in the binding reaction, extraction is promoted by high pH in aqueous solution. High pH during extraction can be achieved by partially saponifying the extractant with NaOH. Highly acidic strip solutions are used to strip the REEs back out of the organic phase (a reversal of Equation 15). Generally, cationic exchangers offer high selectivity, but have the disadvantage of requiring large amounts of other reagents, including bases for saponification and acids to drive stripping. Therefore solvent extraction systems employing cationic exchangers require fewer stages (resulting in lower capital costs) but require greater reagent consumption (resulting in higher operating costs) relative to other extractant types (Krishnamurthy & Gupta, 2004; Xie et al., 2014). Consumption of acid is also one of the major contributors to the environmental impact of REE production (Haque et al., 2014; Vahidi & Zhao, 2016).

7.2.3.2 Anionic Exchangers

Anionic exchangers extract metals as anionic complexes. Anionic exchangers are generally quaternary ammonium salts; other amines including primary, secondary, and tertiary amines have been tested but were found to be less effective (Krishnamurthy & Gupta, 2004; Xie et al., 2014). Extraction by a quaternary ammonium salt in nitrate media may be represented by:



Extraction with anionic exchangers decreases with atomic number, opposite of most other extractants (J. Zhang & Zhao, 2016).

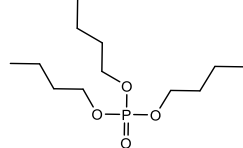
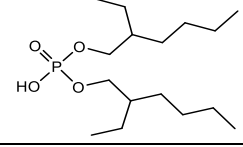
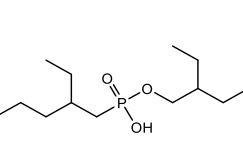
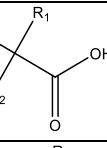
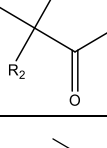
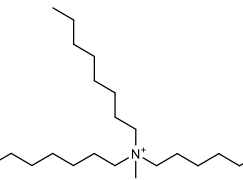
7.2.3.3 Solvating Extractants

Solvating extractants are neutral molecules which can replace some or all of the coordinated water molecules surrounding a cation, thus rendering it soluble in the organic phase. Tributyl phosphate (TBP) is the only commercial solvating extractant for REEs.



TBP binding affinity increases with atomic number, due to the stronger binding forces associated with their smaller atomic radii (depending on the acid concentration, binding affinity may begin decreasing again towards the end of the lanthanide series) (Krishnamurthy & Gupta, 2004; Peppard, Driscoll, Sironen, & McCarty, 1957; J. Zhang & Zhao, 2016). Its selectivity is low relative to other extractants (see Table 16) (Krishnamurthy & Gupta, 2004; J. Zhang & Zhao, 2016). TBP does have some ability to separate light REEs, and is therefore mostly used for producing a mixed rare earth product, or for the concentration of La, Pr, and Nd (Krishnamurthy & Gupta, 2004; Xie et al., 2014; J. Zhang & Zhao, 2016).

Table 16: Most commonly used REE extractants

Extractant	Other Names	Type of Extractant	Aqueous Solution	Structure	Separation Factors	Advantages/Disadvantages
Tributyl Phosphate	TBP	Solvating extractant	Mainly nitrates		1.2 - 2.2 for nitrate medium	Poor selectivity relative to other extractants (Krishnamurthy & Gupta, 2004; Xie et al., 2014)
Di-2-ethyl-hexyl-phosphoric acid	HDEHP, D2EHPA, or TOPS99	Cationic exchanger	Nitrates, chlorides, sulfates, perchlorates		1.25 - 4.26 for nitrate medium	Good for bulk separation of rare earths because REEs are effectively separated as a group from typical impurity metals. Can extract effectively at high acidity, but stripping can be difficult (Krishnamurthy & Gupta, 2004; Xie et al., 2014)
2-ethyl-hexyl-2-ethyl-hexyl-phosphonic acid	EHEHPA, HEHEHP, PC88A, P507, Ionquest 801	Cationic exchanger	Nitrates, chlorides		1.27 - 4.55 for nitrate medium	Can be stripped with higher pH solutions and can be more heavily loaded with extracted metal compared to HDEHP (Xie et al., 2014). Separation factors are higher than those for HDEHP, although overall extraction is lower. Often used for separation of individual REEs, particularly the heavy REEs (Krishnamurthy & Gupta, 2004, p. 173).
Versatic Acid 911		Cationic exchanger	Nitrates, chlorides	 $R_1, R_2 = C_4 - C_5$	1.17 - 3 for nitrate or chloride medium	Separation factors for light REEs are higher than TBP. Beyond Nd/Pr, separation factors are similar to TBP (Krishnamurthy & Gupta, 2004)
Versatic Acid 10		Cationic exchanger	Nitrates, chlorides	 $R_1, R_2 = C_6$		(Krishnamurthy & Gupta, 2004, p. 176)
<i>N</i> -methyl- <i>N,N</i> -dioctyloctan/didecyl-1-ammonium nitrate/thiocyanate	Aliquat 336	Anionic exchanger	Nitrates, thiocyanates		1.02 - 2.97 for nitrate medium	Separation factors are generally lower than EHEHPA (Krishnamurthy & Gupta, 2004)

7.3 *Supercritical Fluid Extraction*

7.3.1 Background

Supercritical carbon dioxide is defined as CO₂ above its critical temperature of 31°C and its critical pressure of 7.39 MPa. At these conditions, CO₂ has a density and solvation power similar to many liquid solvents, yet possesses the high diffusivity of a gas. Supercritical carbon dioxide has several desirable properties as a non-polar solvent, including tunable density/solvation properties and gas-like diffusion rates which facilitate penetration into solid matrices (Teoh, Mammucari, & Foster, 2013). Supercritical carbon dioxide has been used commercially for decades as a non-polar solvent in the food, chemical, and materials industries. For example, it has been adopted as a solvent to remove caffeine from coffee beans and tea (Teoh et al., 2013). In the last twenty-five years, several researchers have explored the use of supercritical CO₂ as an extraction medium for metals. This process is similar to solvent extraction: a metal or metal salt in a solid or aqueous phase bonds with extractant molecules to form a non-polar complex, which can then dissolve into the supercritical phase.

7.3.2 Metal Complex Solubility Behavior

7.3.2.1 *Models*

It can be challenging to model or predict solubility of metal complexes in supercritical CO₂. Solubility will depend on solvation effects from interactions between CO₂ and solute molecules, including Van der Waals, hydrogen bonding, and Lewis acid/Lewis base interactions. The resulting clustering of CO₂ molecules around the solute enhance solubility 2 to 5 orders of magnitude above the concentration predicted by an ideal gas mixture model based on the solute's vapor pressure (Teoh et al., 2013).

This solvation effect leads to an increase in solubility with an increase in density of the supercritical CO₂ phase. Many previous studies have correlated solvation in an empirical fashion using the Chrastil model (Andersen, Sievers, Lagalante, & Bruno, 2001; Chrastil, 1982; Hwang, Tsukahara, Miyamoto, & Ikeda, 2016; Smart, Carleson, & Kast, 1997; L. Y. Zhu, Wang, He, & Tian, 2016):

$$\ln(S) = k_{Chrastil} \ln(\rho) + \frac{A}{T} + B \quad \text{Eq 18}$$

Where S is the solubility of the solute, ρ is the supercritical CO₂ phase density, $k_{Chrastil}$ is the association number (number of CO₂ molecules associated with each complex), T is the temperature in Kelvin, A is an empirical constant (theoretically $A=(\Delta H_{\text{solvation}} + \Delta H_{\text{vaporization}})/R$), and B is an empirical constant (theoretically $B=\ln(M_{\text{solute}} + kM_{\text{CO}_2}) + (\Delta S_{\text{solvation}} + \Delta S_{\text{vaporization}})/R - k_{Chrastil}\ln(M_{\text{CO}_2})$ where M_s is the molar mass of species s) (L. Y. Zhu et al., 2016). The number of CO₂ molecules that associate with a metal complex can be calculated from fitting the Chrastil model (Andersen et al., 2001; Smart et al., 1997) or from molecular dynamics simulations (S. Liu, Chai, & Yang, 2009).

Other empirical solubility models have been attempted, but can be challenging with supercritical CO₂ systems. For example, solubility parameter and regular solution theories have not succeeded in replicating supercritical CO₂ solubility data, likely because of the volume change associated with clustering of CO₂ and/or the significant size and polarity differences between solute and solvent (Lagalante, Hansen, Bruno, & Sievers, 1995; Teoh et al., 2013). Models employing Van der Waals equations of state with simple mixing rules have been attempted with limited success for organometallic complexes due to the lack of information about the critical temperature and pressure of the solutes, as well as the dissimilarity between CO₂ and the solute

(Teoh et al., 2013). Some researchers have attempted to address these challenges using group contribution model and regular solution theory, which has been applied to copper and chromium beta diketones in supercritical carbon dioxide. However, this approach resulted in a poor fit to experimental data, possibly due to invalidity of some simplifying assumptions in regular solution theory (e.g. the assumption of no volume change upon mixing) (Lagalante et al., 1995).

7.3.2.2 *Effect of Metal Properties*

Solubility of a metal complex is generally lower than the solubility of the extractant by itself (Smart et al., 1997; L. Y. Zhu et al., 2016). The electronegativity of the central atom can affect the ionic character of the metal-ligand bond and therefore affect its interaction with nonpolar CO₂. In general, higher oxidation state metals have higher solubility because they are able to bind with more ligands and therefore better shield themselves from the non-polar environment (Smart et al., 1997; Teoh et al., 2013).

7.3.2.3 *Effect of Temperature and Pressure*

Temperature and pressure affects extraction in several different ways.

Firstly, changes in temperature shift the equilibrium of the binding reaction. For example, lower temperatures can favor complexation of the metal, consistent with a shift to a lower-entropy state (Krishnamurthy & Gupta, 2004).

Temperature and pressure can also affect the solubility of the metal-extractant complexes. In general, most studies see increasing extraction with increasing pressure due to higher density as illustrated in the aforementioned Chrastil model (L. Y. Zhu et al., 2016). Previous studies have illustrated that metal complexes can have a maximum solubility at an intermediate temperature due to the competing effect of density and adduct volatility (Teoh et al., 2013; L. Y. Zhu, Duan, Xu, & Zhu, 2011). If water is present in the supercritical extraction system, temperature and

pressure can also affect the solubility of water, and this can affect metal extraction. For example, in a very wet system, an increase in pressure could lead to more dissolution of water which could increase the supercritical phase polarity and thus reduce metal complex solubility. This may explain why some studies with high water content have shown decreasing metal extraction with increasing pressure (Meguro, Iso, & Yoshida, 1998; Tomioka, Enokida, & Yamamoto, 1998).

Finally, temperature and pressure could affect the kinetics of extraction from solids and liquids due to changes in mass transfer properties including viscosity and diffusivity (S. Liu et al., 2009; Yao, Farac, & Azimi, 2017). Of course, mass transfer properties will not affect equilibrium distribution between supercritical and solid/liquid phases, only the time required to reach equilibrium.

7.4 Supercritical Actinide and Lanthanide Extraction

7.4.1 Previous Work

Early supercritical metal extraction studies focused on base and transition metals (Andersen et al., 2001; Lagalante et al., 1995; Laintz, Wai, Yonker, & Smith, 1991). Actinide extraction using TBP as an extractant quickly became an area of focus as a potential replacement for the PUREX solvent extraction process for fission product separation (Yuehe Lin, Smart, & Wai, 1995; Samsonov, Wai, Lee, Kulyako, & Smart, 2001; Smart et al., 1997). The PUREX process uses TBP in a 3-6 M nitric acid medium to separate spent nuclear fuel. This process results in contaminated organic streams which require disposal, therefore supercritical extraction was seen as a viable alternative (Enokida, Tomioka, Lee, Rustenholtz, & Wai, 2003). This area led to numerous studies of the TBP/nitrate/supercritical CO₂ system. Researchers demonstrated extraction of uranium and other actinides from aqueous solutions (Yuehe Lin et al., 1995) and from solid oxides or nitrates (Samsonov et al., 2001; Shamsipur, Ghiasvand, & Yamini, 2001). Molecular dynamics

simulations have also provided important insights, including illustrating the formation of multiple complexes with different numbers of TBP coordinated around the central metal (Schurhammer & Wipff, 2005), interfacial phenomena (Schurhammer, Berny, & Wipff, 2001), and side reactions including the complexation of TBP with water and nitric acid (Schurhammer & Wipff, 2005). In 2009, a small-scale plant demonstrated supercritical extraction of uranium from incinerator fly ash (Koegler, 2010), but the process has yet to reach commercial adoption.

In parallel with the work on actinide extraction, many researchers began using the TBP/nitrate/supercritical CO₂ system to extract REEs from aqueous nitrate solutions (Dehghani, Wells, Cotton, & Foster, 1996; Laintz & Tachikawa, 1994) and from solid nitrate salts (R. V. Fox et al., 2004; R. V. Fox, Ball, Harrington, Rollins, & Wai, 2005; L. Y. Zhu et al., 2016). In a slight variation of this process, a premixed TBP and HNO₃ adduct can be dissolved in supercritical CO₂, and used to extract REEs from acid-soluble minerals such as oxides (Baek et al., 2016; Tomioka, Enokida, & Yamamoto, 1998, 2002; Wuhua, Pijia, & Yongjun, 2010; L. Zhu, Duan, Xu, & Zhu, 2009; L. Y. Zhu et al., 2011). In this latter configuration, the extraction mechanism involves three sequential steps in a single reaction vessel: reaction of REE minerals with nitric acid to form REE nitrates, complexation of the nitrate salt with TBP, and dissolution of the metal complex in CO₂.

While these studies have demonstrated extraction from solutions, oxides, and nitrates, there has been little work on supercritical extraction of REEs from real ores or recycled materials. One study investigated supercritical REE extraction from preprocessed monazite, but questions remain regarding separation of radioactive contaminants (Samsonov et al., 2015). There has also been some work on REE recovery from recycled fluorescent lamp phosphors (Shimizu, Sawada, Enokida, & Yamamoto, 2005) and from nickel-metal-hydride batteries (Yao et al., 2017).

Other extractants have also been explored for supercritical REE extraction including tributyl phosphite (R. V. Fox, 2003), tributyl phosphine oxide (R. V. Fox, 2003), di-2-ethyl-hexyl-phosphoric acid (Samsonov et al., 2015), acetylacetone (Y. Lin & Wal, 1994), trifluoroacetylacetone (Y. Lin & Wal, 1994), hexafluoroacetylacetone (R. V. Fox, 2003; Hwang et al., 2016; Y. Lin & Wal, 1994), thenoyltrifluoroacetone (R. V. Fox, 2003; Y. Lin & Wal, 1994), 2,2,7-trimethyl-3,5-octanedione (Andersen et al., 2001), 2,2,6,6-tetramethyl-3,5-heptanedione (Andersen et al., 2001), and 2,2-dimethyl-6,6,7,7,8,8,8-heptafluoro-3,5-octanedione (Hwang et al., 2016; Y. Lin & Wal, 1994). Some studies have also explored combinations of TBP and beta diketones (Binnemans & Jones, 2014; R. V. Fox, 2003; Miyamoto et al., 2012). Some key results include:

- Fluorinated extractants tend to result in higher extraction than non-fluorinated extractants (Andersen et al., 2001; Hwang et al., 2016; Y. Lin & Wal, 1994)
- Extraction with both beta diketones and TBP results in a higher extraction extent than TBP alone (R. V. Fox, 2003)

7.4.2 Extraction Mechanism

Studies have shown that heavier REEs are preferentially extracted by TBP in supercritical systems, just as they are in liquid/liquid systems (R. V. Fox et al., 2004, 2005; L. Y. Zhu et al., 2016). However, questions remain about the specific separation mechanisms at play, and whether these mechanisms differ fundamentally from a liquid/liquid system.

The first step in solvent extraction or supercritical extraction is coordination of the metal with TBP. Experiments and simulations have confirmed that lighter lanthanides (La to Sm) have a coordination number of 9 in a nitrate solution, whereas heavier lanthanides (Dy to Lu) have a coordination number of 8 (coordination numbers of both 8 and 9 are thought to be possible for the

middle lanthanides). In nitrate solution, these inner coordination spheres are populated with water at low nitrate concentrations, with bidentate nitrate gradually occupying more of the inner coordination sphere as ionic strength increases (Beudaert, Lamare, Dozol, Troxler, & Wipff, 1999; Chatterjee et al., 2015; Cotton, 2006; Duvail & Guilbaud, 2011; P. Zhang, Kimura, & Yoshida, 2004).

When TBP is introduced into this system, the polar phosphate group substitutes for a coordinated water molecule around the metal cation. A trivalent lanthanide can be coordinated with up to 4 TBP molecules according to molecular dynamics simulations (Beudaert et al., 1999). As more TBP molecules surround the central ion, the center becomes progressively more dehydrated and better shielded with nonpolar butyl groups, and the complex eventually becomes soluble in the nonpolar phase.

Many studies have suggested that only the 1:3 complex is extracted into the organic phase in conventional liquid/liquid systems (Krishnamurthy & Gupta, 2004; Peppard et al., 1957; Zhuangfei Wang, Liu, He, Zhu, & He, 2017; J. Zhang & Zhao, 2016). However, some studies have pointed to other stoichiometries in organic and supercritical systems. Studies have suggested that REEs can be extracted as 1:4 complexes (especially at low water availability) (Beudaert et al., 1999; R. V. Fox et al., 2004), and that heavier REEs such as Ho, Tb, and Lu can also be extracted as 1:2 complexes (R. V. Fox et al., 2005; Laintz & Tachikawa, 1994). It is not clear whether the complex stoichiometry is dependent upon the nature of the nonpolar phase (for example, supercritical CO₂ versus organic solvent).

Figure 32 shows a proposed series of structures which were assumed throughout this study. The lanthanide cations were assumed to have coordination numbers of 8-10, based on several experimental (Braatz, Antonio, & Nilsson, 2017; P. Zhang et al., 2004) and computational

(Beudaert et al., 1999; Duvail & Guilbaud, 2011) studies. Bidentate coordination of the nitrate groups dominates, especially in low-water environments (Beudaert et al., 1999; Cotton, 2006; Duvail & Guilbaud, 2011). Though there is some dispute on this topic, most studies suggest that complexes containing 3 or more TBP molecules have fully dehydrated inner coordination spheres, although some dynamic exchange of water in and out of the inner coordination sphere is possible (Beudaert et al., 1999; Navon, Stavola, & Scaatst, 1981; Zhuangfei Wang et al., 2017; P. Zhang & Kimura, 2006; P. Zhang et al., 2004).

7.4.3 Potential Application

If proven viable, supercritical extraction could replace the leaching and/or solvent extraction steps in conventional ore processing. In this proposed process, ores would undergo conventional concentration and digestion steps to isolate and convert REE minerals to an acid-soluble form. Then a supercritical phase containing a dissolved TBP/HNO₃ adduct would be used to extract REEs directly from the solid matrix. After extraction, the REEs could be precipitated via stripping or pressure reduction (which lowers solute solubility in supercritical CO₂), and the CO₂ can be recycled back to the extraction step.

Several different mechanisms could potentially provide for REE separation. If the various REEs have differing kinetics and/or equilibrium distributions during extraction, this could be exploited to achieve separation. Another potential separation mechanism involves the tunable solvation properties of supercritical CO₂: if the various REE complexes have different relationships between pressure and solubility, sequential pressure increases or reductions could be used to separate the REEs from each other.

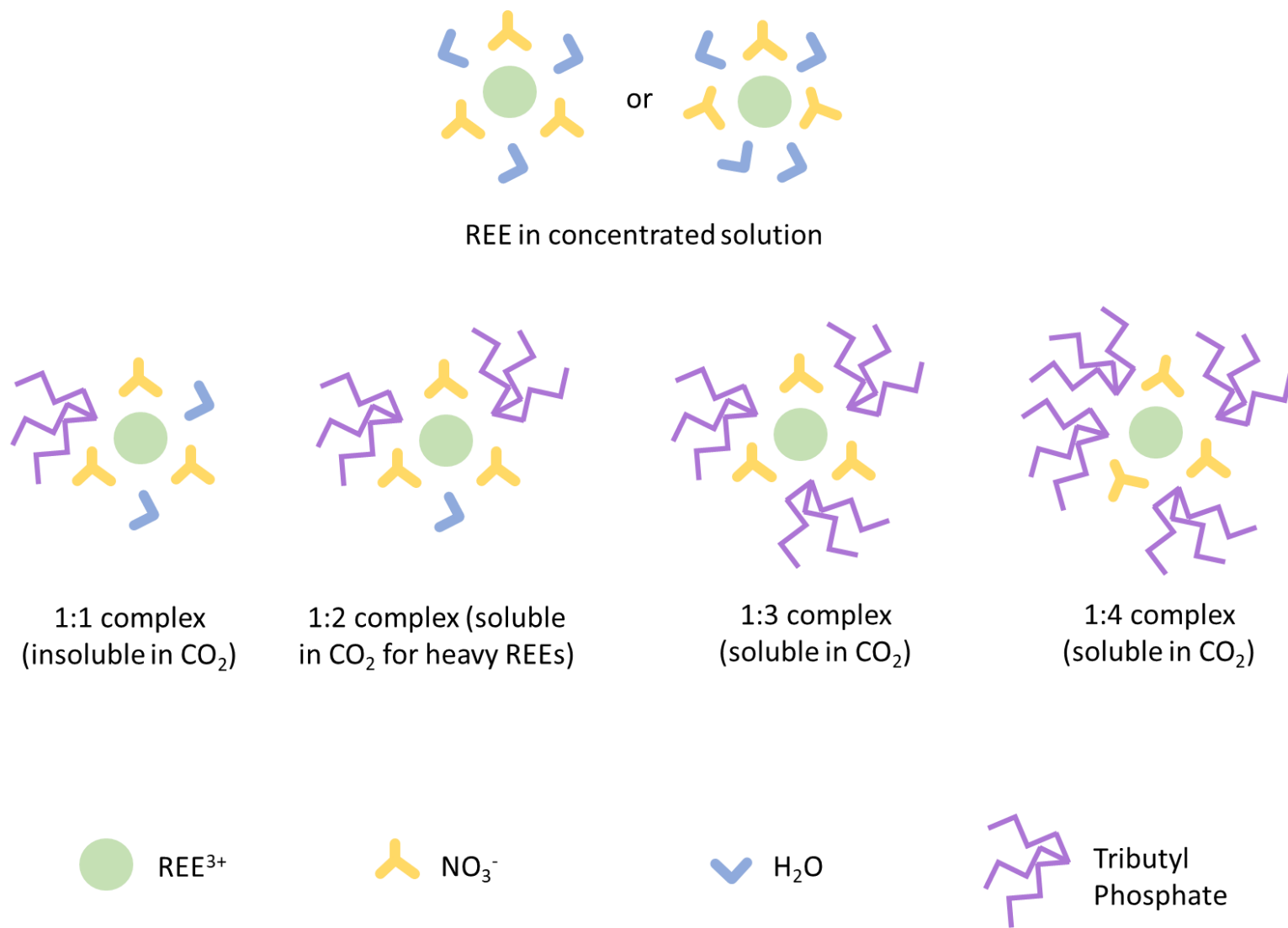


Figure 32 - Structure of REEs in concentrated nitrate solution, and coordinated with 1-4 TBP molecules

A supercritical extraction and separation process could present several advantages over conventional leaching/solvent extraction technology:

- Selective extraction of lanthanides over alkaline, alkaline earth, and transition metals
- Reduced residence time requirements for extraction due to the high diffusivity of supercritical carbon dioxide
- Reduction in the number of equilibrium stages required for separation
- Reduction in acid consumption by precipitating REEs from the supercritical phase via pressure reduction rather than acid stripping
- Elimination of flammability issues through replacement of organic solvents such as kerosene with non-flammable CO₂

7.5 Goal and Scope

7.5.1 Supercritical Extraction from Rare Earth Element Ores/Concentrates

There are several unanswered questions regarding the applicability of supercritical CO₂ to extract REEs from source materials and separate metals into separate REE products. Although extraction from oxides and nitrates has been demonstrated, supercritical extraction from ore samples has been limited (Samsonov et al., 2015). Researchers do not yet understand how the TBP/nitrate/supercritical CO₂ system will behave when exposed to a real REE ore or concentrate containing a mixture of different minerals. Ores and concentrates contain gangue minerals such as barite and calcite; their behavior during supercritical extraction has not yet been established. The first goal of this research is therefore to evaluate the technical feasibility of using supercritical CO₂ to extract REEs from bastnäs site concentrate as a first step in demonstrating the applicability of supercritical extraction to existing primary sources. Two pretreatment methods were evaluated in this study given their dominant use in conventional bastnäs site concentrate processing: roasting and

NaOH digestion. A range of adduct compositions and adduct concentrations in CO₂ were evaluated.

7.5.2 The Role of Water in Extraction and Separation

The second goal of this research is to understand the role of water in separation of REEs with TBP, using neodymium and holmium as model light and heavy REEs respectively. A more water-rich environment will inhibit extraction because of 1) the reduction in REE activity from dilution and 2) the ability of water to form complexes with TBP and thus reduce the TBP available for REE extraction (Hardy, Fairhurst, McKay, & Willson, 1964). To study the effect of water, TBP was used to extract REEs from nitrate salts or solutions in a batch equilibrium system. Absorption spectroscopy in the visible range was used to quantify extraction of Nd and Ho, as demonstrated in previous studies (R. V. Fox et al., 2004; Hwang et al., 2016; L. Y. Zhu et al., 2016). A novel element of this work is the use of near-IR spectroscopy (Zheming Wang et al., 2013) to measure water extraction in conjunction with lanthanide extraction. A range of TBP concentrations, a range of water concentrations, and a range of pressures were explored.

7.5.3 Feasibility of Metal Separation with Pressure Reduction

Nd and Ho extraction was tested at low pressures (<17 MPa) to explore the feasibility of metal separation via sequential pressure reduction. In these experiments, water extraction could not be measured because the pressure was too low.

CHAPTER 8

SUPERCRITICAL EXTRACTION FROM RARE EARTH ELEMENT CONCENTRATES

8.1 Goal and Scope

The first goal of this work is to use supercritical CO₂ to extract REEs from bastnäsite concentrate as a first step in demonstrating the applicability of supercritical extraction to existing primary sources. Bastnäsite is a cerium- and lanthanum-dominant REE fluorocarbonate mineral which accounts for approximately 70% of worldwide REE production (Kul, Topkaya, & Karakaya, 2008). In this study, pretreated bastnäsite concentrate was exposed to a supercritical CO₂ phase containing TBP/HNO₃ adducts to selectively extract the REEs. Two pretreatment methods were evaluated in this study given their dominant use in conventional bastnäsite concentrate processing: roasting and NaOH digestion. A range of adduct compositions (TBP/HNO₃ ratio) and adduct concentrations in CO₂ (mol% adduct in supercritical phase) were evaluated to examine the effect on extraction kinetics. This work was outlined in a recent publication and conference presentation (L.K. Sinclair, Baek, & Fox, 2016; L.K. Sinclair, Baek, Thompson, Tester, & Fox, 2017).

8.2 Materials

8.2.1 Reagents

Dry molecular sieves were acquired from Delta Adsorbents (mSorb 3A 8 × 12 IMS, Delta Adsorbents, Roselle, IL) and dried in a vacuum oven overnight at 523 K (250 °C) prior to use. Tri-n-butyl phosphate (TBP, 97%) and silanized glass wool were purchased from Sigma-Aldrich (St. Louis, MO). The TBP was dried to <300 ppm H₂O with the molecular sieves prior to use. Fuming nitric acid (ACS grade, 21.2 M, >90% w/w) was obtained from Macron Fine Chemicals (Center Valley, PA) and utilized as received. ACS grade sodium hydroxide pellets were purchased from

Thermo Fisher Scientific (Hampton, NH). A bone dry liquid carbon dioxide tank with a siphon was purchased from Airgas (Radnor, PA).

8.2.2 Bastnäsite Concentrate

Bastnäsite concentrate was obtained from the Mountain Pass mine in California, the United States' only recently active REE mine, which ceased operations in 2015. At Mountain Pass, bastnäsite ore grading approximately 7% rare earth oxides was fed to a froth flotation and weak acid leach process where it was concentrated to approximately 70% rare earth oxides (Krishnamurthy & Gupta, 2004).

X Ray Diffraction (XRD) (Bruker D8 Discover, Bruker Corporation, Billerica, MA) was used to confirm the presence of the expected mineral phases in the bastnäsite concentrate sample as shown in Figure 33. The observed peaks correspond to the presence of bastnäsite, hydroxylbastnäsite, and possibly barite. This is consistent with the reported composition of Mountain Pass concentrate (Krishnamurthy & Gupta, 2004).

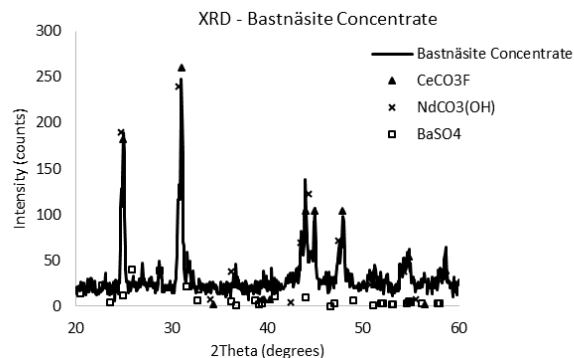


Figure 33 - XRD patterns of bastnäsite (CeCO₃F: PDF#00-011-0340. NdCO₃(OH): PDF#00-038-0400. BaSO₄: PDF#00-005-0448 (The International Centre for Diffraction Data, 2013).

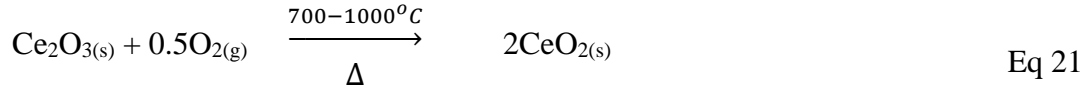
8.3 *Pretreatment Methods*

8.3.1 Roasting

8.3.1.1 *Chemistry*

Conventional bastnäsite concentrate processing often begins with roasting to break down the fluorocarbonate structure. The chosen temperature will depend on the type of processing to be conducted further downstream, and may also depend on the ratio of carbonate to fluoride content in the ore. Roasting has three purposes: to further concentrate the REEs by driving off CO₂, to increase the acid solubility of rare earths, and sometimes to oxidize cerium to its tetravalent state (Xie et al., 2014; Yörükoğlu, Obut, & Girgin, 2003).

The chemistry of the roasting process depends on the roasting temperature chosen and the residence time. If the concentrate is roasted to 400-500°C, the bastnäsite mineral is oxidized to form oxyfluorides (Equation 19), and CO₂ gas is driven off (Krishnamurthy & Gupta, 2004; Xiang, Zhang, Tu, & Ren, 1994). At temperatures between 500°C and 700°C, the oxyfluorides are gradually further transformed into acid-soluble oxides and insoluble trifluorides. HF gas is released in the process (Equation 20) (Suchen et al., 2007; Xiang et al., 1994). Between 700 and 1000°C, cerium can also oxidize to form insoluble cerianite (Equation 21), allowing for the separation of cerium from other REEs in downstream leaching steps (Xiang et al., 1994). The roasted bastnäsite is now much more easily dissolved in mineral acids such as nitric acid (Equation 22).



8.3.1.2 Procedure

In an effort to make a comparison with current methods, conditions were chosen that were similar to conventional bastnäsite roasting temperatures. For this study, bastnäsite was dried overnight under vacuum at 100°C and 15 g was then weighed into a porcelain crucible. The powder was baked for 3 hours at 730°C at atmospheric pressure.

8.3.1.3 Characterization

The elemental composition of the roasted bastnäsite concentrate was obtained via duplicate LiBO₂/Li₂B₄O₇ fusion and Inductively Coupled Plasma Optical Emission Spectrometry (ICP-OES) (SpectroBlue Side-On Plasma, Spectro Analytical Instruments, Kleve, Germany) (see Table 17). The composition of the original bastnäsite concentrate was calculated based on the roasted bastnäsite assay and the measured mass loss during roasting. XRD was used to identify mineral phases (see Figure 34). The results are in agreement with a cerium and lanthanum oxide mixture and/or an oxyfluoride mixture: Ce₂O₃, LaF₃, CeF₃, and Ce(CO₃)F were not identified, suggesting full conversion of the bastnäsite to oxides and/or oxyfluorides with little formation of trifluorides. This could be indicative of low fluoride levels in the source material.

Sonic sifting (model L3P, ATM Corporation, West Allis, WI) was used to measure the particle size distribution (see Figure 35). The results indicated a P80 of approximately 45 microns. Sieves used are considered accurate to +/-2 microns (ASTM E161-12, 2012). Size distributions in the <10 micron range could not be measured.

Table 17: Elemental Composition of Raw and Pretreated Bastnäsité Samples

Material	La	Ce	Pr	Nd	Sm	Eu	Gd	Tb	Ba	Ca	Sr
Raw Bastnäsité	20.7%	28.0%	2.5%	6.6%	0.5%	<0.2%	0.2%	0.1%	3.5%	0.7%	3.5%
Roasted Bastnäsité	25.1%	34.1%	3.0%	8.0%	0.6%	<0.2%	0.2%	0.1%	4.3%	0.9%	4.2%
NaOH Digested Bastnäsité	25.2%	33.1%	3.0%	7.7%	0.5%	<0.2%	0.2%	0.1%	3.6%	1.0%	<1.7%
Reporting Limit (lowest calibration standard)	4.3%	1.0%	0.2%	0.2%	0.1%	0.2%	0.2%	0.03%	0.8%	0.3%	1.7%

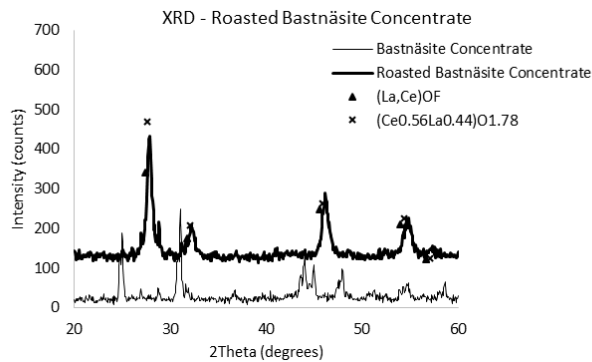


Figure 34 - XRD pattern for roasted bastnäsité concentrate ((La,Ce)OF: PDF#00-057-0608. (Ce_{0.56}La_{0.44})O_{1.78}: PDF#01-071-6545) (The International Centre for Diffraction Data, 2013)

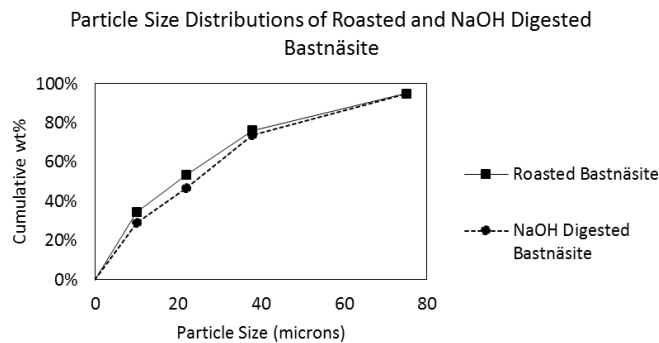


Figure 35 - Measured particle size distribution of roasted and NaOH digested bastnäsité

8.3.2 Sodium Hydroxide Digestion

8.3.2.1 *Chemistry*

Sodium hydroxide digestion can convert bastnäsite into acid-soluble rare earth hydroxides. This involves combining the minerals with a concentrated NaOH solution at elevated temperature (>140°C) for 1-5 hours to convert the fluorocarbonates to solid hydroxides as illustrated in Equation 23. The solid hydroxides are then easily dissolved in mineral acids such as nitric acid with the overall stoichiometry given by Equation 24. Sodium hydroxide digestion is used for commercial bastnäsite processing, often in combination with roasting (Bauer & Shaw, 1964; J. Zhang & Zhao, 2016).



8.3.2.2 *Procedure*

The bastnäsite sample was dried overnight under vacuum at 100°C and 15 g of dried powder was weighed into a 280 mL Parr reaction vessel (Parr Instrument Company, Moline, IL). See Figure 36 for a picture of the NaOH digestion setup. 100 mL of 50 wt% NaOH solution was added. The powder and caustic solution were mixed with a stir bar until a homogenized slurry was achieved. The stirred reactor was then sealed and heated to 150°C using heating tape connected to a controller. Heating the reactor took approximately 75 minutes. The reactor was then held at 150°C for four hours, then allowed to cool below 80°C and opened. Cooling took approximately one hour.



Figure 36 - Setup for NaOH digestion

After the reactor was opened, the slurry was transferred to a polypropylene centrifuge bottle and agitated in an ice bath for 10 minutes. The slurry was washed 3 times with 100 mL of ultrapure water (18.2 M Ω -cm) to remove residual NaOH. After each wash, the slurry was centrifuged and supernatant was removed. Finally, the slurry was filtered on Whatman grade 40 ashless filter paper (8 microns), and dried overnight under vacuum at 100°C.

8.3.2.3 Characterization

Duplicate LiBO₂/Li₂B₄O₇ fusion and ICP-OES was used to establish the composition of the NaOH digested sample (see Table 17). Assays indicated negligible losses of the REEs, with the exception of Eu which could not be measured reliably as the concentration was below the reporting limit. XRD showed the presence of Ba₄La₂O₇ and Nd(OH)₃, with possible presence of Ce(OH)₃ (see Figure 37). La(OH)₃ could not be positively identified.

Sonic sifting was used to obtain a rough particle size distribution (see Figure 35). The results indicated a P80 of approximately 45 microns, nearly identical to the roasted sample.

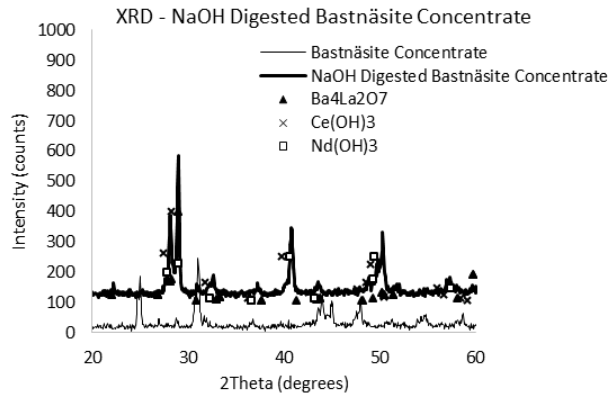


Figure 37 - XRD pattern of NaOH digested bastnäsite concentrate (Ba₄La₂O₇: PDF# 00-052-1324. Ce(OH)₃: PDF#00-055-0556. Nd(OH)₃: PDF#00-006-0601(The International Centre for Diffraction Data, 2013)

8.4 Atmospheric Leaching

Treated and untreated bastnäsite samples were leached with concentrated nitric acid to confirm the formation of soluble REE mineral structures and to provide a baseline recovery for comparison with conventional processing. For these experiments, 1 g of material was leached in 30 mL nitric acid for 3 hours. Solids were washed twice and vacuum filtered. Leachate and wash water were assayed with ICP-OES. As shown in Table 18, high REE recoveries (93-102%) were measured for both of the pretreated samples. The high cerium recovery in the roasted sample suggests that the cerium remained in the trivalent state.

Table 18 - Nitric acid leaching recoveries of REEs in raw and pretreated bastnäsite concentrate samples

Material	La	Ce	Pr	Nd	Ba	Ca	Sr
Raw Bastnäsite	17%	18%	19%	18%	8%	84%	40%
Roasted Bastnäsite	94%	95%	95%	93%	7%	81%	36%
NaOH Digested Bastnäsite	94%	95%	102%	96%	92%	97%	83%
Reporting Limit (lowest calibration standard)	0.04%	0.1%	1.2%	0.1%	0.2%	0.8%	0.02%

8.5 Adduct Preparation

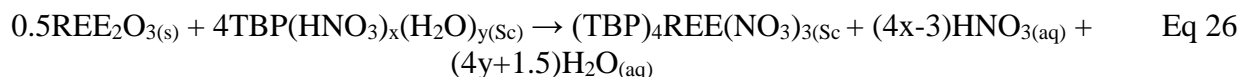
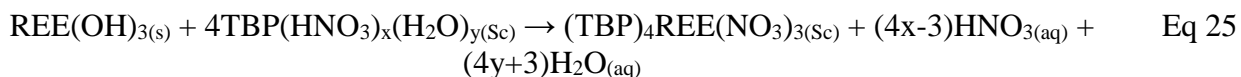
The TBP/HNO₃ adducts were prepared by shaking dry TBP (<300 ppm H₂O) with fuming HNO₃ at various volume ratios for five minutes, following the procedure from previous studies (Baek et al., 2016; Enokida et al., 2003). All of the adduct compositions used in this study resulted

in a single phase. The stoichiometry of the adduct can be represented as $\text{TBP}(\text{HNO}_3)_x(\text{H}_2\text{O})_y$. Karl Fisher titration (Metrohm 831 KF Coulometer, Metrohm, Riverview, FL) and NaOH titration were used to establish the stoichiometry (acid and water content) of each adduct. Results are given in Table 19.

Table 19 - Stoichiometries in the form of $\text{TBP}(\text{HNO}_3)_x(\text{H}_2\text{O})_y$ for different adduct compositions

Mixed HNO_3 :TBP Volume Ratio	0.1	0.18	0.25	0.33	0.43
Adduct H^+ Concentration, mol/L	2	3	4	5	6
x	0.63	1.00	1.38	1.85	2.44
y	0.20	0.36	0.46	0.64	0.86
Density, g/mL	0.99	1.03	1.06	1.07	1.09

Though in-line spectroscopic analysis of the metal complexes was not possible in this study, previous spectroscopic studies of Pr and Nd have demonstrated that four TBP molecules will coordinate with each $\text{REE}(\text{NO}_3)_3$ group during supercritical extraction when an aqueous phase is absent (R. V. Fox et al., 2004). Using the values of x and y as determined above, the extraction reactions for the two REE materials can be balanced (see Equations 25 and 26). It is clear from these reactions that excess water is present during extraction. For all adduct compositions >2 mol/L H^+ , excess nitric acid is present as well.



A note of caution should be given with regard to mixing, handling, use, and storage of TBP and nitric acid mixtures. Mixtures comprised of concentrated (70%) nitric acid and TBP have previously been characterized and widely reported in literature without mishap (Baek et al., 2016;

Samsonov et al., 2015; Tomioka et al., 1998, 2002; Wuhua et al., 2010; L. Zhu et al., 2009). Care should be taken not to formulate mixtures of TBP and fuming nitric acid which would result in a mixture having greater than approximately 10 M H⁺ in the organic phase because such mixtures have been found to be unstable and can undergo rapid exothermic decomposition (hydrolysis). Careful titration of acid reagents prior to use and knowledge of the acid concentration is important for safe practice. Mixtures of nitric with TBP should be made in a small test quantities (less than 10 mL) first prior to creation of larger volume mixtures. Care should be exercised after TBP – HNO₃ mixtures are made to ensure they are stable and not emitting NO_x vapors which could build up and over-pressurize a storage container or centrifuge tube. Fresh solutions should be made and used, and not stored for periods greater than 72 hours. Solutions should be stored in chemically compatible containers and either kept in the hood for immediate use, or stored in an approved acid cabinet until used. If TBP – HNO₃ mixtures >6 M H⁺ in the organic phase cannot be used in the same day, then they should be neutralized and discarded. Extracts arising from a supercritical fluid extraction process that contain metal, acid, and TBP should be handled in the manner described above. TBP – HNO₃ mixtures should not be mixed with other organic reagents such as short-chain alcohols, aldehydes, ketones, and other common organic solvents (or waste solutions) which are incompatible with nitric acid. TBP that has come into contact with nitric acid should be neutralized first prior to being discarded.

8.6 *Supercritical Extraction*

The supercritical extraction system is shown in Figure 38. All tubing and valves were purchased from High Pressure Equipment Company (Erie, PA). The system consisted of a CO₂ pump (Teledyne Isco model 260D, Teledyne ISCO, Lincoln, NE) equipped with a cooling jacket used to cool the CO₂ to 10°C, a high pressure liquid chromatography pump feeding the adduct

(Dionex IP25, Dionex, Sunnyvale, CA), an equilibrium cell (custom machined at Idaho National Laboratory, approximately 45 mL, equipped with a magnetic stir bar), and a reaction column which consisted of a short section of 9.5 mm O.D. steel tubing. The outlet tube was submerged in 20 mL of 0.1 M HNO₃ trap solution in a graduated cylinder, such that the depressurized CO₂ bubbled through the solution.

The column (shown in detail in Figure 41) contained the sample and silanized glass wool packing material, effectively forming a packed bed reactor. Material was held in place during extraction with 2 μm filter frits (9.5 mm diameter, 3.2 mm thickness, Applied Porous Technologies, Tariffville, CT) on each end of the column. Based on the density of silica and bastnäsite, it was estimated that the porosity of the reaction column was 92%. The residence time of the reaction column was estimated at 20 seconds.

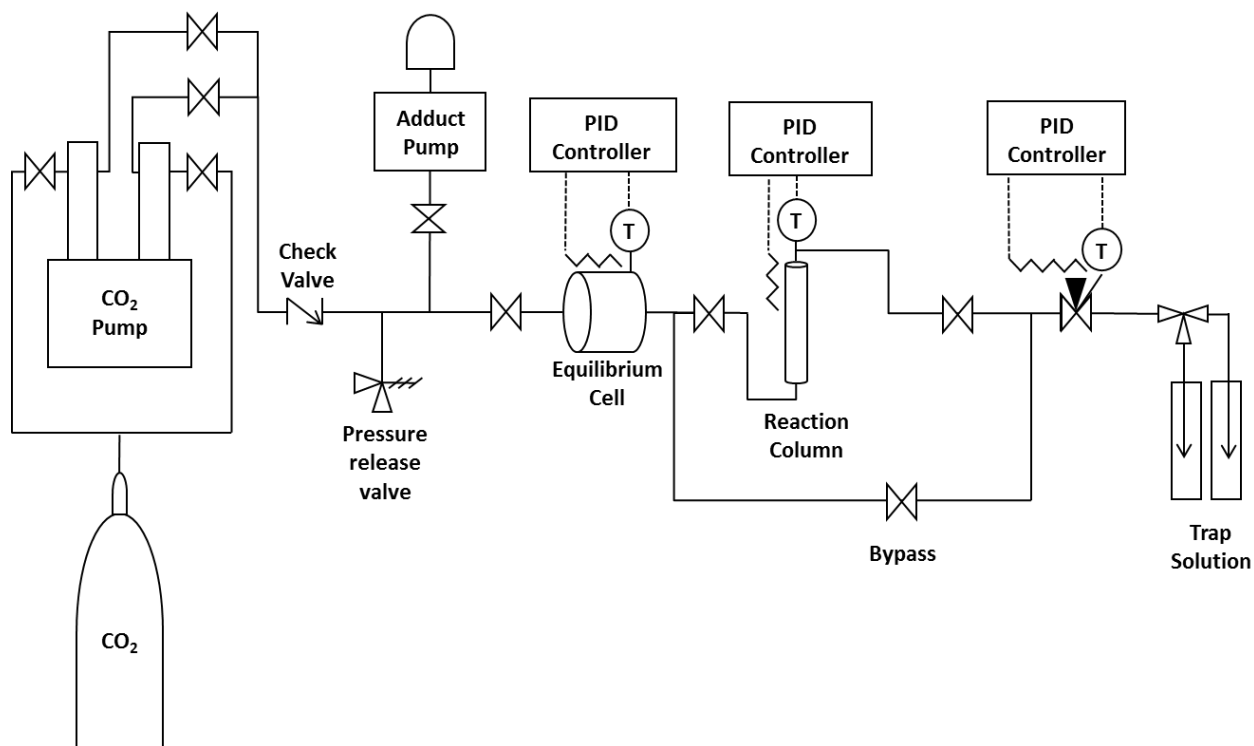


Figure 38 - Process flow diagram of supercritical extraction setup



Figure 39 - Photograph of extraction system



Figure 40 - Equilibrium reactor and paced column. The column was later shortened and submerged in a constant temperature bath.

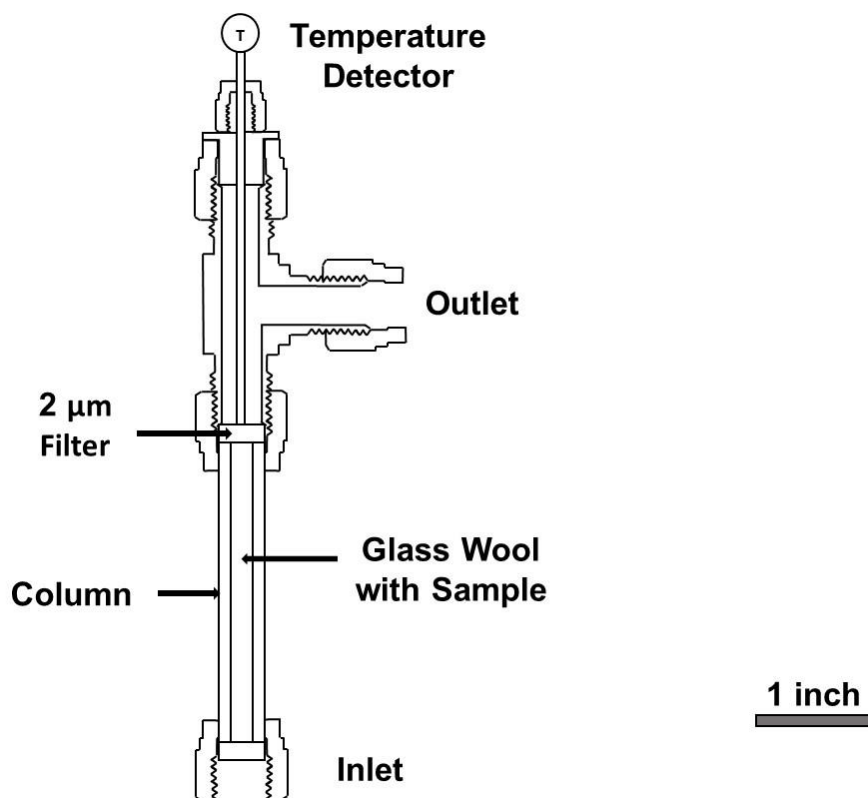


Figure 41 - Drawing of packed column

The extraction pressure was set at 34 MPa to dissolve the full range of adduct compositions by a comfortable margin (Baek et al., 2016) and a reaction column temperature of 65°C because extractions near this temperature had achieved high recoveries in previous studies (Wuhua et al., 2010; L. Zhu et al., 2009; L. Y. Zhu et al., 2011).

At the start of each run, 100 mg of sample and 200 mg of silanized glass wool packing material were loaded into the reaction column. The system was pressurized to 34 MPa. The equilibrium cell was held at 75°C and the reaction column was held at 65°C. The reaction column inlet and outlet valves were then both closed, isolating the reaction column from the rest of the system. CO₂ was fed continuously through the system via the bypass line. The micrometering valve position

was manually adjusted to control the CO₂ flow rate at approximately 3 mL/min. Adduct flow was then initiated, and both the CO₂ and adduct were continuously fed through the bypass line for 40 minutes (approximately 3 times the residence time of the system) to obtain a steady state adduct concentration. At the start of the extraction, the bypass line was closed and the reaction column inlet and outlet lines were opened to direct flow through the reaction column. This type of extraction system is often referred to as "flow mode" or "dynamic mode", since the CO₂ and adduct flow continuously through the reactor. Kinetic samples were taken at various time intervals by switching out different trap solutions at specified time points; this was facilitated by the three-way valve at the outlet. After extraction was finished, CO₂ was fed for another 30 minutes to flush out remaining adduct.

As shown in previous work, the stoichiometries of metal containing complexes are altered when the complex is transferred from CO₂ to a water-rich trap solution (Wai et al., 2011). The resulting trap solutions separated over the course of each run into an aqueous phase and a TBP-rich organic phase. The organic phase from each run was triple stripped with 0.1 M HNO₃ to remove all of the metal, and then this strip solution was combined with the aqueous phase. This was then analyzed via ICP-OES in order to calculate recovery. Several selected samples were stripped a fourth time in order to demonstrate that three strips are sufficient to recover all metal content.

The main sources of error are variations in CO₂ flow rate, variations in the acidity of the fuming nitric acid, and variations in the ore and silica packing in the reaction column. To evaluate reproducibility, several runs were performed in duplicate or triplicate. Standard deviations for final recovery ranged from 1% to 6%.

8.7 Results

8.7.1 Effect of Adduct Composition

The results from the supercritical extraction runs are tabulated in Table 20. All recoveries are cumulative (include both losses incurred during pretreatment and losses incurred during supercritical extraction). An extraction was performed on an untreated bastnäsite sample in order to provide a comparison; REE recoveries were all <10%. The pretreated bastnäsite samples were then treated with a range of adduct compositions (all with 5.2 ± 0.8 mol% adduct in the CO₂ phase) in order to establish the optimum adduct composition for extraction. The recoveries for cerium are shown in Figure 42; data for La, Pr, and Nd can be found in Table 20. It is clear that both low acidity and high acidity adducts result in poor Ce, Pr, and Nd extraction, with the highest extraction rate achieved with the medium acidity adducts (approximately 3-5 mol/L H⁺). La recovery did not seem to fit this pattern – lower acidity adducts showed consistently better extraction. Potential explanations for this behavior are outlined in the Discussion section.

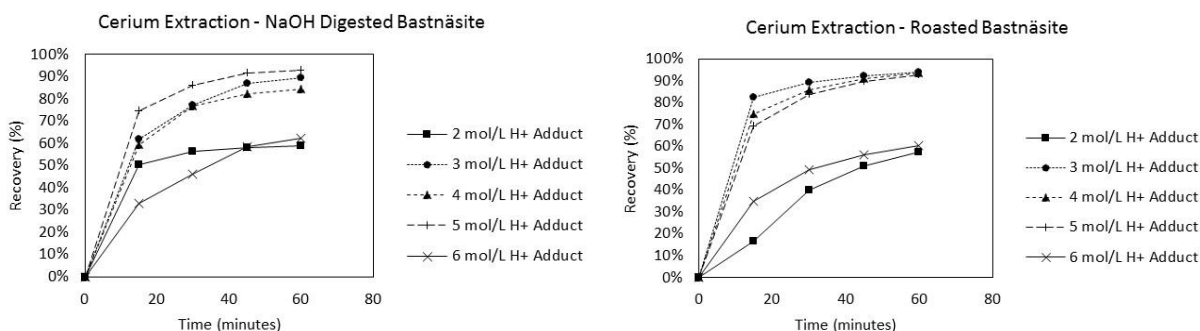


Figure 42 – Cerium recovery curves with various adduct compositions for roasted bastnäsite (left) and NaOH digested bastnäsite (right). Conditions: 34 MPa, 65°C, 5.2 ± 0.8 mol% adduct in CO₂.

8.7.2 Effect of Adduct Concentration in CO₂

After the 4 mol/L H⁺ adduct was selected to be carried forward to the next phase of study, a range of adduct concentrations in the CO₂ phase were tested in order to observe the effect on recovery. The extraction time was extended to 120 minutes for the roasted material and 90 minutes

for the NaOH digested material in order to better resolve the recovery curve. The recovery curves for cerium are shown in Figure 43; data for La, Pr, and Nd can be found in Table 20. As expected, higher adduct concentrations in CO₂ resulted in faster recovery. For the 4 mol/L H⁺ adduct at 5.0 mol% adduct concentration, roasted bastnäsite recoveries were 72% for La, 96% for Ce, 88% for Pr, and 90% for Nd after 120 minutes. For 4 mol/L H⁺ adduct at 5.1 mol% adduct concentration, NaOH digested bastnäsite recoveries were 93% for La, 100% for Ce, 99% for Pr, and 101% for Nd after 90 minutes. This is similar to the recoveries obtained through conventional atmospheric leaching with concentrated acid (93-102%) (see Table 18).

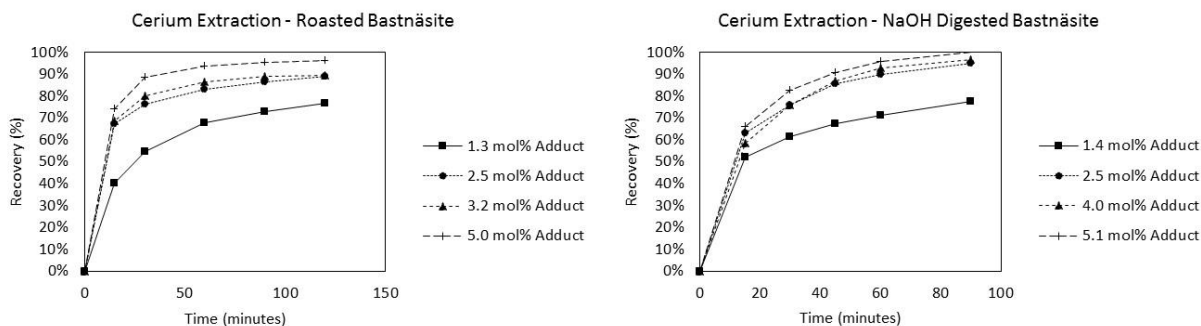


Figure 43 – Cerium recovery curves for various adduct concentrations for roasted bastnäsite (left) and NaOH digested bastnäsite (right). Conditions: 34 MPa, 65°C, 4 mol/L H⁺ adduct composition

8.7.3 Selectivity

As shown in Table 20, barium and strontium analyses were below the reporting limit and recoveries could not be determined for almost all tests, whereas quantified calcium recovery ranged from 29% to 110%. Greater than 100% recoveries for calcium were attributed to contamination resulting from incomplete washing or rinsing of glassware. It can therefore be concluded that although precise recoveries were not always measurable for the three primary gangue elements, selectivity for lanthanides was superior to acid leaching (see Table 18).

Table 20 - Supercritical extraction results. All runs were performed at 65°C and 34 MPa.

Run	Material	Adduct mol% in CO ₂	Adduct	Time (min)	Recovery (%)						
					La	Ce	Pr	Nd	Ba	Ca	Sr
1	Untreated Bastnäsite	5.2%	4 mol/L H ⁺ Adduct	15	1%	1%	3%	3%	<1%	<1%	<1%
				30	3%	2%	5%	6%	<1%	<2%	<1%
				45	4%	3%	6%	8%	<1%	<2%	<1%
				60	5%	4%	8%	9%	<1%	<3%	<1%
2	Roasted Bastnäsite	4.4%	6 mol/L H ⁺ Adduct	15	15%	35%	26%	31%	<3%	19%	<5%
				30	28%	49%	44%	50%	<4%	28%	<7%
				45	36%	56%	53%	61%	<5%	38%	<9%
				60	41%	61%	58%	68%	<6%	47%	<10%
3	Roasted Bastnäsite	4.5%	5 mol/L H ⁺ Adduct	15	16%	69%	41%	40%	<2%	8%	<2%
				30	29%	84%	63%	61%	<3%	12%	<3%
				45	45%	90%	75%	70%	<4%	19%	<4%
				60	56%	93%	81%	75%	<5%	29%	<5%
4	Roasted Bastnäsite	5.2%	4 mol/L H ⁺ Adduct	15	24%	75%	51%	58%	<2%	8%	<4%
				30	39%	86%	70%	77%	<4%	17%	<8%
				45	51%	91%	79%	84%	<6%	26%	<12%
				60	62%	94%	84%	88%	<8%	39%	<15%
5	Roasted Bastnäsite	5.2%	3 mol/L H ⁺ Adduct	15	33%	82%	68%	66%	<1%	16%	<2%
				30	46%	89%	81%	76%	<2%	25%	<2%
				45	57%	92%	87%	80%	<3%	34%	<3%
				60	67%	94%	90%	82%	<3%	47%	<3%
6	Roasted Bastnäsite	6.0%	2 mol/L H ⁺ Adduct	15	30%	17%	19%	16%	<1%	38%	2%
				30	49%	40%	39%	34%	<1%	45%	4%
				45	59%	51%	50%	43%	<2%	50%	5%
				60	66%	58%	57%	49%	<3%	54%	5%
7	Roasted Bastnäsite	5.0%	4 mol/L H ⁺ Adduct	15	21%	74%	48%	54%	<2%	5%	<4%
				30	39%	89%	70%	75%	<4%	11%	<8%
				60	58%	94%	82%	86%	<7%	25%	<14%
				90	67%	96%	86%	89%	<11%	38%	<22%
				120	72%	96%	88%	90%	<15%	50%	<29%
8	Roasted Bastnäsite	3.2%	4 mol/L H ⁺ Adduct	15	10%	69%	36%	40%	<1%	<15%	<1%
				30	18%	80%	53%	60%	<1%	<30%	<1%
				60	33%	87%	69%	75%	<2%	<55%	<2%
				90	47%	89%	77%	81%	<3%	<80%	<3%
				120	52%	90%	79%	82%	<4%	<100%	<4%
9	Roasted Bastnäsite	2.5%	4 mol/L H ⁺ Adduct	15	7%	67%	24%	27%	<1%	<16%	<1%
				30	12%	77%	36%	42%	<1%	<31%	<1%
				60	21%	83%	53%	61%	<2%	<52%	<2%

Run	Material	Adduct mol% in CO ₂	Adduct	Time (min)	Recovery (%)						
					La	Ce	Pr	Nd	Ba	Ca	Sr
				90	28%	87%	61%	67%	<3%	<73%	<3%
				120	35%	89%	67%	72%	<3%	<95%	<3%
10	Roasted Bastnäsite	1.3%	4 mol/L H ⁺ Adduct	15	4%	40%	26%	34%	<1%	<15%	<1%
				30	6%	55%	35%	44%	<1%	<30%	<1%
				60	11%	68%	48%	59%	<2%	<51%	<2%
				90	17%	73%	58%	68%	<3%	<72%	<3%
				120	26%	77%	68%	77%	<3%	<94%	<3%
11	NaOH Digested Bastnäsite	4.6%	6 mol/L H ⁺ Adduct	15	37%	33%	57%	60%	<2%	12%	<5%
				30	60%	46%	75%	78%	<3%	33%	<6%
				45	76%	58%	87%	90%	<5%	57%	<9%
				60	83%	62%	92%	95%	<6%	80%	<11%
12	NaOH Digested Bastnäsite	4.6%	5 mol/L H ⁺ Adduct	15	24%	75%	64%	65%	<2%	19%	<2%
				30	45%	86%	88%	83%	<3%	23%	<3%
				45	71%	92%	98%	89%	<4%	35%	<4%
				60	83%	93%	100%	90%	<5%	44%	<5%
13	NaOH Digested Bastnäsite	4.9%	4 mol/L H ⁺ Adduct	15	36%	59%	62%	68%	<1%	<21%	<1%
				30	62%	77%	85%	89%	<1%	<40%	<1%
				45	81%	82%	95%	96%	<2%	<58%	<2%
				60	94%	85%	99%	98%	<3%	<77%	<3%
14	NaOH Digested Bastnäsite	4.6%	3 mol/L H ⁺ Adduct	15	44%	62%	69%	64%	<1%	8%	<1%
				30	61%	77%	85%	78%	<2%	13%	<2%
				45	83%	87%	94%	84%	<3%	30%	<3%
				60	87%	89%	96%	85%	<3%	33%	<3%
15	NaOH Digested Bastnäsite	5.1%	2 mol/L H ⁺ Adduct	15	86%	50%	88%	75%	<1%	>86%	8%
				30	93%	56%	95%	81%	<1%	105%	14%
				45	94%	58%	96%	82%	<2%	109%	18%
				60	94%	59%	96%	82%	<3%	110%	20%
16	NaOH Digested Bastnäsite	5.1%	4 mol/L H ⁺ Adduct	15	29%	66%	59%	67%	<2%	7%	<4%
				30	53%	83%	82%	87%	<4%	14%	<8%
				45	67%	91%	90%	94%	<6%	22%	<12%
				60	78%	96%	95%	99%	<8%	29%	<16%
				90	93%	100%	99%	101%	<12%	46%	<24%
17	NaOH Digested Bastnäsite	3.9%	4 mol/L H ⁺ Adduct	15	22%	58%	49%	55%	<1%	<16%	<1%
				30	44%	76%	72%	76%	<1%	<31%	<1%
				45	60%	87%	84%	86%	<2%	<47%	<2%
				60	76%	93%	91%	92%	<2%	<63%	<2%
				90	91%	97%	97%	96%	<3%	<91%	<3%

Run	Material	Adduct mol% in CO ₂	Adduct	Time (min)	Recovery (%)						
					La	Ce	Pr	Nd	Ba	Ca	Sr
18	NaOH Digested Bastnäsite	2.5%	4 mol/L H ⁺ Adduct	15	11%	63%	41%	46%	<1%	<16%	<1%
				30	22%	76%	57%	64%	<1%	<32%	<1%
				45	42%	86%	75%	80%	<2%	<52%	<2%
				60	53%	90%	83%	87%	<2%	<68%	<2%
				90	74%	95%	95%	95%	<3%	<90%	<3%
19	NaOH Digested Bastnäsite	1.4%	4 mol/L H ⁺ Adduct	15	7%	52%	34%	38%	<1%	<16%	<1%
				30	12%	61%	42%	48%	<1%	<32%	<1%
				45	17%	67%	50%	56%	<2%	<47%	<2%
				60	21%	71%	56%	61%	<2%	<63%	<2%
				90	27%	78%	64%	69%	<3%	<85%	<3%

8.8 Discussion

Several conclusions can be drawn from the extraction data. As expected, higher extraction rates are seen for heavier REEs due to their smaller atomic radius; for example, with 4 M H⁺ adduct at 5 mol% in CO₂, Nd extraction rates were 30-100% faster than La extraction rates. This is similar to the behavior seen in liquid solvent extraction systems. The same trend has been seen previously in supercritical extraction of lanthanides (R. V. Fox, 2003). It is also evident that reaction rates are similar for the two pretreatment methods, although they are slightly faster for the NaOH digested material. Assessment of the capital and operating costs associated with the two pretreatment methods, as well as the environmental impacts, should be used to fully evaluate the overall performance of the two pretreatment options.

8.8.1 Kinetics

Due to the number of steps involved in extraction (mass transfer to/from particle surface, formation of REE nitrate, coordination of the REE nitrate with TBP, and separation of the metal-containing complex from the particle surface), several assumptions were made in order to interpret the kinetic results:

- Temperature and pressure are constant within the reaction column
- Reaction rates are not limited by fluid-phase mass transfer; this is justified based on the high porosity of the reaction column (estimated at 92 volume %), the high diffusivity of the supercritical phase, and the small reaction column inner diameter (5 mm)
- Reaction rates are not limited by solid-phase diffusion;
- Adduct concentrations were constant in the reaction column; given that the adduct was present in stoichiometric excess by a factor of 40-600 depending on the run, depletion of the adduct as it moved through the reaction column can safely be neglected.

Based on these assumptions, the reaction rates are limited by phenomena at the particle surface (nitration, complexation with TBP, and/or desorption of the complex). A shrinking particle model is appropriate, therefore, since this model is based on the principle that reaction rate is proportional to particle surface area (Smith, 1970):

$$1 - (1 - X_B)^{\frac{1}{3}} = k't \quad \text{Eq 27}$$

Note that this is a simplified form of Equation 3 from section 2.3.3. X_B is the fraction of mineral B reacted, t is time (s), and k' is a lumped reaction rate constant (s^{-1}). A reaction rate constant “ k ” was fitted to each recovery curve using a simple iterative solver to minimize residual square error. Because there were 19 tests with 4 REE extraction curves each, this resulted in 76 k' values. Each k' value effectively encompasses the rate of reaction in a single number, allowing for the reaction rate to be plotted against relevant variables. These k' values were plotted against TBP and HNO_3 concentrations in the CO_2 phase (which depends on both the adduct composition and the mole % adduct in CO_2).

In the case of lanthanum, the reaction rate constant appears to show a linear dependence on the TBP concentration in the CO₂ phase, regardless of the HNO₃ concentration present (see Figure 44). This suggests that complexation of the lanthanum nitrate with TBP is the rate-limiting step. A slow rate of lanthanum-TBP complexation is logical as lanthanum has the least affinity for TBP due to its large atomic radius. It appears that the trend becomes nonlinear at low concentrations.

For cerium, there is an increase in reaction rate with HNO₃ concentration up to about 1.5 mol/L HNO₃ in the CO₂ phase (corresponding to the 4 M H⁺ adduct at approximately 5 mol% in CO₂). At this point recovery rates decrease again (see Figure 44). This suggests that nitration is the rate-limiting step, but high acid concentrations inhibit extraction. A similar trend was seen for praseodymium and neodymium (not shown).

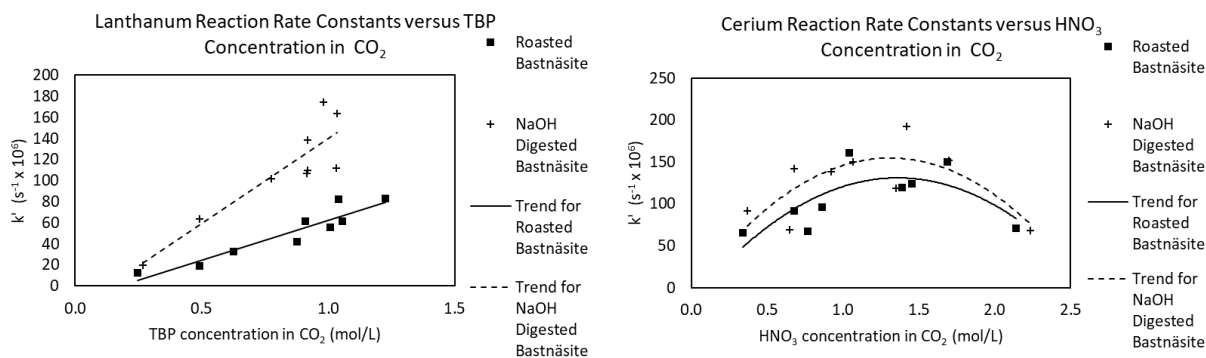


Figure 44 – Lanthanum reaction rate constant versus TBP concentration in CO₂ phase (left) and cerium reaction constant rate constant versus HNO₃ concentration in CO₂ phase (right)

A previous study of the supercritical extraction of neodymium oxide with TBP/HNO₃ adducts also found that reaction rates peaked with adducts containing 3-4 mol/L H⁺. It was suggested that high HNO₃ concentrations resulted in the formation of an aqueous phase which sequestered the REEs (Wuhua et al., 2010). Another study found that a 3.9 mol/L H⁺ adduct was more effective at recovering REEs in supercritical CO₂ than a 4.9 mol/L H⁺ adduct, and a similar mechanism was proposed (Shimizu et al., 2005). Droplet formation can be exacerbated by the water generated during the reaction between REE minerals and the adduct (see Equations 25 and 26). A second

possible explanation for the drop in recovery rate at high acid concentration is competition between HNO_3 and the lanthanide nitrates for complexation with TBP. Such a phenomenon has been seen in conventional TBP/ HNO_3 solvent extraction; extraction of lanthanides increases with aqueous phase acidity up to 3-5 mol/L H^+ , then recovery begins decreasing again as nitric acid competes with lanthanide nitrates for TBP complexation (Peppard et al., 1957; J. Zhang & Zhao, 2016).

CHAPTER 9

THE ROLE OF WATER IN EXTRACTION AND SEPARATION OF RARE EARTH ELEMENTS

9.1 Goal and Scope

In this work, neodymium and holmium nitrate were extracted using TBP in supercritical CO₂. Absorption spectroscopy in the visible range was used to quantify extraction of Nd and Ho, as demonstrated in previous studies (R. V. Fox et al., 2004; Hwang et al., 2016; L. Y. Zhu et al., 2016). A novel element of this work is the use of near-IR spectroscopy (Zheming Wang et al., 2013) to measure water extraction in conjunction with lanthanide extraction. A range of TBP concentrations, a range of water concentrations, and a range of pressures were explored to observe the effect on Nd/Ho extraction and separation. A set of affinity constants for Nd, Ho, and water extraction were fit in agreement with the observed data. This work was outlined in a recent publication (L.K. Sinclair, Tester, Thompson, & Fox, 2018).

9.2 Materials

Neodymium nitrate (Nd(NO₃)₃·6H₂O), holmium nitrate (Ho(NO₃)₃·5H₂O), and tri-n-butyl phosphate (TBP, 97%) were purchased from Sigma-Aldrich (St. Louis, MO). The TBP was dried with molecular sieves (mSorb 3A 8 × 12, Delta Adsorbents, Roselle, IL) prior to use. Karl Fisher titration indicated that the water concentration in the dried TBP was 170 ppm. A bone-dry liquid carbon dioxide tank with a siphon was purchased from Airgas (Radnor, PA).

The extraction system is shown in Figure 45 and Figure 46. All tubing and valves were purchased from High Pressure Equipment Company (Erie, PA). The CO₂ delivery system consisted of a CO₂ pump (Teledyne Isco model 260D, Teledyne ISCO, Lincoln, NE) equipped with a cooling jacket used to cool the CO₂ to 10°C. A reactor with an internal volume of

approximately 50 mL (3.05 cm inner diameter and 7.1 cm length) was used for the extraction experiments (Thar Technologies, Pittsburgh, PA). The reactor is shown in detail in Figure 47 and Figure 48. Sapphire windows capped each end (Thar Technologies, Pittsburgh, PA), and the seal was formed using fluoropolymer encapsulated Viton gaskets (McMaster Carr, Elhurst, IL). Temperature was monitored via a 1/8" thermocouple immersed in the supercritical phase, and the pressure was monitored with a pressure transducer from Omega (Stamford, CT). A magnetic stir bar and stir plate were used to agitate the cell.

9.3 Procedure

Each experiment began by loading the cell with the nitrate salts, TBP, and water if applicable. Care was taken to ensure that the sapphire windows remained clean and free of solids or droplets. The cell was heated to 60°C and pressurized with CO₂ to the required pressure. The cell was then allowed to stir for 30 minutes.

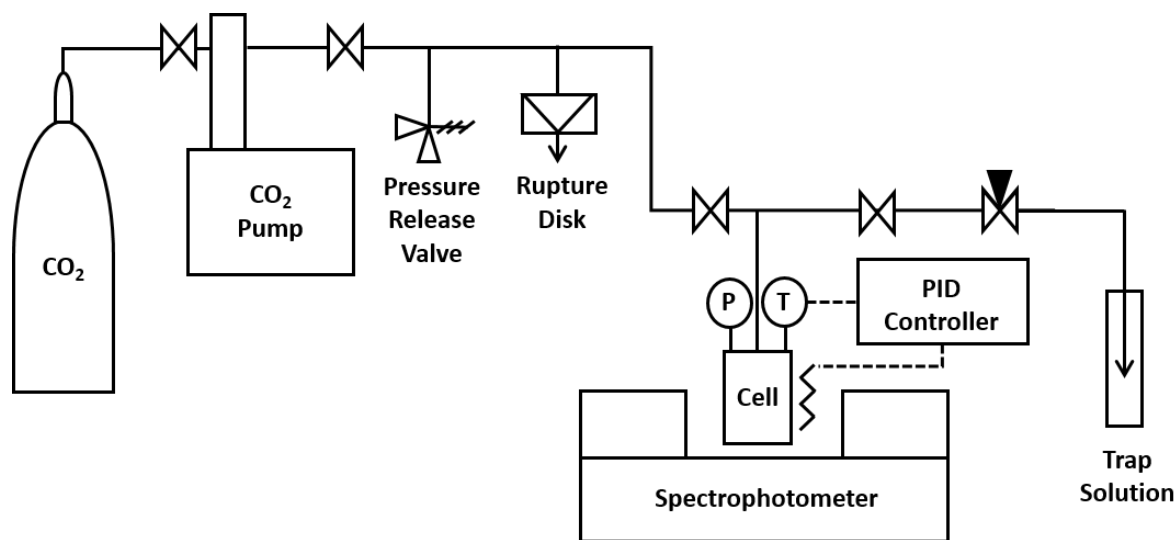


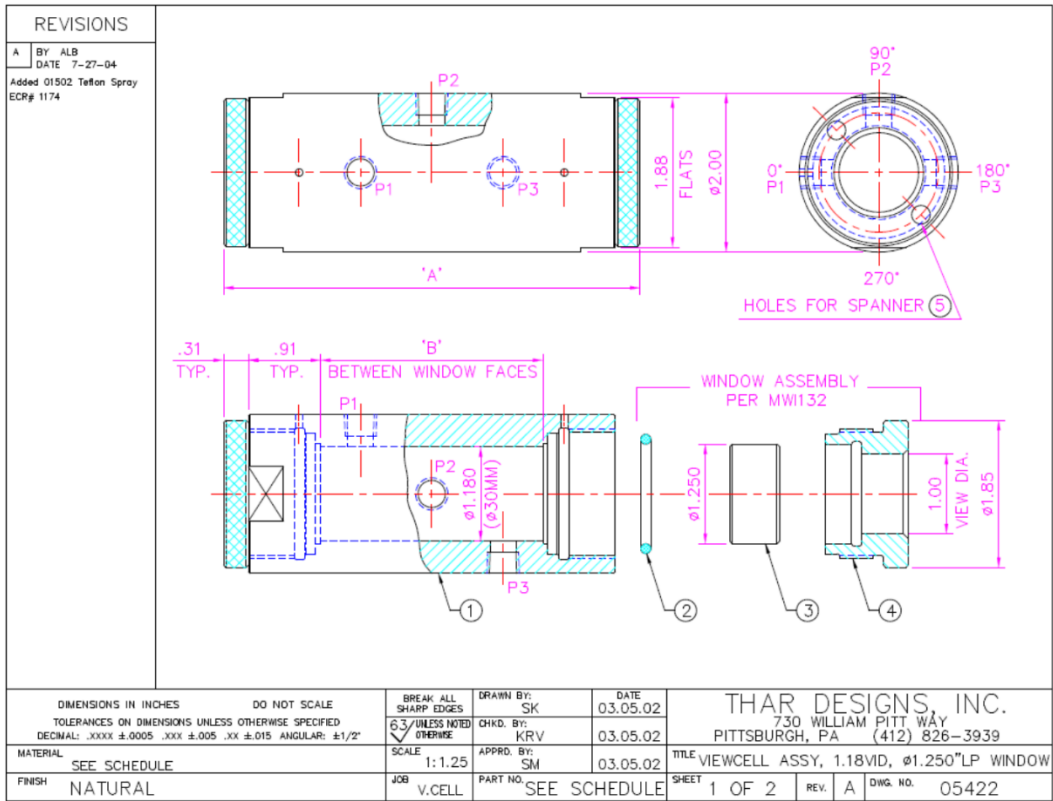
Figure 45 – Schematic of supercritical extraction system



Figure 46 - Photograph of extraction system



Figure 47 - Cell with Nd and Ho nitrate salts



BILL OF MATERIALS			VIEWCELL ASSEMBLY AND QTY. SCHEDULE					
ITEM	DESCRIPTION	DWG#	PART#	05422-1	05422-2	05422-3	05422-4	05422-5
1	VIEWCELL BODY, 10ML, 1.18VID, Ø1.250" LP WINDOW	05421	05421-1	1	---	---	---	---
	VIEWCELL BODY, 25ML, 1.18VID, Ø1.250" LP WINDOW	05421	05421-2	---	1	---	---	---
	VIEWCELL BODY, 50ML, 1.18VID, Ø1.250" LP WINDOW	05421	05421-3	---	---	1	---	---
	VIEWCELL BODY, 100ML, 1.18VID, Ø1.250" LP WINDOW	05421	05421-4	---	---	---	1	---
	VIEWCELL BODY, 250ML, 1.18VID, Ø1.250" LP WINDOW	05421	05421-5	---	---	---	---	1
2	ORING, #218 TEFLON ENCAPSULATED SILICONE	---	04316	2	2	2	2	2
3	WINDOW, 1.250" DIA. LP SAPPHIRE	03192	03192	2	2	2	2	2
4	WINDOW NUT, 1.250" DIA. LP	03218	03218	2	2	2	2	2
5	WRENCH, SPANNER, 1.50" PIN CENTERS	---	03224	1	1	1	1	1
6	SPRAY, TFE DRY LUBRICANT, 10 OZ (Not Shown)	---	01502	1	1	1	1	1

VIEWCELL SPECIFICATIONS										
ASSEMBLY			DIMENSIONS		PORTS			MATERIALS		PRESSURE RATING
PART#	VOLUME	WEIGHT LBS	'A'	'B'	P1	P2	P3	VIEWCELL BODY	WINDOW NUT	MAWP
05422-1	10ML	1.73	3.00	.56	1/8" NPT			316 STAINLESS STEEL	304 STAINLESS STEEL	6000 PSI @ 302°F (414BAR @ 150°C)
05422-2	25ML	2.21	3.84	1.39	1/8" NPT					
05422-3	50ML	3.00	5.23	2.79	1/8" NPT					
05422-4	100ML	4.61	8.02	5.58	1/8" NPT					
05422-5	250ML	9.42	16.39	13.95	1/8" NPT					

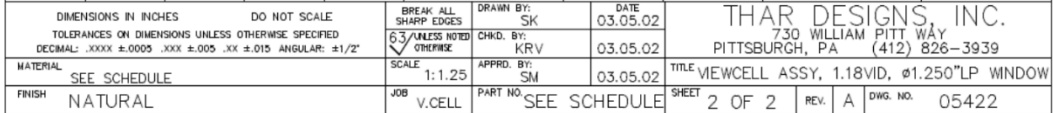


Figure 48 - Diagram of spectroscopy cell (courtesy of Thar Technologies Inc.)

Previous studies have shown that 30 minutes of stirring is sufficient to reach equilibrium concentrations of metal complexes in supercritical CO₂ (Ashraf-Khorassani, Combs, & Taylor, 1997; R. V. Fox, 2003; Hwang et al., 2016; Miyamoto et al., 2012). This was confirmed by measuring spectra at regular intervals; it was found that 30 minutes was sufficient to reach steady state.

A Shimadzu UV3600 spectrophotometer was used to measure the absorbance spectra of the supercritical phase using a sampling interval of 1 nm. Baseline spectra were taken every few hours. Each run was repeated in triplicate. Because of the differences in equilibration pressure among repeat runs, the pressure can be considered accurate within 0.7 MPa.

9.4 Calibration

9.4.1 Neodymium

f-f electronic transitions result in absorption peaks which can be used to measure lanthanide concentrations. TBP does not have an absorption band in this range and therefore does not interfere with the spectra. However, changes in the amount of free TBP dissolved in the supercritical phase can cause minor changes in the absorption spectra resulting from deviations in the effective polarity and refractive index of the solvent (R. V. Fox, 2003).

Neodymium undergoes a hypersensitive f-f transition at 584 nm (R. V. Fox et al., 2004). To construct a calibration curve, approximately 190 mM neodymium nitrate was dissolved into TBP to form a single phase. Varying amounts of this liquid was then pipetted into the reactor. The reactor was heated to 60°C and pressurized to 17 MPa with CO₂. Full dissolution of the liquid phase was confirmed with visual inspection through the sapphire windows. The integrated peak area from 556 nm to 610 nm was correlated with the neodymium concentration in the supercritical

phase. The peaks are shown in Figure 49 and the calibration plot is shown in Figure 50. The R^2 value was 0.998 and the calibration slope was 1.4762 ± 0.0373 .

9.4.2 Holmium

Holmium undergoes a hypersensitive f-f transition at 451 nm (R. V. Fox et al., 2005). To construct a calibration curve, approximately 190 mM of holmium nitrate was dissolved in TBP to form a single phase. Various amounts of this liquid were dissolved in CO₂ at 17 MPa and 60°C using the same procedure outlined above. The integrated peak area from 436 to 500 nm was correlated with holmium concentration. The peaks are shown in Figure 49 and the calibration plot is shown in Figure 50. The R^2 value was 0.998 and the calibration slope was 0.9487 ± 0.0231 .

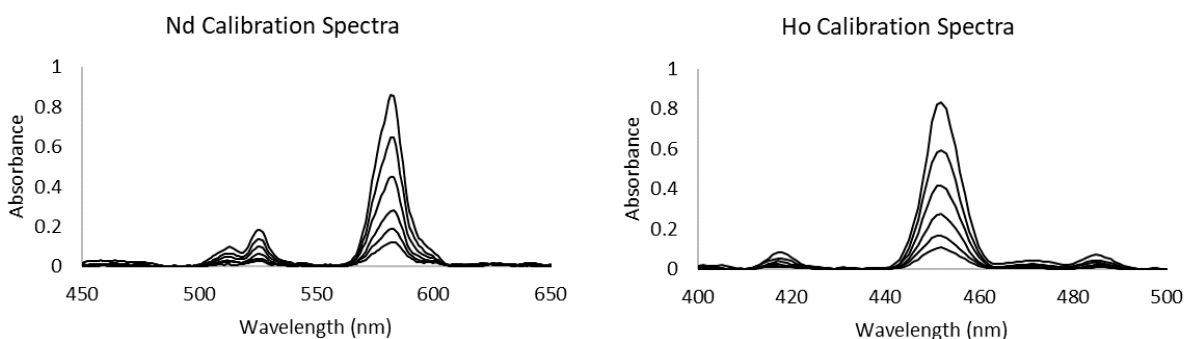


Figure 49 - Spectra for Nd and Ho calibration. 17 MPa, 60°C.

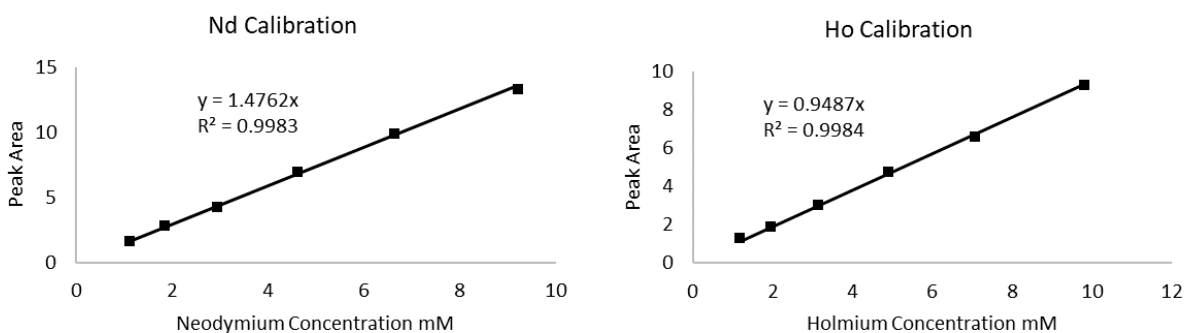


Figure 50 - Calibration curves for neodymium and holmium. 17 MPa, 60°C.

9.4.3 Water

A water absorption peak associated with the $2\nu_3$ overtone band has previously been observed in supercritical CO₂ at 1387 nm (Zheming Wang et al., 2013). To construct a calibration curve,

varying amounts of deionized water (ranging from 0 to 0.125 mL, equivalent to 0 to 139 mM) were pipetted into the reactor, along with varying amounts of TBP (ranging from 0 to 2.2 mL, equivalent to 0 to 161 mM). The reactor was heated to 60°C and pressurized to 17, 21, 24, and 28 MPa with CO₂. The reactor was stirred for at least 30 minutes for each pressure increment to ensure full dissolution. Full dissolution was confirmed by visual inspection through the sapphire windows (see section 9.5.1 for further discussion on water saturation). A spectrum was then collected in the near infrared range between 1200 and 1520 nm. It was found that pressure had a negligible effect on the absorption peak in this range. Therefore, only the data at 24 MPa were used for calibration purposes. This signal was correlated with water and TBP concentration using a nonlinear model constructed in the software package GRAMSIQ. The R² value of the calibration was 0.993 for water and 0.997 for TBP (see Figure 51 and Figure 52). It was observed that the peak height was primarily correlated with water concentration, and the peak width was primarily correlated with TBP concentration.

The water content of the neodymium and holmium nitrate salts was confirmed by measuring the water peak during Nd and Ho calibration. It was found that the H₂O:Nd ratio in the salt was approximately 8.2, and the H₂O:Ho ratio was 5.6. This implies that water occupied both the inner and outer coordination spheres in the nitrate salts.

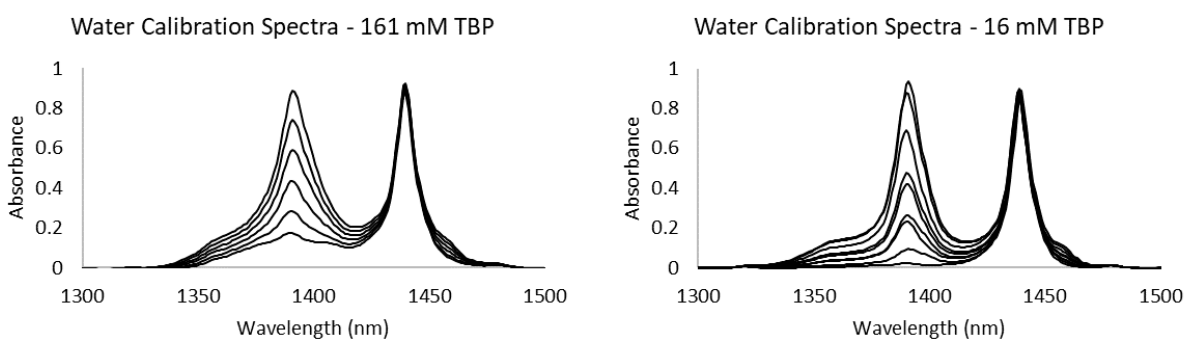


Figure 51 - Spectra from water calibration showing two example TBP concentrations. 24 MPa, 60°C

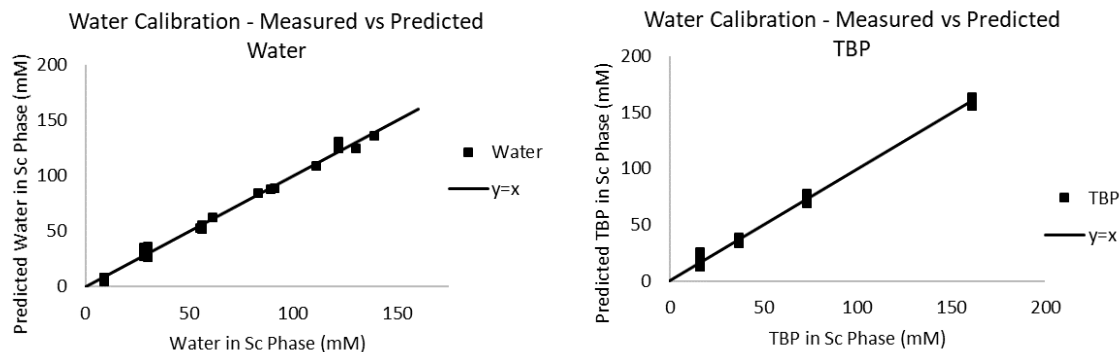


Figure 52 - Calibration parity plot for water and TBP from water calibration. 24 MPa, 60°C. “Sc” abbreviation indicates supercritical phase.

9.5 Results

9.5.1 TBP/H₂O/Supercritical CO₂ System: Water Saturation

To observe the equilibrium supercritical concentration of water at various TBP concentrations, varying amounts of water and TBP were pipetted into the reactor and stirred for 30 minutes. Visual inspection was used to confirm the presence of an aqueous phase at the bottom of the reactor. A spectrum was then measured and the supercritical water concentration was determined.

The results are shown in Figure 53. The no-zero y intercept suggest the presence of both free (un-complexed) water and water complexed with TBP. The equilibrium concentration of free water was found to range from 106 mM at 17 MPa to 144 mM at 28 MPa. This is in agreement with previous studies at similar temperatures and pressures (Bamberger, Sieder, & Maurer, 2000). The linear trend with TBP suggests the formation of a 1:1 complex (H₂O·TBP). This is in agreement with previous studies involving TBP in organic solvents at atmospheric pressure (Hardy et al., 1964), and also agrees with molecular dynamics simulations of the water/TBP/CO₂ system (Schurhammer et al., 2001).

These linear trends were fit with a least-square method as shown in Figure 53.

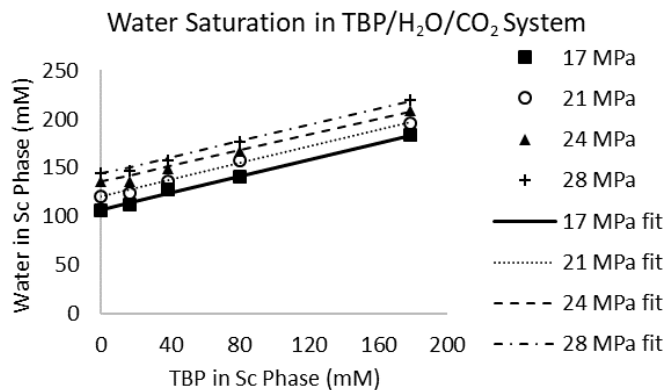


Figure 53 - Equilibrium concentration of water in supercritical CO₂ as a function of TBP concentration. “Sc” abbreviation indicates supercritical phase.

9.5.2 TBP/H₂O/REE Nitrate/Supercritical CO₂ System: Effect of Water Concentration

To observe the effect of water on extraction and separation of Nd and Ho, 8 mM of Nd and 8 mM of Ho were added to the reactor, along with 16 mM of TBP. Varying amounts of water ranging from 0 to 0.18 mL (equivalent to 0 to 200 mM) were added. The equilibrium extraction of Nd, Ho, and H₂O at 21 MPa are plotted in Figure 54. Error bars denote standard errors for triplicate runs.

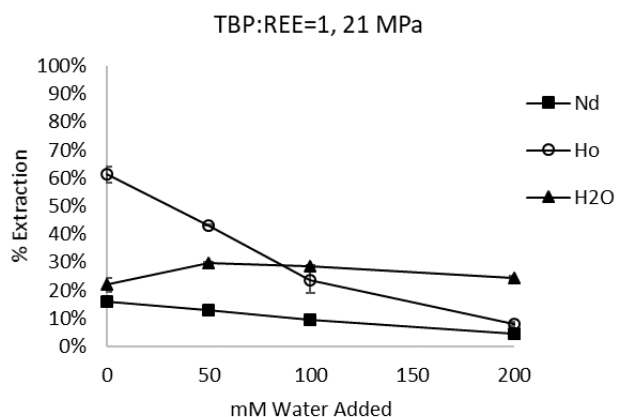


Figure 54 – Extraction of Nd, Ho, and H₂O as a function of water added

The results for all tested pressures are shown in Table 21. It should be noted that even when 0 mM of water was added to the system, there is still water present from the nitrate salts, and thus water extraction can still be quantified. As anticipated, additional water resulted in less extraction of REEs, though the effect seemed to be more pronounced for holmium. Nd and Ho were best

separated in a dry environment. Interestingly, the percent extraction of water remained relatively constant regardless of the amount of water added.

9.5.3 TBP/H₂O/REE Nitrate/Supercritical CO₂ System: Effect of TBP Concentration

To observe the effect of TBP concentration on extraction and separation of Nd and Ho, 8 mM of Nd and 8 mM of Ho were each added to the reactor, along with varying amounts of TBP ranging from 8 mM to 80 mM. No water was added, though the hydrated water present from the nitrate salts and (minor) water entrained in TBP was estimated to 102-106 mM. This set of experiments was then repeated in a wet environment by adding 0.18 mL H₂O (equivalent to 200 mM) to the reactor. For this latter set of experiments, the total water present was approximately 302-306 mM, an amount sufficient to exceed the solubility of water in CO₂. Visual observations confirmed the presence of a standing aqueous phase. The measured equilibrium extraction of Nd, Ho, and H₂O at 21 MPa are plotted in Figure 55.

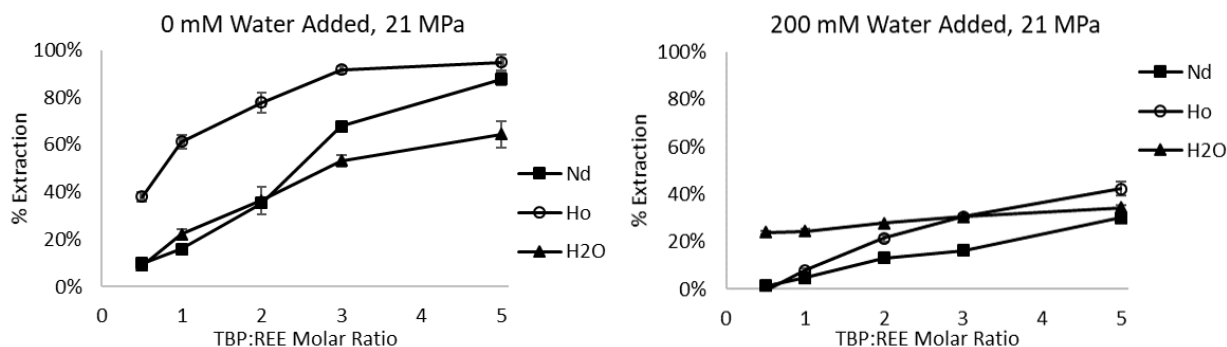


Figure 55 - Percent extraction of Nd, Ho, and H₂O at varying TBP concentrations with and without water added

The results at 17, 21, 24, and 28 MPa are shown in Table 21. Separation was effective, but the extent of Nd/Ho separation did not appear to be significantly different from an equivalent system in hexane (Zhuangfei Wang et al., 2017).

9.5.4 Effect of Pressure

As shown in Table 21, pressure appears to have little effect on the percent extraction of REEs and water in the range of 17-28 MPa (see section 10 for extraction at lower pressures).

Table 21 – Experimental Nd, Ho, and water extraction results

Pressure (MPa)	Supercritical CO ₂ Density (g/L)*	TBP:REE Molar Ratio	Water Added (mM)**	Average Extraction			Standard Error (Triplicates)		
				Nd	Ho	H ₂ O	Nd	Ho	H ₂ O
17	675.3	0.5	0	8.6%	35.7%	11.8%	2.6%	1.3%	1.8%
17	675.3	1	0	14.6%	59.9%	23.6%	1.4%	5.8%	2.6%
17	675.3	2	0	34.1%	79.1%	35.2%	2.4%	6.8%	6.0%
17	675.3	3	0	56.0%	80.3%	40.9%	3.3%	5.5%	2.4%
17	675.3	5	0	83.4%	88.2%	56.9%	4.1%	2.5%	6.9%
21	736.8	0.5	0	9.8%	38.1%	9.1%	1.8%	2.0%	1.2%
21	736.8	1	0	16.0%	61.2%	22.1%	1.2%	3.0%	2.4%
21	736.8	2	0	35.4%	77.8%	36.5%	1.4%	4.3%	5.7%
21	736.8	3	0	67.8%	91.7%	53.3%	2.2%	1.5%	2.4%
21	736.8	5	0	87.6%	94.8%	64.4%	2.7%	3.3%	5.7%
24	780.1	0.5	0	8.6%	39.4%	7.9%	2.3%	1.9%	1.1%
24	780.1	1	0	15.2%	62.8%	21.0%	1.0%	4.3%	2.3%
24	780.1	2	0	35.9%	79.0%	38.1%	1.2%	5.1%	5.5%
24	780.1	3	0	69.1%	92.8%	55.5%	2.2%	2.5%	2.7%
24	780.1	5	0	89.6%	97.6%	67.5%	2.0%	2.2%	3.1%
28	812.1	0.5	0	8.8%	38.0%	6.9%	1.0%	1.9%	1.3%
28	812.1	1	0	16.3%	62.0%	19.9%	1.5%	5.8%	1.9%
28	812.1	2	0	35.8%	77.5%	38.0%	1.1%	4.6%	5.6%
28	812.1	3	0	68.7%	91.1%	56.3%	2.2%	2.5%	3.1%
28	812.1	5	0	90.7%	94.8%	69.4%	1.1%	1.0%	2.5%
17	675.3	0.5	200	2.1%	4.3%	20.2%	0.3%	1.5%	1.0%
17	675.3	1	200	5.5%	13.9%	22.0%	1.6%	1.6%	1.0%
17	675.3	2	200	14.8%	22.1%	25.6%	2.4%	3.4%	0.4%
17	675.3	3	200	21.0%	30.8%	28.2%	2.8%	2.1%	0.4%
17	675.3	5	200	32.9%	46.1%	32.5%	2.1%	5.0%	0.6%
21	736.8	0.5	200	1.4%	0.0%	24.0%	0.8%	0.6%	0.7%
21	736.8	1	200	4.7%	8.1%	24.4%	1.2%	0.7%	0.9%
21	736.8	2	200	13.2%	21.4%	27.9%	1.9%	1.3%	0.2%
21	736.8	3	200	16.4%	30.6%	30.5%	1.5%	1.1%	0.5%
21	736.8	5	200	30.1%	42.4%	34.3%	2.3%	3.0%	1.0%
24	780.1	0.5	200	1.9%	2.2%	25.9%	0.5%	1.2%	1.0%
24	780.1	1	200	2.8%	9.9%	26.1%	0.5%	2.6%	0.9%
24	780.1	2	200	11.0%	19.9%	29.4%	2.2%	2.0%	0.7%
24	780.1	3	200	15.4%	29.9%	32.3%	1.1%	2.0%	0.3%

Pressure (MPa)	Supercritical CO ₂ Density (g/L)*	TBP:REE Molar Ratio	Water Added (mM)**	Average Extraction			Standard Error (Triplicates)		
				Nd	Ho	H ₂ O	Nd	Ho	H ₂ O
24	780.1	5	200	28.6%	44.2%	34.7%	2.6%	3.6%	1.8%
28	812.1	0.5	200	0.9%	3.2%	27.0%	0.3%	1.8%	1.0%
28	812.1	1	200	3.9%	11.2%	27.4%	0.7%	1.9%	0.8%
28	812.1	2	200	11.6%	20.7%	30.8%	1.9%	1.0%	0.7%
28	812.1	3	200	17.1%	30.2%	33.5%	0.7%	0.9%	0.5%
28	812.1	5	200	26.9%	41.9%	35.2%	2.4%	4.5%	2.9%
17	675.3	1	50	13.5%	41.1%	29.0%	2.4%	0.1%	0.7%
17	675.3	1	100	9.4%	24.4%	26.7%	2.5%	4.4%	0.3%
21	736.8	1	50	12.9%	43.2%	29.8%	1.7%	0.2%	0.6%
21	736.8	1	100	9.6%	23.6%	28.8%	1.2%	4.7%	0.3%
24	780.1	1	50	12.6%	41.8%	31.5%	1.8%	2.0%	0.7%
24	780.1	1	100	9.1%	25.2%	30.1%	2.1%	4.1%	0.4%
28	812.1	1	50	13.0%	44.5%	32.4%	2.7%	0.9%	1.1%
28	812.1	1	100	8.7%	26.2%	30.9%	1.6%	3.4%	0.2%

*Pure CO₂ density estimated using REFPROP software (National Institute of Standards & Technology, 2013)

**Liquid water pipetted into reactor. Additional water (approximately 100 mM) is also present in metal nitrate crystals and in TBP.

9.6 Equilibrium Model

A set of affinity constants was fit to the 21 MPa data given in Table 21. In each experiment, a large and dilute supercritical phase (50 mL, <16 mM REEs, <110 mM water) was mixed with a small and highly concentrated aqueous phase (<0.5 mL, 2000-6500 mM REEs). All reactions were assumed to be at equilibrium. Accordingly, it was assumed that all species had reached their equilibrium distribution between the aqueous and supercritical phases. To construct an equilibrium model for this system, it was necessary model to estimate species fugacities or activities in each phase (relative to a reference state), define a system of reactions, and fit the associated affinity constants to match with the observed data.

9.6.1 Supercritical Phase Activities

Solutes in the supercritical CO₂ phase were present in dilute concentrations. Based on spectroscopy measurements, total metal complexes were below 16 mM. Solubility of the metal

complexes could not be measured, and therefore their saturation state was not known. The supercritical water concentration was below 110 mM. The presence of a visible aqueous phase in the reactor during some experiments indicated that water had reached saturation in at least some cases. Free TBP concentrations were known to be under 80 mM because that was the maximum TBP added in this set of experiments. The solubility of TBP has been reported as 1986 mM at 60°C and 25 MPa, and therefore TBP is well under saturation in this system (Pitchaiah, Sivaraman, Lamba, & Madras, 2016).

The infinite dilution reference state was considered appropriate, as the pure component reference state is not meaningful in a solubility-limited system. Unfortunately, determining reference fugacities and activity coefficients for the metal complexes would require impractical measurements, including solubility of the individual metal complexes. Therefore, the mole fraction of each solute in the supercritical phase was used as a stand-in for rigorously modeled solute activities. This is equivalent to assuming a reference fugacity of unity and an activity coefficient of unity at infinite dilution. As demonstrated with a range of organic solutes, the solvation effects of CO₂ can be strongly non-ideal (Tester & Modell, 1997), and therefore this particular reference state assumption precludes calculating thermodynamically rigorous equilibrium constants. Results from this fitting exercise should therefore be interpreted as affinity constants only (Prigogine & Defay, 1954).

9.6.2 Aqueous Phase Activities

The water activity and mean ionic activity coefficients for the aqueous phase were estimated based on the empirical extended Pitzer equations as shown in Equations 28-36 (see List of Symbols). The reference state is defined as 1 molal solute (1 mole solute per kg solvent). The equations are considered accurate to a maximum ionic strength of 38 molal. The literature values

for the Pitzer coefficients are shown in Table 22. Several assumptions and approximations were necessary due to lack of available data:

- Fit Pitzer coefficients from literature were used (see Table 22). These coefficients were based on studies conducted with aqueous solutions at 25°C and atmospheric pressure, while the present study was conducted at 60°C and 17-28 MPa. While some studies have investigated the effect of temperature on Pitzer coefficients (Simoes, Hughes, Ingham, Ma, & Pourkashanian, 2017), the effect of temperature and pressure on activity coefficients is not documented for neodymium and holmium nitrates.
- Since θ_{NdHo} and ψ_{NdHoNO_3} were not available experimentally, literature values for θ_{NdEr} and ψ_{NdErNO_3} were used as approximations (He et al., 2011).

9.6.3 Equilibrium Reactions

As noted previously, the unavailability of reference fugacities for the supercritical solutes at infinite dilution precludes rigorous calculations of supercritical phase activity. Supercritical phase mole fraction was used instead to represent the activity of the solutes. The constants defined in Equations 37-44 should therefore be interpreted as affinity constants rather than true equilibrium constants (Prigogine & Defay, 1954). For the aqueous phase, concentrations are expressed in molality with all non-idealities modeled using the extended Pitzer method as discussed above.

$$\frac{-\ln(a_{H_2O aq})}{M_w \sum_C v_{CX} m_{CX}} = 1 + \left(\frac{2}{\sum_i m_i} \right) \left[\frac{-A_\varphi I^{\frac{3}{2}}}{1 + bI^{\frac{1}{2}}} + \sum_C m_C m_X (B_{CX}^\varphi + \left(\sum_i m_i |z_i| \right) C_{CX}) \right] \quad \text{Eq 28}$$

$$+ \left(\frac{2}{\sum_i m_i} \right) \left[\sum_{C < C'} m_C m_{C'} (\theta_{CC'} + m_X \psi_{CC'X}) \right]$$

$$\ln(\gamma_{\pm, MX}) = -|z_M z_X| A_\varphi \left[\frac{I^{\frac{1}{2}}}{1 + bI^{\frac{1}{2}}} + \frac{2 \ln(1 + bI^{\frac{1}{2}})}{b} \right] \quad \text{Eq 29}$$

$$+ \frac{v_M v_X}{v_{MX}} m_T \left[2B_{MX} + (v_M v_X)^{\frac{1}{2}} m_T C_{MX}^\gamma \right]$$

$$+ \sum_C \frac{v_C v_X}{v_{CX}} m_{CX} m_T \left[(v_C v_X)^{\frac{1}{2}} C_{CX}^\gamma \right] + \frac{v_M v_X}{v_{MX}} m_{MX} m_T \left[(v_M v_X)^{\frac{1}{2}} C_{MX}^\gamma \right]$$

$$+ \frac{v_M}{v_{MX}} \sum_C m_C [2\theta_{MC} + m_X \psi_{MCX}] + \frac{v_X}{v_{MX}} \sum_{C < C'} m_C m_{C'} \psi_{CC'X}$$

$$B_{CX}^\varphi = \beta_{CX}^{(0)} + \beta_{CX}^{(1)} \exp(-\alpha_{B1} I^{\frac{1}{2}}) + \beta_{CX}^{(2)} \exp(-\alpha_{B2} I^{1/2}) \quad \text{Eq 30}$$

$$C_{CX}^\varphi = 2[C_{CX}^{(0)} + C_{CX}^{(1)} \exp(-\alpha_{c1} I) + C_{CX}^{(2)} \exp(-\alpha_{c2} I) + C_{CX}^{(3)} \exp(-\alpha_{c3} I)] \quad \text{Eq 31}$$

$$C_{CX} = \frac{C_{CX}^\varphi}{2|z_C z_X|^{1/2}} \quad \text{Eq 32}$$

$$B_{CX} = \beta_{CX}^{(0)} + \beta_{CX}^{(1)} g(\alpha_{B1} I^{\frac{1}{2}}) + \beta_{CX}^{(2)} g(\alpha_{B2} I^{\frac{1}{2}}) \quad \text{Eq 33}$$

$$C_{CX}^\gamma = 3C_{CX}^{(0)} + C_{CX}^{(1)} [g(\alpha_{c1} I) + 2 \exp(-\alpha_{c1} I)] + C_{CX}^{(2)} [g(\alpha_{c2} I) + 2 \exp(-\alpha_{c2} I)] \quad \text{Eq 34}$$

$$+ C_{CX}^{(3)} [g(\alpha_{c3} I) + 2 \exp(-\alpha_{c3} I)]$$

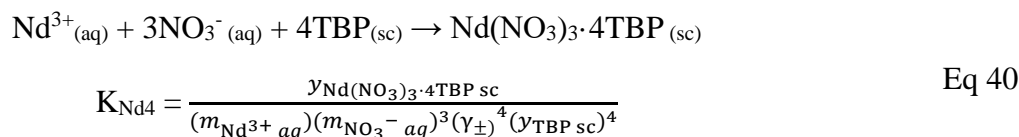
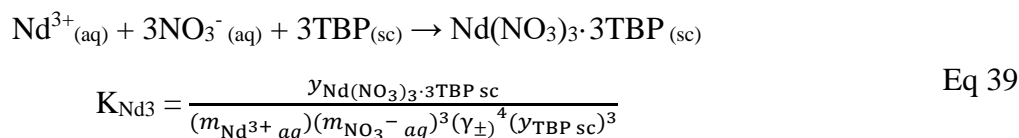
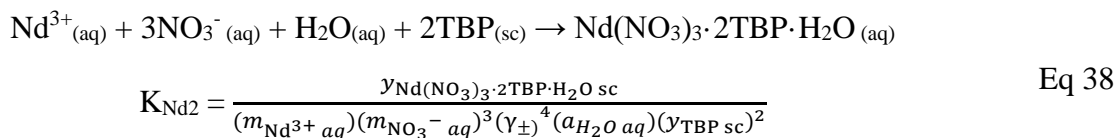
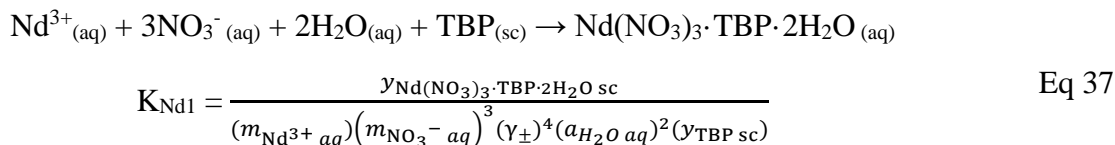
$$g(x) \equiv \frac{2[1 - (1 + x) \exp(-x)]}{x^2} \quad \text{Eq 35}$$

$$I \equiv \sum_i m_i z_i^2 / 2 \quad \text{Eq 36}$$

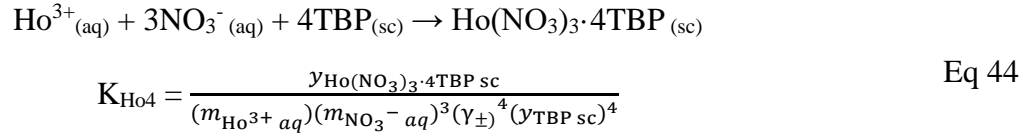
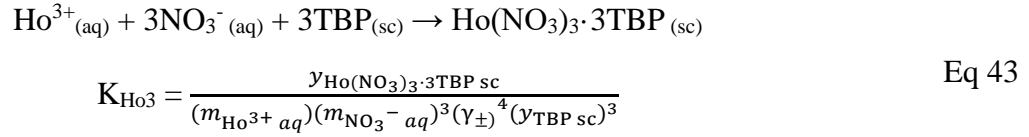
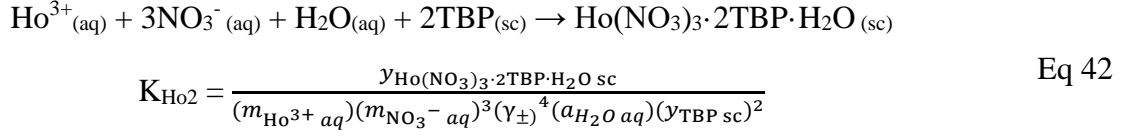
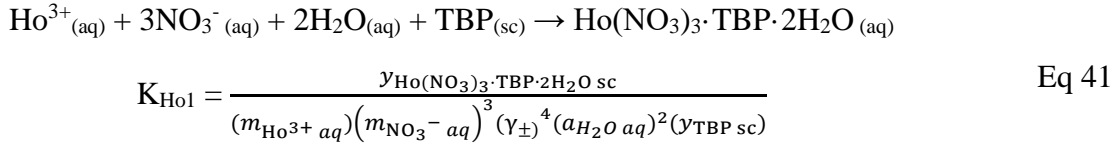
Table 22 – Adjustable fit parameters for the extended Pitzer equations based on literature(He et al., 2011; Z.-C. Wang et al., 2006)

Parameter	Value	Unit
A_ϕ	0.3915	$\text{kg}^{1/2}/\text{mol}^{1/2}$
b	1.2	$\text{kg}^{1/2}/\text{mol}^{1/2}$
α_{B1}	1.8	$\text{kg}^{1/2}/\text{mol}^{1/2}$
α_{B2}	6	$\text{kg}^{1/2}/\text{mol}^{1/2}$
α_{C1}	0.15	kg/mol
α_{C2}	0.25	kg/mol
α_{C3}	0.35	kg/mol
$(3/2)\beta^{(0)}_{\text{Nd}(\text{NO}_3)_3}$	0.3436	kg/mol
$(3/2)\beta^{(1)}_{\text{Nd}(\text{NO}_3)_3}$	7.32	kg/mol
$(3/2)\beta^{(2)}_{\text{Nd}(\text{NO}_3)_3}$	-2.51	kg/mol
$(3^{3/2})C^{(0)}_{\text{Nd}(\text{NO}_3)_3}$	-0.0123	kg^2/mol^2
$(3^{3/2})C^{(1)}_{\text{Nd}(\text{NO}_3)_3}$	0.3763	kg^2/mol^2
$(3^{3/2})C^{(2)}_{\text{Nd}(\text{NO}_3)_3}$	-0.5732	kg^2/mol^2
$(3^{3/2})C^{(3)}_{\text{Nd}(\text{NO}_3)_3}$	1.3968	kg^2/mol^2
$(3/2)\beta^{(0)}_{\text{Ho}(\text{NO}_3)_3}$	0.4412	kg/mol
$(3/2)\beta^{(1)}_{\text{Ho}(\text{NO}_3)_3}$	8.17	kg/mol
$(3/2)\beta^{(2)}_{\text{Ho}(\text{NO}_3)_3}$	-6.03	kg/mol
$(3^{3/2})C^{(0)}_{\text{Ho}(\text{NO}_3)_3}$	-0.01982	kg^2/mol^2
$(3^{3/2})C^{(1)}_{\text{Ho}(\text{NO}_3)_3}$	0.3689	kg^2/mol^2
$(3^{3/2})C^{(2)}_{\text{Ho}(\text{NO}_3)_3}$	-0.3555	kg^2/mol^2
$(3^{3/2})C^{(3)}_{\text{Ho}(\text{NO}_3)_3}$	1.2416	kg^2/mol^2
θ_{NdEr}	-0.01371	kg/mol
ψ_{NdErNO_3}	0.001397	kg^2/mol^2

Neodymium and TBP were assumed to form complexes with Nd:TBP ratios ranging from 1:1 to 1:4 (see Equations 37-40), but that only the 1:3 and 1:4 complexes are soluble in CO_2 , based off of mole ratio plots in previous studies (R. V. Fox et al., 2004) . This implies that the insoluble complexes remain in the aqueous phase. See section 7.4.2 for further discussion of the structures of various complexes. The assumed reactions and affinity constant definitions are shown below.



Holmium and TBP were assumed to form complexes with Ho:TBP ratios ranging from 1:1 to 1:4 (see Equations 41-44), but that only the 1:2, 1:3, and 1:4 complexes are soluble in CO₂, based off of mole ratio plots in previous studies (see section 7.4.2) (R. V. Fox et al., 2005). The reactions and associated affinity constants are shown below.



It was assumed that water would dissolve in the supercritical phase as free water and as a H₂O·TBP complex as shown in Figure 53. This assumption is based on studies showing 1:1 H₂O·TBP complex formation at atmospheric conditions (Hardy et al., 1964). Dissolution of free water is shown in Equation 45 and the formation of the H₂O·TBP complex is shown in Equation 46.



9.6.4 Fitting

The affinity constants K_{H_2O} and $K_{H_2O \cdot TBP}$ were first fit to the data in Figure 53. The fit affinity constants are shown in Table 23 and correspond to the lines in Figure 53. Although K_{H_2O} increases slightly with pressure, $K_{H_2O \cdot TBP}$ does not have a consistent trend with pressure.

Table 23 - Fit affinity constants for water extraction with TBP at 60°C

Pressure (MPa)	17	21	24	28
$\log_{10} K_{H_2O}$	-2.16	-2.14	-2.12	-2.11
$\log_{10} K_{H_2O \cdot TBP}$	-0.365	-0.370	-0.393	-0.376

The measurement and balance error were computed using the following equations where $v_{i,s}$ is the stoichiometric coefficient of atom i in species s , y_s is the mole fraction of species s , N_s is the number of moles of species s , and M_s is the mass of species s (see Definitions of Symbols) :

$$\begin{aligned} \text{Measurement Error} = & \sum_{\text{all experiments}} \left[\left(\frac{\sum_s v_{Nd,s} y_{s \text{ sc fit}} - y_{\sum Nd \text{ sc measured}}}{N_{Nd \text{ initial}} / N_{CO_2}} \right)^2 \right. \\ & + \left(\frac{\sum_s v_{Ho,s} y_{s \text{ sc fit}} - y_{\sum Ho \text{ sc measured}}}{N_{Ho \text{ initial}} / N_{CO_2}} \right)^2 \\ & \left. + \left(\frac{\sum_s v_{H_2O,s} y_{s \text{ sc fit}} - y_{\sum H_2O \text{ sc measured}}}{N_{H_2O \text{ initial}} / N_{CO_2}} \right)^2 \right] \end{aligned} \quad \text{Eq 47}$$

$$\begin{aligned} & \text{Balance Error} \\ = & \sum_{\text{all experiments}} \left[\left(\frac{N_{CO_2} (\sum_s v_{Nd,s} y_{s \text{ sc fit}}) + M_{H_2O \text{ aq fit}} m_{Nd^{3+} \text{ aq fit}} - N_{Nd \text{ initial}}}{N_{Nd \text{ initial}}} \right)^2 \right. \\ & + \left(\frac{N_{CO_2} (\sum_s v_{Ho,s} y_{s \text{ sc fit}}) + M_{H_2O \text{ aq fit}} m_{Ho^{3+} \text{ aq fit}} - N_{Ho \text{ initial}}}{N_{Ho \text{ initial}}} \right)^2 \\ & \left. + \left(\frac{N_{CO_2} (\sum_s v_{TBP,s} y_{s \text{ sc fit}}) - N_{TBP \text{ initial}}}{N_{TBP \text{ initial}}} \right)^2 \right] \end{aligned} \quad \text{Eq 48}$$

The Nd and Ho extraction data were then fit with Equations 37-44 using the MATLAB “fmincon” algorithm. The optimization algorithm sought to minimize total measurement square error for all 12 experiments as defined in Equation 47. The model was constrained to ensure that the total square balance error for all 12 experiments was less than 0.002 as defined in Equation 48. K_{H_2O} was fixed at $10^{-2.14}$ and $K_{H_2O \cdot TBP}$ was fixed at $10^{-0.370}$ for 21 MPa (see Table 23). The fit affinity constants are shown in Table 24 and the quality of the fit is illustrated in Figure 56.

Table 24 – Fit affinity constants for 21 MPa, 60°C data

Affinity Constant	Fit Value
$\log_{10}K_{Nd1}$	-10.4
$\log_{10}K_{Nd2}$	-1.0
$\log_{10}K_{Nd3}$	2.8
$\log_{10}K_{Nd4}$	-0.5
$\log_{10}K_{Ho1}$	-4.3
$\log_{10}K_{Ho2}$	-0.7
$\log_{10}K_{Ho3}$	-4.5
$\log_{10}K_{Ho4}$	3.8

The model showed good agreement with the measured metal concentrations (modeled metal concentrations were all within 1 mmol/L of the measurements). Modeled water concentrations were approximately double the measured values for the drier conditions. This may reflect the presence of water in hydrated Nd and Ho crystal structures from incomplete mixing in drier conditions, thus reducing water activity.

The model results indicate that Nd in the supercritical phase exists almost exclusively as the 1:3 complex. The results also indicate that dissolution of Ho is dominated by the 1:2 complex, although the 1:4 complex increases as more TBP is added to the system. These results suggest that the dominant mechanism driving separation is based on differences in solubility: namely that the 1:2 Ho complex is soluble and the 1:2 Nd complex is insoluble. This explains why separation is highest at lower TBP concentrations: at these conditions, complexes with lower TBP numbers dominate, thus magnifying the effect of the 1:2 Ho complex.

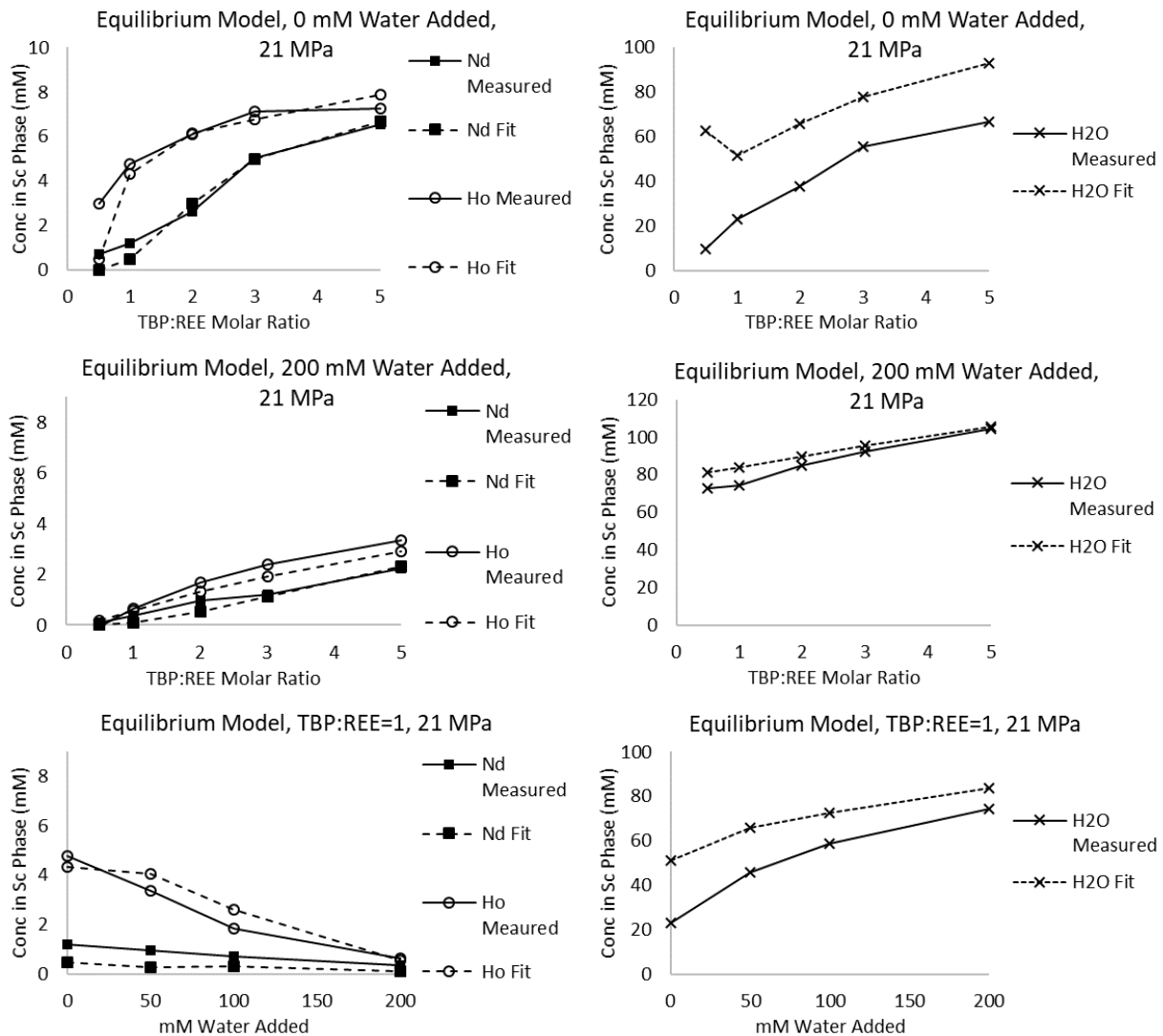


Figure 56 - Fit supercritical Nd and Ho concentrations from equilibrium model. "Sc" abbreviation indicates supercritical phase.

The model results suggest that the primary cause for enhanced separation in drier systems is the thermodynamics of the aqueous phase. The mean ionic activity coefficient of holmium nitrate becomes significantly larger than neodymium nitrate at high ionic strength, as holmium is more effectively able to replace water in its second coordination sphere with anions (Chatterjee et al., 2015; Rard, Miller, & Spedding, 1979; Rard & Spedding, 1981).

CHAPTER 10

FEASIBILITY OF METAL SEPARATION WITH PRESSURE REDUCTION

10.1 Goal and Scope

Nd and Ho nitrate salts were extracted at low pressures (<17 MPa) to test the feasibility of separating REEs through sequential pressure reduction. UV Vis absorption spectroscopy was used to quantify REE extraction. This was repeated for a range of TBP:REE ratios.

10.2 Materials and Procedure

A description of the supercritical extraction and UV Vis spectroscopy system used for this set of experiments is found in sections 9.2 and 9.3. Calibration for Nd and Ho is described in section 9.4.

As described in section 9.3, approximately 8 mM of Nd nitrate and 8 mM of Ho nitrate were loaded to the cell, along with varying amounts of TBP. No water was added in these tests. The reactor was heated to 60°C and pressurized. In this set of experiments, the initial pressure was set below 10 MPa in order to resolve the entire dissolution curve. The reactor was allowed to stir for at least 30 minutes to achieve equilibrium, and then a spectrum was measured. Pressure was increased sequentially up to approximately 30 MPa. The Nd and Ho calibration curves from section 9.4 were used to quantify metal extraction. Notably, water extraction at these low pressures could not be quantified due to calibration difficulties. Each run was repeated at least twice.

10.3 Results

Nd and Ho extraction as a function of pressure is plotted in Figure 57 for a range of TBP:REE ratios. Trendlines are also shown.

The results showed that extraction of both Nd and Ho TBP complexes increases rapidly between 10 and 15 MPa. This pressure range appears to be independent of TBP concentration,

possibly implying that pressure/solubility behavior is independent of which complexes are formed (see Equations 37-44). Because both Nd and Ho will precipitate from the supercritical phase at approximately the same pressure, the results imply that Nd and Ho separation via sequential pressure reduction is not feasible.

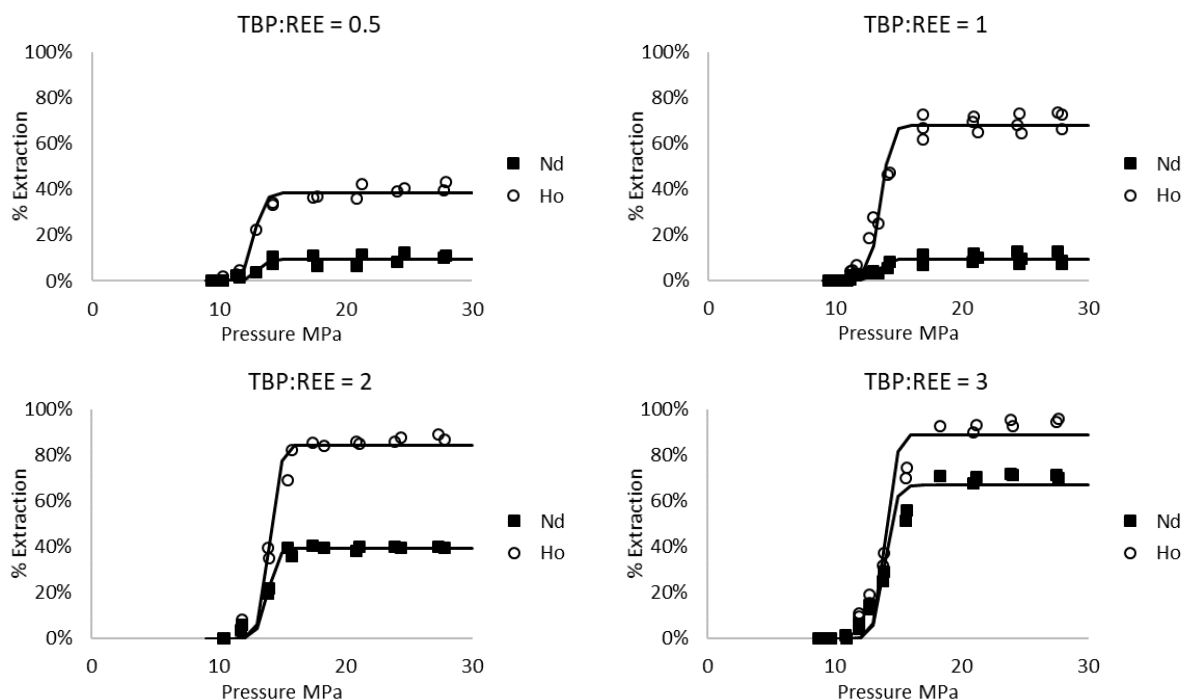


Figure 57 – Experimentally determined pressure versus extraction curves for Nd and Ho nitrate salts extracted with varying amounts of TBP

CHAPTER 11

CONCLUSIONS AND RECCOMENTATIONS

11.1 Summary

This study has made some important advancements in extraction and separation of rare earth elements using the TBP/nitrate system in supercritical CO₂. However, it has also pointed to some important challenges that must be addressed if this process is to achieve commercial adoption.

The first part of this study demonstrated that rare earth elements can be extracted from bastnäsite concentrate using standard pretreatment methods followed by supercritical carbon dioxide extraction with tributyl phosphate/nitric acid adducts. La, Ce, Pr, and Nd recoveries were similar to conventional leaching with concentrated nitric acid. Selectivity for REEs over gangue elements was superior to concentrated nitric acid leaching: with 4 M H⁺ adduct at 5 mol% in CO₂, calcium recoveries were approximately half of those observed in concentrated nitric acid leaching, and barium and strontium were generally below the reporting limit. Though both roasted and NaOH digested bastnäsite achieved similar recoveries, extraction was marginally faster for the NaOH digested sample, particularly for lanthanum extraction.

In general, the extraction rate increased with atomic number, corresponding to greater affinity to TBP. For example, with 4 M H⁺ adduct at 5 mol% in CO₂, Nd extraction rates were 30-100% faster than La extraction rates. Various adduct compositions (TBP/HNO₃ ratios) and adduct mole % in the CO₂ phase were compared. By fitting the recovery curves to a surface-reaction limited model, the lumped first-order reaction rate constant for cerium, praseodymium, and neodymium increased with HNO₃ concentration in the CO₂ phase up to approximately 1.5 mol/L HNO₃, at which point recovery decreased, likely due to droplet condensation or competition between lanthanide nitrates and nitric acid for TBP complexation. For lanthanum, the reaction rate simply

increased with TBP concentration in the CO₂ phase, possibly indicating that the lanthanum extraction rate is limited by TBP complexation.

This study also advanced fundamental understanding of rare earth element separation in carbon dioxide and illustrated how water affects the supercritical extraction process. Extraction of neodymium and holmium nitrates with tributyl phosphate was investigated in supercritical carbon dioxide. UV-Vis and near infrared spectroscopy were used to measure concentrations of Nd, Ho, and H₂O in situ. Extraction and separation of Nd and Ho was investigated as a function of pressure (17-28 MPa), TBP concentration (8-80 mM), and water concentration (0-200 mM added). It was found that maximum Nd and Ho separation was achieved with a TBP:REE ratio of 1-2. Separation was also highest when the water concentration was at a minimum. Pressure was found to have a minimal effect on extraction and separation in the 17-28 MPa range. While the results showed effective separation, the extent of Nd/Ho separation did not differ significantly from an equivalent system in hexane (Zhuangfei Wang et al., 2017).

The data were correlated with an equilibrium model, with aqueous phase activities based on published Pitzer coefficients for Nd and Ho. Metal complex stoichiometries were based off of mole ratio plots in previous studies (R. V. Fox et al., 2005). Fit affinity constants showed good agreement with the measured data, though water dissolution was somewhat over-estimated by the model. The model suggested that the separation between Nd and Ho is primarily driven by the fact that the 1:2 complex is soluble for Ho but not for Nd. The importance of this 1:2 Ho complex explains why separation is highest at low TBP concentrations. Enhanced separation in drier conditions is likely driven by deviation between the Nd and Ho mean ionic activity coefficients at higher ionic strengths.

Nd and Ho extraction experiments at low pressures (<17 MPa) showed that both Nd and Ho TBP complexes will precipitate from the supercritical phase between 10 and 15 MPa. There did not appear to be a difference in the precipitation pressure of each metal, regardless of the TBP:REE ratio.

11.2 Implications

These experiments illustrate several important considerations for supercritical extraction and separation of REEs from primary sources. Importantly, this study demonstrated selective extraction of REEs from bastnäsite concentrate which had been pretreated with conventional preprocessing steps. This study also showed that direct extraction with TBP/HNO₃ adducts can achieve greater selectivity for REEs than nitric acid leaching. These results could allow for a process in which metals are directly (and selectively) removed from concentrate, bypassing acid leaching stages. This keeps water concentrations to a minimum, which benefits separation as shown in this study. Heavier REEs were shown to have faster extraction kinetics, which could potentially be used as part of a separation process. Further downstream stages could achieve separation of various REEs by equilibration with a highly concentrated aqueous or solid phase. This study suggested that REE separation via sequential pressure reduction is not feasible.

However, it is important to note that this study did not show any complexation, dissolution, or separation behavior that differed from a liquid/liquid extraction system. The extent of Nd/Ho separation was similar to a liquid/liquid system (Zhuangfei Wang et al., 2017). The enhanced separation at higher ionic strengths has also been demonstrated for liquid/liquid systems (J. Zhang & Zhao, 2016).

11.3 Recommendations

Further work is recommended to determine whether supercritical extraction and separation can be competitive with conventional solvent extraction, specifically:

1. Further work is required to demonstrate how different primary and recycled source materials would respond to SFE. For example, the F/CO₃ ratio in a bastnäsite ore could affect trifluoride formation and REE solubility after roasting. F/CO₃ ratios can vary significantly between deposits or within the same deposit. REE supercritical extraction from other materials could also be further explored. As previously noted, supercritical extraction has been applied to other REE source materials such as monazite, fluorescent lamp phosphors, and batteries, but questions remain about separation of contaminants (Samsonov et al., 2015; Shimizu et al., 2005; Yao et al., 2017).
2. Although this study has illustrated effective separation of Nd and Ho, further work is required to understand the separation of adjacent light or heavy lanthanides. Nd and Ho separation appeared to be linked to a difference in the solubility of the 1:2 complex, and therefore adjacent lanthanides which both have insoluble 1:2 complexes may not separate as effectively. For example, supercritical extraction studies have shown minimal separation of Nd and Pr (R. V. Fox et al., 2004; L. Y. Zhu et al., 2016). Notably, not all lanthanides have absorption peaks in the UV or visible spectrum, and therefore absorption spectroscopy cannot be used to study separation of all lanthanides. It is recommended that future studies use an aqueous phase with a large volume relative to the supercritical phase volume, similar to several previous studies (Dehghani et al., 1996; Meguro, Iso, & Yoshida, 1998). A large aqueous phase allows for the aqueous phase composition to be

treated as a constant, allowing for simpler comparisons between various extraction conditions.

3. Reagent consumption and recycle needs to be evaluated for a commercial process design. Solvent extraction allows for closed-loop recycling of both solvent and extractant. Demonstrating the ability to recycle CO₂ and TBP would be an important consideration for design of a commercial process.
4. Further study is required to understand the behavior of other extractants in supercritical CO₂. Extractants based on different extraction mechanisms (for example, cation exchange versus solvating extractants) may show fundamentally different behavior in supercritical CO₂. For example, there has been some promising work in beta diketones for supercritical REE extraction and separation (R. V. Fox, 2003; Hwang et al., 2016).
5. A comparative technoeconomic assessment of supercritical extraction relative to conventional solvent extraction would be valuable. High-pressure processing can result in significant equipment costs that are not required in conventional solvent extraction. These costs are especially high if large vessel volumes and/or corrosion-resistant materials are required. Therefore supercritical extraction economics will strongly depend on how many extraction and separation stages are necessary, and on the vessel volumes required for equilibrium metal distribution and phase separation. Further study is required to establish whether purification of saleable lanthanide products can be achieved at costs that compete with current solvent extraction technology.

If these issues can be adequately addressed, supercritical extraction may be able to offer a novel and competitive separation process for rare earth elements.

APPENDIX A – DATA FROM PREVIOUS COPPER IN SITU LEACHING PROJECTS

Mine Name	Location	Host Rock	Major Copper Mineralization	Minor Copper Mineralization	Average Copper Grade (wt. %)	Description	Area Involved (m ²)*	Maximum Depth (m)*	Fracture Spacing (fractures per meter)*	Leach Solution	Leach Solution Flow Rate (L/min)*	Porosity (vol. %)	Permeability (mD)	Pregnant Solution Grade (g/L copper)	Reagent Consumption	Copper Production (kg/day)*	Years Active
Kimbley	NV, USA	Limey sediments intruded by biotite porphyry (Ahlness & Pojar, 1983)	Chalcocite (Ahlness & Pojar, 1983)		0.32% (Ahlness & Pojar, 1983)	Injection and recovery wells drilled and leached above an old exploration drift (Ahlness & Pojar, 1983)	110 (Ahlness & Pojar, 1983)	80.8 (Ahlness & Pojar, 1983)		Sulfuric acid (Ahlness & Pojar, 1983)	190 injected, 0.8 recovered (Ahlness & Pojar, 1983)		6029 (Ahlness & Pojar, 1983)	0.15 (Ahlness & Pojar, 1983)			1970-1971 (Ahlness & Pojar, 1983)
Safford (Lone Star)	AZ, USA	Andesitic volcanics (Ahlness & Pojar, 1983)	Chalcopyrite (Bartlett, 1998)	Bornite, brochantite, chalcocite, covellite, chrysocolla (Ahlness & Pojar, 1983)	0.41% (Ahlness & Pojar, 1983)	Two "pads" leached: one with four wells and one with five wells. One additional angled leach well drilled outside of pad area (L.M. Cathles et al., 1978).	A pad: 900. B pad: 4000 (L.M. Cathles et al., 1978)	A pad: 980. B pad: 1100 (L.M. Cathles et al., 1978)	0-70 for vuggy veins. Major fractures were 20 m apart (L.M. Cathles et al., 1978).	Ammonium sulfate, ammonia, and oxygen gas (Lawrence M. Cathles, 2014)	100 (based on B pad tests) (Lawrence M. Cathles, 2014)	3% (Lawrence M. Cathles, 2014)	Non-vuggy material: 0. Vuggy zones: ~0.1. >1000 for channels (L.M. Cathles et al., 1978).	0-1.6 for A pad. 0-0.2 for B pad (Lawrence M. Cathles, 2014).		5 (based on B pad tests) (Lawrence M. Cathles, 2014)	1971-1978 (L.M. Cathles et al., 1978)
Emerald Isle	AZ, USA	Conglomerate (Ahlness & Pojar, 1983)	Chrysocolla (Ahlness & Pojar, 1983)	Dioptase, tenorite, cuprite (Ahlness & Pojar, 1983)	1.0% (Ahlness & Pojar, 1983)	Bottom of pit leached. Solution recovered in 7 recovery wells (Ahlness & Pojar, 1983).	2612.9 (Ahlness & Pojar, 1983)	20 (Ahlness & Pojar, 1983)	6.2 (D'Andrea, Larson, Fletcher, Chamberlain, & Engelman, 1977)	Sulfuric acid pH 1.10 (Ahlness & Pojar, 1983)	440 (Ahlness & Pojar, 1983)			0.65 (Ahlness & Pojar, 1983)	10.0 kg acid/kg copper, 2.75 kg iron/kg copper (Ahlness & Pojar, 1983)	339 (Ahlness & Pojar, 1983)	1974-1975 (Ahlness & Pojar, 1983)
Nacimiento	NM, USA	Sandstone overlain by shale and underlain by mudstone (Ahlness & Pojar, 1983)	Chalcocite (Ahlness & Pojar, 1983)		0.3% (O'Gorman et al., 2004)	Leaching conducted via 9 contiguous five spot patterns drilled into bottom of the open pit (Schlitt, 1992, p. 1517).		120 (Cowart et al., 2004)	Sandstone (not fractured) (Ahlness & Pojar, 1983)	Ferric sulfate (Schlitt, 1992, p. 1517)		21% (Cowart et al., 2004)	300-3000 before leaching (Ahlness & Pojar, 1983)				1984-1991 (Cowart et al., 2004)
Chuquicamata (Mina Sur)	Chile	Gravel-filled paleochannels (Axen, 2014)	Atacamite (Axen, 2014)	Chrysocolla (Axen, 2014)	1.38% (Pallauta, 1985)	2 well leaching near open pit (Axen, 2014)	Wells were 12 m apart (Pallauta, 1985)	227 (Pallauta, 1985)		Sulfuric acid (Pallauta, 1985)	200 (Pallauta, 1985)	5% effective porosity (Pallauta, 1985)	The two wells measured 2.9 and 3.5 before leaching, 4.6 and 4.8 after leaching (Pallauta, 1985)	First test: 9.4. Second test: 11 for first 48 hours, then 4-5 (Pallauta, 1985)	3.3 kg acid/kg copper (Pallauta, 1985)		1985 (Pallauta, 1985)

Mine Name	Location	Host Rock	Major Copper Mineralization	Minor Copper Mineralization	Average Copper Grade (wt. %)	Description	Area Involved (m ²)*	Maximum Depth (m)*	Fracture Spacing (fractures per meter)*	Leach Solution	Leach Solution Flow Rate (L/min)*	Porosity (vol. %)	Permeability (mD)	Pregnant Solution Grade (g/L copper)	Reagent Consumption	Copper Production (kg/day)*	Years Active
San Manuel (1 of 2)	AZ, USA	Quartz monzonite intruded by granodiorite porphyry (Wiley, Ramey, & Rex, 1994)	Chrysocolla (Wiley et al., 1994)		0.4% (as of 1992) (Niemuth, 1994)	Over 1,000 injection and recovery wells drilled from benches of open pit (Parker & Braun, 2004; Williamson, 1998)			9.2 (Williamson, 1998)	Sulfuric acid pH 1.6 (Williamson, 1998)	About 20,000-30,000 (Williamson, 1998)			0.5-3.5 (Williamson, 1998)		About 20,000 (Williamson, 1998)	1986-2002 (Niemuth, 1994; Parker & Braun, 2004)
Casa Grande (also known as Lakeshore and Tohono)	AZ, USA	Granodiorite porphyry (Sainath, 1991)	Chrysocolla (Sainath, 1991)		0.8%-1.2% (Schmidt, Behnke, & Friedel, 1990)	58 wells drilled from underground tool storage crib. Each could serve as an injection or a recovery well (Schmidt et al., 1990).	5000 (Schmidt et al., 1994)	300 (Schmidt et al., 1994)	20.3 (Ellenberger & Jones, 1994)	Sulfuric acid pH 0.88-1.6 (Schmidt et al., 1994)	Injected: 49 in year 1, 43.5 in year 2. Recovered: 12.9 in year 1, 19.3 in year 2 (Schmidt et al., 1994).	5% (Earley & Jones, 1992)	0.016 (saturated permeability) (Michael J. Friedel, 1991)	0.89 in first year, 0.80 in second year (Schmidt et al., 1994)		About 10 (Earley & Jones, 1992)	1989-1991 (Schmidt et al., 1994)
San Manuel (2 of 2)	AZ, USA	Quartz monzonite intruded by granodiorite porphyry (Wiley et al., 1994)	Chrysocolla (Wiley et al., 1994)		0.799% (Beane & Ramey, 1995)	Pilot study using 3 recovery wells and 16 injection wells on bench of open pit (Beane & Ramey, 1995)	864 (Beane & Ramey, 1995)	150 (Beane & Ramey, 1995)		Sulfuric acid averaging 24.2 g/L acid (Beane & Ramey, 1995)	1147 injected, 999 recovered (Beane & Ramey, 1995)		361-594 before leaching, 9.52-747 after leaching** (Beane & Ramey, 1995)	1.39 (Beane & Ramey, 1995)	6.05 kg acid/kg copper (Beane & Ramey, 1995)	About 2000 (Beane & Ramey, 1995)	1992-1993 (Beane & Ramey, 1995)
Mineral Park	AZ, USA	Quartz monzonite porphyry (Schmidt & Earley, 1997)	Chalcocite (Schmidt, Dahl, Kim, Paillet, & Earley, 1995)	Chalcopyrite (Schmidt et al., 1995)	0.41% (Schmidt & Earley, 1997)	4 injection wells and 4 recovery wells drilled into sloped surface next to open pit (Schmidt & Earley, 1997)	7000 (Schmidt et al., 1995)	91 (Schmidt et al., 1995)	1.06 (Yegulalp & Kim, 1996)	Sulfuric acid (50 g/L for acid cure, pH 0.5-2 for leaching) (Earley, 2014)	66 recovered (Schmidt & Earley, 1997)	1.3-2.0% effective porosity (Schmidt & Earley, 1997)	23 in chalcocite zone (Schmidt & Earley, 1997)	0.42 (Schmidt & Earley, 1997)		23 (Earley, 2014)	1997 (Schmidt & Earley, 1997)
Florence (also known as Poston Butte)	AZ, USA	Quartz monzonite intruded by granodiorite dikes (J. R. Davis, 1997)	Chrysocolla (J. R. Davis, 1997)	Tenorite, neotocite, cuprite, native copper, clays, brochantite (J. R. Davis, 1997)	0.358% (Zimmerman et al., 2013)	4 injection wells, 9 recovery wells, and 6 observation wells (Brewer, 1998)	40,000 (Brewer, 1998)	About 200 (Stubben & LaBrecque, 1998)	30 (J. R. Davis, 1997)		610 injection, 720 recovery (Zimmerman et al., 2013)	6% effective porosity (Zimmerman et al., 2013)	42 to 367 (Brewer, 1998)	0.15 maximum (Earley & Johnson, 2012)			1997-1998 (Zimmerman et al., 2013)

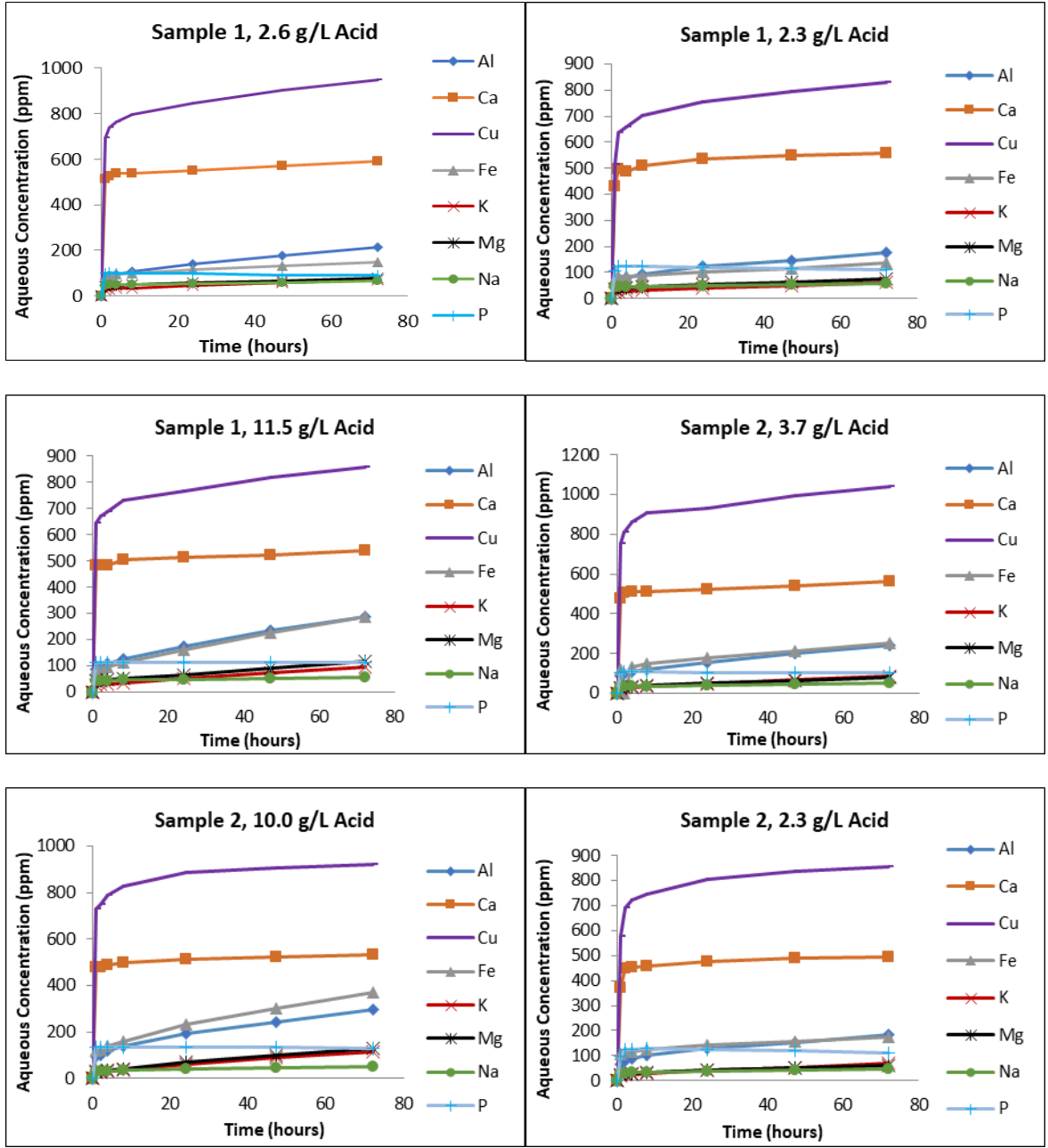
Mine Name	Location	Host Rock	Major Copper Mineralization	Minor Copper Mineralization	Average Copper Grade (wt. %)	Description	Area Involved (m ²)*	Maximum Depth (m)*	Fracture Spacing (fractures per meter)*	Leach Solution	Leach Solution Flow Rate (L/min)*	Porosity (vol. %)	Permeability (mD)	Pregnant Solution Grade (g/L copper)	Reagent Consumption	Copper Production (kg/day)*	Years Active
Santa Cruz	AZ, USA	Granite intruded by granodiorite porphyry dikes (O'Neil, 1991)	Atacamite and chrysocolla (Nelson, 1991)	Copper in plagioclase, chalcocite (Nelson, 1991)	0.6% (O'Neil, 1991)	One injection well with four recovery wells (Kreis, 1994)	1500 (Kreis, 1994)	539 (Kreis, 1994)	20 (O'Neil, 1991)	Sulfuric acid (Weber et al., 2000)	49-80 (Amrich Minerals, 2013)	2.5%-13% (Lantz & Statham, 1994)	30-200 before leaching (Weber et al., 2000)	0.3-1.8 (Amrich Minerals, 2013)		51.3*** (Amrich Minerals, 2013)	1997-1998 (Amrich Minerals, 2013)

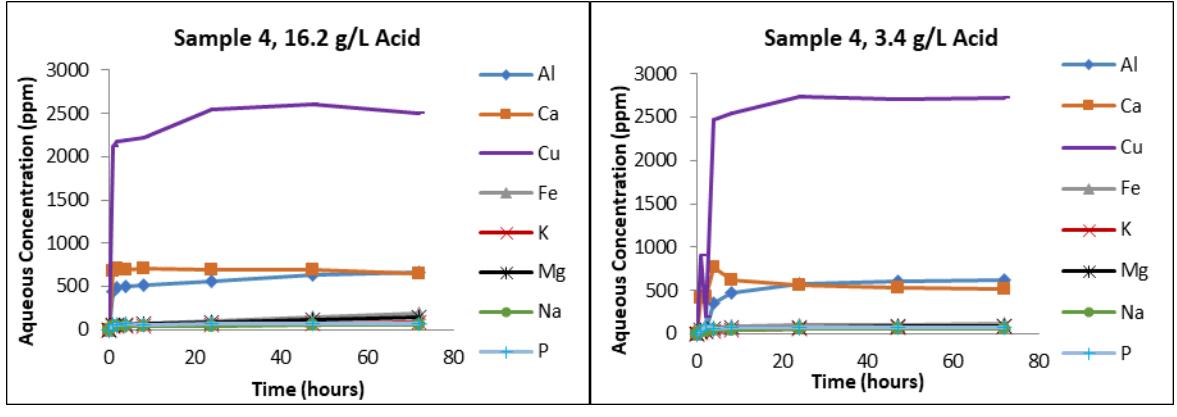
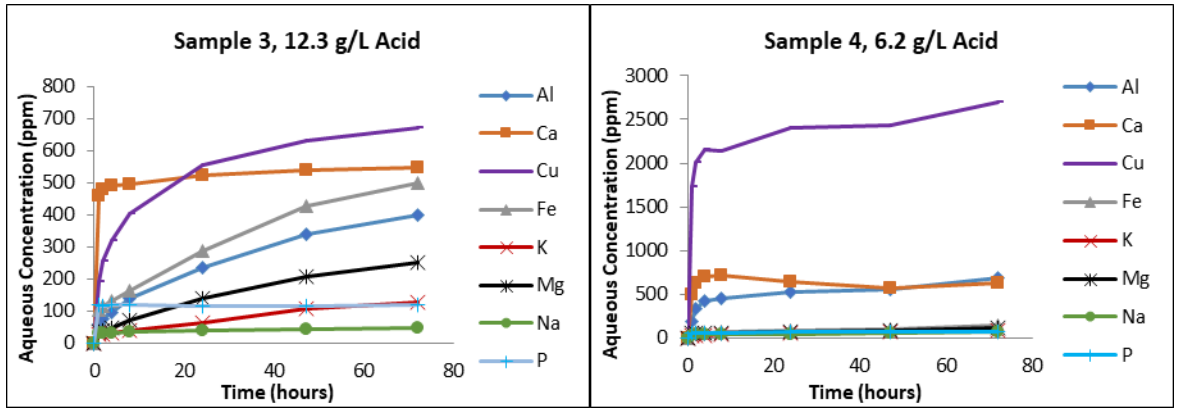
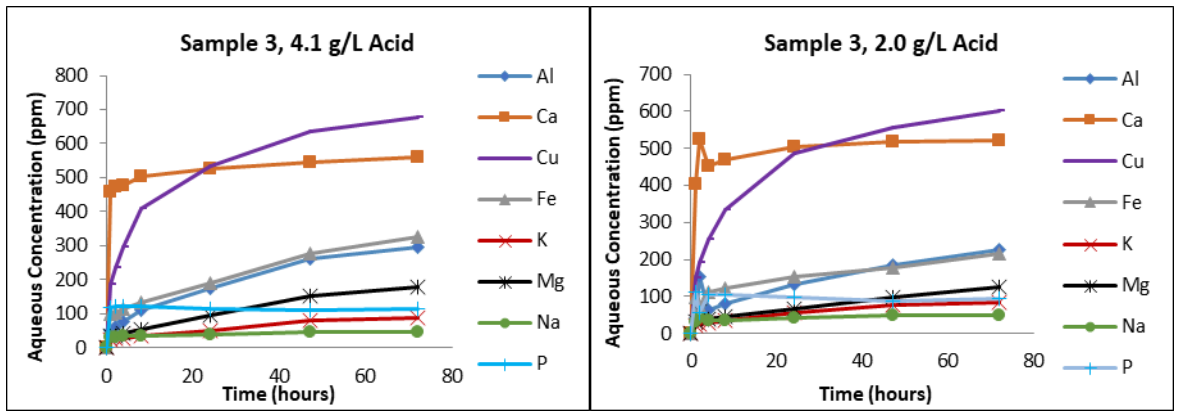
*All data has been converted to SI units, retaining the number of significant figures from the original source

**From recovery/control well pumping tests without injection

***Source specified production rate in "t" or "tons". These were assumed to be short tons as imperial units were used throughout the source article.

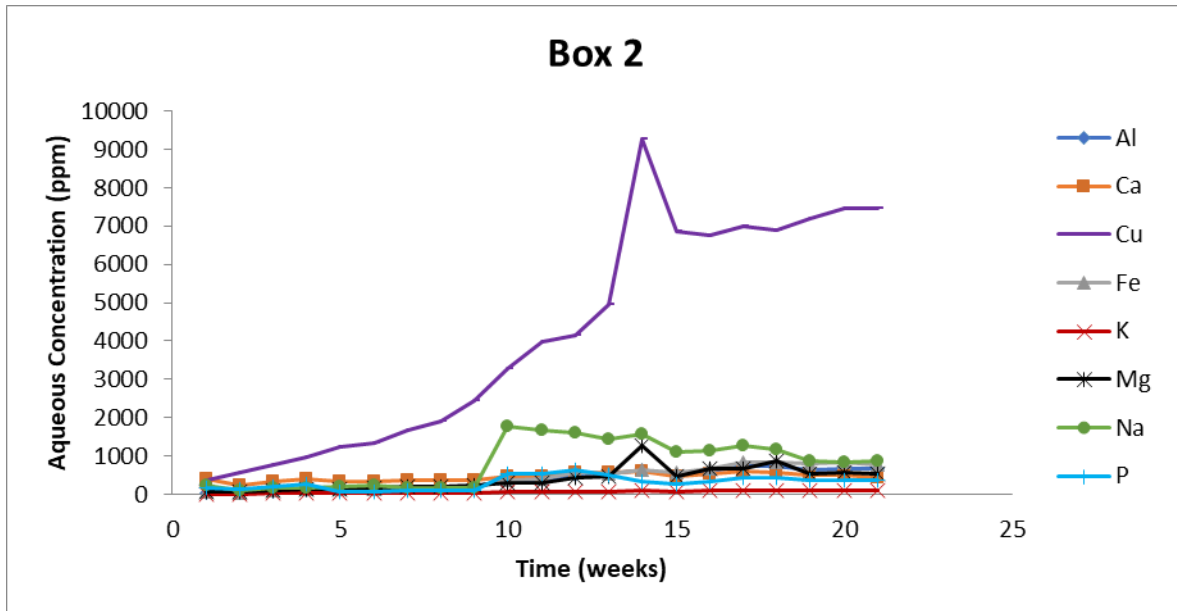
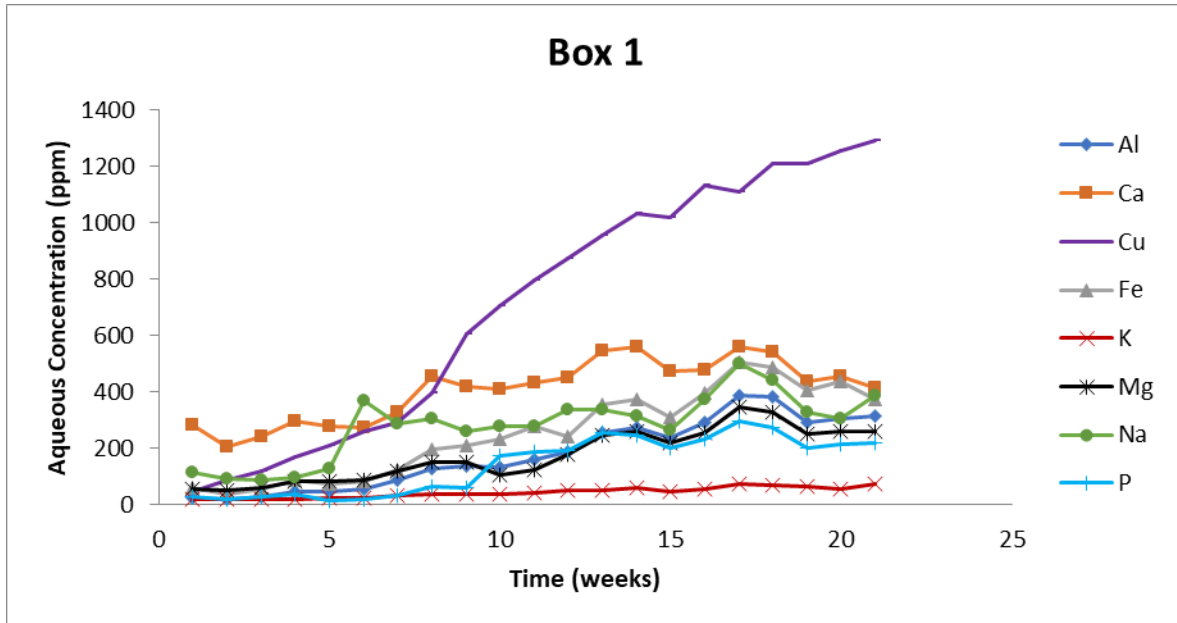
APPENDIX B – GROUND ORE LEACHING TEST RESULTS

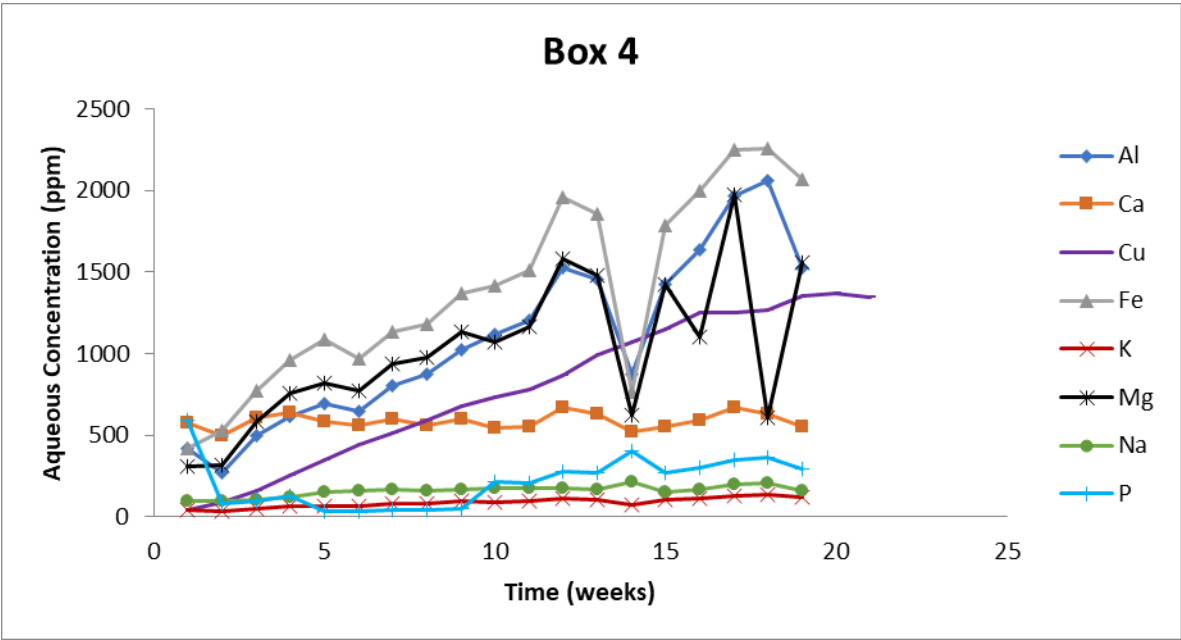
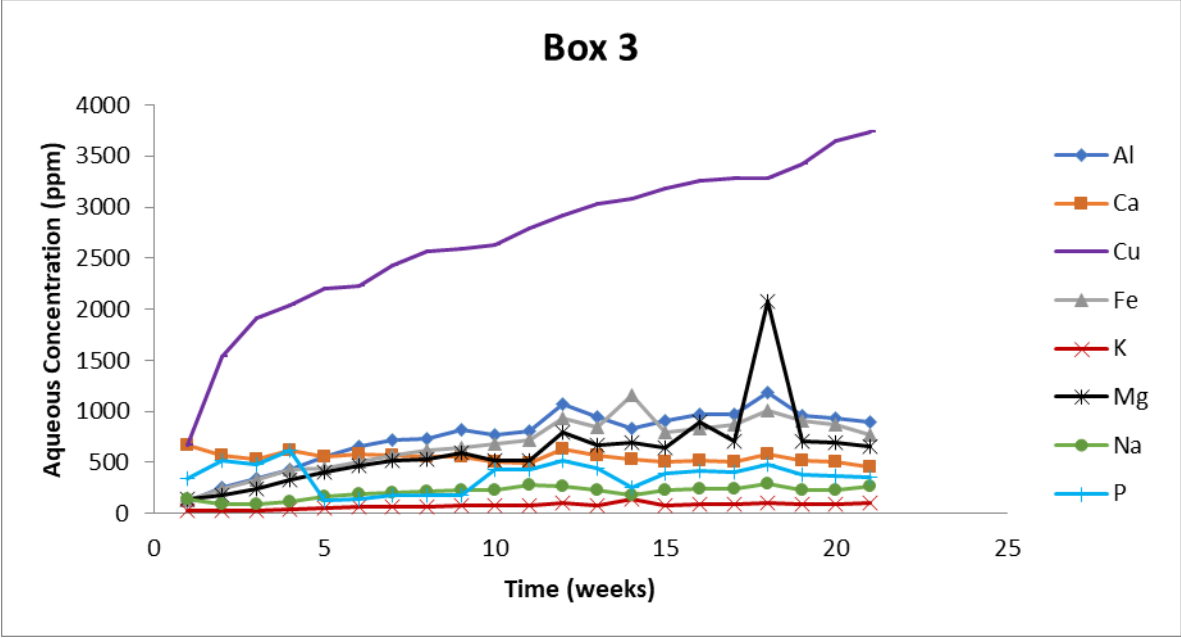


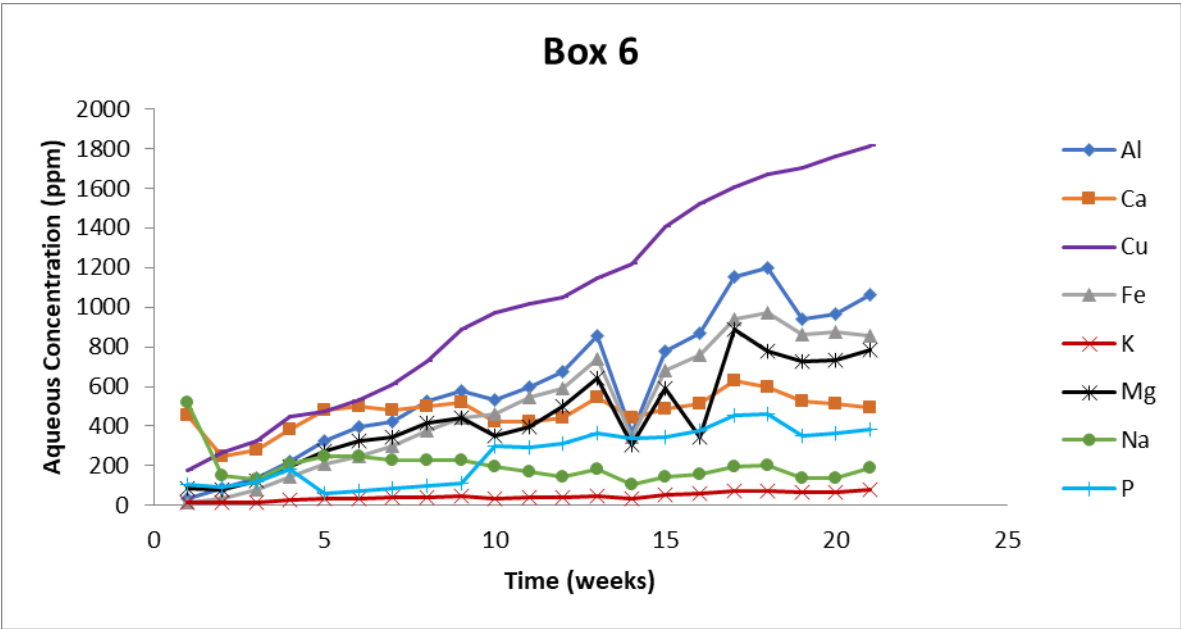
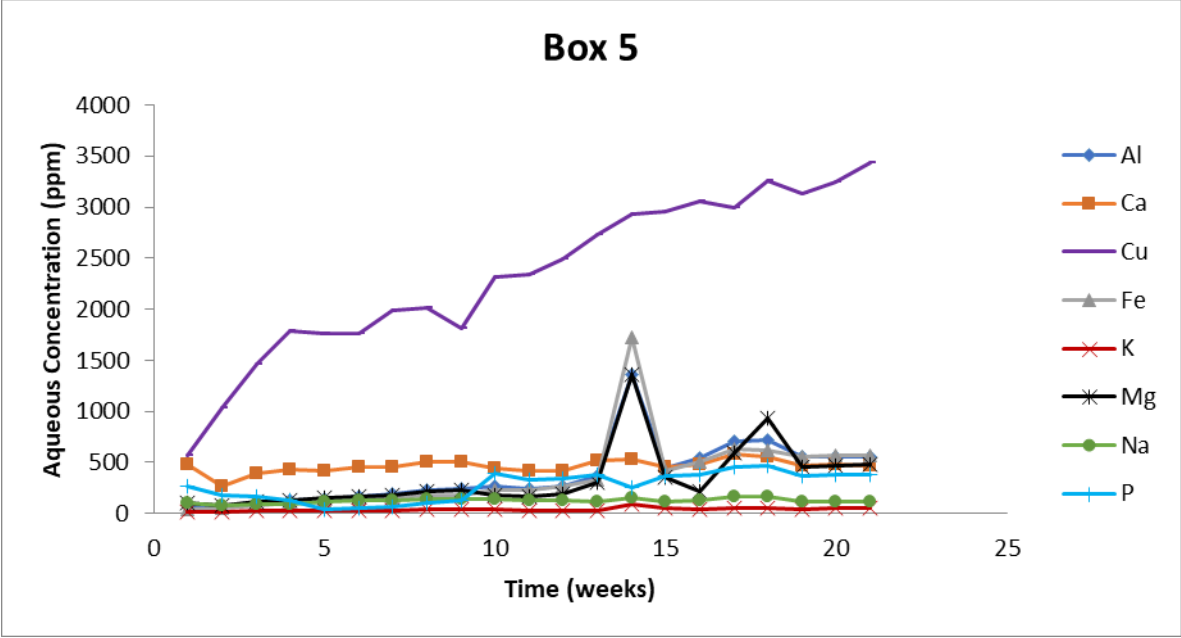


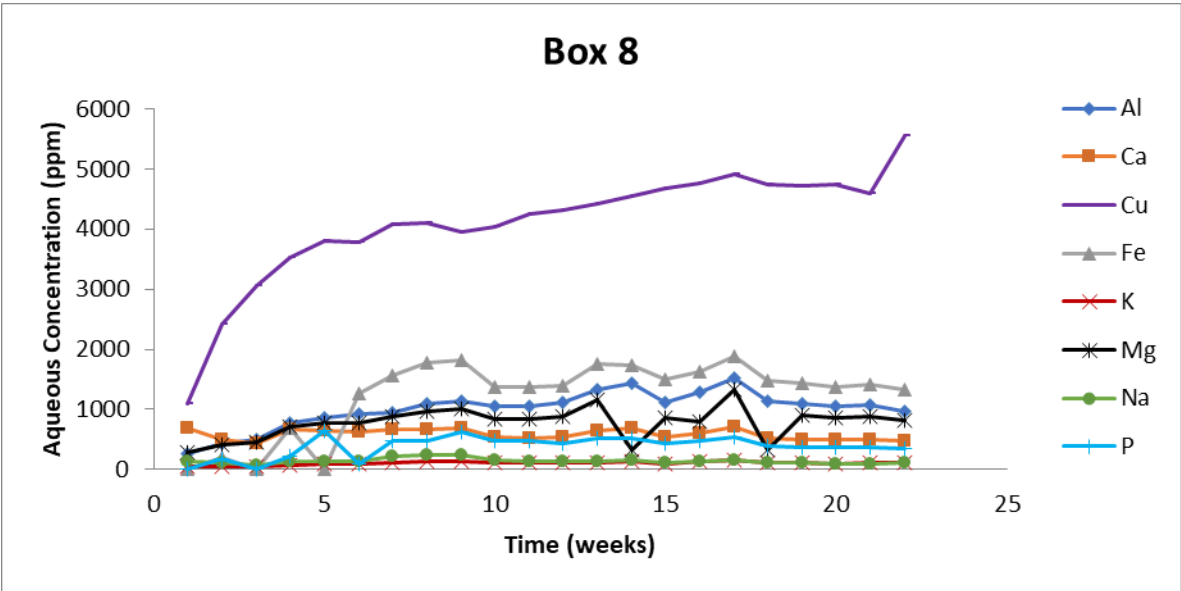
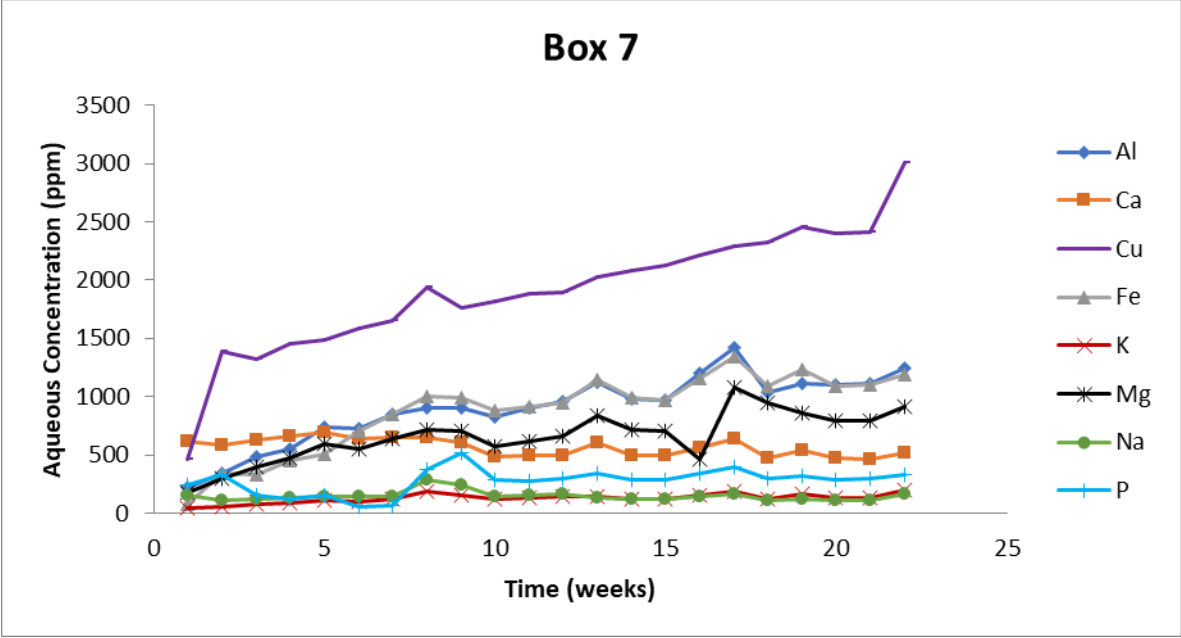
APPENDIX C – BOX LEACHING TEST RESULTS

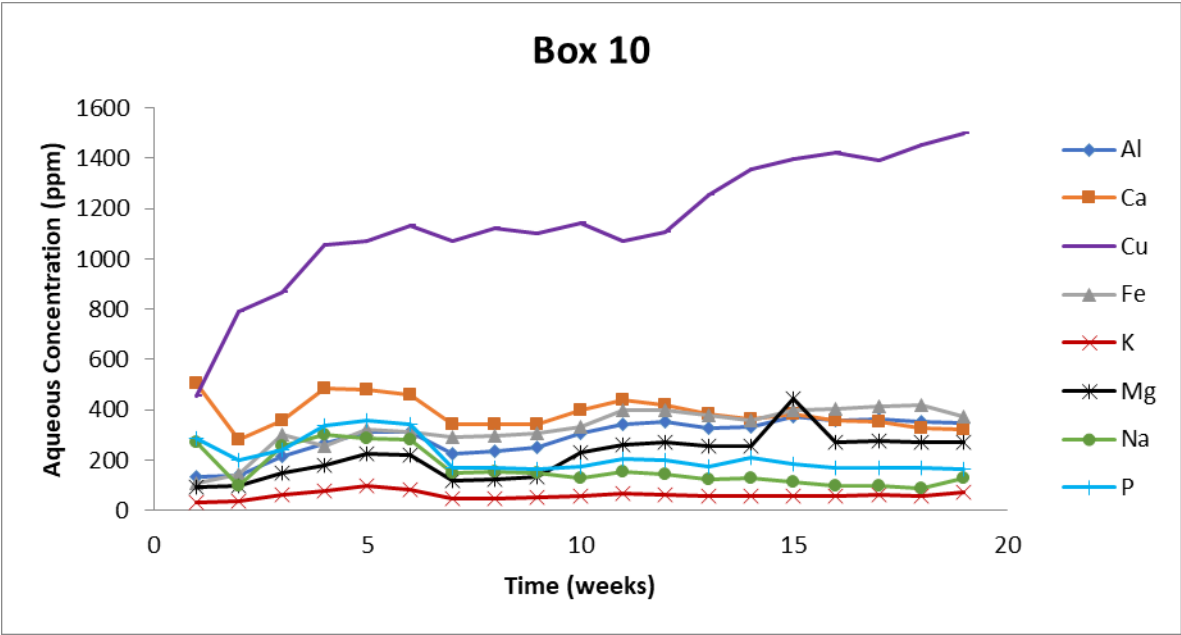
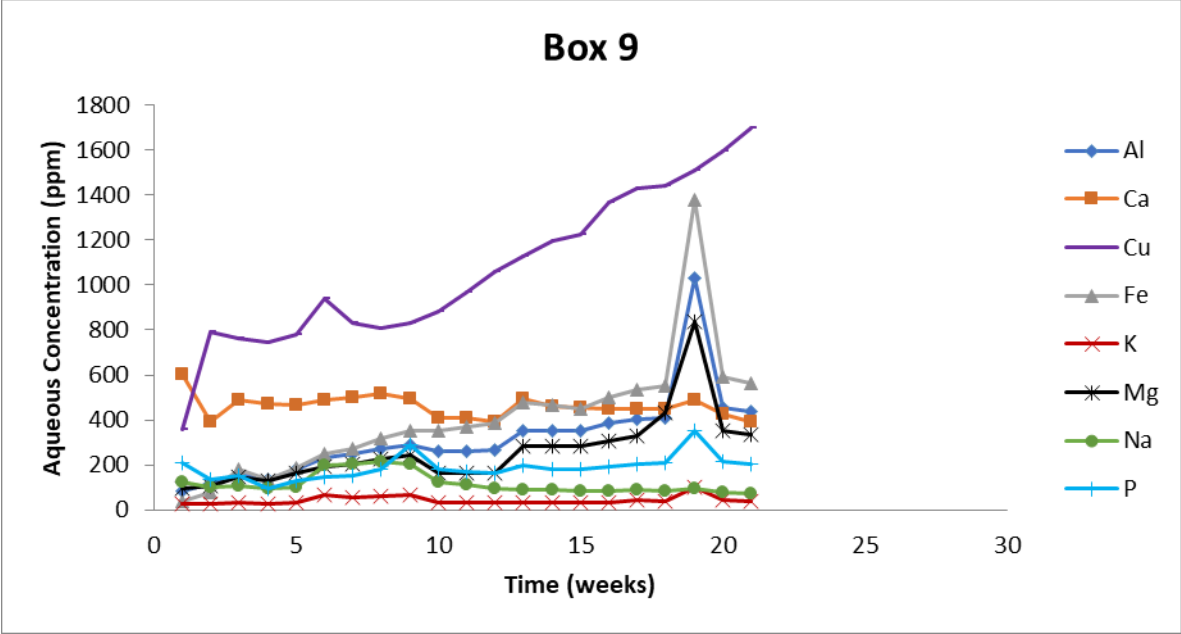
Concentrations of aqueous elements from the box leaching tests are shown below. Some data is missing. It should be noted that the equivalent copper concentrations are calculated (copper was removed each week in solvent extraction if the 1.8 g/L target was reached).

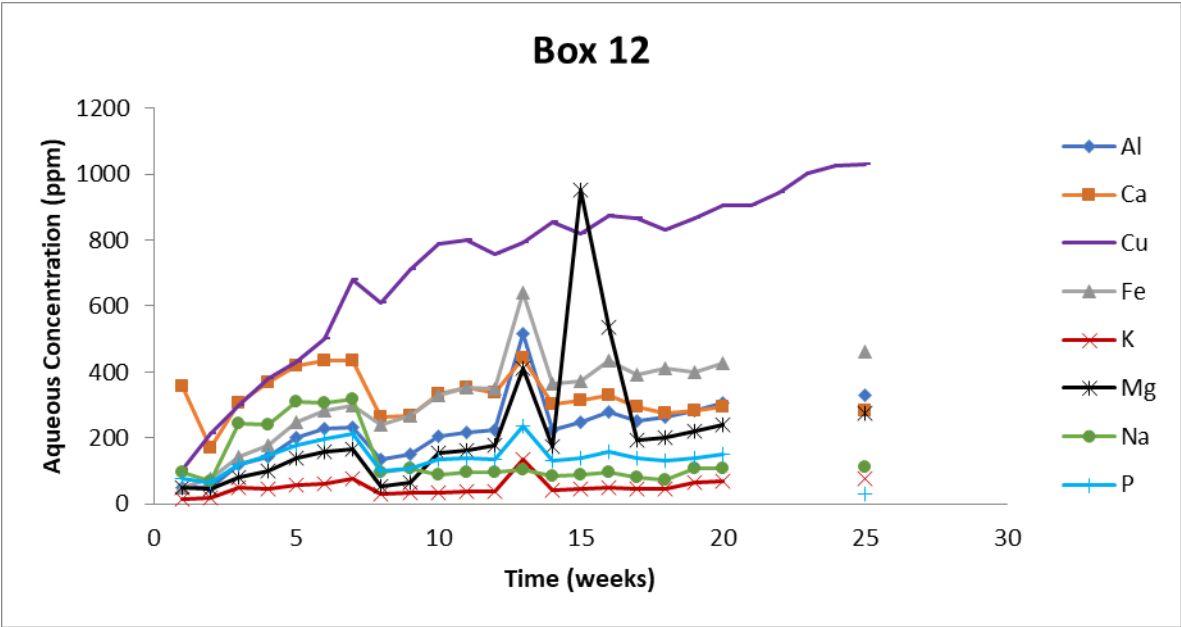
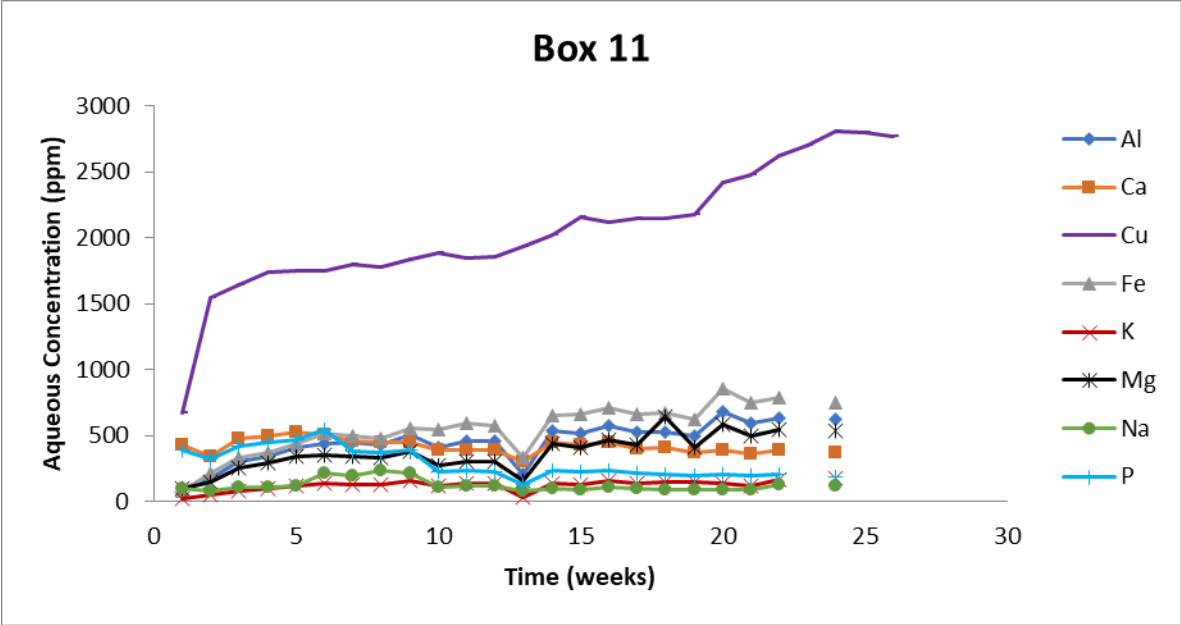


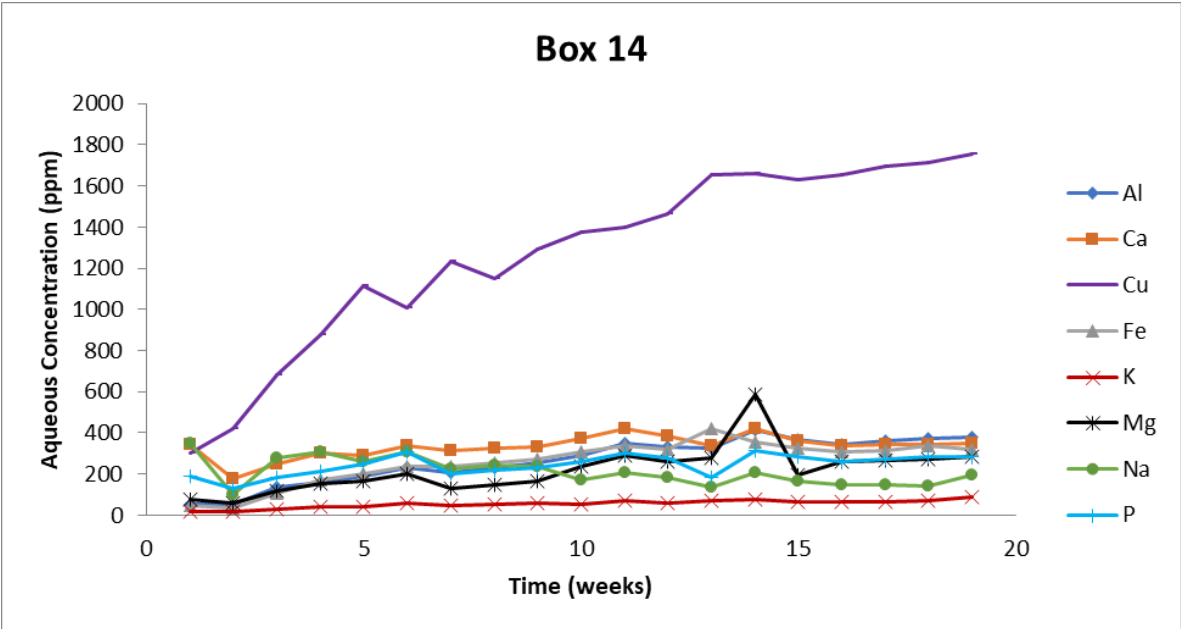
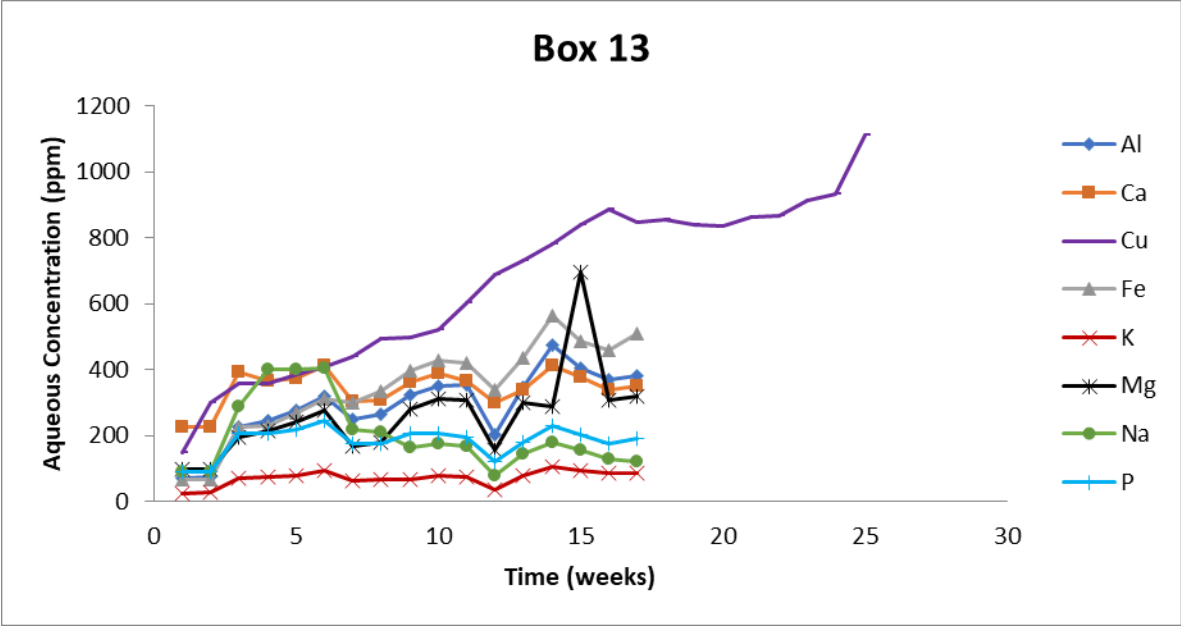


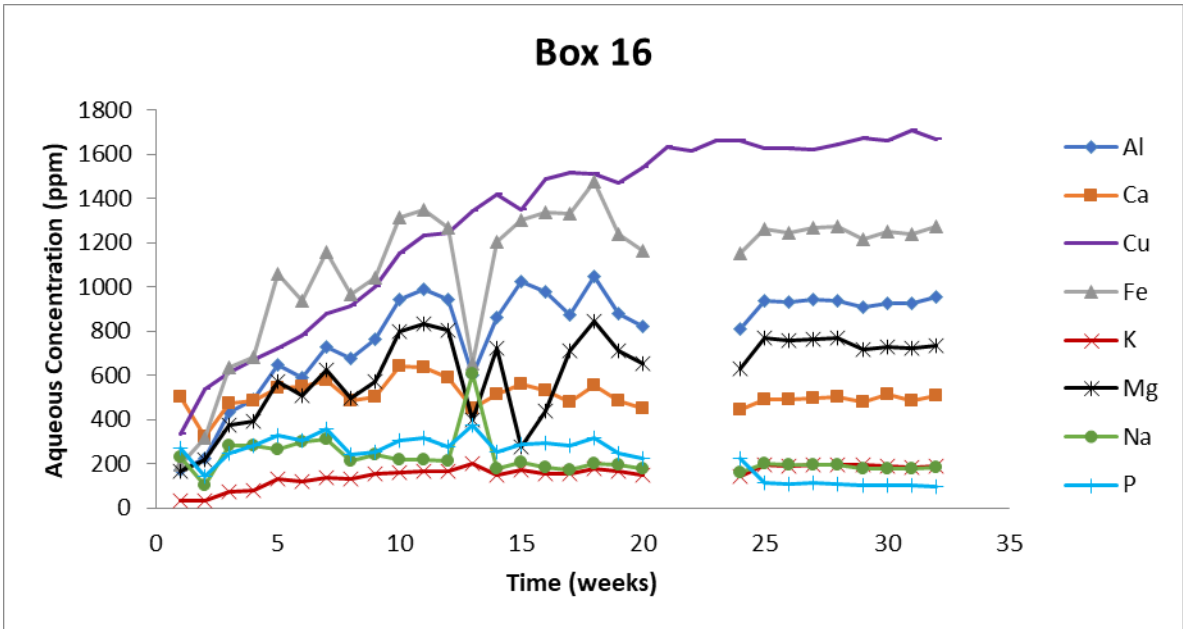
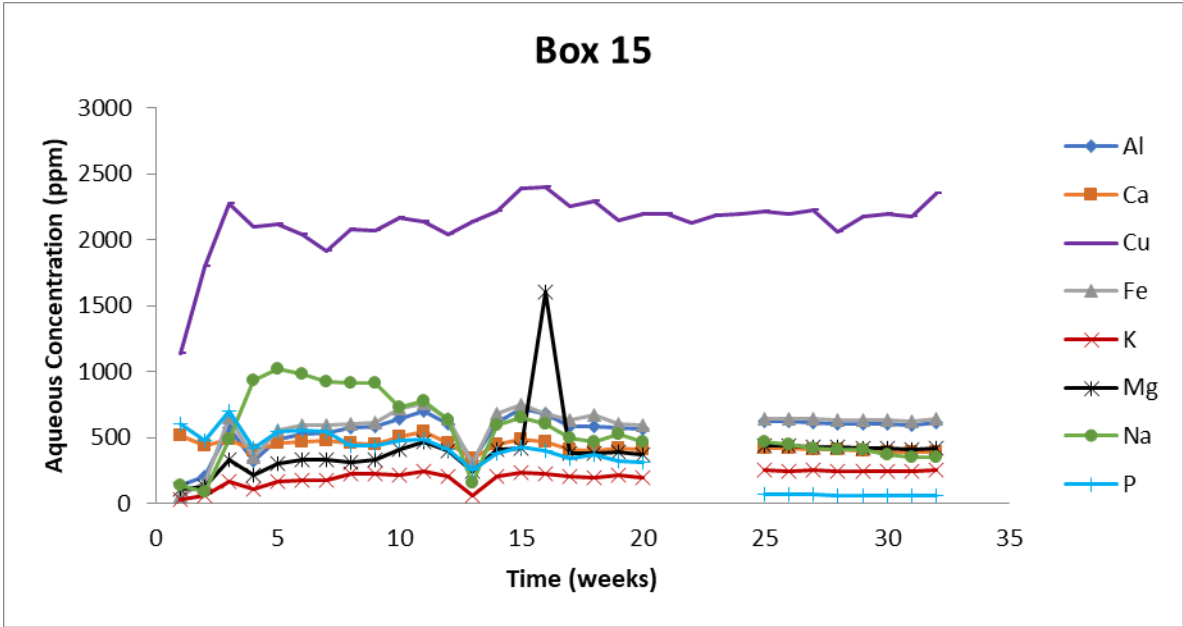












REFERENCES

- Ahlness, J. K., & Pojar, M. G. (1983). In situ copper leaching in the United States: case histories of operations. Avondale, MD: United States Bureau of Mines.
- Amrich Minerals. (2013). Santa Cruz Project. Retrieved July 2, 2015, from <http://www.studiocreek.com/~amrich/wp-content/uploads/2013/10/Amrich-Minerals-Santa-Cruz-Project.pptx>
- Andersen, W. C., Sievers, R. E., Lagalante, A. F., & Bruno, T. J. (2001). Solubilities of Cerium (IV), Terbium (III), and Iron (III) Beta Diketonates in Supercritical Carbon Dioxide. *Journal of Chemical Engineering Data*, 46, 1045–1049.
- Ashraf-Khorassani, M., Combs, M. T., & Taylor, L. T. (1997). Solubility of metal chelates and their extraction from an aqueous environment via supercritical CO₂. *Talanta*, 44(5), 755–763. [http://doi.org/10.1016/S0039-9140\(96\)02075-9](http://doi.org/10.1016/S0039-9140(96)02075-9)
- ASTM E161-12. (2012). Standard Specification for Precision Electroformed Sieves. West Conshohocken, PA: ASTM International. <http://doi.org/10.1520/E0161-12>
- Axen, S. (2014). Personal Communication.
- Baek, D. L., Fox, R. V., Case, M. E., Sinclair, L. K., Schmidt, A. B., McIlwain, P. R., ... Wai, C. M. (2016). Extraction of Rare Earth Oxides Using Supercritical Carbon Dioxide Modified with Tri-*n*-Butyl Phosphate–Nitric Acid Adducts. *Industrial & Engineering Chemistry Research*, 55(26), 7154–7163. <http://doi.org/10.1021/acs.iecr.6b00554>
- Bamberger, A., Sieder, G., & Maurer, G. (2000). High-pressure (vapor+liquid) equilibrium in binary mixtures of (carbon dioxide+water or acetic acid) at temperatures from 313 to 353 K. *The Journal of Supercritical Fluids*, 17(2), 97–110. [http://doi.org/10.1016/S0896-8446\(99\)00054-6](http://doi.org/10.1016/S0896-8446(99)00054-6)
- Bantis, L. (2012). Normfitc. Retrieved September 21, 2017, from <https://www.mathworks.com/matlabcentral/fileexchange/38226-fit-distributions-to-censored-data?focused=5247621&tab=function>
- Barbosa, T. S. (2016). *Spatial Models for Censored Data: Estimation and Diagnostics*. Universidade

Estadual de Campinas.

- Bartlett, R. W. (1973). A combined pore diffusion and chalcopyrite dissolution kinetics model for in situ leaching of a fragmented copper porphyry. In D. J. I. Evans & R. S. Shoemaker (Eds.), *International Symposium on Hydrometallurgy* (pp. 331–373). New York, NY: AIME.
- Bartlett, R. W. (1998). *Solution Mining: Leaching and Fluid Recovery of Materials* (Kindle). Routledge. Retrieved from <https://books.google.com/books?id=Na2ffdf1NL8C>
- Bauer, D. J., & Shaw, V. E. (1964). *Metathesis of bastnasite and solvent extraction of cerium*. Washington, D.C. Retrieved from <https://hdl.handle.net/2027/mdp.39015077557083>
- Beane, R., & Ramey, D. (1995). In-situ leaching at the San Manuel porphyry copper deposit, Arizona, USA. In W. C. Cooper, D. B. Dreisinger, J. E. Dutrizsac, H. Hein, & G. Ugane (Eds.), *Copper 95-Cobre 95 International Conference Volume III: Electrowinning and Hydrometallurgy of Copper* (pp. 363–375). Santiago, Chile: Canadian Institute of Mining, Metallurgy and Petroleum.
- Beaudoin, A., & De Dreuzy, J. R. (2013). Numerical assessment of 3-D macrodispersion in heterogeneous porous media. *Water Resources Research*, 49(5), 2489–2496. <http://doi.org/10.1002/wrcr.20206>
- Becker, M. W., & Shapiro, A. M. (2003). Interpreting tracer breakthrough tailing from different forced-gradient tracer experiment configurations in fractured bedrock. *Water Resources Research*, 39(1), n/a-n/a. <http://doi.org/10.1029/2001WR001190>
- Berkowitz, B., Cortis, A., Dentz, M., & Scher, H. (2006). Modeling non-Fickian transport in geological formations as a continuous time random walk. *Time*, (2005), 1–49. <http://doi.org/10.1029/2005RG000178.1>.INTRODUCTION
- Bernal, R. L., & Venero, O. D. (1985). Origin and treatment of underground waters from Cero de Pasco Mine, Peru. In R. Fernández-Rubio (Ed.), *2nd International Mine Water Congress* (pp. 27–40). Granada, Spain: International Mine Water Association.
- Bethke, C. M. (1996). *Geochemical Reaction Modeling: Concepts and Applications*. Oxford University Press. Retrieved from <https://books.google.ca/books?id=QfOIj7yfC0UC>
- Beudaert, P., Lamare, V., Dozol, J.-F., Troxler, L., & Wipff, G. (1999). Molecular dynamics simulations

- on europium nitrate complexes with neutral organophosphorus ligands. What governs the stoichiometry and extractability of the complex? *Journal of the Chemical Society, Perkin Transactions 2*, (11), 2515–2523. <http://doi.org/10.1039/a905063i>
- Bhappu, R. B. (1985). In situ mining and extraction. In G. V. Jergensen & J. F. Spisak (Eds.), *Frontier Technology in Mineral Processing* (pp. 123–132). New York, NY: Society of Mining Engineers of the American Institute of Mining, Metallurgical, and Petroleum Engineers.
- BHP Copper Growth and Technology Group. (1997a). Florence Project Final Pre-Feasibility Report Volume IV Hydrologic and Metallurgic Evaluations. Retrieved from <https://portal.azoah.com/oedf/documents/12-005-WQAB/SWVP-0064-1997-12-BHP-Florence-Project-Final-Pre-Feasibility-Rpt-Vol-IV.pdf>
- BHP Copper Growth and Technology Group. (1997b). *Florence Project Final Pre-Feasibility Report Volume II Geology*. Retrieved from <https://portal.azoah.com/oedf/documents/12-005-WQAB/SWVP-0062-1997-12-BHP-Florence-Project-Final-Pre-Feasibility-Rpt-Vol-II.pdf>
- Binnemans, K., & Jones, P. T. (2014). Perspectives for the recovery of rare earths from end-of-life fluorescent lamps. *Journal of Rare Earths*, 32(3), 195–200. [http://doi.org/10.1016/S1002-0721\(14\)60051-X](http://doi.org/10.1016/S1002-0721(14)60051-X)
- Bohling, G. C., Liu, G., Knobbe, S. J., Reboulet, E. C., Hyndman, D. W., Dietrich, P., & Butler, J. J. (2012). Geostatistical analysis of centimeter-scale hydraulic conductivity variations at the MADE site. *Water Resources Research*, 48(2), 1–16. <http://doi.org/10.1029/2011WR010791>
- Braatz, A. D., Antonio, M. R., & Nilsson, M. (2017). Structural study of complexes formed by acidic and neutral organophosphorus reagents. *Dalton Trans.*, 46(4), 1194–1206. <http://doi.org/10.1039/C6DT04305D>
- Brantley, S. L., Kubicki, J. D., & White, A. F. (2008). *Kinetics of Water-Rock Interaction*. New York, NY: Springer-Verlag. <http://doi.org/10.1007/978-0-387-73563-4>
- Brewer, M. D. (1998). *Column leaching experiments and mass balance modeling simulating in situ leaching within the oxide zone of the Florence porphyry copper deposit, Pinal County, Arizona*.

University of Arizona.

- Catanach, C. B. (1976). Development of in place leaching of Mountain City chalcocite ore body. In J. C. Yannopoulos & J. C. Agarwal (Eds.), *Extractive Metallurgy of Copper, Volume II* (pp. 849–872). New York, NY: American Institute of Mining.
- Cathles, L. M. (2014). Personal Communication.
- Cathles, L. M., Glenn, W. E., Lenzi, G. W., Nigrini, A., Deans, W. S., & Huff, R. V. (1978). *Fluid flow in naturally fractured igneous rocks: a case history*. Lexington, MA: Legemont Laboratory, Kennecott Copper Corporation.
- Charalampides, G., Vatalis, K. I., Apostoplos, B., & Ploutarch-Nikolas, B. (2015). Rare Earth Elements: Industrial Applications and Economic Dependency of Europe. *Procedia Economics and Finance*, 24(15), 126–135. [http://doi.org/10.1016/S2212-5671\(15\)00630-9](http://doi.org/10.1016/S2212-5671(15)00630-9)
- Chatterjee, S., Campbell, E. L., Neiner, D., Pence, N. K., Robinson, T. A., & Levitskaia, T. G. (2015). Aqueous Binary Lanthanide(III) Nitrate $\text{Ln}(\text{NO}_3)_3$ Electrolytes Revisited: Extended Pitzer and Bromley Treatments. *Journal of Chemical and Engineering Data*, 60(10), 2974–2988. <http://doi.org/10.1021/acs.jced.5b00392>
- Chrastil, J. (1982). Solubility of solids and liquids in supercritical gases. *Journal of Physical Chemistry*, 86(15), 3016–3021. <http://doi.org/10.1021/j100212a041>
- Classen, M., Althaus, H.-J., Blaser, S., Scharnhorst, W., Tuchschnid, M., Jungbluth, N., & Emmenegger, M. F. (2007). *Life Cycle Inventories of Metals*. Dübendorf, Switzerland: Ecoinvent.
- Committee on Technologies for the Mining Industry, Committee on Earth Resources, & National Research Council. (2002). *Evolutionary and Revolutionary Technologies for Mining*. Washington, D.C.: National Academy Press. Retrieved from <http://www.nap.edu/catalog/10318.html>
- Constantine, P., & Wang, Q. (2012). Random Field Simulation. Retrieved from <https://www.mathworks.com/matlabcentral/fileexchange/27613-random-field-simulation>
- Cotton, S. (2006). *Lanthanide and Actinide Chemistry*. Rutland, UK: John Wiley & Sons, Inc.
- Cowart, J. B., Rudy, R., & Milne, J. J. (2004). Remediation of 25 million gallons of acidic groundwater,

- Nacimiento Copper Mine site, Cuba, New Mexico. In *Tailings and Mine Waste '04* (pp. 167–172). London, UK: Taylor & Francis. <http://doi.org/10.1201/9780203021637.ch20>
- D'Andrea, D. V., Larson, W. C., Fletcher, L. R., Chamberlain, P. G., & Engelmann, W. H. (1977). *In situ leaching research in a copper deposit at the Emerald Isle mine*. Washington, D.C.: United States Bureau of Mines.
- Dahl, L. J. (1989). Methods for determining the geologic structure of an ore body as it relates to in situ mining. In *In situ leach mining: proceedings: Bureau of Mines technology transfer seminars* (pp. 37–48). Phoenix, AZ, and Salt Lake City, UT: United States Bureau of Mines.
- Dahl, L. J. (1994). Joint system characterization for in situ mining. In S. A. Swan & K. R. Coyne (Eds.), *In Situ Recovery of Minerals II* (pp. 323–350). New York, NY: Engineering Foundation.
- Davis, J., & Curtis, G. (2007). *Consideration of geochemical issues in groundwater restoration at uranium in-situ leach mining facilities. Division of Fuel, Engineering, and Radiological Research, Office of Nuclear Regulatory Research*. Washington, D.C.: United States Nuclear Regulatory Commission.
- Davis, J. R. (1997). *The fracture controlled mineralogy within the oxide zone of the Florence porphyry copper deposit, Pinal County, Arizona*. University of Arizona.
- Davis, M. W. (1987). Production of conditional simulations via the LU triangular decomposition of the covariance matrix. *Mathematical Geology*, *19*(2), 91–98. <http://doi.org/10.1007/BF00898189>
- Dehghani, F., Wells, T., Cotton, N. J., & Foster, N. R. (1996). Extraction and Separation of Lanthanides Using Dense Gas CO₂ Modified with Tributyl Phosphate and di (2-Ethylhexyl) Phosphoric Acid. *The Journal of Supercritical Fluids*, *9*, 263–272.
- Dixon, D. (2011). *Metallurgical Testing Summary Report - Florence In Situ Leaching*. Delta, British Columbia.
- Dogan, M., Van Dam, R. L., Liu, G., Meerschaert, M. M., Butler, J. J., Bohling, G. C., ... Hyndman, D. W. (2014). Predicting flow and transport in highly heterogeneous alluvial aquifers. *Geophysical Research Letters*, *41*(21), 7560–7565. <http://doi.org/10.1002/2014GL061800>
- Doughty, C., & Tsang, C. F. (2005). Signatures in flowing fluid electric conductivity logs. *Journal of*

Hydrology, 310(1–4), 157–180. <http://doi.org/10.1016/j.jhydrol.2004.12.003>

Duvail, M., & Guilbaud, P. (2011). Understanding the nitrate coordination to Eu³⁺ ions in solution by potential of mean force calculations. *Physical Chemistry Chemical Physics*, 13(13), 5840. <http://doi.org/10.1039/c0cp02535f>

Earley, D. (2014). Personal Communication.

Earley, D., & Johnson, D. (2012). Geochemical computer modelling of in situ copper recovery and groundwater restoration. In F. Valenzuela & J. Wiertz (Eds.), *3rd International Congress on Water Management in the Mining Industry*. Santiago, Chile: Center for Water in the Minerals Industry, Gecamin.

Earley, D., & Jones, P. M. (1992). Geochemical effects on the hydrology of in situ leach mining of copper oxide ore at the Cyprus Casa Grande mine, Arizona. In *Society for Mining Metallurgy and Exploration Annual Meeting Preprint*. Phoenix, AZ: Society for Mining Metallurgy and Exploration.

Ellenberger, J. L., & Jones, P. M. (1994). Rock quality alteration surrounding drifts and an in situ leaching design using underground workings. In *Society for Mining Metallurgy and Exploration Annual Meeting Preprint*. Albuquerque, NM: Society for Mining Metallurgy and Exploration.

Englert, A., Vanderborght, J., & Vereecken, H. (2006). Prediction of velocity statistics in three-dimensional multi-Gaussian hydraulic conductivity fields. *Water Resources Research*, 42(3), 1–15. <http://doi.org/10.1029/2005WR004014>

Enokida, Y., Tomioka, O., Lee, S., Rustenholtz, A., & Wai, C. M. (2003). Characterization of a Tri- n - butyl Phosphate - Nitric Acid Complex : a CO₂ -Soluble Extractant for Dissolution of Uranium Dioxide. *Industrial & Engineering Chemistry Research*, 42, 5037–5041.

Fiori, A., Dagan, G., Jankovic, I., & Zarlenga, A. (2013). The plume spreading in the MADE transport experiment: Could it be predicted by stochastic models? *Water Resources Research*, 49(5), 2497–2507. <http://doi.org/10.1002/wrcr.20128>

Fox, R. V. (2003). *Complexation reactions of lanthanides in supercritical fluid carbon dioxide*. University of Idaho.

- Fox, R. V., Ball, R. D., Harrington, P. D. B., Rollins, H. W., Jolley, J. J., & Wai, C. M. (2004). Praseodymium nitrate and neodymium nitrate complexation with organophosphorus reagents in supercritical carbon dioxide solvent. *Journal of Supercritical Fluids*, 31(3), 273–286. <http://doi.org/10.1016/j.supflu.2003.11.006>
- Fox, R. V., Ball, R. D., Harrington, P. D. B., Rollins, H. W., & Wai, C. M. (2005). Holmium nitrate complexation with tri-n-butyl phosphate in supercritical carbon dioxide. *Journal of Supercritical Fluids*, 36(2), 137–144. <http://doi.org/10.1016/j.supflu.2005.05.003>
- Friedel, M. J. (1991). *Modeling in situ copper leaching in an unsaturated setting*. Washington, D.C.: United States Bureau of Mines.
- Friedel, M. J. (1993). Scale-dependence and the hydrologic design of in situ copper leaching operations. *Society for Mining Metallurgy and Exploration Transactions*, 294, 1918–1926.
- Gelhar, L. W., & Axness, C. L. (1983). Three-Dimensional Stochastic Analysis of Macrodispersion in Aquifers. *Water Resources Research*, 19(1), 161–180. <http://doi.org/10.1029/WR019i001p00161>
- Ginn, T. R. (2001). Stochastic-convective transport with nonlinear reactions and mixing: Finite streamtube ensemble formulation for multicomponent reaction systems with intra-streamtube dispersion. *Journal of Contaminant Hydrology*, 47(1), 1–28. [http://doi.org/10.1016/S0169-7722\(00\)00167-4](http://doi.org/10.1016/S0169-7722(00)00167-4)
- Goovaerts, P. (2009). AUTO-IK: A 2D indicator kriging program for the automated non-parametric modeling of local uncertainty in earth sciences. *Computers and Geosciences*, 35(6), 1255–1270. <http://doi.org/10.1016/j.cageo.2008.08.014>
- Hackman, D. B. (1982). *The evaluation of supergene copper deposits for in situ leaching*. University of Arizona.
- Haque, N., Hughes, A., Lim, S., & Vernon, C. (2014). Rare Earth Elements: Overview of Mining, Mineralogy, Uses, Sustainability and Environmental Impact. *Resources*, 3, 614–635. <http://doi.org/10.3390/resources3040614>
- Hardy, C. J., Fairhurst, D., McKay, H. A. C., & Willson, A. M. (1964). Extraction of water by tri-n-butyl phosphate. *Transactions of the Faraday Society*, 60, 1626–1636. <http://doi.org/10.1039/tf9646001626>

- He, M., Dong, L., & Li, B. (2011). Interactions in aqueous 3-1 rare earth electrolyte quaternary systems and their ternary subsystems to very high concentrations. *Journal of Chemical and Engineering Data*, 56(11), 4068–4075. <http://doi.org/10.1021/jc200497g>
- Hiskey, J. B. (1994). In-situ leaching recovery of copper: what's next? In *Hydrometallurgy '94 SE - 4* (pp. 43–67). Springer Netherlands. http://doi.org/10.1007/978-94-011-1214-7_4
- Hohn, M. E. (1999). *Geostatistics and Petroleum Geology* (2nd ed.). Dordrecht, Netherlands: Springer Science and Business Media, B.V.
- Huff, R. V., Axen, S. G., & Baughman, D. R. (1988). Case history: Van Dyke ISL copper project. In *Society of Mining Engineers Annual Meeting Preprint*. Phoenix, AZ: Society of Mining Engineers of the American Institute of Mining, Metallurgical, and Petroleum Engineers.
- Huss, C., Welhener, H., Drielick, T., Roman, R., & Lenton, P. (2014). *Gunnison Copper Project Technical Report Prefeasibility Study*. Tucson, AZ.
- Hwang, D., Tsukahara, T., Miyamoto, N., & Ikeda, Y. (2016). Spectrophotometric studies on solubility of lanthanoid(III) complexes with fluorinated β -diketonates in supercritical carbon dioxide. *Journal of Supercritical Fluids*, 110, 251–256. <http://doi.org/10.1016/j.supflu.2015.12.002>
- Johnson, D. (2017). *NI 43-101 Technical Report Florence Copper Project*. Vancouver,.
- Kang, P., Borgne, T. Le, Dentz, M., Bour, O., Juanes, R., Kang, P., ... Juanes, R. (2015). Impact of velocity correlation and distribution on transport in fractured media: Field evidence and theoretical model. *Water Resources Research RESEARCH*, 940–959. <http://doi.org/10.1002/2014WR015799>. Received
- Koegler, S. (2010). Development of a Unique Process for Recovery of Uranium from Incinerator Ash. In *ACS Symposium Series* (pp. 65–78). American Chemical Society. <http://doi.org/10.1021/bk-2010-1046.ch006>
- Kreis, H. G. (1994). Overview of the Santa Cruz in situ copper mining research project, Pinal county, Arizona. In S. A. Swan & K. R. Coyne (Eds.), *In Situ Recovery of Minerals II* (pp. 123–144). New York, NY: Engineering Foundation.
- Krishnamurthy, N., & Gupta, C. K. (2004). *Extractive Metallurgy of Rare Earths*. CRC Press. Retrieved

from https://books.google.com/books?id=F0Bte_XhzoAC

- Kroll, C. N., & Stedinger, J. R. (1996). Estimation of Moments and Quantiles using Censored Data. *Water Resources Research*, 32(4), 1005–1012. <http://doi.org/10.1029/95WR03294>
- Kul, M., Topkaya, Y., & Karakaya, I. (2008). Rare earth double sulfates from pre-concentrated bastnasite. *Hydrometallurgy*, 93(3–4), 129–135. <http://doi.org/10.1016/j.hydromet.2007.11.008>
- Lagalante, A. F., Hansen, B. N., Bruno, T. J., & Sievers, R. E. (1995). Solubilities of Copper (II) and Chromium (III) Beta-Diketonates in Supercritical Carbon Dioxide. *Inorg. Chem.*, 34, 5781–5785.
- Laintz, K. E., & Tachikawa, E. (1994). Extraction of lanthanides from acidic solution using tributyl phosphate modified supercritical carbon dioxide. *Analytical Chemistry*, 66(13), 2190–2193. Retrieved from <http://pubs.acs.org/doi/abs/10.1021/ac00085a040>
- Laintz, K. E., Wai, C. M., Yonker, C. R., & Smith, R. D. (1991). Solubility of fluorinated metal diethyldithiocarbamates in supercritical carbon dioxide. *The Journal of Supercritical ...*, 4(3), 194–198. [http://doi.org/10.1016/0896-8446\(91\)90008-T](http://doi.org/10.1016/0896-8446(91)90008-T)
- Lantz, R. B., & Statham, W. (1994). Modeling fluid movement at the Santa Cruz project. In S. A. Swan & K. R. Coyne (Eds.), *In Situ Recovery of Minerals II* (pp. 539–590). New York, NY: Engineering Foundation.
- Le Borgne, T., & Gouze, P. (2008). Non-Fickian dispersion in porous media: 2. Model validation from measurements at different scales. *Water Resources Research*, 44(6). <http://doi.org/10.1029/2007WR006279>
- Leaist, D. G. (1984). Diffusion in aqueous solutions of sulfuric acid. *Canadian Journal of Chemistry*, 62(9), 1692–1697. <http://doi.org/10.1139/v84-290>
- Lewis, M. F., Chase, C. K., & Bhappu, R. B. (1976). Economic evaluation of in situ extraction for copper, gold, and uranium. In A. Weiss & N. Kōgyōkai (Eds.), *Proceedings of the joint MMIJ-AIME meeting* (pp. 333–348). New York, NY: American Institute of Mining, Metallurgical, and Petroleum Engineers.
- Lin, Y., Smart, N. G., & Wai, C. M. (1995). Supercritical fluid extraction of uranium and thorium from

- nitric acid solutions with organophosphorus reagents. *Environmental Science and Technology*, 29(10), 2706–2708. <http://doi.org/10.1021/es00010a036>
- Lin, Y., & Wal, C. M. (1994). Supercritical fluid extraction of lanthanides with fluorinated β -diketones and tributyl phosphate. *Analytical Chemistry*, 66(13), 1971–1975. <http://doi.org/10.1021/ac00085a008>
- Liu, J., & Brady, B. H. (1998). Evaluation of velocity-dependent in situ leaching processes: Single-porosity model. *Metallurgical and Materials Transactions B*, 29(6), 1227–1234. <http://doi.org/10.1007/s11663-998-0045-7>
- Liu, S., Chai, J., & Yang, X. (2009). Beta-Diketones at Water/Supercritical CO₂ Interface: A Molecular Dynamics Simulation. *Chinese Journal of Chemical Engineering*, 17(6), 990–998. [http://doi.org/10.1016/S1004-9541\(08\)60307-9](http://doi.org/10.1016/S1004-9541(08)60307-9)
- Lottermoser, B. G. (2003). *Mine Wastes: Characterization, Treatment and Environmental Impacts; with 45 Tables*. Heidelberg, Germany: Springer-Verlag. Retrieved from <https://books.google.com/books?id=Klc5GN2uDwoC>
- Meguro, Y., Iso, S., & Yoshida, Z. (1998). Correlation between Extraction Equilibrium of Uranium(VI) and Density of CO₂ Medium in a HNO₃/Supercritical CO₂-Tributyl Phosphate System. *Analytical Chemistry*, 70(7), 1262–7. <http://doi.org/10.1021/ac970818b>
- Miyamoto, N., Tsukahara, T., Kachi, Y., Harada, M., Kayaki, Y., Ikariya, T., & Ikeda, Y. (2012). Studies on solubility of uranyl complexes in supercritical carbon dioxide and its controlling factors using UV-visible and ¹⁷O- and ¹⁹F-NMR spectroscopy. *Journal of Nuclear Science and Technology*, 49(1), 37–46. <http://doi.org/10.1080/18811248.2011.636531>
- Mudd, G. M. (2001). Critical review of acid in situ leach uranium mining: 2. Soviet Block and Asia. *Environmental Geology*, 41(3–4), 404–416. <http://doi.org/10.1007/s002540100405>
- Mudd, G. M. (2001). Critical review of acidic in-situ leach uranium mining: 1 USA and Australia. *Environmental Geology*, 41(3–4), 390–403. <http://doi.org/10.1007/s002540100406>
- Murphy, W. M., Oelkers, E. H., & Lichtner, P. C. (1989). Surface reaction versus diffusion control of mineral dissolution and growth rates in geochemical processes. *Chemical Geology*, 78(3–4), 357–380.

[http://doi.org/10.1016/0009-2541\(89\)90069-7](http://doi.org/10.1016/0009-2541(89)90069-7)

National Institute of Standards & Technology. (2013). REFPROP. Boulder, CO. Retrieved from <https://www.nist.gov/srd/refprop>

Navon, S., Stavola, M., & Scaatst, M. G. (1981). on the Hydration of the Inner Sphere of Extraction System. *Journal of Inorganic Nuclear Chemistry*, 43, 575–578.

Nelson, P. H. (1991). Geophysical logs from a copper oxide deposit, Santa Cruz Project, Casa Grande, Arizona. Retrieved from <http://pubs.er.usgs.gov/publication/ofr91357>

Niemuth, N. J. (1994). *The primary copper industry of Arizona in 1992*. Phoenix, AZ: Arizona Department of Mines and Mineral Resources.

Norgate, T. E., Jahanshahi, S., & Rankin, W. J. (2007). Assessing the environmental impact of metal production processes. *Journal of Cleaner Production*, 15(8–9), 838–848. <http://doi.org/10.1016/j.jclepro.2006.06.018>

O’Gorman, G., Michaelis, H., & Olson, G. (2004). Novel in-situ metal and mineral extraction technology. Retrieved July 2, 2015, from [http://www.ironmountainmine.com/iron mountain/florence uic.pdf](http://www.ironmountainmine.com/iron%20mountain/florence%20uic.pdf)

O’Neil, T. (1991, August). In situ copper mining at Santa Cruz: A project update. *Mining Engineering*, Aug 1991, 1031–1034.

Pallauta, J. (1985). Lixiviacion in situ, Yacimiento Chuqui Sur, Codelco Chile, division Chuquicamata. In *Instituto de Ingenieros de Minas de Chile 36A Convencion*. Viña del Mar, Chile: Instituto del Ingenieros de Minas de Chile.

Parker, J., & Braun, T. (2004). Closure at the San Manuel mine site, Arizona, USA. In *Society for Mining Metallurgy and Exploration Annual Meeting Preprint*. Denver, CO: Society for Mining Metallurgy and Exploration.

Peppard, D. E., Driscoll, W. J., Sironen, R. J., & McCarty, S. (1957). Nonmonotonic ordering of lanthanides in tributyl phosphate-nitric acid extraction systems. *Journal of Inor*, 4, 326–333.

Phanikumar, M. S., Hyndman, D. W., Zhao, X., & Dybas, M. J. (2005). A three-dimensional model of microbial transport and biodegradation at the Schoolcraft, Michigan, site. *Water Resources Research*,

- 41(5), 1–17. <http://doi.org/10.1029/2004WR003376>
- Pitchaiah, K. C., Sivaraman, N., Lamba, N., & Madras, G. (2016). Experimental determination and model correlation for the solubilities of trialkyl phosphates in supercritical carbon dioxide. *RSC Adv.*, 6, 51286–51295. <http://doi.org/10.1039/C6RA10897K>
- Pitzer, K. S., Wang, P., Rard, J. A., & Clegg, S. L. (1999). Thermodynamics of Electrolytes. 13. Ionic Strength Dependence of Higher-Order Terms; Equations for CaCl₂ and MgCl₂. *Journal of Solution Chemistry*, 28(4), 265–282. <http://doi.org/10.1023/A:1022695525943>
- Prigogine, I., & Defay, R. (1954). *Chemical Thermodynamics*. Wiley. Retrieved from <https://books.google.com/books?id=8wsJAQAAIAAJ>
- Raghavan, S., & Fuerstenau, D. W. (1977). Characterization and pore structure analysis of a copper ore containing chrysocolla. *International Journal of Mineral Processing*, 4, 381–394. [http://doi.org/https://doi.org/10.1016/0301-7516\(77\)90015-1](http://doi.org/https://doi.org/10.1016/0301-7516(77)90015-1)
- Ramey, D., & Beane, R. (1995). In-situ project evaluation: Magma Copper's approach. In W. C. Cooper, D. B. Dreisinger, J. E. Dutrizsac, H. Hein, & G. Ugane (Eds.), *Copper 95-Cobre 95 International Conference Volume III: Electrorefining and Hydrometallurgy of Copper* (pp. 351–361). Santiago, Chile: Canadian Institute of Mining, Metallurgy and Petroleum.
- Rard, J. A., Miller, D. G., & Spedding, F. H. (1979). Isopiestic determination of the activity coefficients of some aqueous rare earth electrolyte solutions at 25 °C. 4. La(NO₃)₃, Pr(NO₃)₃, and Nd(NO₃)₃. *Journal of Chemical & Engineering Data*, 24(4), 348–354. <http://doi.org/10.1021/je60083a028>
- Rard, J. A., & Spedding, F. H. (1981). Isopiestic Determination of the Activity Coefficients of Some Aqueous Rare-Earth Electrolyte Solutions at 25 °C. 5. Dy(NO₃)₃, Ho(NO₃)₃, and Lu(NO₃)₃. *Journal of Chemical and Engineering Data*, 26(4), 391–395. <http://doi.org/10.1021/je00026a013>
- Rawlings, D. E., & Johnson, D. B. (2006). *Biomining*. Springer Berlin Heidelberg. Retrieved from <https://books.google.com/books?id=gnyIXJPG0HAC>
- Sainath, N. R. (1991). *Dynamic behavior of flow during leaching of copper ores*. University of Arizona.
- Samsonov, M. D., Trofimov, T. I., Kulyako, Y. M., Vinokurov, S. E., Malikov, D. A., Batorshin, G. S., &

- Myasoedov, B. F. (2015). Recovery of rare earth elements, uranium, and thorium from monazite concentrate by supercritical fluid extraction. *Radiochemistry*, 57(4), 343–347. <http://doi.org/10.1134/S1066362215040025>
- Samsonov, M. D., Wai, C. M., Lee, S. C., Kulyako, Y., & Smart, N. G. (2001). Dissolution of uranium dioxide in supercritical fluid carbon dioxide. *Chemical Communications (Cambridge, England)*, (18), 1868–1869. <http://doi.org/10.1039/b103468p>
- Schlitt, W. J. (1992). Section 15 Surface and Hybrid Mining: Aqueous Extraction Methods. In H. Hartman (Ed.), *Mining Engineering Handbook: Volume 1* (2nd ed., pp. 1453–1528). Littleton, CO: Society for Mining Metallurgy and Exploration. Retrieved from <http://www.scribd.com/doc/270400438/TITLETOC#scribd>
- Schmidt, R. D., Behnke, K. C., & Friedel, M. J. (1990). Hydrologic considerations of underground in situ copper leaching. In *Society of Mining Engineers Annual Meeting Preprint*. Salt Lake City, UT: Society of Mining Engineers of the American Institute of Mining, Metallurgical, and Petroleum Engineers.
- Schmidt, R. D., Dahl, L. J., Kim, K., Paillet, F. L., & Earley, D. (1995). Characterization of a chalcocite copper ore deposit for in situ leach mining. In *Society for Mining Metallurgy and Exploration Annual Meeting Preprint*. Denver, CO: Society for Mining Metallurgy and Exploration.
- Schmidt, R. D., & Earley, D. (1997). *In situ leaching of fracture hosted chalcocite copper ore at the Cyprus, Mineral Park Mine*. Washington, D.C.: United States Bureau of Reclamation.
- Schmidt, R. D., Earley, D. I., & Friedel, M. J. (1994). Dynamic influences on hydraulic conductivity during in situ copper leaching. In S. A. Swan & K. R. Coyne (Eds.), *In Situ Recovery of Minerals II* (pp. 259–288). New York, NY: Engineering Foundation.
- Schurhammer, R., Berny, F., & Wipff, G. (2001). Importance of interfacial phenomena in assisted ion extraction by supercritical CO₂: a molecular dynamics investigation. *Physical Chemistry Chemical Physics*, 3(5), 647–656. <http://doi.org/10.1039/b007238i>
- Schurhammer, R., & Wipff, G. (2005). Effect of the TBP and water on the complexation of uranyl nitrate

- and the dissolution of nitric acid into supercritical CO₂. A theoretical study. *Journal of Physical Chemistry A*, 109(23), 5208–5216. <http://doi.org/10.1021/jp051029y>
- Sedda, L., Atkinson, P. M., Barca, E., & Passarella, G. (2012). Imputing censored data with desirable spatial covariance function properties using simulated annealing. *Journal of Geographical Systems*, 14(3), 265–282. <http://doi.org/10.1007/s10109-010-0145-1>
- Shamsipur, M., Ghiasvand, A. R., & Yamini, Y. (2001). Extraction of uranium from solid matrices using modified supercritical fluid CO₂. *The Journal of Supercritical Fluids*, 20(2), 163–169. [http://doi.org/10.1016/S0896-8446\(01\)00052-3](http://doi.org/10.1016/S0896-8446(01)00052-3)
- Shimizu, R., Sawada, K., Enokida, Y., & Yamamoto, I. (2005). Supercritical fluid extraction of rare earth elements from luminescent material in waste fluorescent lamps. *The Journal of Supercritical Fluids*, 33(3), 235–241. <http://doi.org/10.1016/j.supflu.2004.08.004>
- Simoës, M. C., Hughes, K. J., Ingham, D. B., Ma, L., & Pourkashanian, M. (2017). Temperature Dependence of the Parameters in the Pitzer Equations. *Journal of Chemical and Engineering Data*, 62(7), 2000–2013. <http://doi.org/10.1021/acs.jced.7b00022>
- Sinclair, L. K. (2015). Test work and geochemical modeling for copper in situ leaching. In *Conference of Metallurgists*. Toronto, Canada: Canadian Institute of Mining.
- Sinclair, L. K. (2016). Metallurgical test work and process modeling for copper in situ leaching. In *ALTA Conference*. Perth, Australia.
- Sinclair, L. K., Baek, D. L., & Fox, R. V. (2016). Pretreatment Methods for Rare Earth Element Extraction in Supercritical Carbon Dioxide. In *XXVIII International Mineral Processing Congress*. Quebec City, Canada: Canadian Institute of Mining, Metallurgy and Petroleum.
- Sinclair, L. K., Baek, D. L., Thompson, J., Tester, J. W., & Fox, R. V. (2017). Rare Earth Element Extraction From Pretreated Bastnäsite in Supercritical Carbon Dioxide. *The Journal of Supercritical Fluids*, 124, 20–29. <http://doi.org/10.1016/j.supflu.2017.01.005>
- Sinclair, L. K., Tester, J. W., Thompson, J. F. H., & Fox, R. V. (2018). The role of water in extraction and separation of rare earth elements in supercritical carbon dioxide. *Journal of Supercritical Fluids*.

<http://doi.org/https://doi.org/10.1016/j.supflu.2018.02.009>

Sinclair, L. K., & Thompson, J. F. H. (2015). In situ leaching of copper: Challenges and future prospects.

Hydrometallurgy, 157, 306–324. <http://doi.org/10.1016/j.hydromet.2015.08.022>

Smart, N. G., Carleson, T., & Kast, T. (1997). Solubility of chelating agents and metal containing compounds in supercritical fluid carbon dioxide, 44, 137–150.

[http://doi.org/https://doi.org/10.1016/S0039-9140\(96\)02008-5](http://doi.org/https://doi.org/10.1016/S0039-9140(96)02008-5)

Smith, J. M. (1970). *Chemical engineering kinetics*. McGraw-Hill. Retrieved from <https://books.google.com/books?id=U8ZTAAAAMAAJ>

Stubben, M. A., & LaBrecque, D. J. (1998). 3-D ERT inversion to monitor an injection experiment. In R. Bell, M. Powers, & T. Larson (Eds.), *Symposium on the Application of Geophysics to Environmental and Engineering Problems* (pp. 603–612). Chicago, IL: Environmental and Engineering Geophysical Society. <http://doi.org/10.4133/1.2922549>

Suchen, S., Zhiying, W., Bo, G., Xue, B., Wenyuan, W., & Ganfeng, T. (2007). Effect of CaO on Fluorine in the Decomposition of REFCO₃. *Journal of Rare Earths*, 25(4), 508–511.

[http://doi.org/10.1016/S1002-0721\(07\)60465-7](http://doi.org/10.1016/S1002-0721(07)60465-7)

Taylor, G., Farrington, V., Woods, P., Ring, R., & Molloy, R. (2004). Review of environmental impacts of the acid in-situ leach uranium mining process. Clayton South, Australia: CSIRO Land and Water. Retrieved from http://www.epa.sa.gov.au/files/4771310_isl_review.pdf

Teoh, W. H., Mammucari, R., & Foster, N. R. (2013). Solubility of organometallic complexes in supercritical carbon dioxide: A review. *Journal of Organometallic Chemistry*, 724, 102–116.

<http://doi.org/10.1016/j.jorganchem.2012.10.005>

Tester, J. W., & Modell, M. (1997). *Thermodynamics and Its Applications*. Prentice Hall PTR. Retrieved from <https://books.google.com/books?id=DiVhQgAACAAJ>

The International Centre for Diffraction Data. (2013). PDF-2 Technical Bulletin. Newtown Square, PA, USA: International Centre for Diffraction Data.

Tomioka, O., Enokida, Y., & Yamamoto, I. (1998). Solvent Extraction of Lanthanides from their Oxides

- with TBP in Supercritical Carbon Dioxide. *Journal of Nuclear Science and Technology*, 35(7), 515–516.
- Tomioka, O., Enokida, Y., & Yamamoto, I. (2002). Selective recovery of neodymium from oxides by direct extraction method with supercritical CO₂ containing TBP–HNO₃ complex. *Separation Science and Technology*, 37(5), 1153–1162. <http://doi.org/10.1081/SS-120002247>
- United States Bureau of Mines. (1989). Introduction. In *In situ leach mining: proceedings: Bureau of Mines technology transfer seminars* (pp. 2–3). Phoenix, AZ, and Salt Lake City, UT: United States Bureau of Mines. Retrieved from <https://books.google.com/books?id=HpqD5YM11mgC>
- United States Congress Office of Technology Assessment. (1988). *Copper, Technology & Competitiveness*. Washington, D.C.: Congress of the U.S., Office of Technology Assessment. Retrieved from <https://books.google.com/books?id=cswHg1Pfl78C>
- United States Department of Energy. (2011). *Critical materials strategy*. Retrieved from http://energy.gov/sites/prod/files/DOE_CMS2011_FINAL_Full.pdf
- United States Geological Survey. (2017). Rare Earth Statistics and Information. Retrieved December 8, 2017, from https://minerals.usgs.gov/minerals/pubs/commodity/rare_earths/
- Vahidi, E., & Zhao, H. (2016). Life Cycle Analysis for Solvent Extraction of Rare Earth Elements from Aqueous Solutions. In *Rewas 2016: Towards Materials Resource Sustainability*. The Minerals, Metals & Materials Society. <http://doi.org/1002/9781119275039.ch17>
- Wai, C. M., Liao, Y.-J., Liao, W., Tian, G., Addleman, R. S., Quach, D., & Pasilis, S. P. (2011). Uranium dioxide in ionic liquid with a tri-n-butylphosphate–HNO₃ complex--dissolution and coordination environment. *Dalton Transactions (Cambridge, England: 2003)*, 40(18), 5039–5045. <http://doi.org/10.1039/c0dt01518k>
- Wang, Z.-C., He, M., Wang, J., & Li, J.-L. (2006). Modeling of Aqueous 3–1 Rare Earth Electrolytes and Their Mixtures to Very High Concentrations. *Journal of Solution Chemistry*, 35(8), 1137–1156. <http://doi.org/10.1007/s10953-006-9050-0>
- Wang, Z., Felmy, A. R., Thompson, C. J., Loring, J. S., Joly, A. G., Rosso, K. M., ... Dixon, D. A. (2013).

- Fluid Phase Equilibria Near-infrared spectroscopic investigation of water in supercritical CO₂ and the effect of CaCl₂. *Fluid Phase Equilibria*, 338, 155–163. <http://doi.org/10.1016/j.fluid.2012.11.012>
- Wang, Z., Liu, T., He, X., Zhu, L., & He, H. (2017). Competitive complexation of solid lanthanide nitrates with tri-n-butyl phosphate in n-hexane. *Journal of Radioanalytical and Nuclear Chemistry*, 311(1), 483–489. <http://doi.org/10.1007/s10967-016-5027-7>
- Weber, D. S., Barter, C. F., & Kreis, H. G. (2000). Hydraulic testing for identification of fluid movement patterns at Santa Cruz in situ copper mining research project, Pinal County, Arizona. In *Society for Mining Metallurgy and Exploration Annual Meeting Preprint*. Salt Lake City, UT: Society for Mining Metallurgy and Exploration.
- Wen, X. H. (1994). Estimation of statistical parameters for censored lognormal hydraulic conductivity measurements. *Mathematical Geology*, 26(6), 717–731. <http://doi.org/10.1007/BF02086868>
- Wiley, K. L., Ramey, D. S., & Rex, M. J. (1994). In situ leaching wellfield design at San Manuel. *Mining Engineering*, 46(8), 991–994.
- Williamson, C. (1998). *Hydrologic mechanisms and optimization of in situ copper leaching: case study - BHP Copper, San Manuel, Arizona*. University of Arizona.
- Wuhua, D., Pijia, C., & Yongjun, Z. (2010). Extraction of rare earth elements from their oxides using organophosphorus reagent complexes with HNO₃ and H₂O in supercritical CO₂. *Journal of Rare Earths*, 28(2), 221–226. [http://doi.org/10.1016/S1002-0721\(09\)60084-3](http://doi.org/10.1016/S1002-0721(09)60084-3)
- Xiang, J., Zhang, C., Tu, G., & Ren, C. (1994). Thermal Decomposition Behaviour of Natural Bastnasite Crystal in Calcination. *Transactions of Nonferrous Metals Society of China*.
- Xie, F., Zhang, T. A., Dreisinger, D., & Doyle, F. (2014). A critical review on solvent extraction of rare earths from aqueous solutions. *Minerals Engineering*, 56, 10–28. <http://doi.org/10.1016/j.mineng.2013.10.021>
- Yao, Y., Farac, N. F., & Azimi, G. (2017). Supercritical Fluid Extraction of Rare Earth Elements from Nickel Metal Hydride Battery. *ACS Sustainable Chemistry & Engineering*, acssuschemeng.7b03803. <http://doi.org/10.1021/acssuschemeng.7b03803>

- Yegulalp, T. M., & Kim, K. (1996). Application of percolation theory to the assessment of permeability enhancement by micro-hydrofracturing for in situ copper leaching. *Mining Engineering, Jan 1996*, 45–48.
- Yörükoğlu, A., Obut, A., & Girgin, I. (2003). Effect of thiourea on sulphuric acid leaching of bastnaesite. *Hydrometallurgy*, 68(1–3), 195–202. [http://doi.org/10.1016/S0304-386X\(02\)00199-8](http://doi.org/10.1016/S0304-386X(02)00199-8)
- Young, S. (1999). A look at leach SX-EW with 2020 vision. In S. K. Young, D. Dreisinger, R. P. Hacki, & D. G. Dixon (Eds.), *Copper 99-Cobre 99 Volume IV - Hydrometallurgy of Copper* (Vol. 4, pp. 611–619). Phoenix, AZ: The Minerals, Metals, & Materials Society.
- Zhang, J., & Zhao, B. (2016). *Separation Hydrometallurgy of Rare Earth Elements*. Springer. <http://doi.org/10.1007/978-3-319-28235-0>
- Zhang, P., & Kimura, T. (2006). Complexation of Eu(III) with dibutyl phosphate and tributyl phosphate. *Solvent Extraction and Ion Exchange*, 24(2), 149–163. <http://doi.org/10.1080/07366290500464276>
- Zhang, P., Kimura, T., & Yoshida, Z. (2004). Luminescence study on the inner-sphere hydration number of lanthanide(III) ions in neutral organo-phosphorus complexes. *Solvent Extraction and Ion Exchange*, 22(6), 933–945. <http://doi.org/10.1081/SEI-200037439>
- Zhu, L., Duan, W., Xu, J., & Zhu, Y. (2009). Kinetics of Reactive Extraction of Nd from Nd₂O₃ with TBP-HNO₃ Complex in Supercritical Carbon Dioxide. *Chinese Journal of Chemical Engineering*, 17(2), 214–218. [http://doi.org/10.1016/S1004-9541\(08\)60196-2](http://doi.org/10.1016/S1004-9541(08)60196-2)
- Zhu, L. Y., Duan, W. H., Xu, J. M., & Zhu, Y. J. (2011). Conversion of neodymium oxide with N₂O₄ into nitrate followed by supercritical fluid extraction of nitrate.pdf, 443–448. <http://doi.org/10.1007/s10967-010-0701-7>
- Zhu, L. Y., Wang, Z. F., He, H., & Tian, G. (2016). Competition between lanthanides in extraction with tri-n-butyl phosphate in supercritical CO₂ from solid nitrates. *RSC Adv.*, 6(99), 96531–96537. <http://doi.org/10.1039/C6RA20687E>
- Zimmerman, R., Young, M. R., Hoag, C., McNulty, T., Tucker, D., & Frechette, R. (2013). *Technical Report Pre-Feasibility Study Florence, Pinal County, Arizona*. Tucson, AZ.